Characterization and early detection of dynamic behavior of isolated and interacting flames

Thesis submitted by
Arijit Bhattacharya

Doctor of Philosophy (Engineering)

Department of Mechanical Engineering
Faculty Council of Engineering & Technology
Jadavpur University
Kolkata, India

2022

JADAVPUR UNIVERSITY
FACULTY OF ENGINEERING AND TECHNOLOGY

INDEX NO. **193/17/E**

1. **Title of the Thesis**: Characterization and early detection of dynamic behavior of isolated and interacting flames

2. **Name, Designation and Institution of the Supervisor/s:**

   (a) **Prof. Achintya Mukhopadhyay**
   Professor, Department of Mechanical Engineering
   Jadavpur University, Kolkata –700032

   (b) **Prof. Swarnendu Sen**
   Professor, Department of Mechanical Engineering
   Jadavpur University, Kolkata –700032

3. **List of Publications:**

   (a) **Journals**

      i. **Arijit Bhattacharya**, Somnath De, Sirshendu Mondal, Achintya Mukhopadhyay and Swarnendu Sen, "Recurrence network analysis exploring the routes to thermoacoustic instability in a Rijke tube with inverse diffusion flame", Chaos: An Interdisciplinary Journal of Nonlinear Science, 31(3), p.033117, 2021 (DOI: 10.1063/5.0026943).

      ii. **Arijit Bhattacharya**, Somnath De, Sirshendu Mondal, Achintya Mukhopadhyay and Swarnendu Sen,"Early detection of lean blowout using recurrence network for varying degrees of premixedness", Chaos: An Interdisciplinary Journal of Nonlinear Science, 32, 063105, 2022 (DOI: 10.1063/5.0077436).

      iii. **Arijit Bhattacharya**, Sirshendu Mondal, Somnath De, Achintya Mukhopadhyay and Swarnendu Sen, "Synchronization behavior between two candle flame oscillators with similar and dissimilar amplitudes of oscillations",Combustion Theory and Modelling (DOI: 10.1080/13647830.2023.2165966) .

      iv. **Arijit Bhattacharya**, Sabyasachi Mondal, Somnath De, Achintya Mukhopadhyay and Swarnendu Sen, "Early prediction of lean blowout using topological data analysis", (communicated).

   (b) **International Conferences**

      i. **Arijit Bhattacharya**, Sirshendu Mondal, Srinjoy Saha, Arnab Chakroborty, Pritam Singh , Somnath De, Achintya Mukhopadhyay and Swarnendu Sen, "Dynamic Transitions in Coupled Candle Flame Oscillators", Proceedings of International Conference on Energy and Sustainable Development, 2020.

ii. **Arijit Bhattacharya**, Bikash Gupta, Satyajit Hansda, Zohadul Haque, Ashish Kumar, Manohar Kumar Mishra , Somnath De, Achintya Mukhopadhyay, Swarnendu Sen, "Lean blowout phenomena and prior detection of lean blowout in a premixed model annular combustor", Proceedings of the ASME 2019 Gas Turbine India Conference, 2019.

iii. **Arijit Bhattacharya**, Somnath De, Soumyadeep Das, Achintya Mukhopadhyay, Swarnendu Sen, "Detection of thermoacoustic instability for an inverse diffusion flame in a Rijke tube using recurrence network approach", Proceedings of the 12th Asia-Pacific Conference on Combustion, 2019.

iv. **Arijit Bhattacharya**, Somnath De, Achintya Mukhopadhyay, Swarnendu Sen, "Detection of Flame Instability Prior to Lean Blowout using Recurrence Network Approach", Proceedings of the 7th International and 45th National Conference on Fluid Mechanics and Fluid Power, 2018.

(c) **National Conferences**

i. **Arijit Bhattacharya**, Somnath De, Raunak Basak, Shanu Pratap, Achintya Mukhopadhyay, Swarnendu Sen, "Dynamic characteristics of inverse diffusion flame", Proceedings of the 2nd National Aero Propulsion Conference, 2018.

4. **List of Patents:** None

5. **List of Presentations in National/International Conferences:**

   (a) **Arijit Bhattacharya**, Sirshendu Mondal, Srinjoy Saha, Arnab Chakroborty, Pritam Singh , Somnath De, Achintya Mukhopadhyay and Swarnendu Sen, "Dynamic Transitions in Coupled Candle Flame Oscillators", Proceedings of International Conference on Energy and Sustainable Development, 2020.

   (b) **Arijit Bhattacharya**, Bikash Gupta, Satyajit Hansda, Zohadul Haque, Ashish Kumar, Manohar Kumar Mishra , Somnath De, Achintya Mukhopadhyay, Swarnendu Sen, "Lean blowout phenomena and prior detection of lean blowout in a premixed model annular combustor", Proceedings of the ASME 2019 Gas Turbine India Conference, 2019.

   (c) **Arijit Bhattacharya**, Somnath De, Soumyadeep Das, Achintya Mukhopadhyay, Swarnendu Sen, "Detection of thermoacoustic instability for an inverse diffusion flame in a Rijke tube using recurrence network approach", Proceedings of the 12th Asia-Pacific Conference on Combustion, 2019.

   (d) **Arijit Bhattacharya**,Somnath De, Achintya Mukhopadhyay, Swarnendu Sen, "Detection of Flame Instability Prior to Lean Blowout using Recurrence Network Approach", Proceedings of the 7th International and 45th National Conference on Fluid Mechanics and Fluid Power, 2018.

   (e) **Arijit Bhattacharya**, Somnath De, Raunak Basak, Shanu Pratap, Achintya Mukhopadhyay, Swarnendu Sen, "Dynamic characteristics of inverse diffusion flame", Proceedings of the 2^{nd} National Aero Propulsion Conference, 2018.

JADAVPUR UNIVERSITY
FACULTY OF ENGINEERING AND TECHNOLOGY

STATEMENT OF ORIGINALITY

I, **Shri Arijit Bhattacharya** registered on **10^{th} August, 2017**, do hereby declare that this thesis entitled **"Characterization and early detection of dynamic behavior of isolated and interacting flames"** contains literature survey and original research work done by the undersigned candidate as part of Doctoral studies.

All information in this thesis have been obtained and presented in accordance with existing academic rules and ethical conduct. I declare that, as required by these rules and conduct, I have fully cited and referred all materials and results that are not original to this work.

I also declare that I have checked this thesis as per the Policy on Anti Plagiarism, Jadavpur University, 2019, and the level of similarity as checked by iThenticate software is 5_%.

Signature of the Candidate : Arijit Bhattacharya

Date : 2.11.2022

Certified by Supervisors :
(Signature with date, seal)

1. Achintya Mukhopadhyay 2.11.2022
(Prof. Achintya Mukhopadhyay)

Professor
Dept. of Mechanical Engineering
Jadavpur University, Kolkata-32

2. Swarnendu Sen 2/11/2022
(Prof. Swarnendu Sen)

Professor
Dept. of Mechanical Engineering
Jadavpur University, Kolkata-32

Professor
Dept. of Mechanical Engineering
Jadavpur University, Kolkata-32

JADAVPUR UNIVERSITY
FACULTY OF ENGINEERING AND TECHNOLOGY

CERTIFICATE FROM THE SUPERVISOR/S

This is to certify that the thesis entitled **"Characterization and early detection of dynamic behavior of isolated and interacting flames"** submitted by **Shri Arijit Bhattacharya**, who got his name registered on 10^{th} August, 2017 for the award of **Ph.D. (Engg.)** degree of Jadavpur University is absolutely based upon his own work under the supervision of **Prof. Achintya Mukhopadhyay** and **Prof. Swarnendu Sen** and that neither his thesis nor any part of the thesis has been submitted for any degree/diploma or any other academic award anywhere before.

1. Achintya Mukhopadhyay 2.11.2022
(Prof. Achintya Mukhopadhyay)
Signature of the Supervisor
and date with Official seal

Professor
Dept. of Mechanical Engineering
Jadavpur University, Kolkata-32

2. Swarnendu Sen 2/11/2022
(Prof. Swarnendu Sen)
Signature of the Supervisor
and date with Official seal

Professor
Dept. of Mechanical Engineering
Jadavpur University, Kolkata-32

. . . . . .

Dedicated to my parents

. . . . . .

Acknowledgements

When I asked **Prof. Achintya Mukhopadhyay** and **Prof. Swarnendu Sen** for the opportunity to pursue my PhD research work under their guidance, I had little knowledge of how rigorous research is conducted. Understanding my plight, my supervisors have patiently helped me through the process of identifying research problems, carrying out the research and writing up the results in a manner that is understandable to the broad audience. Their understanding and observations on the various experimental phenomena enabled me to occasionally correct my course during this research work. I frequently came across obstacles that seemed insurmountable until my supervisors, **Prof. Achintya Mukhopadhyay** and **Prof. Swarnendu Sen**, offered a simple solution based on their extensive knowledge of experimental research. Therefore, I take this opportunity to thank my supervisors for guiding me through the research process.

I must thank the respected professors, **Prof. Kamalesh Majumdar**, **Prof. Sankar Dhar**, **Prof. Dipankar Sanyal**, **Prof. Rana Saha**, **Prof. Saikat Mookherjee**, **Prof. Kaushik Ghosh**, **Prof. Nirmal Manna**, **Prof. Sandip Sarkar**, of the Project Peptune Laboratory, for their encouragement and valuable discussions I had with them, during the course of my research work.

I can not thank enough my esteemed senior of the Project Neptune Laboratory, **Dr. Sirshendu Mondal** (currently professor, Department of Mechanical Engineering, NIT Durgapur) who has painstakingly and selflessly taught me invaluable lessons on how to do better research. I am thankful to **Dr. Somnath De**, senior member of the Project Neptune Laboratory, from whom I learnt how to perform the combustion experiments and analyze the results. I am eternally grateful to **Mr. Sabyasachi Mondal**, junior member of the Project Neptune Laboratory, who has selflessly helped me in conducting the experiments on multi-burner combustors.

A number of UG students have helped me during setting up of the combustor rigs as well as helped me during the experiments. The hard work and innovative thinking of **Mr. Raunak Basak, Mr. Shanu Pratap, Mr. Bikash Gupta, Mr. Satyajit Hansda, Mr. Zohadul Haque, Mr. Ashish Kumar, Mr. Manohar Misra**, former UG students of Department of Mechanical engineering, Jadavpur University, helped me to overcome the difficult setting-up process of the two multi-burner combustors. I must thank **Mr. Pritam Singh**, UG student from Rajasthan Technical University, who did his summer training in Project Neptune Laboratory and helped me in my experiments. I am grateful to **Mr. Srinjoy Basu** and **Mr. Arnab Chakroborty**, former UG students of Department of Mechanical engineering, Jadavpur University, for their diligence and innovative thinking, due to which we were able to build up the interacting candle flame setup in a quick and simple manner.

I am thankful to **Dr. Shouvik Chaudhuri** and **Mr. Niladri Naskar**, for helping me set up various sensors and data acquisition systems. I am grateful to **Dr. Mrinmoy Jana** who generously helped me when taking measurement of various critical components of the multi-burner combustors.

I am grateful to **Dr. Pranibesh Mondal, Mr. Sourav Sarkar, Dr. Priyankan Datta, Dr. Aranyak Chakravarty, Dr. Ritabrata Saha,**

Dr. Nirmalendu Biswas, Dr. Parichoy Basu, Dr. Swagatam Paul, Dr. Snehashish Bhattacharjee, Dr. Sukalpa Chaudhuri, Mr. Abu Bakar Siddiqui Thakur, Mr. Krishnendu Maji, Mr. Abhinava saha, Dr. Nitesh Mondal, Mr. Aniruddha Sarkar, Mr. Gaurav Banerjee, Mr. Arindam Mondal, Mr. Soumendra misra, Mr. Sudipto Saha, senior and junior members of the Project Neptune Laboratory, for the insightful discussions I had with them and their help during my research work. I must thank **Mr. Tuhin Mitra, Dr. Joydeep Munshi, Mr. Sachin Jain, Mr. Anish Pal**, former Masters students of Project Neptune Laboratory, for their invaluable inputs and discussions during the course of my study.

I am thankful to **Dr. Tamonash Jana, Dr. Sushanta Ghuku, Dr. Avishek Roy, Mr. Sujit Saha**, present and former Ph.D scholars from Mechanical Engineering Department, Jadavpur University, for their encouragement and valuable discussions during the course of this work.

I gratefully acknowledge the financial support by Science and Engineering Research Board, Government of India, during the course of this study. I am immensely grateful for the financial supports from Rashtriya Uchchatar Shiksha Abhiyan (RUSA) 2.0 of Jadavpur University during my research work.

Lastly, I thank my parents, without whose unconditional support, I could not have ventured into the long and difficult path of scientific research.

Arijit Bhattacharya
Ph.D. Fellow, Jadavpur University

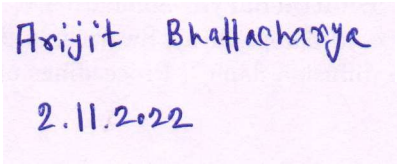

Abstract

Increasingly strict emission norms have led to the development of alternative combustion technologies having low NO_X emission. One commonly used low NO_X technology is lean premixed or, partially premixed combustion. However, this technology is susceptible to lean blowout (LBO) and thermoacoustic instability (TAI) which can prevent the combustor to run safely and reliably. LBO is caused by a sudden drop in the equivalence ratio in the combustor, often during sudden load changes in aircraft. On the other hand, power-plant gas turbine combustors run very close to the LBO limit. Due to this LBO can be triggered by intrinsic instabilities in the flame. Moreover, often the LBO and TAI limit in a lean premixed combustor are separated by a small margin of equivalence ratio, so that triggering of one can cause the other. Another potential technology that generates low NO_X and soot is the inverse diffusion flame (IDF). IDF is significantly less susceptible to lean blowout and flashback as compared to premixed flames. However, a confined IDF is still susceptible to TAI.

Consequently, there is a strong motivation to avoid LBO and TAI. Unfortunately, the operating point at which LBO/TAI would be triggered is not fixed. The LBO/TAI limit depends on several operating conditions many of which are outside of human control (*e.g.*, ambient temperature and pressure). Further, there is a lack of reliable technology for accurate early prediction of impending LBO and TAI. Therefore, to avoid LBO and TAI, the current practice is to operate the combustor with a relatively large safety margin. This, however, results in sub-optimal operation of combustor and increased NO_X emissions. Therefore, it is of utmost importance to devise reliable techniques that can early predict LBO and TAI even before they occur so that sufficient time is available to take appropriate action to prevent the onset of LBO/TAI. Moreover, such tools must be robust so that they apply to a wide range of combustor configurations with minimal additional experimentations and calibrations.

Previous studies have mostly focused on the flame behavior at TAI/LBO with single-burner combustors. However, practical combustors have multiple flames which often interact with each other. Consequently, the flame behavior in practical combustors is likely to have significant differences from the flame behavior in single-burner combustors. In addition, most aircraft gas turbine combustors employ partially premixed flames due to space constraints and less time available for air-fuel mixing.

To bridge these gaps in the literature, in this work we systemically study the dynamical behavior of isolated flame and interacting flame. We explore the flame

behavior for various degrees of premixedness and also for various combustor configurations. To understand the flame dynamics, flame visualization is carried out. We also explore the dynamical transition to LBO/TAI, for the various configurations studied, using well-established tools of dynamical science. Such an approach may be useful to devise robust tools for early detecting impending LBO/TAI that can be used for a wide range of combustors, with minimal calibrations. Below, a brief description of the thesis content is provided.

In the first chapter of this thesis, a brief discussion on the current state of the art, concerning the different flame instabilities encountered in gas turbine combustors, is provided. Based on this discussion, the research gaps are identified and the objective of this thesis work is set.

An important part of exploring flame behavior is to study the underlying dynamical nature of the flame. As the first step to this goal, **in the second chapter** we explore the dynamical characteristics of thermoacoustic instability (TAI), which is a simple and distinct dynamical phenomenon. For this study, a Rijke tube with an inverse diffusion flame (IDF) is used. IDF is a type of partially premixed flame that is suitable for practical applications in gas turbine combustors. Previous studies have reported that the flame behavior of IDF is significantly different from that of premixed flame. Therefore, studying the dynamical transition to thermoacoustic instability with IDF is of practical significance especially as IDF includes the benefits of both diffusion flame and premixed flame (namely, high stability against LBO and flashback while having a low NO_X emission).

The thermoacoustic instability phenomenon is investigated with various well-known tools of dynamical science, including recurrence network (RN). RN is a type of complex network that can capture a dynamical transition with a short time series and is robust against noise. We quantify the characteristics of the recurrence network with three metrics: global efficiency (η), average degree centrality (k), and global clustering coefficient (C_G). These metrics are found to correctly capture the dynamical transition of the combustor from the stable combustion state to TAI. Further, the RN metrics follow monotonic trends during the approach to TAI. This indicates that the RN metrics can be used to fine-tune the safety margin to TAI with carefully chosen RN metric thresholds at which an impending TAI alert should be issued. Moreover, using the RN tool, we uncover various significant differences in the dynamic characteristics of inverse diffusion flame and lean premixed flame at the thermoacoustic instability state, the latter being reported in previous literature.

In the third chapter, a lean premixed single-burner combustor is studied to explore its dynamical characteristics. A lean premixed flame has a significantly lower temperature as compared to a diffusion flame. The lower flame temperature

results in a significant reduction in NO_X emission. On the other hand, the combustors operating on lean premixed technology are prone to lean blowout which can prevent stable and reliable operation of the combustor.

Modern gas turbine combustors often have multiple burners with an annular or a can configuration. Still, single-burner combustors have often been explored as a simple model for practical, multi-burner combustors. Moreover, the flame corresponding to the single-burner combustor is an isolated flame. It is helpful to study the flame instabilities with the single-burner combustor before we explore flame instabilities with multi-burner combustors, which are much more complex. Such a step-by-step approach would help to bring out the differences in flame instabilities caused by flame-flame interactions. Therefore, next, we explore the lean blowout instability in a swirl-dump stabilized single-burner combustor.

We find that the single-burner combustor suffers LBO without a preceding TAI, as the equivalence ratio is reduced, regardless of the degree of premixedness in the combustor. The route to LBO with a preceding TAI has been reported in the literature. With the recurrence network analysis, we discover that when LBO occurs without a preceding TAI, the dynamical transition to LBO is considerably different than when LBO occurs with a preceding TAI. We observe that the recurrence network tool is a robust and computationally inexpensive early LBO detection tool.

As discussed above, most modern combustors are of annular or can type configuration, having multiple flames arranged on a circumference. In such combustors, flame-flame interaction plays a significant role to influence the flame behavior. For example, previous studies indicate that the physics associated with various combustion instabilities in multi-burner combustors cannot be captured with single-burner combustors.

Therefore, in the fourth chapter, we consider two flames exhibiting self-sustained oscillations and study whether the interaction between these two flames affects their oscillation dynamics in any significant way. To simplify the problem, we explore the flame-flame interaction of a pair of candle flame oscillators (CFO), which is one of the simplest types of flame.

Many studies have investigated the flame-flame interaction between two identical (in other words, closely similar) flames. However, in practical scenarios, the flames corresponding to different burners of a multi-burner combustor will have some dissimilarities. This is because it is not possible to manufacture identical burners, due to manufacturing considerations. The effects of flame-flame interaction between such dissimilar flames have not been explored in a systematic way to date. Therefore, we explore the effect of flame-flame interaction between two CFOs by parametrically varying the distance between the oscillators. Moreover,

we study how the resulting flame behavior is affected by the dissimilarity of the amplitude of oscillations in the two interacting flames. We observe significantly different flame dynamics for a couple of interacting CFOs as compared to that for a single isolated CFO. Moreover, we find that the degree of dissimilarity and distance between the interacting CFOs profoundly affect the resulting flame dynamics. The interaction of CFOs having a similar amplitude of oscillations shows a simple dynamical transition as the distance between the CFOs is varied. In contrast, the interaction between CFOs having a dissimilar amplitude of oscillations shows a more complex dynamical transition.

In modern multi-burner combustors, flame-flame interactions are likely as the adjacent burners are placed in close proximity. Based on the above discussions on interacting candle flames, we infer that the flame behavior in multi-burner combustors may have significant differences compared with that in single-burner combustors. However, almost all previous studies have explored the LBO phenomena with single-burner combustors.

To bridge this gap in the literature, **in the fifth chapter** we study the LBO phenomena in an annular combustor and a linear array combustor. From visual inspection of flame, we find that the flame behavior at the near-LBO state is markedly different in the annular and linear array combustors as compared to that in an analogous single-burner combustor (the flame behavior in the analogous single-burner combustor has been reported in a previous study). It is seen that the flame-to-flame and burner-to-burner interactions, at the near-LBO state, reduce the severity of the extinction events in the annular and linear array combustors. For example, often a lifted flame is anchored (and thus prevented from blowing out) by the flame from an adjacent burner. Further, an extinguished burner is often reignited by the flame from an adjacent burner. In short, several phenomena including partial attachment-detachment of flame from burner tip, flame merging-unmerging, partial extinction-reignition, flame-to-flame, and burner-to-burner interactions, etc. phenomena are seen at the near-LBO state for the annular and linear array combustors, which cannot be captured in single-burner combustors.

Previous literature and also the results obtained during the present thesis work indicate that significant differences are likely in the near-LBO flame dynamics of the single-burner combustor (having a solitary flame) and the multi-burner combustor (having several interacting flames). However, the flame dynamics cannot be explored in detail with flame visualization only. Thus it would be worthwhile to compare the dynamical transition to LBO in multi-burner and single-burner combustors with well-established dynamical science-based tools. This study is also practically relevant as most of the early LBO detection tools have been developed based on single-burner combustor data. Consequently, their efficacies to

early detect LBO in multi-burner combustors are little explored to date.

Therefore, **in the sixth chapter**, we study the dynamical transition to LBO in the annular and linear array combustors with various well-known dynamical science-based tools. We find that the recurrence network tool is unable to capture the transition to LBO in the annular and linear array combustors. This might be due to the additional complexity in the flame dynamics, introduced by the presence of several oscillating flames, instead of a single oscillating flame. Thus in this study, we propose a novel and robust technique, topological data analysis (TDA), as an early LBO prediction tool. We observe that TDA metrics follow monotonic trends during the transition to LBO. Such monotonic trends would enable fine-tuning of the LBO safety margin. Next, we observe that a type of TDA, the sub-level set TDA tool, is highly effective as an early LBO prediction tool. Further, the sub-level set TDA tool is suitable for fine-tuning the LBO safety margin. This is a highly desirable feature from a practical implementation point of view. The sub-level set TDA tool does not require phase-space embedding, therefore enabling easier implementation in a practical scenario. Further, we observe that the TDA metrics have closely matching monotonic trends at various sampling rates. This fact indicates that TDA may be implemented on data taken with a low sampling rate sensor. Therefore, a low-cost, simple and rugged sensor can be used for data acquisition. Such a sensor is highly desirable from a practical application point of view. In short, the results indicate TDA is a highly effective tool for early LBO prediction in single-burner combustors (having a solitary flame) as well as multi-burner combustors (having several interacting flames).

In the seventh chapter, the findings of this thesis work are summarized and future work recommendations are prescribed. In short, this thesis work explores the flame behavior in the solitary and interacting flames, for various degrees of premixedness, using flame visualization and well-established dynamical science-based tools. Several insights are obtained during this thesis work which may prove useful in understanding the TAI and LBO instabilities in practical gas turbine combustors.

Contents

List of Figures

List of Tables

List of Abbreviations

Symbols

3/3 case	Interacting candle flame oscillators having 3 candles in each oscillator
3/4 case	Interacting candle flame oscillators having 3 and 4 candles in the two candle flame oscillators
3/5 case	Interacting candle flame oscillators having 3 and 5 candles in the two candle flame oscillators

A

AC	Annular combustor
AC-F1 - AC-F4	Annular combustor configurations. Fuel is injected through F1-F4 ports, respectively
AD	Amplitude death
AP	Anti-phase synchronization

C

CB	Central burner (for linear array combustor)
CFB	Center-front burner (for the annular combustor)
CFO	Candle flame oscillators
CRB	Center- rear burner (for the annular combustor)

D

DS	Desynchronization

I

IP	In-phase synchrony

L

LAC	Linear array combustor

LAC-F1-45, and LAC-F1-65 Linear array combustor configurations, having burner-to-burner distance of 45 mm and 65 mm, respectively. Fuel is injected through F1 port.

LAC-F1-55 - LAC-F4-55 Linear array combustor configurations, having burner-to-burner distance of 55 mm. Fuel is injected through F1-F4 ports, respectively

LBO Lean blowout

LS Lag synchronization

LSB Left-hand side burner

P

PAD Partial amplitude death

R

RMS Root mean square

RQA Recurrence quantification analysis

RSB Right-hand side burner

T

TAI Thermoacoustic instability

TDA Topological data analysis

List of Symbols

A list of frequently used symbols in this thesis, along with their meanings, is provided below.

Scalar Symbols (English Alphabets)

$\dot{Q}_{air}$ Volumetric air flow

C_L Autocorrelation function

D Persistent diagram

DET Determinism

$E(D)$ Persistent entropy

$E'(D)$ Normalized persistence entropy

E_{trans} Translational error

f Frequency of the candle flame oscillators (Hz)

H_0, H_1 Connected components and loops, respectively, in the topological space

K Coupling strength of the two candle flame oscillators

k Average degree centrality

L Average path length

l Spacing between the candle flame oscillators (mm)

$L(D)$ Sum of persistences (i.e. lifetimes) of different classes in the persistent diagram D

LAM Laminarity

$maxpers(D)$ Maximum persistence among all the classes present in the persistent diagram D

$P(X)$ Probability of nodes having degree X in the RN

Re_{air} Reynold number of air flow

$Rips(X, \epsilon)$ Rips filtration complex obtained with ϵ threshold, obtained with a point cloud X

S_W Swirl number

$X_1(t), X_2(t)$ Normalized time series of the two candle flame oscillators

Scalar Symbols (Greek Alphabets)

$\dot{m}_f$	Mass flow rate of fuel (LPG)	Kg/sec
$\dot{m}_{ox}$	Mass flow rate of oxidizer	Kg/sec
η	Global efficiency	
γ	Power law exponent	
κ	Mixture fraction heterogeneity	
Λ	Largest Liapunov coefficient	
λ_2	Second minimum Eigen value of the Laplacian matrix	
$\langle\phi(t)\rangle$	Average relative phase	
μ_{air}	Dynamic viscosity of air	Ns/m^2
ϕ	Equivalence ratio	
$\phi(t)$	Instantaneous relative phase	
ψ	Mixture fraction	
ρ	Pearson correlation coefficient	
ρ_p	Phase space density	
ρ_{air}	Density of air	Kg/m^3
τ_c	The time delay of coupling	
τ_d	Optimal time delay	
$\xi(t)$	Analytical time series	
C_G	Global clustering coefficient	

Vector Symbols (English & Greek Alphabets)

a Adjacency matrix

R Recurrence matrix

Z Reconstructed phase space vector

CHAPTER 1

Introduction

1.1 Background

In today's world, various modes of combustion are used to provide much of the world's energy needs, including electricity generation and the energy requirement for transport. In general, the combustion process is driven by a premixed or diffusion flame. Till recently, gas turbines, which are a popular choice in stationary power plants and air-crafts, used diffusion flame due to its high stability. However, diffusion flames emit a high amount of soot and NO_X. Increasingly strict emission norms have led to the development of alternative combustion technologies having low NO_X emission [1].

One commonly used low NO_X technology is lean premixed combustion. Unfortunately, a lean fuel-air mixture is also susceptible to lean blowout (LBO) and thermoacoustic instability (TAI) [2], [3]. Lean blowout occurs due to the imbalance of local flow rate and flame speed [4]. Lean blowout can occur in aircraft combustors as well as in stationary combustors. In aircraft engines, often when the fuel flow rate is throttled, the fuel supply rate reduces quickly. On the other hand, airflow is governed by compressor inertia and takes a much longer time to change. This leads to a sudden drop in the equivalence ratio in the combustor for a short period of time. Often during this transitory period, the weakened lean flame blows out. In the case of stationary gas turbines, the combustor often operates close to the LBO limit. Due to this, slightest changes in the operating condition may trigger LBO. Lean blowout leads to prolonged downtime and loss of productivity in power station gas turbines and fatal accidents in aircraft.

On the other hand, thermoacoustic instability (TAI) is characterized by high amplitude near-periodic oscillations [3]. It occurs due to a positive coupling of fluctuating heat release rate in the combustor and acoustic waves inside the combustor [3], [5]. Thermoacoustic instability poses significant problems to the operation of

gas turbine combustors; these include unreliable operation, structural damages, and fatal accidents[6].

Consequently, there is a strong motivation to avoid LBO and TAI. Recent literature [7], [8] showed that the thermoacoustic instability and lean blowout are often separated by a small range of equivalence ratios. Unfortunately, the stability margins of the combustor, corresponding to LBO and TAI, changes with operating conditions that cannot be controlled in practice (*e.g.*, ambient temperature and pressure). This highlights the importance of online monitoring of the combustor stability limits. Unfortunately, even today the combustor stability limits cannot be monitored in real time due to the lack of reliable methods. Therefore, to avoid LBO/TAI, the current practice is to operate the combustor with a relatively large factor of safety. This, however, results in sub-optimal operation of combustor and increased NO_X emissions. Therefore, it is of utmost importance to devise techniques that can monitor combustor stability limits in real-time. Such techniques must be able to detect the impending onset of LBO/TAI early enough so that sufficient time for control action is available.

1.2 Literature survey

Because the thermoacoustic instability (TAI) and lean blowout (LBO) pose significant operational difficulties in gas turbine combustors, a wide number of studies have explored these phenomena from various angles. It is important to describe the state of the art in the characterization and early detection of TAI and LBO instabilities, for completeness of this work. Standard approaches to study the LBO and /or TAI consist of mainly the following approaches:

1. Full 3D LES numerical solution.
2. Acoustic solvers.
3. Experimental approach including flame visualization.
4. Dynamical science-based characterization and early detection of TAI/LBO.

According to Previous research, full **3D LES** outperforms RANS modelling in capturing the multiple modes relating to thermoacoustic instability in annular combustors [9]–[11]. On the other hand, **acoustic solvers** — often referred to as Helmholtz solvers — solve the wave equation by assuming that the flow is in stopped condition. In these solvers, the flame effect is introduced using the flame transfer function (FTF). Several works have been able to predict the modes in annular combustors with acoustic solvers [12]–[17].

Many experimental studies have explored the flame characteristics near the LBO limit. Chaudhuri and Cetegen [18] studied the blow-off equivalence ratio of a lean premixed propane-air mixture with a spatial mixture gradient. Stöhr *et al.* [19] studied the dynamics of a swirl-stabilized partially premixed flame operating near the LBO limit. They showed that the flame root becomes intrinsically unstable just prior to LBO and exhibit frequent extinction and reignition. They further observed that flame blowout happens when the flame root is in extinguished condition at least for 2 milliseconds.

Flame characteristics corresponding to TAI, too, have been explored in a large number of studies. With a full-scale annular gas turbine combustor, operating at atmospheric pressure, Lepers *et al.* [20] investigated the effects of Helmholtz resonators on the thermoacoustic instability. Gelbert *et al.* [21] studied control of thermoacoustic instability in a Rijke tube (a cylindrical tube in which sound is generated by a continuous supply of heating).

Various rich dynamics in multi-burner combustors have been found recently. For example, several experimental studies have found the presence of standing, spinning, and slanting azimuthal modes in annular combustors during thermoacoustic instability [22]–[24]. Studies have uncovered several insights on the ignition and burner-to-burner propagation of flame (light-around) in multi-burner combustors [25]–[27].

There is a large body of work on the use of dynamical science-based techniques for the early diagnosis and characterization of LBO and TAI. Only a few pertinent studies are briefly covered next for the sake of conciseness. With an acoustic signal, Nair and Lieuwen [28] detected LBO in a premixed combustor using a threshold-based approach. They observed a strong correlation between the approach of LBO and low-frequency component of acoustic signal. Some bursts in acoustic signals were detected which corresponds to local re-ignition events. These bursts were seen to increase in frequency and duration as LBO was approached. As the flame approaches LBO, the flame is observed to detach and reattach itself to the flame holder repeatedly. Muruganandam *et al.* [29] designed a control system so that the gas turbine combustors can be run safely near the LBO limit. In their study, the fuel supply had two components: the main supply and the pilot supply. As the precursors to LBO were detected, a small fraction of fuel was added through the pilot. Yi and Gutmark [30] investigated the efficacy of an optical LBO sensing method with a multi-swirl and partially premixed gas turbine combustor. Two parameters were used to predict the approach of LBO: (i) the normalized chemiluminescence root mean square (RMS) and (ii) the normalized duration of LBO precursor events. They also reported that chemiluminescence bursts are the result of flame loss and re-ignition events.

Bompelly [31] developed an algorithm to detect impending LBO for both dynamically stable and dynamically unstable (i.e. at TAI) situations. They filtered the high-frequency oscillations (corresponding to TAI) for both optical and acoustic emissions before applying a threshold-based LBO detection technique. Chaudhari *et al.* [32] have used a technique to detect impending LBO using a flame color-based technique. This LBO detection method was seen to have a high efficacy for a wide range of degrees of premixing.

Recently many works have focused on the detection of thermoacoustic instability and lean blowout using machine learning algorithms. A few such studies are discussed below. Mukhopadhyay *et al.* [2] used a D-Markov machine to predict impending LBO under premixed as well as partially premixed scenarios. This study was done with $D = 1$, confining the time domain of the study to the immediate past. Sarkar *et al.* [33] showed that a D-Markov machine with $D > 1$ has a higher efficacy as an early LBO prediction tool as compared to a D-Markov machine with $D = 1$. Hidden Markov model-based TAI detection techniques have been demonstrated to function satisfactorily in recent investigations [34]. Recently, Bhattacharya *et al.* [35] compared the efficacies of the hidden Markov method and symbolic time series analysis, as early detection tools for impending thermoacoustic instability, using data from an annular combustor.

Machine learning-based algorithms however suffer from a disadvantage in that they are highly dependent on the training data. Therefore, these algorithms may not always translate to other combustors. On the other hand, tools from dynamical sciences access the dynamical state of the combustor and hence their accuracy is not directly dependent on the training data. Thus the dynamical science-based algorithms for early detection of LBO and/or, TAI should easily translate to other combustor configurations that exhibit similar dynamical transitions to LBO/TAI.

This thesis primarily focuses on the dynamic behavior of different types of flames. Thus, it is worth discussing in detail the studies that explored different combustor configurations with dynamical science-based tools. Recent experimental results have uncovered several interesting and complex dynamics in combustor systems. Kabiraj *et al.* [36] experimentally studied the blow-out phenomena in ducted premixed flame. They observed irregular bursts in the acoustic signal just prior to blowout. Rich dynamical phenomena: bifurcations, type-II intermittency, and quasi-periodicity were seen prior to blowout. Gotoda and his group [8], [37]–[39] reported that the route to TAI (periodic limit cycle behavior) is as follows: stochastic noise $\rightarrow$ low dimensional chaos $\rightarrow$ TAI. Nair and Sujith [40] reported the presence of homoclinic orbits during the intermittent region preceding LBO.

Unni and Sujith [41] did a recurrence quantification analysis (RQA) using the time series signal obtained with a pressure transducer. They used recurrence

rate, trapping time and entropy, etc. metrics for prediction of LBO. They also showed that RQA without phase-space embedding (in other words, RQA using the pressure time series itself) can be used as a computationally inexpensive tool for early LBO prediction on a real-time basis. De *et al.* [42] have explored the efficacy of recurrence quantification analysis, based on CH* chemiluminescence signal, for early detection of LBO in a single-burner combustor, for a wide range of air-fuel premixing.

Unni and Sujith [43] determined Hurst exponents in a laboratory scale combustor during the dynamical transition to LBO. In the intermittent regime prior to LBO, the dynamics were dominated by periodicity. However, close to lean blowout, this periodicity was seen to be lost. A different low NO_X technology, inverse diffusion flames, have also been reported to be susceptible to TAI by Sen *et al.* [44]. They observed the presence of type-II intermittent dynamics prior to TAI.

Some experimental studies have also explored the effects of flame-flame interaction on flame dynamics. In the majority of these research, it has been discovered that isolated and interacting flames behave quite differently in terms of flame dynamics. Some of the important studies, relevant to this thesis, are discussed next. Lee *et al.* [45] studied the interaction between non-premixed flames with parametric variations of nozzle distance, fuel flow rate, and burner arrangements. They reported that interacting flames exhibit higher blowout velocities than isolated flames do. They also found that the placement of the burners affects the LBO limit significantly. Fanaca *et al.* [46] explored the thermoacoustic instability phenomena in (i) an annular combustor (AC) and (ii) a single-burner combustor, both having the same burner geometry. Flow fields in these two cases differed markedly. For an annular combustor, they observed a free-swirling jet flow, while for a single-burner combustor, they observed a wall jet flow.

Flame-flame synchronization even in simple flames often leads to significantly rich and novel dynamics [47]–[53]. Worth and Dawson [54] reported that flame-flame interaction results in new physics in comparison with a single flame. Recently Ciardiello *et al.* [55], [56] has discussed the mechanisms of LBO in annular and linear array combustors. They found that the LBO limits of an annular combustor and an analogous linear array combustor are similar.

1.3 Literature gap and objective of thesis

Most studies have focused on the dynamic behavior at TAI/LBO with single-burner premixed flame combustors. However, practical combustors have multiple flames which often interact with each other. As discussed above, the flame-flame

interaction is likely to affect the dynamical transitions to LBO/TAI in a significant manner. In addition, most aircraft gas turbine combustors employ partially premixed flames due to space constraints and less time available for air-fuel mixing.

To bridge these gaps in literature, in this work we systemically study the dynamical behavior of isolated flame and interacting flame. We explore the flame behavior with various types of flames (premixed, partially premixed as well as diffusion flames) and combustor configurations using well-established tools of dynamical science. To understand the flame dynamics, flame visualization is also carried out. This study may be useful in understanding the TAI and LBO instabilities occurring inside a practical multi-burner gas turbine combustor.

1.4 Overview of thesis organization

This thesis is organized in the following way. In chapter two, we explore the dynamical characteristics of a inverse diffusion flame (IDF), which is a type of partially premixed flame, with a Rijke tube test rig. In chapter three, we study the efficacy of a few well-known dynamical tools in early detecting lean blowout in a single-burner combustor. In this study, we also vary the degree of premixedness in the combustor in a systematic way and examine how the dynamical transition to LBO varies with degree of premixedness. In chapter four, we study the dynamic behavior of solitary and interacting candle flame oscillators. We note that candle flame oscillators are diffusion flames that exhibit self-sustained oscillations due to oxygen deficiency. In chapter five, flame visualization is carried out in annular and linear array combustors for various degrees of premixedness and for various distances between the burners. In this study, we mostly focus on the interaction of the flames in the near-LBO regime. In chapter six, the dynamical transitions to LBO in annular and linear array combustors are explored using various well-established tools of dynamical science. These tools are recurrence network analysis and topological data analysis. Finally, in chapter seven, the summary of the findings of this work and future direction of work are described.

CHAPTER 2

Characterization of thermoacoustic instability with inverse diffusion flame using recurrence network analysis

2.1 Introduction

Thermoacoustic instability [3] poses significant problems to the operation of gas turbine combustors. These include unreliable operation, structural damages and fatal accidents [6]. Thermoacoustic instability occurs due to positive coupling of fluctuating heat release rate from the flame and acoustic waves inside the combustor [3], [5]. Recent studies [36], [57]–[60] have shown a plethora of dynamical states and different routes to thermoacoustic instability. Most studies on thermoacoustic instability have focused on lean premixed [8], [36], [38], [39], [61] and nonpremixed flames [62], [63]. Lean premixed flames are increasingly being used in modern combustors as it causes low pollution [38]. However, lean premixed flames are prone to flame stability problems including flashback [64], thermoacoustic instability [38] and blowout [42].

On the other hand, normal diffusion flame (NDF) enjoys high stability and reliable operation [65]. In NDF, fuel is introduced as the central jet and air encircles the coaxial fuel jet. However, NDF generates significant amount of thermal NO_X and soot [6], [66] and thus cannot meet the strict emission norms of today.

Another potential technology is inverse diffusion flame (IDF) which is suitable for practical applications such as boilers and gas turbines [65], [67]–[69]. In an IDF, a central air jet is surrounded by a coaxial fuel jet. High velocity central air jet in IDF entrains fuel into it. Such fuel entrainment into air jet significantly improves air fuel mixing [70] as compared to NDF. The higher air-fuel mixing in IDF results in considerably low amount of NO_X and soot [71]–[73]. Moreover, IDF is comparatively less susceptible to lean blowout and has higher stability margin [65], [66], [69] as compared to NDF.

Understanding the thermoacoustic instability dynamics in IDF will be a starting point for application of IDF in gas turbine combustors. Normal diffusion flames, partially premixed flames and perfectly premixed flames exhibit significantly different dynamical features near flame instabilities like lean blowout or thermoacoustic oscillations [42], [74], [75]. IDF is a diffusion flame with the characteristics of partially premixed flames [65], [76], [77]. On the other hand, lean blowout, which is a significantly nonlinear phenomenon [41], occurs without preceding lift-off in IDF combustors [66]. This is in stark contrast to premixed flames where lift-off precedes lean blowout [42]. In view of these facts, it is important to study the dynamical transition to thermoacoustic instability with IDF. To the best of our knowledge, only one study [44] to date have explored the thermoacoustic instability with IDF. Sen *et al.* [44] have reported the susceptibility of IDF to thermoacoustic instability near equivalence ratio $\phi \approx 1.0$. However, the dynamical transition from stable combustion (also known as combustion noise) to thermoacoustic instability with IDF has not been systematically explored and discussed till date.

The aim of the present study is to explore the routes to thermoacoustic instability with IDF, the associated dynamical states and their phase space topologies under the purview of recurrence network analysis [78] (RNA). Recurrence network (RN) is a type of complex network, based on the recurrence information embedded in the original time series [3], [78]–[81]. Complex network analysis (CNA) considers a system to consist of a large number of interconnected elements, which may or may not be mutually interacting [78]. Thermoacoustic systems with turbulent flows can be considered as complex systems due to presence of nonlinear interaction between combustion process [61], turbulent flow with high degrees of freedom [82], [83], and acoustic field. CNA is often used to analyze such systems. A brief discussion of complex network theory may be found in Appendix A, at the end of this chapter.

Recurrence network (RN) is a well-known type of complex network, which provides insights into the time invariant structural properties of the underlying attractor and has been successfully applied in different fields of science and tech-

nology, including engineering [39], [57], climate science [81], physics[84], bioscience [85], etc. The advantages of recurrence network over other types of complex networks have been described in detail in Donner *et al.* [78]. Here, we briefly discuss a few pertinent points for completeness of this chapter. In recurrence network, the results depend on only one parameter: recurrence threshold (ϵ)[80]; however, in transition network, the results depend on both the phase space partition width and the particular partition boundaries chosen [78]. Recurrence network can be easily linked with phase space properties of the underlying attractor unlike the visibility network [57], [78]. In recurrence network, the local degree centrality can be directly linked to the local phase space density. This is in stark contrast to the k-nearest neighbor network, where the local phase space density information is lost[78]. Based on above reasoning, we found recurrence network to be most suitable for exploring the dynamical transition from stable combustion to thermoacoustic instability.

There are many advantages of RNA over other well-known time series analysis techniques. RNA is applicable to short time series, is robust against noise [86] and accurately preserves the attractor structure [57], [80]. As temporal ordering is lost in RN, the measures obtained from RNA indicate time invariant structural properties of the underlying attractor alone [80] unlike most nonlinear tools, such as Lyapunov exponent or recurrence quantification analysis. Thus, RNA is a complementary technique to the typical time series analysis tools [80]. Further, the RN parameters, defined in local, intermediate or global scale, are simply different statistical metrics linked to the phase space density of the attractor [78]. Therefore, RNA having a sound theoretical basis is a suitable tool to explore the dynamics during the transition to thermoacoustic instability.

Several studies have adopted complex network, especially recurrence network based analysis to explore the transition to thermoacoustic instability. Gotoda *et al.* [39] reported a technique for detecting flame instability using visibility based and recurrence based complex networks in a premixed turbulent combustor and observed the presence of power law degree distribution in the recurrence network near lean blowout limit. However, they did not explore the underlying dynamical states. Godavarthi *et al.* [57] showed that RNA can be used as an useful tool for early prediction of thermoacoustic instability in a predominantly premixed combustor. With the help of average betweenness centrality parameter, they also observed the geometric fragmentation in the RN to reduce as thermoacoustic instability is approached. As calculating betweenness centrality is computationally very expensive [78], it is important to study the ability of other RN metrics to capture the onset of thermoacoustic instability. Further, both the aforementioned studies have focused only on the typical intermittency route to thermoacoustic in-

stability, where intermittency is defined as a state showing alternative appearance of periodic and aperiodic oscillations in apparently random manner [36], [39], [40], [57], [58], [87].

In the present study, however, different routes to thermoacoustic instability are identified using RNA. The dynamical states of the system are shown to be accurately determined with the help of different RN metrics. Further, a discussion linking the changes in network parameters and the changes in network structure is provided. Such a discussion would be helpful to understand the physical significance of the changes in the RN metrics as thermoacoustic instability is approached. Three RN metrics, global efficiency (η), average degree centrality (k) and global clustering coefficient (C_G) are chosen, which are linked with important structural properties of recurrence networks [78], [81], [88], [89]. In short, new routes and dynamical states prior to thermoacoustic instability are explored in this study with RNA, leading to a better understanding of thermoacoustic instability with inverse diffusion flame.

Towards this, experiments are conducted using a Rijke tube with inverse diffusion flame, which is a simple system to study the occurrence of thermoacoustic instability [90]. In the present study, thermoacoustic instability is approached through two protocols. In the first protocol, air flow rate is gradually increased, thereby varying equivalence ratio and Reynolds number (denoted as increasing air protocol or protocol IA, in short). In protocol IA, the increase in bulk flow changes the flow from laminar ($Re_{air} < 2300$) to turbulent regime ($Re_{air} > 4000$) through transition regime ($2300 < Re_{air} < 4000$). In the authors' knowledge this is the first application of recurrence network to study the dynamic transition from stable combustion to thermoacoustic instability by varying Reynolds number from laminar to turbulent regimes. Thus we study the robustness of the RN metrics for detecting the dynamical transition to thermoacoustic instability, as the underlying nature of flow in the combustor also changes. In the second protocol, the input power is varied while keeping the equivalence ratio and flow Reynolds number nearly constant (denoted as increasing power protocol or protocol IP, in short). Here, input power is calculated by multiplying fuel flow rate with the calorific value of fuel.

Route to thermoacoustic instability is found to be significantly complex compared to that commonly reported for premixed or predominantly premixed combustors [39], [57], [58], [87]. In protocol IA, we observe an intermediate state prior to thermoacoustic instability, which consists of low amplitude aperiodic and high amplitude aperiodic oscillations and referred to here as 'amplitude varying aperiodic oscillations'. On the other hand, when thermoacoustic instability is approached through protocol IP, we observe the intermediate state to have low

amplitude apparently periodic oscillation and referred to here as 'low amplitude limit cycle-like oscillations'. A discussion linking the recurrence network topologies with the different RN metrics has been presented to enhance the understanding of the variations in the RN metrics as the system approaches thermoacoustic instability. During thermoacoustic instability, the RN formed is observed to be a non-regular network. On the other hand, during combustion noise, the degrees of RN do not follow a scale-free distribution. Moreover, RN corresponding to combustion noise do not follow a single power law degree distribution. These findings are in stark contrast to properties of RN during thermoacoustic instability and combustion noise for premixed configurations.

In short, the present chapter presents a number of novel findings, which are enumerated below.

1. This work applies first time a recurrence network analysis on inverse diffusion flame to characterize thermoacoustic instability.

2. For the first time, this work links the changes in various RN metrics with the changes in RN topology as thermoacoustic instability is approached, based on the topologies created with Gephi software.

3. We report two novel intermediate routes to thermoacoustic instability, namely the 'amplitude varying aperiodic oscillations' and 'low amplitude limit cycle-like oscillations'.

4. We show that at thermoacoustic instability with inverse diffusion flame, the RN formed is a non-regular network. This is in contrast with premixed flame configuration, where RN formed at thermoacoustic instability is typically a regular network [57].

5. RN formed at stable combustion state for inverse diffusion flame is not a scale-free network or, a power-law abiding network. In fact, at this state, two power law are present in the degree distribution of the RN. This is in contrast with premixed flame configuration, where RN formed at stable combustion is typically a scale-free/power-law abiding network [39], [57]. Findings (4) and (5) are in stark contrast to previously reported properties of RN at thermoacoustic instability and combustion noise for premixed configurations [39], [57].

2.2 Brief theoretical background

Reconstruction of phase space and creation of adjacency matrix therefrom are the initial steps to construct recurrence networks. They are briefly discussed

below.

2.2.1 Constructing complex network from recurrence information

The experimental time series is embedded in D-dimensional phase space using an optimal time delay (τ_d) in order to construct the phase space vectors [91]. Embedding dimension (D) is calculated using false nearest neighbors (FNN) [92], [93] method. If a system is embedded with a lower than optimal embedding dimension, a point in the phase space will have a number of false neighbors. If the embedding dimension is increased by one, then the number of false neighbors to the above mentioned point would reduce. At the optimal embedding dimension, the system trajectory will be completely unfolded and the number of false neighbors would be zero.

Optimal time delay (τ_d) is taken as the time delay at which the first zero of the autocorrelation function is obtained [92]. The autocorrelation function is defined as follows,

$$C_L(\tau) = \frac{\frac{1}{N}\sum_{m=1}^{N}[y(m+\tau)-\bar{y}][y(m)-\bar{y}]}{\frac{1}{N}\sum_{m=1}^{N}[y(m)-\bar{y}]^2} \tag{2.1}$$

Here, $y(t)$ is the time series of the measured variable. $\bar{y}$ is mean value of $y(t)$. Mathematically, $\bar{y} = \frac{1}{N}\sum_{m=1}^{N} y(m)$. $y(m)$ is the sampled data at $t = t_0 + m\tau$. t_0 is the time at the start of the time series and τ is the time delay. m has an integer value and N is the number of data points in the time series.

With the time series $y(t)$, phase space vectors can be constructed as,

$$\mathbf{Z}(t_i) = [y(t_i), y(t_i+\tau_d), y(t_i+2\tau_d), \cdots, y(t_i+(D-1)\tau_d)], \tag{2.2}$$

where, $\mathbf{Z}(t_i)$ and $y(t_i)$ are the reconstructed phase space vector and the audio signal, respectively at time instant t_i. $\mathbf{Z}$ is considered to recur between instants i and j, if the D-dimensional hyperspheres of radius ϵ, centered around $\mathbf{Z}_i$ and $\mathbf{Z}_j$, overlaps with each other. The recurrence threshold ϵ is found here to be approximately 15% of maximum phase space distance following the method of Eroglu *et al.* [94]. This method chooses the minimum ϵ as the optimal threshold, at which no node of the resulting complex network remains disconnected. Detailed description of the method of Eroglu *et al.* is provided in Appendix B, at the end of this chapter.

The recurrence information are stored in a recurrence matrix $\mathbf{R}$ [95], whose

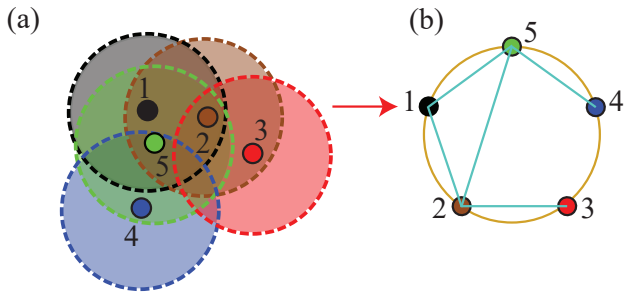

Figure 2.1: Construction of recurrence network (RN) from phase space plot. (a) and (b) show the phase space plot and corresponding recurrence network, respectively.

elements are calculated as follows,

$$\mathbf{R}_{i,j} = \theta(\epsilon - \|\mathbf{Z}_i - \mathbf{Z}_j\|), \tag{2.3}$$

where, $i, j = 1, 2, \cdots, N$. $\|\mathbf{Z}_i - \mathbf{Z}_j\|$ is the Euclidean norm, N is the number of phase space vectors and θ is the Heaviside function. The adjacency matrix $\mathbf{a}$ required to construct a recurrence network is calculated from $\mathbf{R}$ by eliminating the self-loops ($\mathbf{R}_{i,i}, \forall i = 1, 2, \cdots, N$) as,

$$\mathbf{a}_{i,j} = \mathbf{R}_{i,j} - \delta_{i,j}. \tag{2.4}$$

Here, δ is kronecker delta. In the constructed RN, nodes i and j have a link between them if $\mathbf{R}_{i,j} = 1$. If $\mathbf{R}_{i,j} = 0$, no direct link between nodes i and j exists.

A schematic representation of how RN is constructed from phase space plot is shown in Fig. 2.1, where the nodes of the RN are arranged over circumference of a circle. The 5 phase space vectors are numbered 1-5. The phase vectors are shown by small circles in the phase plot (Fig. 2.1a) whereas the ϵ-hyperspheres around the phase vectors are indicated by large circles. The ϵ-hypersphere around phase space vector 2 is seen to contain the vectors 1, 3 and 5. Thus node 2 have direct links with node 1, 3 and 5 in the constructed recurrence network (Fig. 2.1b).

In this study, the RN topologies for different dynamic states are constructed using Force Atlas 2 algorithm [96], [97], in-built in the Gephi software [98]. This algorithm iteratively solves the network where connected nodes attract and unconnected nodes repel each other. Gephi has been used in many scientific studies [57], [97] to study complex network topologies.

2.2.2 Description of recurrence network parameters

RN parameters are statistical measures which can capture the structural features in RN. In this chapter, the different RN parameters are calculated using

in-house Matlab codes. The definitions and physical significance of different parameters are briefly described below [78]–[81].

Shortest path length ($l_{i,j}$): The minimum number of links required to travel from one node i to another node j is called the shortest path length between these two nodes. $l_{i,j}$, calculated using breadth-first search algorithm [89], is required to calculate different RN metrics including the global efficiency (η) which is used in the current chapter. Average path length [81] (L), a commonly used metric of RNA, is a mean of all shortest path lengths in RN and given by, $L = \frac{1}{N(N-1)} \sum_{i,j=1,i\neq j}^{N} l_{i,j}$. L is a quantitative measure of the average distance between two nodes of the network. However, the measure L would suffer a divergence problem if any two nodes in the RN belongs to two completely separate clusters of the RN [88]. This problem can be avoided with the metric, global efficiency.

Global efficiency (η): This parameter, which indicates how efficiently information propagation happens through a complex network [88], is estimated as,

$$\eta = \frac{1}{N(N-1)} \sum_{i,j=1,i\neq j}^{N} \frac{1}{l_{i,j}}. \tag{2.5}$$

Here, N is the number of nodes in the network. Because recurrence network is not an information network, the concept of information transfer does not apply here directly. However, information network analogy can be used in a geometric way as discussed by Donner *et al.* [78]. η being a harmonic mean of shortest path lengths avoids the divergence problem of the measure L. In the present study, η is used as a measure of the average distance between the nodes of the RN.

For a perfectly periodic signal, all the neighboring nodes remain connected to each other and each of the shortest paths in the RN have unit length [81]. Therefore, L assumes its lowest possible value, 1 and η assumes its highest possible value, 1. On the other hand, for chaotic signals, L takes greater values [99], whereas the values of η become lower. Therefore, it can be reasoned that the greater the value of η, the higher is the determinism of the underlying time series.

Average degree centrality (k): The relative importance of a node i in the RN is given by the degree centrality of the concerned node (k_i). The number of nodes, which are directly connected to node i, is given by k_i.

$$k_i = \sum_{j=1,i\neq j}^{N} \mathbf{a}_{i,j}. \tag{2.6}$$

Degree centrality can be averaged over the whole network to get average degree

centrality (k) as,

$$k = \frac{1}{N}\sum_{i=1}^{N} k_i. \tag{2.7}$$

k can be linked with the average phase space density of the attractor [78]. Therefore, average phase space density and the value of k become higher for a periodic signal due to higher recurrence, where each neighboring nodes remain connected to each other. Similarly, k approaches lower values when the system is chaotic as the extent of recurrence becomes considerably less in such state.

Global clustering coefficient (C_G): Highly interconnected set of nodes are called cliques. The cliquishness of a node i is measured by local clustering coefficient (C_i). If the number of links in the neighborhood nodes of i (the nodes directly adjacent to node i) is e_i, then C_i is given as [78], [81], [88],

$$C_i = \frac{e_i}{k_i(k_i-1)/2} = \frac{2\sum_{j,v}\mathbf{a}_{i,j}\mathbf{a}_{j,v}\mathbf{a}_{v,i}}{k_i(k_i-1)}. \tag{2.8}$$

Here, j and v are the neighbors of node i. The global clustering coefficient (C_G) is evaluated by averaging local clustering coefficient (C_i) over the network as,

$$C_G = \frac{1}{N}\sum_{i=1}^{N} C_i \tag{2.9}$$

C_G can capture the presence of any clustered phase space vectors which forms, for example, in intermittent or periodic dynamics [81]. As divergence of trajectory becomes smaller in periodic attractor or in regions of an attractor where unstable periodic objects (corresponding to intermittency) are detected, the corresponding nodes in RN have considerably high local clustering coefficients [78]. Therefore, C_G approaches a highest value for periodic or near periodic states [37]. Further, a higher C_G value is obtained during intermittency as compared to chaotic state where the presence of nodes with higher local clustering is much less. As a result, C_G becomes lowest for a state of high dimensional chaos. In short, C_G becomes maximum for fully periodic dynamics [81] and lowest for chaotic regimes [80]. The reasoning based on the divergence of trajectories can be further extended to claim that C_G for low dimensional chaos becomes higher compared to high dimensional chaos, and lower compared to periodicity.

This indicates that the values of local clustering coefficient become higher in the regions of attractor with low dimensional structures [78] (corresponding to laminar states or unstable periodic objects). Therefore, an overall increase in low dimensional structures in the attractor leads to an increase in C_G value. Thus, the global clustering coefficient, C_G can be a potential RN metric which is able to quantify the changes in dimensionality of the system. Further, local

clustering coefficient can be linked with the directional alignment of nodes in the neighborhood of the concerned node [78]. Thus, a low value of C_G indicates the overall lack of structures with directional alignments in the RN. These implications of C_G values help interpreting the dynamical transition from combustion noise to thermoacoustic instability.

At this point it is important to define what we mean by the terms high dimensional chaos (HDC) and low dimensional chaos (LDC). Though, there is no formal definition of HDC and LDC [100], we find different measures to characterize such dynamical states. For example, Harrison and Lai [100] has considered the case where a single positive Lyapunov exponent exists to be LDC and the case where more than one positive Lyapunov exist to be HDC. They observed dynamic transitions from regular dynamics to HDC through LDC with help of (i) three dimensional maps, (ii) two coupled Rössler oscillators and (iii) a four dimensional ecological population model. They further showed that the fractal dimension changes in a smooth way as dynamics changes from LDC to HDC [101]. However, another study [102], indicated the fractal dimensions and number of positive Liapunov exponents to be of less importance while distinguishing HDC and LDC. They also showed that the difference between HDC and LDC is merely quantitative and not qualitative. Gotoda *et al.* [37], [38], [103], [104] considered the chaotic dynamics corresponding to Lorenz oscillators as LDC. They have used two metrics, translational error and permutation entropy, in order to distinguish between HDC and LDC. In the current manuscript, the terms HDC and LDC respectively indicate the higher and lower degree of complexity of the attractor in a relative sense.

In the present study, the recurrence network parameters such as global efficiency (η), average degree centrality (k) and global clustering coefficient (C_G) are used to investigate the transition to thermoacoustic instability for inverse diffusion flame as the metrics characterize the important time invariant structural properties of the attractor.

2.3 Experimental setup

2.3.1 Rijke tube rig

The experimental Rijke tube test rig is shown in Fig. 2.2 and the corresponding schematic is shown in Fig. 2.3. The experimental setup consists of a vertically held Rijke tube (Fig. 2.3) which is a cylindrical quartz tube of length 800 mm with inner diameter of 60 mm and thickness 2.5 mm. There is a provision to vary flame position inside the Rijke tube by varying the tip location of the co-

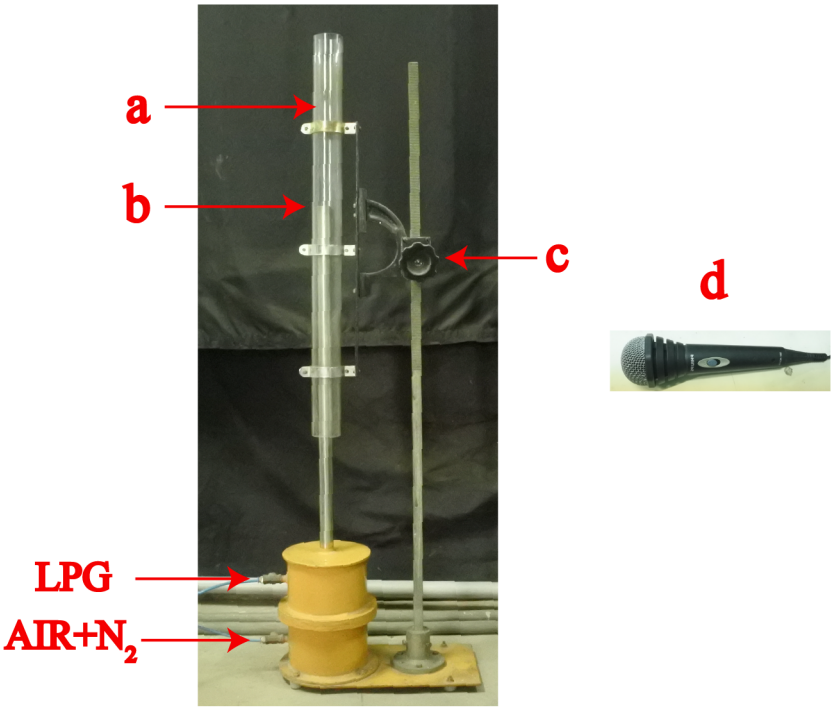

Figure 2.2: (a) Combustion chamber, (b) co-flow burner tip and (c) rack-pinion mechanism to vary height of the combustion chamber, (d) microphone.

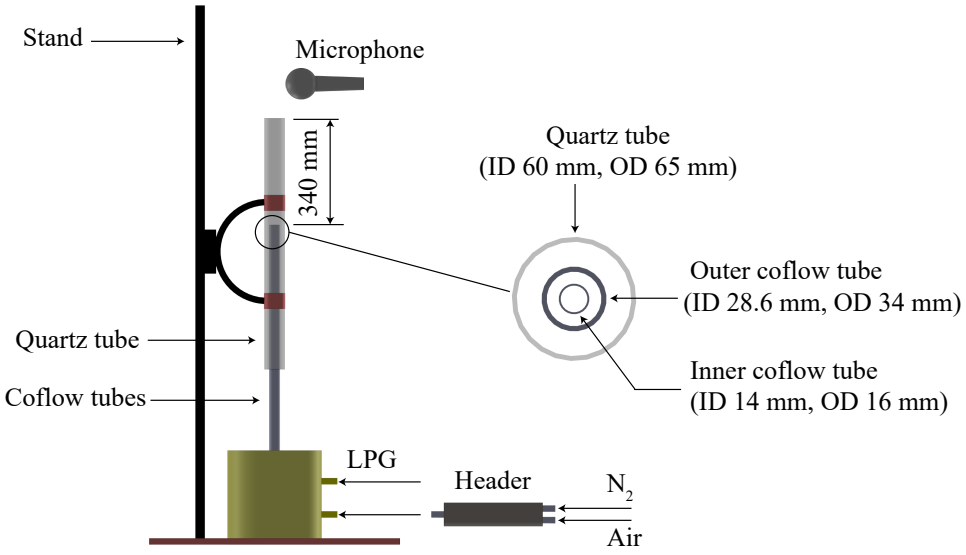

Figure 2.3: Schematic of the experimental Rijke tube rig, which is used to study thermoacoustic instability for inverse diffusion flame in this work.

flow burner tube. For the present study, the flame position is fixed at 340 mm from the top end of the quartz tube at which position the Rijke tube has been shown to exhibit thermoacoustic instability [44]. The co-flow burner consists of two concentric tubes. The inner tube has an ID of 14 mm and OD of 16 mm whereas the outer tube has an ID of 28.6 mm and OD of 34 mm.

Liquefied petroleum gas (LPG, 40% propane and 60% butane by volume) is used as fuel as it is readily available and inexpensive [1]. LPG is supplied through the annular section between inner and outer tubes and metered using a mass flow controller (make: Aalborg, range: 0-10 lpm CH_4, calibrated for LPG, accuracy: 1 % of full scale reading). Air is supplied at ambient pressure through the inner tube and metered using a air mass flow controller (make: Alicat, range: 0-250 lpm, accuracy: 0.8 % of reading + 0.2 % of full scale reading). N_2 is used when Reynolds number and equivalence ratio are maintained approximately constant (protocol IP) to compensate the change in reactant mixture flow rate. N_2 is supplied from a pressurized cylinder and metered using a mass flow controller (make: Aalborg, range: 0-60 lpm CH_4, calibrated for N_2, accuracy: 1 % of full scale reading). N_2 and air are mixed in a header before being supplied through the inner tube as inner oxidizer jet.

2.3.2 Experimental procedure and data acquisition

During experiments, after each adjustment of operating condition, 2 minutes time is allowed for the transients to die down. The audio signal is then acquired using a microphone (Philips SBCMD110/01) positioned near the top end of the Rijke tube for a duration of 10 seconds. However, it is found that 2 seconds long data is enough for capturing the dynamics completely. The audio signal is sampled at 44.1 kHz. To reduce the computational burden, the 2 seconds long data is further divided into 10 equal windows and RNA is applied on each of these windows independently. An average value of each of the RN parameters for the 10 windows is then calculated. Such an approach has been used in previous studies [36], [44], [105].

The values of operating parameters for the different cases considered in this study are presented in table 2.1. Two representative cases with different input power are considered for protocol IA. In protocol IP, bulk flow rate and global equivalence ratio (ϕ) are kept constant while input power (obtained by multiplying LPG flow rate with calorific value of LPG) is gradually increased to attain thermoacoustic instability. Initially, the flow rate of reactant mixture consisting

[1]The data pertaining to liquefied petroleum gas (LPG) is taken from Indian oil corporation website (https://www.iocl.com).

Case	Air (lpm)	Re	LPG (lpm)	N_2 (lpm)	Input power (kW)	ϕ
IA-i	$15-57$	$1566-5950$	0.2	0	0.39	0.37-0.098
IA-ii	$21-60$	$2192-6263$	0.3	0	0.59	0.4-0.14
IP	$37-50$	$5116-5168$	0.26-0.35	13-0	$0.50-0.68$	0.2

Table 2.1: Operating conditions for the IA and IP cases

of air and LPG at $\phi = 0.2$, is minimum (table 2.1), and therefore, N_2 flow rate is maximum. Input power can be increased keeping ϕ constant only by increasing the flow rate of reactant mixture. In such a situation, N_2 flow rate is reduced by the same amount to keep the overall bulk flow constant. Thus, the Reynolds number also remains almost constant (table 2.1).

The air Reynolds number, Re_{air} is calculated as, $Re_{air} = 4\dot{Q}_{air}\rho_{air}/(\pi\mu_{air}d_i)$ where, d_i is the diameter of inner tube, $\dot{Q}_{air}$ is volumetric air flow, ρ_{air} and μ_{air} are density and dynamic viscosity of air, respectively. For the IP protocol, the flow Reynolds number Re_{flow} is calculated with the average density and average dynamic viscosity of the air and N_2 mixture, according to their volume flow rate; $\dot{Q}_{air}$ is replaced with total flow rate of air and N_2 mixture. The global equivalence ratio, ϕ is given by,

$$\phi = \frac{(\dot{m}_{LPG}/\dot{m}_{air})}{(\dot{m}_{LPG}/\dot{m}_{air})_{stoichiometric}}, \tag{2.10}$$

where, $\dot{m}$ denotes the mass flow rate.

We conducted this experiment in a single day to keep the ambient conditions approximately same. It may be reasoned that the system acoustics corresponding to cold flow would remain approximately same under such situation. To ensure the repeatability of the experimental data obtained, we performed the experiments at least 10 times with similar ambient conditions to find that the flame dynamics exhibits a similar transition. The measurement uncertainty corresponding to the flow rates can be calculated from the accuracy ratings of the mass flow controllers. The uncertainty for air is ± 0.4 lpm for a flow range of 15 – 60 lpm, that for LPG is ± 0.03 lpm for a flow range of 0.2 – 0.3 lpm and that for N_2 is ± 0.3 lpm for a flow range of 0 – 13 lpm (table 2.1).

2.4 Results and discussions

As mentioned in the introduction, two protocols namely protocol IA (increasing air) and protocol IP (increasing power) are set to observe the transition to

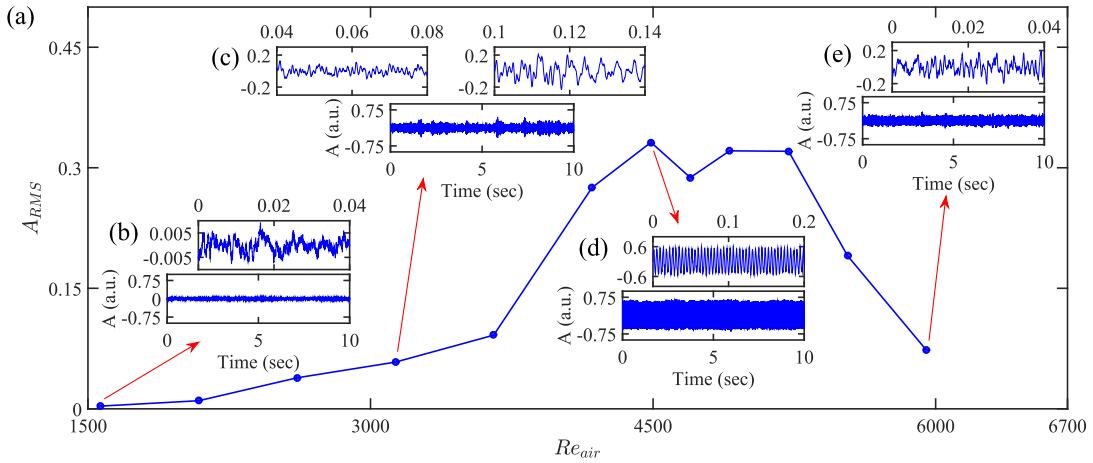

Figure 2.4: (a) RMS amplitudes (A_{RMS}) for different air flow rate, keeping power constant as 0.39 kW (case IA-i) and corresponding time series at different air Reynolds numbers, (b) Re_{air} = 1566, (c) Re_{air} = 3132, (d) Re_{air} = 4489, (e) Re_{air} = 5950. A denotes the amplitude of sound signal with arbitrary unit.

thermoacoustic instability. The results of the different cases as mentioned in table. 2.1 are discussed next sequentially.

2.4.1 Dynamic transition observed for protocol IA

2.4.1.1 Identification of dynamical states by visual inspection of time series

In IA-i (corresponding to input power of 0.39 kW), the amplitude of sound emitted is observed to increase gradually with air flow rate as thermoacoustic instability is approached (Fig. 2.4a). At low air flow rate (Re_{air} = 1566), a small amplitude aperiodic signal is observed (Fig. 2.4b) which is generally referred to as combustion noise [106]. At Re_{air} = 3132, a increase in overall signal amplitude with occasional high amplitude oscillations can be observed (Fig. 2.4c) indicating a significant departure in dynamical features from combustion noise. This dynamical state consists of low amplitude aperiodic oscillations with the occasional burst of high amplitude aperiodic oscillations. On the other hand, intermittency typically observed in premixed or predominantly premixed combustors is characterized by an ensemble of periodic and aperiodic oscillations [36], [39], [40], [57], [58], [87]. Clearly, the dynamical state at Re_{air} = 3132 is a different type of intermittent behavior which has been little explored in previous studies. Kasthuri *et al.*[58] observed the presence of a mixed mode oscillation consisting of low and high amplitude periodic signal. We refer the dynamical state at Re_{air} = 3132 as 'amplitude varying aperiodic oscillations'. With further increase in air flow rate (Re_{air} = 4489), significantly increased amplitude and periodicity of the signal can

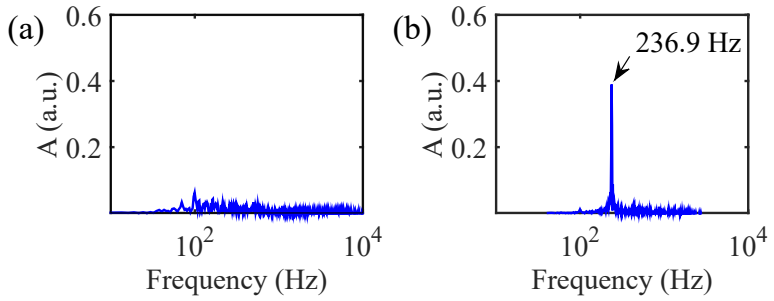

Figure 2.5: Power spectrum at (a) stable combustion state (Re_{air} = 1566) and (b) at TAI (Re_{air} = 4489), for the IA-i case. A indicates amplitude (a.u.) at various frequencies.

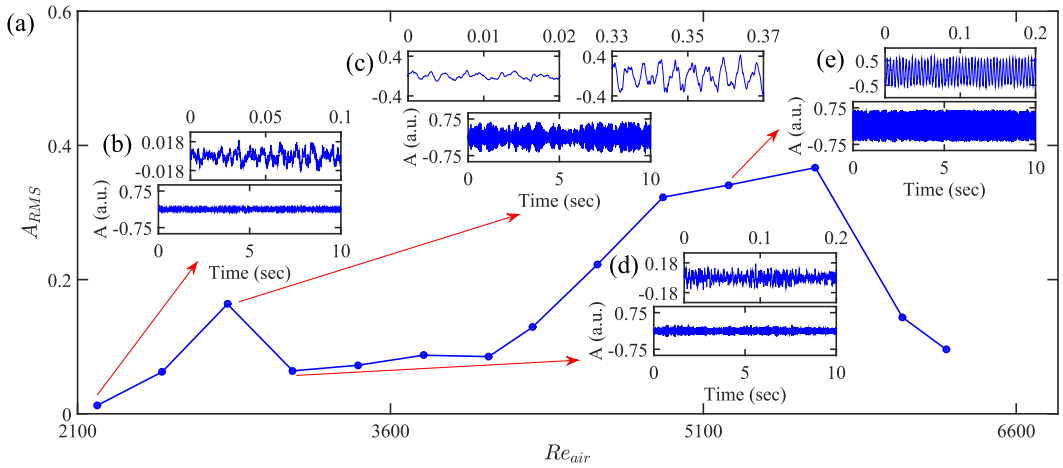

Figure 2.6: (a) RMS amplitudes (A_{RMS}) for different air flow rate, keeping power constant as 0.59 kW (case IA-ii) and corresponding time series at different air Reynolds numbers, (b) Re_{air} = 2192, (c) Re_{air} = 2818, (d)Re_{air} = 3132, (e) Re_{air} = 5220. A denotes the amplitude of sound signal with arbitrary unit.

be seen (Fig. 2.4d), which corresponds to thermoacoustic instability. The system deviates from thermoacoustic instability as air flow rate is further increased to Re_{air} = 5950, and the audio signal appears to be low amplitude aperiodic (Fig. 2.4e). Low amplitude aperiodic oscillations post thermoacoustic instability has been observed in many combustors [40], [57]. Note that even with further increase in air flow rate, lean blowout does not occur.

It may be worthwhile to look at the frequency characteristics of the Rijke tube test rig. For brevity, we describe only the IA-i case here (Fig. 2.5). The Power spectrum at stable combustion state (Fig. 2.5a) do not exhibit any prominent peak. On the other hand, a prominent peak at 236.9 Hz is seen at TAI (Fig. 2.5b).

In IA-ii (corresponding input power of 0.59 kW), the dynamical transition is more complex. The variation of RMS amplitude as air flow rate is increased

is shown in Fig. 2.6(a). Initially combustion noise with low amplitude aperiodic oscillations is observed at low air flow rate (Re_{air} = 2192; Fig. 2.6b). At Re_{air} = 2818 (Fig. 2.6c), the dynamical state consists of small amplitude aperiodic oscillations with frequent bursts of high amplitude aperiodic oscillations and thus corresponds to 'amplitude varying aperiodic oscillations'. The amplitude of signal then abruptly reduces at Re_{air} = 3132 and the audio signal consists of low amplitude aperiodic oscillation (Fig. 2.6d). Further increase in Re_{air} again increases the RMS of time series and introduces high amplitude bursts. At Re_{air} = 5220 the Rijke tube exhibits full blown thermoacoustic instability (Fig. 2.6e). The corresponding zoomed in time series shows the periodicity of the dynamics. Further increase in air flow rate (Re_{air} = 6054) deviates the system from thermoacoustic instability and returns to a state of low amplitude aperiodic oscillation. The time series being similar to as shown in Fig. 2.4(d) is not shown.

It is known that combustors are prone to thermoacoustic instability at lean operating conditions[6], which is reproduced in protocol IA-i. However, the transition encountered in IA-ii is more intriguing. Venkataraman *et al.* [107] reported a similar complex path to thermoacoustic instability, which was attributed to the varying nature of flame-vortex interactions as equivalence ratio ϕ was gradually varied.

2.4.2 Determination of optimal embedding parameters

A more elaborate understanding cannot be obtained with the visual inspection of time series. Therefore, next we explore the dynamical transition with phase plots. In order to obtain accurate phase plots, a delayed time series has to be constructed with optimal time delay. First, the autocorrelation function of the time series is obtained at various time delays. The optimal time delay is the time delay where the first zero of the autocorrelation function is obtained [92]. In Fig. 2.7, the variation in autocorrelation function ($C_L(\tau)$) with time delay τ is shown for a stable combustion state (Re_{air} = 1566) corresponding to the IA-i case. Here it is seen that $C_L(\tau) \approx 0$ at $\tau = 64$. Therefore, optimal time delay, $\tau_d = 64$.

The phase plots at stable combustion state and at TAI state, corresponding to the IA-i case, are shown in Fig. 2.8. At the stable combustion state (Re_{air} = 1566), the phase plot reveals a complex attractor structure (Fig. 2.8a) whereas at TAI (Re_{air} = 4489), the attractor has a distinct limit cycle nature (Fig. 2.8b).

In order to ensure correct embedding of the time series in phase space, the optimal embedding dimension has to be calculated. The method to calculate the optimal embedding dimension, using False nearest neighbor (FNN) algorithm, is shown in Fig. 2.9. Here, we consider three representative cases corresponding

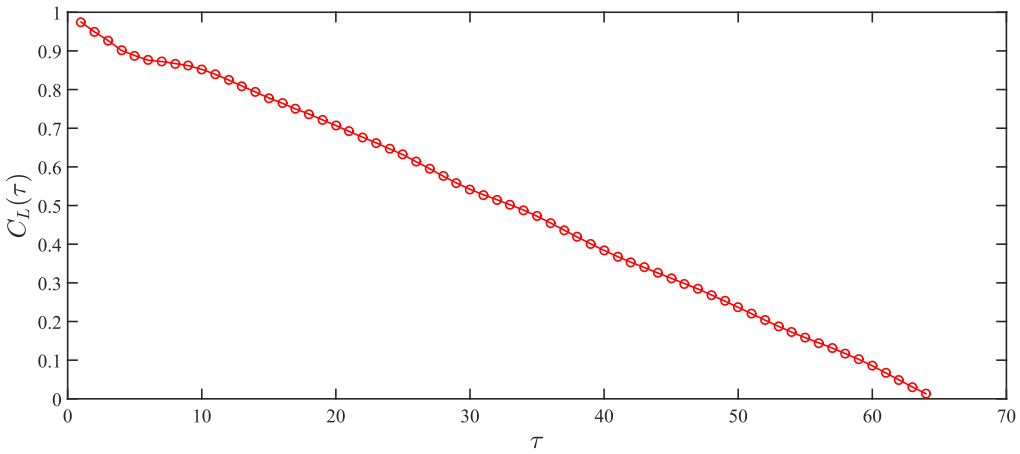

Figure 2.7: The autocorrelation function ($C_L(\tau)$) with time delay τ at the stable combustion regime ($Re_{air} = 1566$) for the IA-i case.

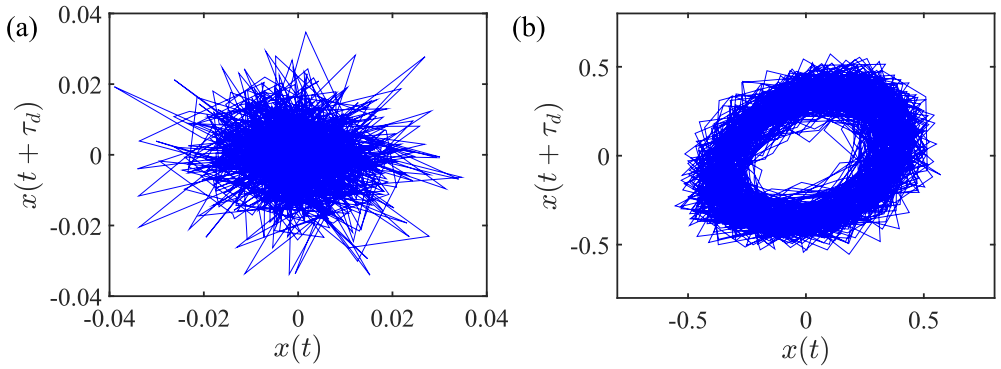

Figure 2.8: Phase plot (a) at stable combustion state ($Re_{air} = 1566$) and (b) at TAI ($Re_{air} = 4489$), for IA-i case. $x(t)$ is the acoustic signal and $x(t + \tau_d)$ is the delayed time series. τ_d is optimal time delay.

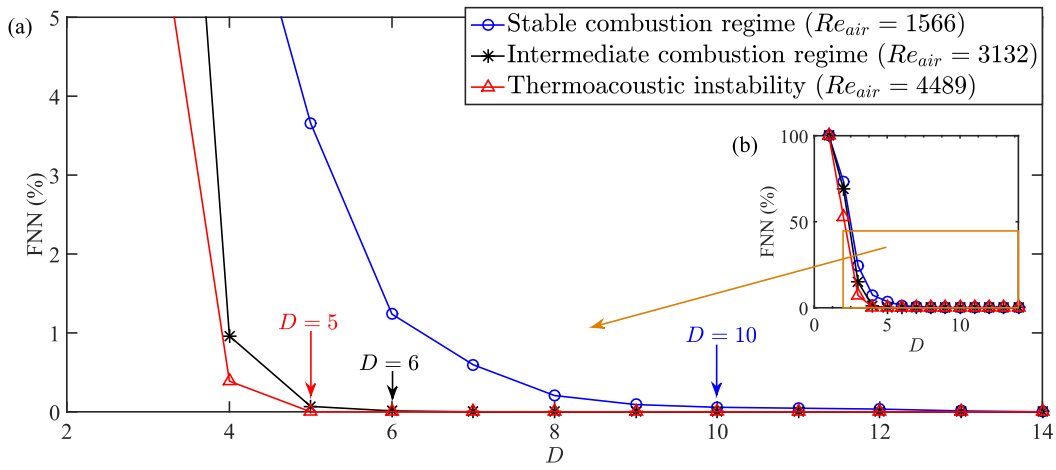

Figure 2.9: False nearest neighbor (FNN) algorithm to calculate optimal embedding dimensions. Here, three representative cases corresponding to the IA-i case is shown: stable combustion regime (Re_{air} = 1566), intermediate combustion regime (Re_{air} = 3132) and thermoacoustic instability (Re_{air} = 4489). (a) shows the zoomed in FNN plots whereas (b) shows the FNN plots without magnification.

to the IA-i case: stable combustion regime (Re_{air} = 1566), intermediate combustion regime (Re_{air} = 3132) and thermoacoustic instability (Re_{air} = 4489). For these cases, the optimal embedding dimensions (D) are found to be 10, 6 and 5 respectively.

2.4.2.1 Application of network parameters to identify different dynamic regimes

As precise and accurate identification of dynamical states is not possible solely from the time series, RN metrics are evaluated to explore the dynamical transition to thermoacoustic instability in the present system. Based on RN metrics and observed time series, the operating ranges of IA-i and IA-ii cases are divided into a number of regimes for ease of further discussion.

Figure 2.10 shows the variations of different network parameters for case IA-i. The variation of global efficiency (η) as Re_{air} is increased can be seen from Fig. 2.10(a). During combustion noise (regime I), η appears to be very low. Based on the discussions in section 2.2, we reason that a low value of η indicates large distances between the nodes. A lower value of η is indicative of aperiodic fluctuations of acoustic pressure which might be due to chaotic nature of the dynamics and inherent noise in the system. On the other hand, a higher value of η would indicate shift towards periodicity, as discussed in section 2.2. The low value of average degree centrality (k) is due to low average phase space density, and indicates possible chaotic dynamics and the lack of periodicity (Fig. 2.10b). Further, the low value of global clustering coefficient (C_G) indicates lack of lower

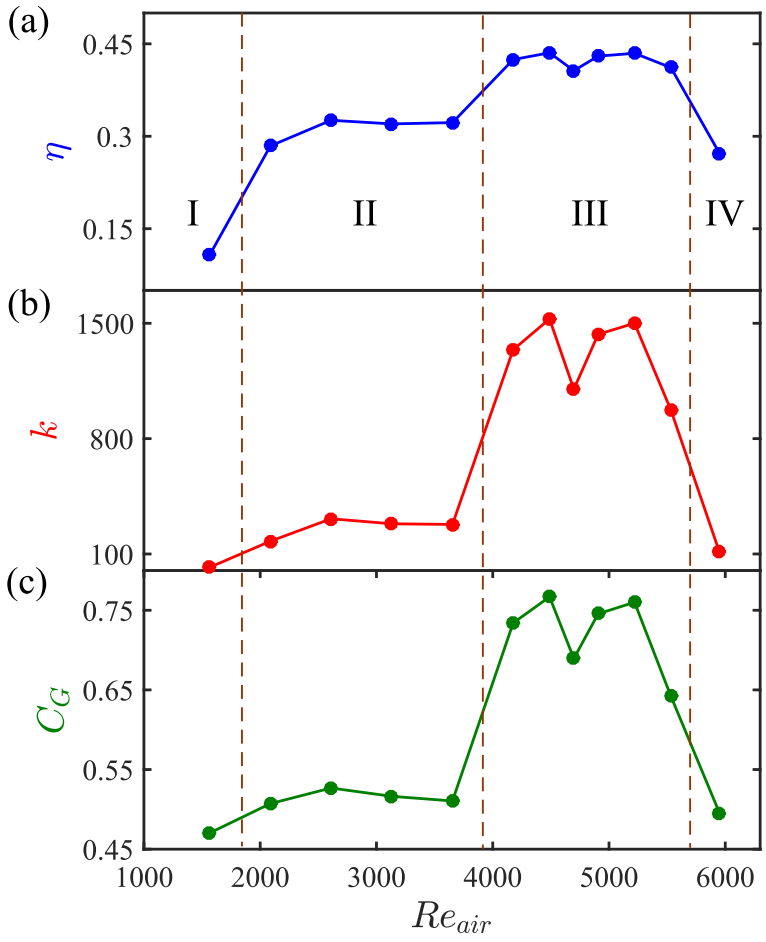

Figure 2.10: Variation of (a) global efficiency (η), (b) degree centrality (k), and (c) global clustering coefficient (C_G) for IA-i case, as air flow rate is increased.

dimensional structures in the attractor. It may be noted that a low value of C_G is likely due to chaotic nature of dynamics and a shift toward higher C_G can be linked to increasingly periodic dynamics, as reasoned in section 2.2. In regime II, the higher values of η and k signifies the reduction in distance between RN nodes and increase in number of links. C_G also slightly increases. Both regime I and regime II consist of aperiodic oscillations, indicating that both the dynamics are possibly chaotic in nature. In short, the values of η, k and C_G in regime II are significantly higher compared to regime I but lower compared to regime III, where thermoacoustic instability occurs (Fig. 2.10). Following the discussion in Section 2.2, we conclude that regime II exhibits comparatively higher determinism and lower dimensionality as compared to regime I.

Further, we have observed 'amplitude varying aperiodic oscillations' in regime II. Based on these observations, we reason that the dynamics in regime I and II possibly correspond to high dimensional chaos (HDC) and low dimensional chaos (LDC), respectively. The high dimensional chaotic nature of combustion noise in a turbulent combustor has been discussed by Tony *et al.* [108] through a rigorous treatment of time series analysis. On the contrary, in regime III, the high values of η and k indicate that average distance between the nodes becomes even smaller and the number of links in the network becomes much higher as compared to regime II. The high value of C_G indicates the trapping of trajectory within a small neighborhood, which is expected for near-periodic oscillations[79]. These results indicate a high determinism, but not fully periodic dynamics. For periodic dynamics, η and C_G would approach 1.

Finally, in regime IV consisting of small amplitude aperiodic oscillations, all three parameters (η, k and C_G) reduce indicating a departure from thermoacoustic instability. Thus, the route to thermoacoustic instability for IA-i is HDC $\rightarrow$ LDC $\rightarrow$ periodicity. The dynamical states inferred from the RN metrics will be further validated through a nonlinear metric, translational error later in this chapter.

Similarly, for case IA-ii also, the values of η, k and C_G are low during combustion noise (regime I) (Fig. 2.11a) implying high dimensional chaos. In regime II, values of η, k and C_G increases to a higher value compared to regime I, indicating a shift towards higher determinism and lower dimensionality (Fig. 2.11b). Thus, regime II marks the transition of system from high dimensional chaos to low dimensional chaos. At $Re_{air} = 3132$ (which is at the start of regime III), the system again reverts to low amplitude aperiodic oscillations. At this condition η, k and C_G becomes low again, implying high dimensional chaos (Fig. 2.11). Thus between $Re_{air} = 2818$ and $Re_{air} = 3132$, an abrupt change of dynamics occurs from LDC to HDC. Further increase of Re_{air} in regime III results in increase of η, k and C_G. Therefore, regime III represents a transition from HDC to LDC (Fig.

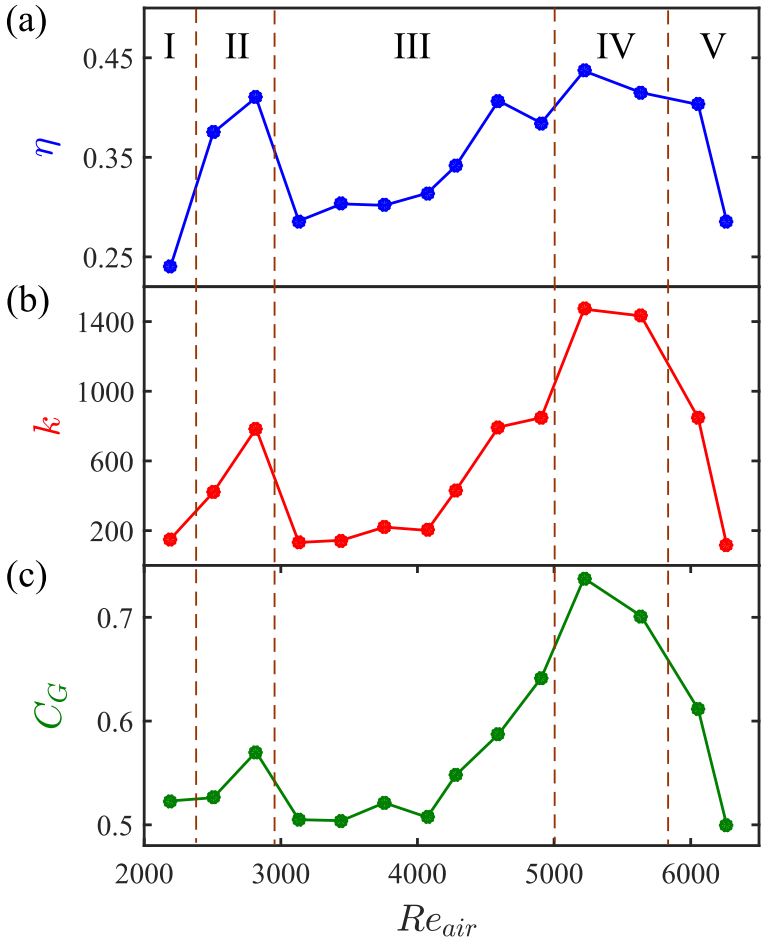

Figure 2.11: Variation of (a) global efficiency (η), (b) degree centrality (k), and (c) global clustering coefficient (C_G) for IA-ii case, as air flow rate is increased.

2.11). At regime IV, the system exhibits thermoacoustic instability, where the highest values of η, k and C_G are obtained, pointing to the strong determinism in the underlying time series. As Re_{air} is further increased, the system deviates from thermoacoustic instability and exhibits low amplitude aperiodic oscillation again (regime V, Fig. 2.11). This transition from combustion instability to low amplitude aperiodic oscillation with decreasing ϕ has been reported earlier [39], [57].

In regime V, the decreasing trends of η, k and C_G imply that the dynamics undergoes a gradual shift towards high dimensional chaos. It may be noted that the RMS amplitude at $Re_{air} = 6054$ and $Re_{air} = 6263$ in regime V show a small difference (Fig. 2.6a) while the RN metrics show a significant difference between these two points (Fig. 2.11). This fact highlights the sensitivity of the RN metrics to the dynamical transition. At $Re_{air} = 6054$, where the system deviates from thermoacoustic instability, value of η is similar to that during thermoacoustic instability; however, the values of k and C_G become low. Thus, it possibly indicates an intermediate dynamical state between periodicity and high dimensional chaos (at $Re_{air} = 6263$). However, the degeneration of the dynamical state from thermoacoustic instability to low amplitude aperiodic oscillation requires a separate study and will not be focused here.

Analysis of RN metrics indicate that, for protocol IA, η shows higher sensitivity for the transition from high dimensional chaos to low dimensional chaos, while C_G shows high sensitivity for the transition from low dimensional chaos to periodicity (Figs. 2.10 and 2.11). In short, we observe that case IA-ii exhibits a more complex route to thermoacoustic instability (HDC $\rightarrow$ LDC $\rightarrow$ HDC $\rightarrow$ LDC $\rightarrow$ periodicity) compared to case IA-i. These inferences on the dynamical states for case IA-ii also will be validated through translational error in Secion 2.2, with a view to check the efficacy of RN analysis in detecting the dynamical states encountered.

2.4.2.2 Network topology at different conditions for case IA-i

RN topologies can help to understand the changes in the RN metrics, such as degree centrality (k) and global clustering coefficient (C_G), as thermoacoustic instability is approached. Representative Gephi topologies shown in Fig. 2.12 are constructed for 0.2 second long data which is down-sampled by a factor of 4 to reduce computational burden. The down-sampling used here is reasonable enough to correctly capture the dynamics at different conditions [44]. The individual nodes are coded by their size and color to obtain visual representations of the networks. The links connecting the nodes are colored the same as their source node. The node sizes are linearly scaled from a size of 1 to 100 with 1 corresponding to

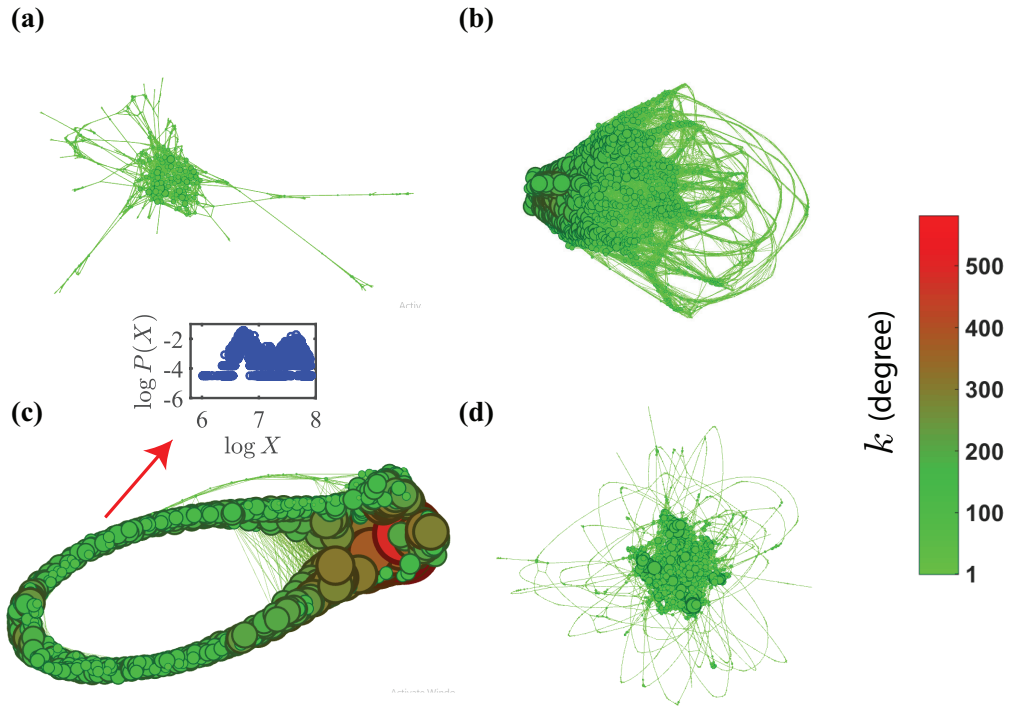

Figure 2.12: Network topology for IA-i case, at (a)Re_{air} = 1566, (b) Re_{air} = 3132,(c)Re_{air} = 4489 and (d)Re_{air} = 5950

minimum degree (i.e. 1) and 100 to maximum degree.

Figure 2.12 shows network topologies for different dynamical states observed in case IA-i. In the topology corresponding to combustion noise at Re_{air} = 1566 (Fig. 2.12a), where the dynamical state is high dimensional chaos, the small sized and bright greenish colored nodes indicate the prevalence of low degree nodes. This explains low values of k at this dynamical state. Also, the network during combustion noise (Re_{air} = 1566) consist of a single giant component [89], [109] which contains almost all the nodes and links of the network. Further, absence of directional alignment results in low C_G during combustion noise.

Figure 2.12(b) shows the topology during 'amplitude varying aperiodic oscillations' at Re_{air} = 3132, where dynamical state is low dimensional chaos. At this state, the links in the RN become more evenly spread compared to that during combustion noise (Re_{air} = 1566). The RN at this condition still mostly consists of the giant component. However, a higher number of links remain outside of the giant component as compared to the RN during combustion noise (Fig. 2.12a). Some larger nodes appear which explain the increase in k. Further, at Re_{air} = 3132 some directional alignment of nodes can be seen which would explain the moderately high value of C_G as compared to Re_{air} = 1566.

Figure 2.12(c) shows a highly connected and ring-like structure of the network observed during thermoacoustic instability at Re_{air} = 4489, where the dynamics is observed to be periodic. At this state, a cluster of highly connected nodes is still

present in the RN which may be considered as the giant component of the network. However, a significant number of the nodes and links are evenly distributed throughout the RN, outside of the giant component. Therefore, during thermoacoustic instability, the RN does not consist entirely of a single giant component unlike the RN corresponding to combustion noise. We infer that the number of links in the RN outside the giant component increases as thermoacoustic instability is approached. Presence of a significant number of high degree nodes explains the high values of k during thermoacoustic instability. The high values of C_G during thermoacoustic instability is due to presence of distinct ring-like alignment of nodes. It is noted that k and C_G are mutually independent [78].

At $Re_{air} = 5950$, where the dynamical state corresponds to high dimensional chaos, the number of high degree nodes in the RN significantly reduces causing a lower value of k (Fig. 2.12d). The giant component is again observed to contain most of the nodes and links. Again, the absence of directional alignment of nodes causes C_G to reduce.

In turbulent partially premixed combustors, the complex network and recurrence network corresponding to thermoacoustic instability have been reported to be a regular network [57], [87], consisting of nodes having same number of links. However, in the current study, nodes with significantly varying degrees are present even during thermoacoustic instability, as marked by different sizes and colors of the nodes in Fig. 2.12(c). The degree distribution of corresponding RN, shown in inset of Fig. 2.12(c), further corroborates this. Note that, $P(X)$ is the probability of nodes having degree X in the RN. Recently, Kasthuri *et al.* [110] have observed the RN topology corresponding to thermoacoustic instability to consist of a ring-like structure typical of periodic signals along with highly clustered regions and protrusions. They reasoned that such RN topology can be due to slow and fast time scales present in the system at thermoacoustic instability. In the present study, we observe absence of a regular network and presence of a cluster of high degree nodes in the RN corresponding to thermoacoustic instability. Such characteristics may be due to presence of multiple time scales even at thermoacoustic instability. The spectral power and scaling laws related to sound emission have been shown to be significantly different for premixed and diffusion flames [111], [112]. Therefore, the different scaling behavior observed for inverse diffusion flame might be due to the difference in mixing and combustion processes also.

2.4.2.3 Validation of the results with translational error metric

Next, we validate the different dynamical states inferred from RN metrics through a established nonlinear metric, translational error (E_{trans}), which is a

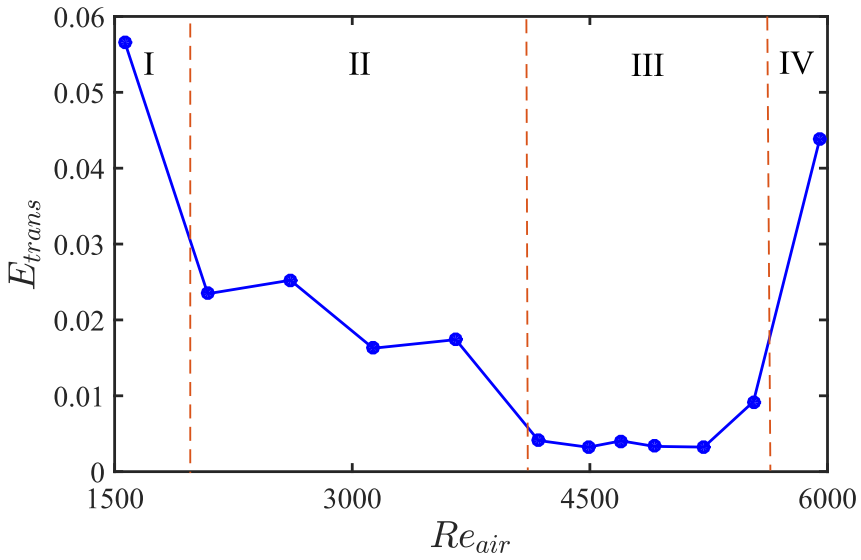

Figure 2.13: Variation of E_{trans} for IA-i case as air flow rate is increased.

modified version of the Wayland method [113] and proposed by Gotoda *et al.* [37]. This method quantifies the divergence of neighbouring vectors in phase space with time. The mathematical details for evaluating the metric is given in Appendix B, at the end of this chapter. The values of E_{trans} at different dynamical states has been reported by Gotoda *et al.* [37], which is reproduced in table 2.2.

Dynamical states	E_{trans}
Stochastic signal	> 0.1
High dimensional chaos	< 0.1
Lorenz attractor (low dimensional chaos)	≈ 0.01
Thermoacoustic instability (High periodicity)	0.0018

Table 2.2: Values of E_{trans} for different dynamical states as reported in Gotoda *et al.*[37]

Values of E_{trans} for protocol IA-i is shown in Fig. 2.13. E_{trans} takes the value of 0.0564 for combustion noise ($Re_{air} = 1566$), suggesting a high dimensional chaotic dynamics. E_{trans} takes the value of 0.0163 for the 'amplitude varying aperiodic oscillations' ($Re_{air} = 3132$), which is close to but slightly higher compared to that of Lorenz attractor. Thus it may be reasoned that the dynamics corresponding to 'amplitude varying aperiodic oscillations' is low dimensional chaos. E_{trans} takes the value of 0.0032 during thermoacoustic oscillation ($Re_{air} = 4489$), suggesting a highly deterministic dynamics. Thus, the dynamical states inferred from recurrence network analysis and E_{trans} corroborate each other. Similar agreement can be observed for protocol IA-ii comparing Figs. 2.11 and 2.14. The discussion for protocol IA-ii is omitted here for brevity. Based on these observations, it can be said that RNA can be used to qualitatively identify the different dynamical states

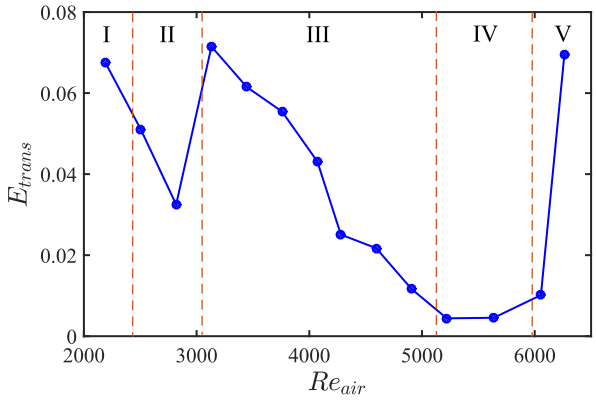

Figure 2.14: Variation of E_{trans} for IA-ii case as air flow rate is increased.

encountered during transition to thermoacoustic instability.

2.4.3 Dynamic transition observed for protocol IP

2.4.3.1 Identification of dynamical states by visual inspection of time series

Next, the transition to thermoacoustic instability is discussed when input power to the IDF is increased. This approach to thermoacoustic instability has been reported by Subramanian *et al.*[114] in a Rijke tube by increasing heater power. The current system is observed to be particularly susceptible to thermoacoustic instability between global equivalence ratios of $\phi = 0.1$ and $\phi = 0.3$. Therefore, one representative case, denoted by IP ($\phi = 0.2$; $Re_{flow} = 5116-5168$), is analysed below. We note that in protocol IP, the flow is always in the turbulent regime ($Re_{flow} > 4000$), unlike in protocol IA.

Figure 2.15(a) shows the gradual increase of RMS amplitude as input power is increased. At input power of 0.50 kW (Fig. 2.15b), low amplitude aperiodic oscillation, characteristic of combustion noise, is observed. At input power of 0.60 kW (Fig. 2.15c), the time series attains a low amplitude seemingly periodic oscillation with approximately constant peak to peak amplitude. Recently, Karlis *et al.* [115] have reported similar type of oscillation of reduced amplitude and argued that such a dynamics occurred due to weakened coupling between pressure oscillation and heat release oscillation. With further increase of input power, the RMS amplitude of signal (Fig. 2.15a) and the periodicity of the oscillation go on increasing till thermoacoustic instability is obtained at input power of 0.68 kW (Fig. 2.15d). In short, the amplitude of the near-periodic oscillations gradually increases as we move towards thermoacoustic instability and away from combustion noise. Thus, the bifurcation undergone closely mimics supercritical Hopf bifurcation[3], especially as we did not find any hysteresis effect on this case.

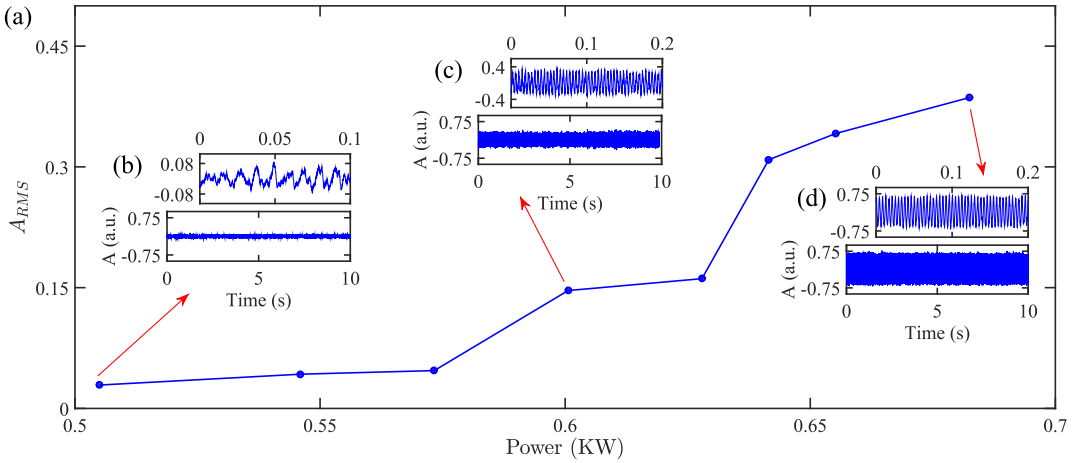

Figure 2.15: (a) RMS amplitude (A_{RMS}) of audio signal as input power is varied (case IP) and corresponding time series at different input powers, (b) 0.50 kW, (c) 0.60 kW and (d) 0.68 kW. A denotes the amplitude of sound signal with arbitrary unit.

Apart from the intermittency route to thermoacoustic instability, other intermediate states prior to thermoacoustic instability also have been reported in literature. Gotoda *et al.*[37] observed an amplitude modulated periodic signal in their study as an intermediate dynamical state prior to thermoacoustic instability.

There are only a few studies on the above mentioned routes to thermoacoustic instability, especially in which the analysis is done in the framework of complex network. The intermediate state found by Gotoda *et al.* [37] had similar peak to peak amplitude to that of the full blown thermoacoustic instability. However, in the current study, we observe that the signal shown in Fig. 2.15(c) has approximately constant peak to peak amplitude which is much lower than the peak to peak amplitude during thermoacoustic instability. Clearly, this dynamical state appears due to an insufficient power (or heat release rate) in the flame to achieve full blown thermoacoustic instability. In the present study, this dynamical state is thus denoted as 'low amplitude limit cycle-like oscillations' in further discussion.

2.4.3.2 Application of network parameters to identify different dynamic regimes

Next, the transition to thermoacoustic instability in protocol IP is explored with the help of RN metrics. Similar to IA cases, the operating range is divided into 3 regimes to aid the discussion. Global efficiency (η) and average degree centrality (k) are observed to be low in regime I (Fig. 2.16) indicating high average distance between the nodes and low phase space density. Further, a low value of global clustering coefficient (C_G) in this regime indicates the absence of

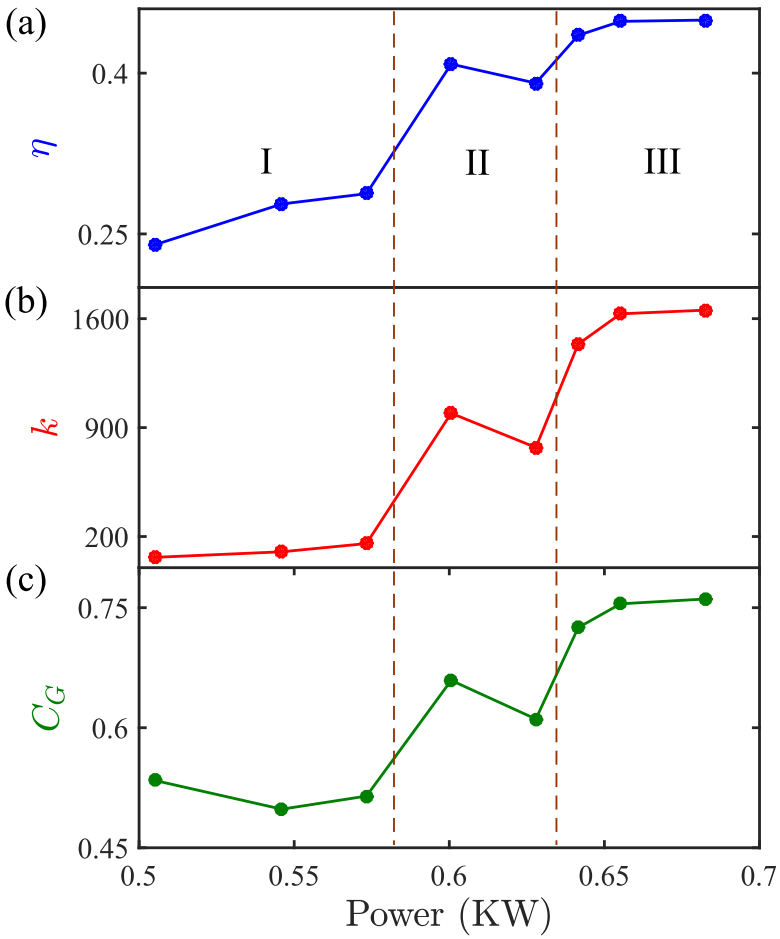

Figure 2.16: Variation of (a) global efficiency (η), (b) degree centrality (k) and (c) global clustering coefficient (C_G) as power input is varied for IP case.

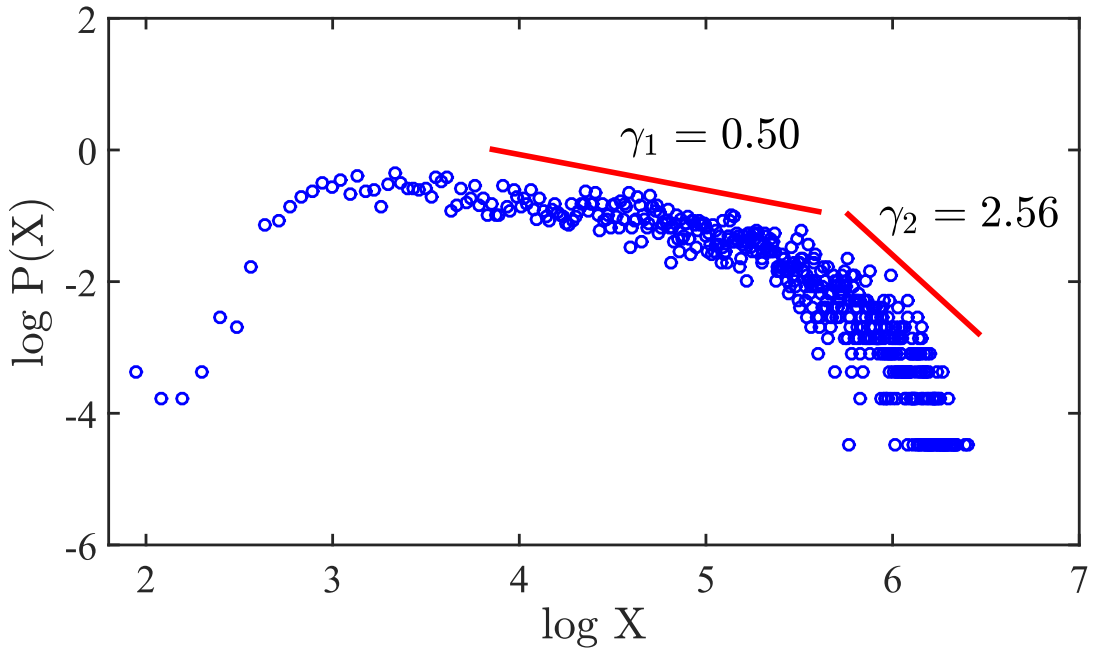

Figure 2.17: Degree distribution plot for the IP case at Power = 0.50 kW (regime I). $P(X)$ indicates frequency of nodes with degree X.

low dimensional objects in the phase space. These imply that regime I exhibits high dimensional chaos.

Regime II corresponding to the 'low amplitude limit cycle-like oscillations' shows moderately high values of η, k and C_G whereas regime III shows high values of η, k and C_G. Therefore, regime III shows very strong determinism whereas regime II is more deterministic than high dimensional chaos observed in regime I, but less deterministic compared to thermoacoustic instability in regime III. Thus, the RN analysis imply low dimensional chaos for regime II. We note that for protocol IP, each of η, k and C_G show similar sensitivity throughout the transition from combustion noise to thermoacoustic instability, unlike in protocol IA.

2.4.3.3 Degree distribution of recurrence networks during combustion noise

A Complex network is said to exhibit scale-free behavior [109], when its degree distribution follows the power law, $P(X) \sim X^{-\gamma}$ where, $P(X)$ is the probability of nodes having degree X in the RN and γ is a positive number such that $(2 < \gamma < 3)$. Previous studies in predominantly premixed turbulent combustors [57], [87] have reported combustion noise to exhibit scale-free behaviour, which was further linked to the underlying turbulent flow [87]. In scale-free networks of the realistic systems, a few nodes may be present, which do not obey the above-mentioned scaling law

[57]. Godavarthi *et al.* [57] used the criteria that if at least 90 percent of the nodes in the RN follows the power law, the RN can be considered to exhibit scale-free behaviour. Further, Gotoda *et al.* [39] observed power law degree distribution near lean blowout instability in a premixed turbulent combustor.

In the present study, the degree distribution during combustion noise is observed not to follow a single power law. As a representative case, the degree distribution at the input power of 0.50 kW is shown in Fig. 2.17. It depicts two different power laws though the previous studies have observed a single power law during combustion noise in premixed or predominantly premixed combustors [39], [57], [87]. While one of the power law exponents is very low ($\gamma_1 = 0.50$), the other power law exponent satisfies the criterion for scale-free nature ($\gamma_2 = 2.56$). However, the corresponding RN cannot be said to have scale-free degree distribution as a significant number of nodes do not follow the corresponding scale-free law. It is known that scale-free nature of RN cannot be captured for larger thresholds [57]. However, as we have chosen the minimum recurrence threshold at which the RN becomes devoid of any disconnected node, it is unlikely to be the case here.

These observations show that combustion noise for premixed and inverse diffusion flame have significantly different characteristics. As stated earlier, the scaling nature corresponding to sound emission in premixed and diffusion flames are known to be different [111], [112]. Therefore, the absence of scale-free nature or a single power law degree distribution during combustion noise is likely to be due to the difference in underlying mixing and combustion processes between premixed configuration and inverse diffusion configuration. Another possible reason for absence of scale-free nature may be absence of isotropic turbulence in the present configuration, as we have not implemented any turbulence grid to generate isotropic turbulence.

2.5 Summary

Inverse diffusion flame (IDF) is a reliable low NO_X technology which is suitable for various industrial applications including gas turbines. However, a confined IDF may exhibit thermoacoustic instability, a kind of dynamic instability, which is characterized by catastrophically large amplitude pressure oscillations. Transition to thermoacoustic instability for an inverse diffusion flame is less explored compared to other types of flame. To bridge this gap in literature, in this study we approach thermoacoustic instability with two protocols: (i) by increasing airflow (protocol IA) and (ii) by increasing power input (protocol IP). This study is carried out with a Rijke tube test rig having a inverse diffusion flame. The transition from combustion noise to thermoacoustic instability is analyzed under the purview of

recurrence network. The important findings of this study are summarized below.

1. In protocol IA, the flow regime changes from laminar ($Re_{air} < 2300$) to transition regime ($2300 < Re_{air} < 4000$) as thermoacoustic instability is approached. However, the RN measures are found to be robust enough to detect the onset of thermoacoustic instability, even though laminar and transition flow regimes are fundamentally different.

2. The dynamic transition observed for protocol IA and protocol IP are different. The IA protocol encounters 'amplitude varying aperiodic oscillations' as an intermediate state. Protocol IP encounters 'low amplitude limit cycle-like oscillations' as an intermediate state, which consists of low amplitude seemingly periodic oscillations. Dynamic analysis with RNA however reveals that both the 'amplitude varying aperiodic oscillations' and 'low amplitude limit cycle-like oscillations' are low dimensional chaos.

3. RNA can be used to identify the different dynamical states of the combustor during transition to thermoacoustic instability. The inferences drawn with RNA in this regard are validated though a well-established nonlinear dynamical metric, translational error (E_{trans}).

4. In this work, network topologies are visualized graphically to enhance understanding of the changes occurring in RN metrics as underlying dynamics shift. RN during combustion noise is observed to consist almost entirely of a giant component. However, the RN during thermoacoustic instability have a significant number of links outside the giant component.

5. A single characteristic scale was found to be present at TAI in previous literature that explored TAI in premixed flame. A network that exhibits such dominance of a single characteristic scale is called a regular network. In the present study, however, multiple scales are seen in the recurrence network even during thermoacoustic instability, showing that the regular network does not form at TAI for an inverse diffusion flame. Additionally, the degree distribution during combustion noise in the current investigation does not adhere to a scale-free nature or even a single power-law. Previous studies with premixed combustors, however, has observed the occurrence of scale-free or single power-law degree distribution in the recurrence networks at stable combustion states. In summary, there are notable differences between IDF and premixed flames in the recurrence network topology during combustion noise and thermoacoustic instability states. These differences in the dynamical properties at different combustion regimes may result from

the inverse diffusion flame's differing mixing and scaling laws with those of premixed flames.

6. The novel dynamical characteristics, encountered in Rijke tube test rig with inverse diffusion flame, points to the need for studying the dynamical transition to thermoacoustic instability in other nonpremixed and co-flow type combustors.

Citation acknowledgment

Some parts of this chapter are reproduced with permission from the publication(s) listed below.

1. "Recurrence network analysis exploring the routes to thermoacoustic instability in a Rijke tube with inverse diffusion flame", Chaos: An Interdisciplinary Journal of Nonlinear Science, 31(3), p.033117, 2021 (DOI: 10.1063/5.0026943).

2. "Early detection of lean blowout using recurrence network for varying degrees of premixedness", Chaos: An Interdisciplinary Journal of Nonlinear Science, 32, 063105, 2022 (DOI: 10.1063/5.0077436).

Appendix A

Here, a brief description of the complex network theory is provided for the interested reader. An elaborate discussion on the network theory may be found in Newman *et al.* [89]. A complex network (CN) is simply a collection of points along with lines so that each line connects a pair of points [89]. The points contained in the complex network are called nodes (or, vertices) of the CN while the lines connecting the pair of nodes are called the edges (or, links) of the CN.

Complex systems, which can be thought of as complex networks, abound in nature and man-made structures. Networks in nature include metabolic networks, disease networks, networks of neurons (in the brain), etc. Networks created by technology are many, including telephone networks, the world-wide-web, electric grids, gas pipelines, railway lines, etc [89]. Such complex systems are almost always made of a high number of interacting elements. Interactions within complex systems often affect the whole system's behavior in significant ways [89]. In the complex network framework, a system is considered to consist of a large number of interacting sub-systems. Consequently, complex network analysis (CNA) is often highly effective in understanding the behavior of complex systems.

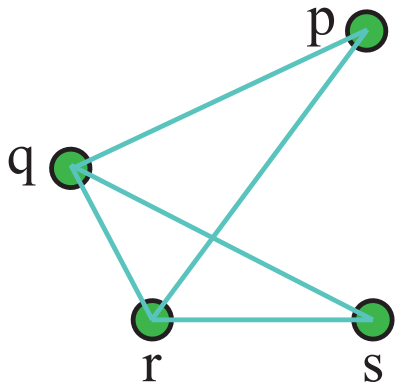

Figure 2.18: An unweighted, undirected complex network, having four nodes (nodes 'p', 'q', 'r' and 's') and five edges.

Many types of complex networks are possible, namely, undirected and directed, weighted or unweighted, etc. In directed networks, edges have specific directions while in undirected networks, edges do not have any directions. On the other hand, in weighted networks, each edge is assigned a weightage, signifying the importance of the edge on the behavior of the complex system. In unweighted networks, all edges have equal importance. We find that the unweighted, undirected complex network is sufficient to explore the dynamical transitions encountered during this thesis work. Hence, only the unweighted, undirected complex network is described in detail next.

Complex networks are mathematically represented by adjacency matrix **a**. They can also be visually represented by an ensemble of nodes and edges for ease of understanding the interactions between the sub-systems. A unweighted, undirected complex network (CN) is shown in Fig. 2.18. Here, the CN consists of 4 nodes (nodes 'p', 'q', 'r' and 's') and 5 edges. The nodes are denoted as circles and edges by lines. In an undirected, unweighted network, the existence of an edge is represented in the adjacency matrix by 1. In equation 2.11, the adjacency matrix **a**, corresponding to Fig. 2.18, is shown. In this adjacency matrix, the four rows from top to bottom may be considered as the rows corresponding to 'p', 'q', 'r', and 's' nodes respectively. Similarly, the four columns from left to right may be considered as the columns corresponding to 'p', 'q', 'r', and 's' nodes respectively.

$$\mathbf{a} = \begin{pmatrix} 0 & 1 & 1 & 0 \\ 1 & 0 & 1 & 1 \\ 1 & 1 & 0 & 1 \\ 0 & 1 & 1 & 0 \end{pmatrix} \tag{2.11}$$

The nodes 'p' and 'r' are connected by one edge in the complex network (Fig. 2.18), so that in $\mathbf{a}$, in column 'p' and row 'r', the value assigned would be 1. This point in the adjacency matrix may be represented by $\mathbf{a}_{p,r}$ in short. As the complex network of Fig. 2.18 is undirected, if 'p' is connected to node 'r', it also means node 'r' is connected to node 'p'. Therefore, $\mathbf{a}_{p,r} = \mathbf{a}_{r,p} = 1$, in this case i.e. $\mathbf{a}$ is a symmetric matrix. On, the other hand, 'p' and 's' nodes are not connected. Therefore, $\mathbf{a}_{p,s} = \mathbf{a}_{s,p} = 0$. Often, the self-loops, i.e. connection of a node with itself are considered redundant information in the complex network framework. Therefore, the self-loops are often not considered when calculating the adjacency matrix. In such cases, the diagonal elements of $\mathbf{a}$ would be zero.

Another relevant concept in the complex network theory is the Laplacian matrix ($\mathbf{L}$) of the adjacency matrix ($\mathbf{a}$). For an adjacency matrix corresponding to an unweighted, undirected complex network, the Laplacian matrix can be calculated as [89],

$$\mathbf{L}_{p,q} = \begin{cases} k_p & \text{if } p = q \\ -1 & \text{if } p \neq q \text{ and the nodes } p \text{ and } q \text{ are connected} \\ 0 & \text{in all other cases} \end{cases} \tag{2.12}$$

Here, k_p indicates the degree of the node 'p'. Equation 2.12 can be represented also in the following way [89],

$$\mathbf{L}_{p,q} = k_p \delta_{p,q} - \mathbf{a}_{p,q} \tag{2.13}$$

The structural properties of the CN can be quantified using several metrics, for example, degree centrality, clustering coefficient, efficiency, etc. Often, these metrics are calculated on a local basis and then averaged over the whole network to obtain the global CN metrics, for example, global efficiency, global clustering coefficient, etc. The global metrics can provide important insights into the overall behavior of the complex system being investigated. Often the local CN metrics also contain significant information. For example, the local degree centrality metric may reveal the most important nodes in the CN [89]. Therefore, the local and global CN metrics may be studied in tandem to better understand the complex network behavior.

Appendix B

Choice of recurrence threshold

As the RN measures are very sensitive to threshold ϵ, it must be chosen with a sound theoretical basis. In this work, the method prescribed by Eroglu *et al.* [94] is used to calculate ϵ. It is described here in brief. ϵ is varied parametrically and the Laplacian matrix [89] of adjacency matrix **a** is calculated for each ϵ. The second minimum Eigen value (λ_2) of the Laplacian matrix is calculated for each Laplacian matrix. Then, λ_2 is plotted against ϵ (Fig. 2.19). The minimum value for which $\lambda_2 > 0$ would be the optimal ϵ. Theoretically at this condition, the RN would contain no disconnected node. However, in practice we find a slightly larger threshold ($\lambda_2 > 0.03$) is required to make the RN devoid of any disconnected node. The optimal threshold ϵ_{opt} is found to be approximately 15% of maximum phase space distance.

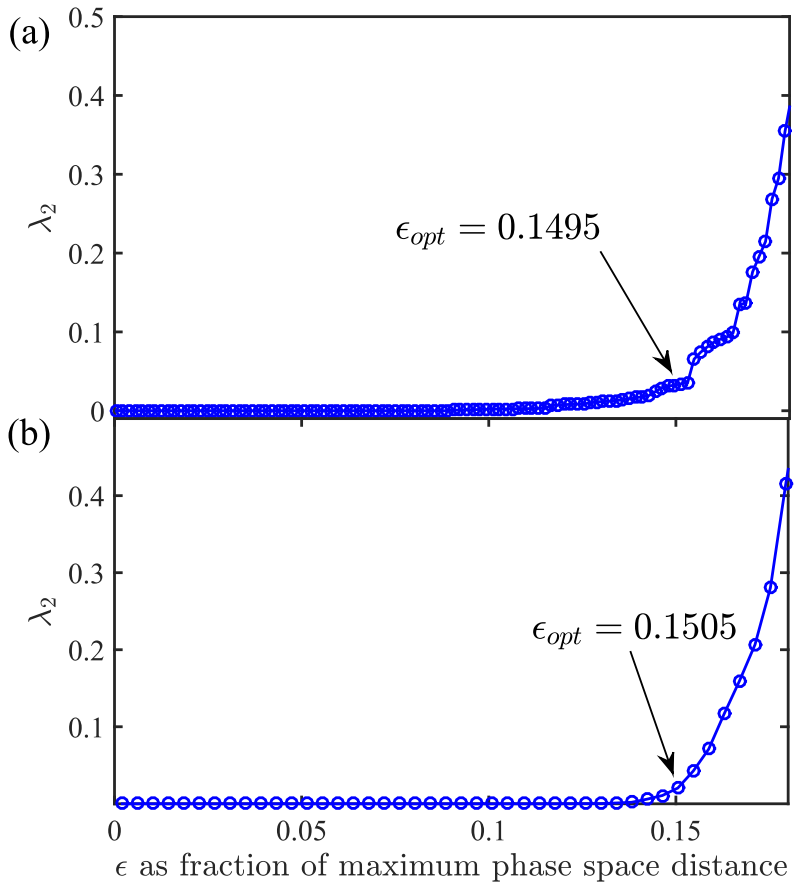

Figure 2.19: λ_2 vs ϵ plots of combustion noise regime for (a) IP case at Power = 0.50 kW and (b) IA-i case at $Re_{air} = 1566$.

Translational error technique to identify dynamic states of a system

A concise description of the translational error method is given here. For a vector $\mathbf{Z}(t)$, M number of neighborhood points are chosen. E_{trans} measures the divergence of vectors with passage of time and is given by,

$$E_{trans} = \frac{1}{(M+1)} \sum_{m=0}^{M} \frac{||\mathbf{Q}(t_m) - \overline{\mathbf{Q}}||}{||\overline{\mathbf{Q}}||} \tag{B1}$$

$$\overline{\mathbf{Q}} = \frac{1}{(M+1)} \sum_{m=0}^{M} \mathbf{Q}(t_m) \tag{B2}$$

$$\mathbf{Q}(t_m) = \mathbf{Z}(t_m + \Delta T) - \mathbf{Z}(t_m) \tag{B3}$$

Here, ΔT is the time step after which the divergence of vectors are checked and $\mathbf{Q}(t_m)$ is the instantaneous tangential vector at instant t_m. The parameters corresponding to translation error analysis, such as M, are chosen as in previous literature [37], [38]. For 10 sets of randomly chosen $\mathbf{Z}(t)$ from the 2 second long data library, the median E_{trans} is calculated and shown in Figs. 2.13 and 2.14.

CHAPTER 3

Early detection of lean blowout in single-burner combustor using recurrence network

3.1 Introduction

Modern gas turbine combustors operate on premixed or partially premixed mode of combustion in order to reduce NO_X emission [30]. Lean premixed combustion reduces NO_X significantly while still having a high cycle efficiency [29], [116]. Other low NO_X technologies, including fuel staging and inert gas injection, have a lower cycle efficiency and are not that effective in reducing NO_X emission[116]. However, lean combustion is inherently weak and suffers from instabilities, including thermoacoustic instability and lean blowout [19], [43].

Lean blowout (LBO) is caused by an imbalance of flow rate and flame speed [4]. In aircraft engines, sudden changes in power setting may result in abrupt reduction in fuel flow; however, the air flow rate takes significantly longer time to reduce due to compressor inertia [28]. During this brief transition period, equivalence ratio of the air-fuel mixture may fall below the lean blowout limit resulting in flame extinction. On the other hand, stationary gas turbines has to operate very close to lean blowout limit to meet stringent emission regulations. Thus the stationary gas turbines are highly susceptible to fluctuations inherent in combustion systems, changes of environmental conditions and small fluctuations in fuel composition [28]. These factors alone or together can cause LBO in stationary gas turbines. If LBO occurs, lengthy shutdown and restart in stationary gas turbines is required

while for aircraft engines, it may cause fatal accidents [19], [29], [30].

A lot of studies have been done to explore the LBO phenomenon in premixed combustors [18], [19], [29], [117]–[120]. It is known that the lean blowout limit corresponding to a combustor depends on a number of parameters, including temperature and humidity of input air. These parameters keep changing with environmental conditions thereby changing the lean blowout limit [121]. However, accurate prior estimation of LBO limit has not been possible till date due to insufficient understanding about the fundamental combustion mechanisms [19], [30]. Therefore, the stationary and aircraft gas turbine combustors are operated with a higher than optimal safety margin to avoid LBO at the cost of increased NO_X emission [29], [121].

An online early LBO prediction strategy can (i) improve the reliability of the aircraft gas turbine combustors, which have a narrow operational range, especially during faster change of power in aircrafts during take-off, landing and rapid maneuvers [28], (ii) avoid inefficient combustion, resulting in emissions of CO and unburnt hydrocarbons [30] and (iii) subject the combustor to a lower operating temperature, resulting in less wear and tear [28]. Unfortunately, there is no such reliable technology applicable for a wide range of combustors at present. Thus it is important to devise reliable early LBO prediction tools.

In recent times, different strategies have been proposed to early predict LBO, for example, amplitude thresholding, statistical and frequency domain based techniques [28], [30], [122]–[124]. Recently a number of novel tools for early prediction of LBO have been proposed. Giorgi *et al.* [125] used flame image based wavelet and statistical analysis to predict lean blowout for a nonpremixed configuration. Li *et al.* [122] used low frequency content of the ion current signal to early predict lean blowout. Chang *et al.* [126] used the change in low value points in ion current signal, for early prediction purpose. Many of the established LBO detection techniques need to be carefully calibrated depending on different types of combustors with varying size, geometry and operating conditions [30]. Nonlinear dynamics based techniques can also be used as early prediction tools for LBO. Such tools directly capture the changes in combustor dynamics during transition to LBO and thus are likely to be applicable for a broad range of combustors.

Recently, a number of dynamically rich phenomena in combustors have been found [36], [39], [58]. Intermittency prior to LBO has been reported in a number of studies [36], [38], [41]. Pagliaroli and Troiani [120] found a new type of intermittency with pike-like patterns in the recurrence plots near LBO. Most of these studies have been done with a fixed degree of premixedness. However, flame characteristics are known to vary significantly with variation of degree of premixedness [74], [127]–[130]. In a previous study [42], we found black dense patches in the

recurrence plots near LBO for higher degrees of premixedness, indicating presence of type-II intermittency. Such patches in the recurrence plots were not found for lower degrees of premixedness. So, the dynamic transition towards LBO is likely to vary significantly depending on the degree of premixedness.

Moreover, most previous studies have explored the route to lean blowout with preceding thermoacoustic instability [39], [57] where the typical path to LBO is, limit cycle oscillations (at thermoacoustic instability) → intermittency → aperiodic low amplitude oscillations → LBO. The dynamical transition in such case is likely to involve loss of periodicity i.e. determinism reduces as LBO is approached. However, combustors not susceptible to thermoacoustic instability in their operating regime may well be susceptible to LBO [43]. Unni *et al.* [43] reported two different paths through which lean blowout can occur as mixture is progressively made leaner. These routes are (i) lean blowout with preceding thermoacoustic instability and (ii) lean blowout without preceding thermoacoustic instability. Using multifractal analysis of CH* chemiluminescence and pressure signal, they showed that the dynamical transition to LBO in these two cases are significantly different.

In absence of thermoacoustic instability, the most significant dynamic phenomena during approach to LBO are the (i) extinction-reignition events for the more premixed configurations and (ii) flame pulsations for less premixed configurations. Both of these events are intermittent in nature and occur just prior to LBO [42]. The dynamical state corresponding to intermittency typically corresponds to low dimensional chaos [38]. On the other hand, the dynamical state corresponding to stable combustion (otherwise called combustion noise) is high dimensional chaos [108]. Moreover, in our previous study, we found determinism to increase as the system moves from stable combustion to near-LBO regime [42]. So, the dynamic transition to LBO, with and without preceding thermoacoustic instability, are likely to be significantly different. So, it is important to explore the robustness and efficacy of the different early lean blowout prediction techniques (i) for varying degrees of premixedness and (ii) for the transition to lean blowout without preceding thermoacoustic instability, so that their suitability for a wide range of practical situations can be judged.

Thus, the current study explores the dynamical transition towards LBO without preceding thermoacoustic instability, for varying degrees of premixedness. The test rig used in this study is a lean premixed, swirl –bluff stabilized combustor. Swirl-bluff stabilized combustors are often used as a simplified model for stationary gas turbine combustors and lean premixed prevaporized aircraft gas turbine combustors [29], [131].

Turbulent combustors can be considered as ensemble of a number of mutually interacting elements [132] i.e. a complex system. So, complex network is a

suitable tool to explore the dynamical transition towards LBO. A few previous studies [39], [87] have explored the visibility algorithm based complex network analysis for detection of LBO and thermoacoustics instability. However, in visibility based complex network, attractor geometry in phase space is not preserved [57]. Recurrence network (RN) is another well-known type of complex network is constructed using recurrence information embedded in time series [78]. RN discards the temporal information from the time series and only considers the spatial dependencies of the observable at different time instants [78]. Recurrence network preserves attractor structure in phase space [57], [78] [78] and therefore conserves the underlying dynamical properties of the system. Moreover, the RN metrics are statistical measures related to phase space density and thus likely to be robust tools for detecting dynamical transitions. Unlike many well-established nonlinear time series analyses, RN analysis can be used even with small time series [133], is robust against experimental noise [86], [133] and do not require a surrogate test [80]. Due to these advantages, RN has been applied to a wide range fields, e.g. in engineering [39], [57], biological sciences [85], climatology [81] and physical sciences[84] etc. Therefore, in this study we use recurrence network (RN) to explore dynamical transition to LBO in absence of preceding thermoacoustic instability.

In the present study, we observe that the change of dynamics, from stable combustion regime (also known combustion noise regime) to near-lean blowout regime, in absence of preceding thermoacoustic instability, is subtle as compared to that previously reported for lean blowout with preceding thermoacoustic instability [57]. In this route to LBO, the path followed is, low amplitude aperiodic oscillations (in the stable combustion regime) $\rightarrow$ ensemble of high and low amplitude aperiodic oscillations (in the near-LBO regime) $\rightarrow$ LBO. We explore the combustion dynamics with three RN metrics: global efficiency (η), average degree centrality (k) and global clustering coefficient (C_G). Each of these metrics follow an increasing trend during transition to LBO indicating a shift towards periodicity. We infer that the metrics η, k and C_G are robust early LBO detection tools. However, the results also highlight the importance of prior knowledge of the degree of premixedness and route to LBO (i) for accurate early detection of an impending LBO and (ii) to decide the optimal safety margin. These are important observations, as practical gas turbine combustors often have partially premixed configurations [30]. Moreover, we present a comparative discussion on the efficacy and applicability of the RN analysis and recurrence quantification analysis, as early lean blowout prediction tools, at various degree of premixedness. Finally, we link the changes in various RN measures with the visible changes in recurrence network topology, which may help to better understand the dynamical transition to LBO.

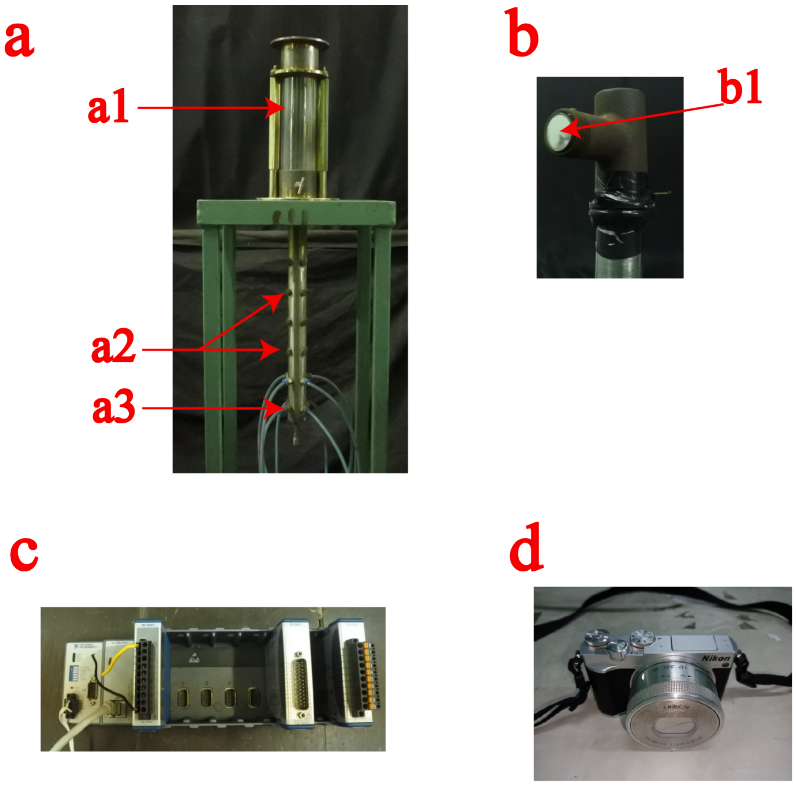

Figure 3.1: (a) Swirl stabilized dump combustor, (a1) combustor chamber made of quartz tube, (a2) fuel input ports, (a3) air input ports, (b) photo-multiplier tube (PMT), (b1) CH* filter, (c) DAQ (cRIO-9073) and (d) camera.

3.2 Experimental setup

The experimental swirl stabilized dump combustor is shown in Fig. 3.1 and the corresponding schematic is shown in Fig. 3.2. The combustor is designed in such a way that the degree of premixedness can be varied by changing the mixing length of the premixing tube. The variation of mixing length is achieved by changing the position of fuel input along the axis of the premixing tube. Successive fuel input positions have a gap of 50 mm between them. At each axial position, four fuel input ports are provided 90° apart to ensure symmetric distribution of fuel throughout the cross-section of the premixing tube. Air is input into the premixing chamber at 50 mm below the lowest fuel input position. The swirler, having 7 vanes, is placed 15 mm upstream of the dump plane and has a swirl number of 1.26[128]. The combustion chamber is made of a quartz tube to allow optical access and have an inner diameter of 60 mm, height of 200 mm and thickness of 2.5 mm.

During this study, liquefied petroleum gas (LPG, 40% propane and 60% butane

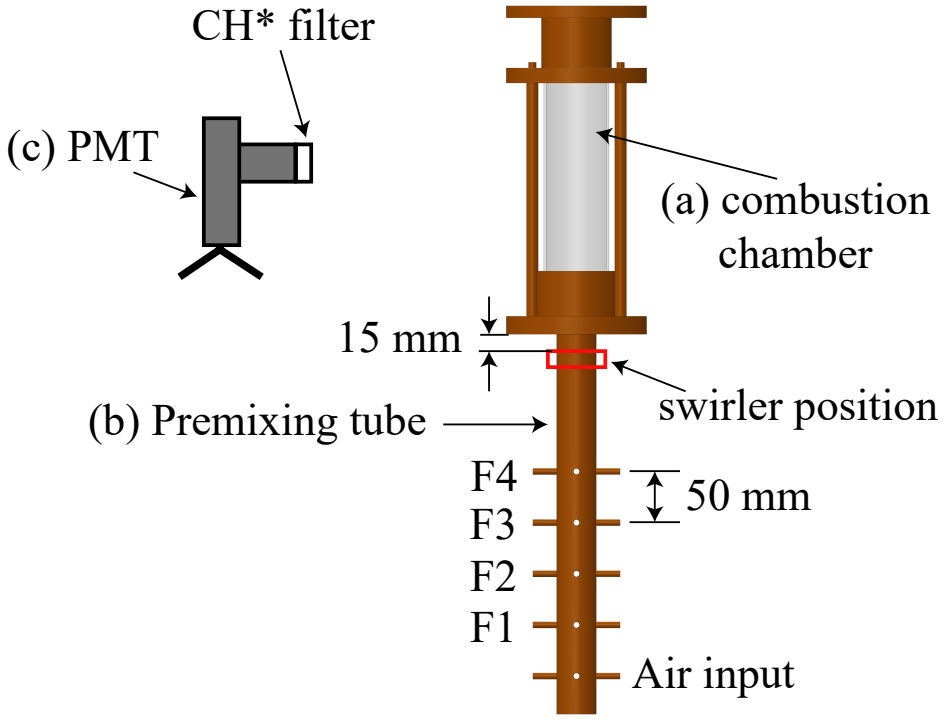

Figure 3.2: Schematic of the experimental test rig. (a) Combustion chamber, (b) premixing tube and (c) photo-multiplier tube (PMT) with CH* filter. F1, F2, F3 and F4 correspond to the fuel input positions 1-4 respectively.

by volume), is used as fuel. LPG shows similar chemical behavior and similar near-extinction behavior as compared to heavy and complex hydrocarbons[2]. Further benefit of using LPG is its low cost and easy availability. Air at atmospheric temperature is supplied through a mass flow controller (Alicat, Air, 1500 lpm; accuracy: 0.8% of measured value + 0.2% of full scale reading). LPG is supplied through another mass flow controller (Alicat, CH_4, calibrated for LPG, 250 lpm; accuracy: 0.8% of measured value + 0.2% of full scale reading).

Lean blowout is obtained by starting the experiment at far away from LBO (Table 3.1), and gradually reducing the LPG flow rate while keeping air flow rate constant. This approach to LBO approximately keeps the total flow rate constant as the changes in LPG flow rate is much smaller in comparison with the air flow rate. Thus the non-reacting flow rate of the combustor and Reynolds number (Re) remain approximately constant ($Re = 6634$) as LBO is approached. Here, Reynolds number is calculated as, $Re = 4\dot{m}_{air}/(\pi d\mu_{air})$, where $\dot{m}_{air}$ is the mass flow rate of the air, d is the effective diameter at the dump plane and μ_{air} is the dynamic viscosity of air. So, during the experiment, the flow remains in the turbulent regime ($Re > 4000$). After each adjustment of the LPG flow rate, we wait for 20 seconds before acquiring data, in order to avoid the transient effects.

Fuel input position	F1	F2	F3	F4
Air flow rate (lpm)	80	80	80	80
Global equivalence ratio (ϕ)	0.9-0.65	0.9-0.65	0.85-0.6	0.8-0.5

Table 3.1: Operating regime during transition to LBO, at various degrees of premixedness. F1, F2, F3 and F4 correspond to the fuel input positions 1-4 respectively.

The measurement uncertainty corresponding to the flow rates can be calculated from the accuracy ratings of the mass flow controllers. The uncertainty for air is $\pm$2.3 lpm for a flow rate of 80 lpm, and that for LPG is $\pm$0.3 lpm for a flow range of 2.6 - 1.4 lpm (table 3.1).

CH* chemiluminescence signal is widely regarded as a measure for heat release rate in the combustor for premixed and partially premixed flames [130], [134]. Moreover, CH* chemiluminescence signal has a fast response to changes in combustion dynamics[29]. Yi and Gutmark[30] has noted that acoustic emission has much lower sensitivity to dynamics near LBO and that chemiluminescence signature is a better tool to explore LBO phenomenon. Thus in the present study, CH* chemiluminescence is acquired to explore the LBO dynamics.

A photo multiplier tube (PMT) (Hamamatsu, model 931A), fitted with a CH* band pass filter, is used to obtain CH* signal and positioned in a way that the entire flame is visible to it. The CH* filter centres at 430 nm with 10 nm full width half maximum. The PMT output then passes through the build-in amplifier powered with 15 V DC supply to produce voltage output. The voltage signal is input into a National Instruments data acquisition system (DAQ; cRIO-9073) with a sampling rate of 2 kHz for a duration of 20 seconds for each operating condition.

3.3 Brief description of background theory

3.3.1 Construction of adjacency matrix

The phase space is a high dimensional space such that the state of a dynamic system can be described by a point in it. To uniquely identify the state of the combustor in phase space, a number of phase space vectors are required. These phase space vectors are generated by embedding the experimentally obtained CH* time series $y(t)$ in D-dimensional phase space with help of the embedding theorem [91]. From the embedded time series, the adjacency matrix is calculated using a recurrence threshold (ϵ) as discussed in chapter 2.

Because the recurrence networks constructed depends strongly on the choice

of ϵ, it is important to choose ϵ judiciously. While there are a number of ways to choose recurrence threshold [78], [95], [135], we use a fixed ϵ to explore the dynamical transition to LBO. This approach retains the information about the local phase space density in the RN [78]. We note that the phase space density (ρ_p) is the probability of the state of the combustor to be at a particular point in the phase space [92], [136]. We calculated ϵ with the algorithm prescribed by Eroglu *et al.* [94]. This method chooses the minimum ϵ as the optimal threshold, at which no node of the resulting complex network remains disconnected. We found that ϵ is around 19% of maximum phase space distance for different degrees of premixing. The procedure to calculate ϵ is described in detail in our previous study [42] and thus omitted here for brevity.

As discussed in chapter 2, useful insights about the combustor dynamics can be obtained from the recurrence network metrics [57]. These metrics are higher order statistical measures of the phase space density [78]. Three metrics: Global efficiency (η), average degree centrality (k) and global clustering coefficient (C_G), are chosen to explore the dynamical transition to LBO. A brief description of these RN metrics is provided in chapter 2 and hence is omitted here for brevity.

3.3.2 Recurrence quantification analysis

In this study, we compare the efficacy of the recurrence network analysis (RNA) with recurrence quantification analysis (RQA) as early LBO prediction tools. The results corresponding to RQA as a early LBO prediction tool has been reported in a previous study [42], which are reprinted in this chapter to compare the RN and RQA tools. RQA is a well-known tool of nonlinear science [42], [95], [137]. Next, we discuss the theoretical background of RQA in brief for ease of understanding the results. The recurrence information can be concisely represented in the recurrence matrix ($\mathbf{R}$) as discussed in chapter 2. RQA searches for structural patterns in recurrence plots (RP) to identify dynamic state of a system. For this, RQA uses quantitative metrics that are based on diagonal, horizontal and vertical lines occurring in the recurrence plots. In the present study we show the variation in two recurrence quantification metrics during transition to LBO, namely the determinism (DET) and laminarity (LAM).

Determinism : It is given by the ratio of the number of points which are part of a diagonal to total number of points in the recurrence plot. In other words,

$$DET = \frac{\sum_{l=l_{min}}^{N} lp(l)}{\sum_{i,j=1}^{N} \mathbf{R}_{ij}} \tag{3.1}$$

Here, $p(l)$ indicates the number of diagonal lines having length l. l_{min} indi-

cates the minimum number of recurrent points arranged diagonally in order to be considered as a diagonal line. Here we take $l_{min} = 4$. If the underlying dynamic process is chaotic or stochastic in nature, the diagonal lines in the corresponding recurrence plot would be either absent, or very short [95]. As prevalence of diagonal lines is low, DET would be low when the combustor dynamics is chaotic or stochastic. For periodic systems, the diagonal lines would be longer and hence DET will be higher [95]. So, DET is indicative of the periodicity of the system.

Laminarity : The number of points in the vertical lines to the total number of points in the recurrence plot is called the laminarity (LAM).

$$LAM = \frac{\sum_{v=v_{min}}^{N} vp(v)}{\sum_{v=1}^{N} vp(v)} \tag{3.2}$$

$p(v)$ is the number of vertical lines having length v. Thus LAM would decrease if number of vertical lines reduces. v_{min} is the minimum number of recurrent points arranged vertically for it to be considered as a vertical line. Here we choose $v_{min} = 4$. It is known that LAM can detect the chaos - chaos transition and chaos - order transition [95], [137]. Further, LAM increases significantly as intermittent extinction-reignition events/ flame pulsations start to occur close to LBO [42]. More detail discussion about the RQA may be found in previous literature [95], [137].

3.4 Results and discussions

We have explored the degree of premixedness in the single-burner combustor for various air-fuel mixing lengths using numerical simulations, as reported in our previous study [128]. Here we briefly mention the main results. We quantify the homogeneity of the air-fuel mixture with a simple summary metric κ. κ is based on mixture fraction (ψ) of the air-fuel mixture. We note that mixture fraction is defined as the mass flow rate of fuel divided by the total mass flow rate of oxidizer and fuel. Mathematically,

$$\psi = \frac{\dot{m}_f}{\dot{m}_f + \dot{m}_{ox}}. \tag{3.3}$$

Here, $\dot{m}_f$ and $\dot{m}_{ox}$ indicates the mass flow rate of fuel (LPG) and mass flow rate of oxidizer (air) respectively. κ is defined as the ratio of standard deviation of ψ to mean value of ψ i.e., $\kappa = \sigma_\psi/\overline{\psi}$. κ is calculated at a plane just below the dump plane. Thus defined, κ may be taken as a very simple metric to indicate the heterogeneity in the air-fuel premixedness. κ shows an increasing trend as the mixing length is decreased. At fuel input 1 (denoted by F1 henceforth) where

the air-LPG mixing length is 330 mm, κ is least with a value of 0.073. Value of κ for fuel input 2 (mixing length 280 mm, F2), fuel input 3 (mixing length 230 mm, F3) and fuel input 4 (mixing length 180 mm, F4) are 0.075, 0.104 and 0.174 respectively. Thus it may be reasoned that F1 and F2 have relatively high degrees of premixedness as compared to F3 or F4.

3.4.1 Description of CH* time series obtained at varying degrees of premixedness

As equivalence ratio is reduced, the combustor moves from stable combustion regime to near-LBO regime through a transition regime, for all degrees of premixedness [42]. In our previous papers [42], [128], [129], we have shown the extinction-reignition events to occur only for higher degrees of premixedness (F1-F3). At lower degrees of premixedness (F4), the extinction-reignition events are not present; however, flame oscillations in the near-LBO regime are still present.

First, we explore the transition to LBO for the F1 case (highest premixed case considered during this study) with CH* time series (Fig. 3.3). We normalize the equivalence ratios (ϕ) of different operating points by dividing them with the equivalence ratio at LBO (ϕ_{LBO}). Figure 3.3(a) shows the time series at a condition far away from LBO ($\phi/\phi_{LBO} = 1.41$) for the F1 case. At this condition, the high mean value of CH* signal indicates a comparatively high heat release rate in the combustor. At this point, the CH* time series consists of low amplitude aperiodic oscillations. As the equivalence ratio is decreased ($\phi/\phi_{LBO} = 1.15$), the mean of the signal reduces, signifying reduction in heat release rate (Fig. 3.3b). In the near-LBO regime ($\phi/\phi_{LBO} = 1.01$), the CH* signal consists of high amplitude aperiodic oscillations along with aperiodic low amplitude oscillations (Fig. 3.3c). In our previous papers [42], [128], [129], we have shown that such high amplitude aperiodic bursts occur due to extinction-reignition events. In this regime, the CH* signal approaches almost zero value for short time durations, corresponding to extinction events when the instantaneous heat release rate becomes very low. For the F2 case, the time series are presented in Figs. 3.3(d-f) while the time series corresponding to F3 are shown in Figs. 3.3(g-i). The CH* time series characteristics of F2 and F3 are similar to F1. However, the high amplitude bursts are less prominent for F3 case. Figures 3.3(j-l) show the time series for the F4 case, which is the least premixed case we consider in this study. For F4 case, the extinction-reignition events and corresponding high amplitude aperiodic oscillations in CH* signal are absent unlike the F1-F3 cases. However, a gradual weakening of the mean signal, as equivalence ratio is reduced, is seen similar to F1-F3 cases.

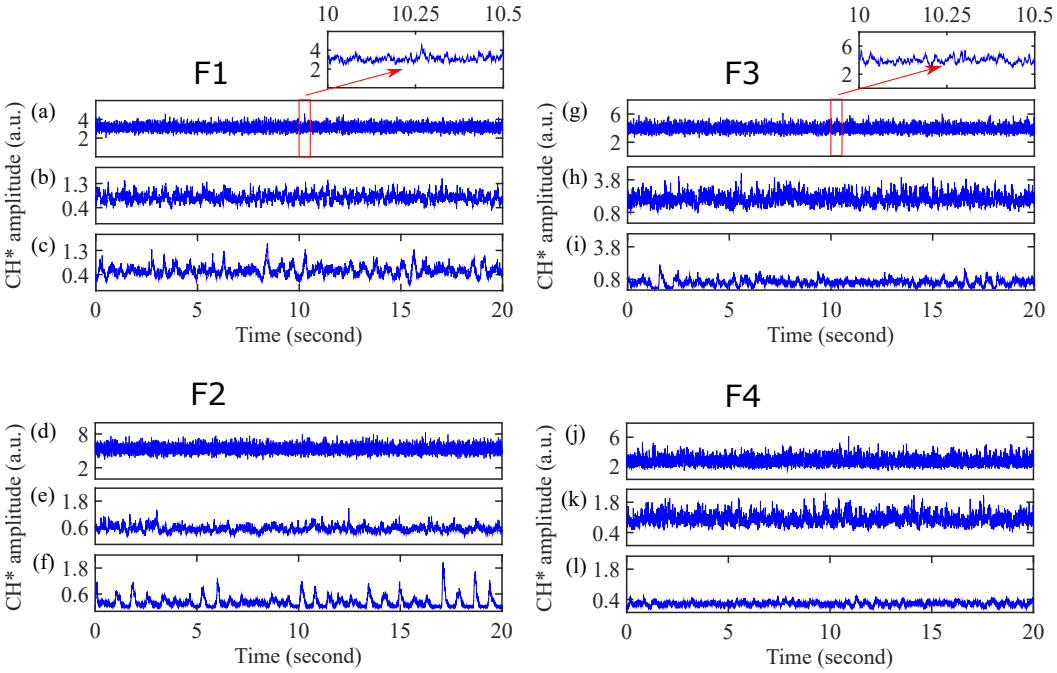

Figure 3.3: CH* chemiluminescence time series for F1 case are shown in (a) $\phi/\phi_{LBO} = 1.41$, (b) $\phi/\phi_{LBO} = 1.15$, (c) $\phi/\phi_{LBO} = 1.01$. CH* chemiluminescence time series for F2 case are shown in (d) $\phi/\phi_{LBO} = 1.4$, (e) $\phi/\phi_{LBO} = 1.15$, (f) $\phi/\phi_{LBO} = 1$. CH* chemiluminescence time series for F3 case are shown in (g) $\phi/\phi_{LBO} = 1.31$, (h) $\phi/\phi_{LBO} = 1.17$, (i) $\phi/\phi_{LBO} = 1.017$. CH* chemiluminescence time series for F4 case are shown in (j) $\phi/\phi_{LBO} = 1.54$, (k) $\phi/\phi_{LBO} = 1.25$, (l) $\phi/\phi_{LBO} = 1$. The CH* signals are in arbitrary unit. Reproduced from Chaos 30, 043115 (2020), with the permission of AIP Publishing.

From the above discussions, significant differences in near-LBO CH* time series characteristics, for different degrees of premixedness, can be seen. For F1–F3 cases, time series characteristics changes from low amplitude aperiodic oscillations (in the stable combustion regime) to ensemble of low amplitude and high amplitude aperiodic oscillations (in the near-LBO regime). Intermittency is typically defined as a dynamical state consisting of low amplitude aperiodic oscillations and high amplitude periodic oscillations [40]. Most of the studies on lean blowout with preceding thermoacoustic instability have observed the typical intermittent oscillations as LBO is approached [39], [40], [57]. So, the near-LBO dynamics, observed in the present study, for the F1-F3 cases refers to a type of intermittency that is relatively less explored. For the F4 case, the changes in time series characteristics is less apparent. A more elaborate understanding of combustor dynamics cannot be obtained with visual inspection of CH* time series. Therefore, we apply the recurrence network tool to explore the dynamical transition to LBO.

3.4.2 Variation of RN metrics for premixed flames

For ease of discussion, the transition to LBO is classified into three regimes based on visual inspection of time series. The methodology to divide the entire operating range into different regimes is reported in detail in one of our previous papers [42]. Regimes A, B and C indicate the stable combustion regime (far away from LBO), transition regime (between the stable combustion regime and near-LBO regime) and near-LBO regime respectively, for each of the F1-F4 cases [42]. For the RN metrics to be effective as early LBO prediction tool, they must detect the impending LBO early enough so that control action can be actuated before the flame blows out. In this context, next we discuss the efficacy and robustness of the RN metrics as early LBO prediction tools.

To study the variation of RN metrics as LBO is approached, we consider CH* time series of 20 second duration for each operating point. However, constructing RN with data of 20 second, i.e. 40000 data points, is found to be computationally very expensive. Thus, we break down the total duration into 4 windows, each window being 5 second long and of 10000 data points. The RN metrics from each of these windows are calculated independently. The mean values of the different RN metrics, obtained from the 4 windows, are presented in the results that follow.

Figure 3.4 shows the changes observed in the different RN metrics, as LBO is approached, for premixed configurations (F1 and F2). We observe global efficiency (η) to be low during the stable combustion regime (Fig. 3.4a). η follows a gradually increasing trend as equivalence ratio is reduced. We note that higher values of η indicates a lower average distance between the nodes of the network while lower

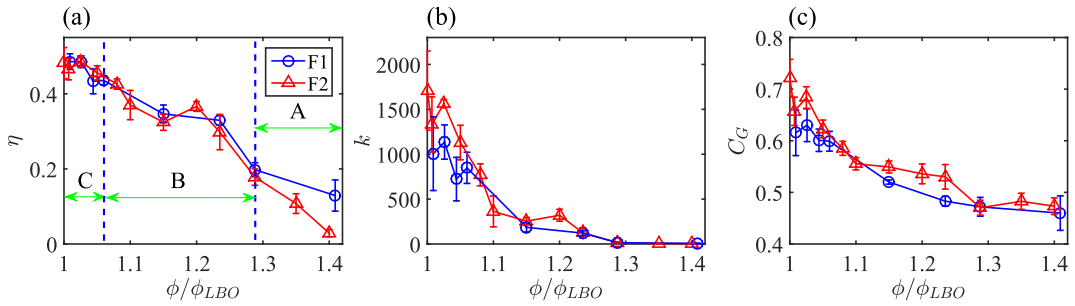

Figure 3.4: Variations of (a) global efficiency (η), (b) average degree centrality (k) and (c) global clustering coefficient (C_G) for F1 and F2 cases, as LBO is approached. A, B and C zones indicate the stable combustion regime, the transition regime and the near-LBO regime respectively for both F1 and F2 cases. The regimes A, B and C are demarcated by the blue dashed lines as shown in (a). The error bars indicate the standard deviations calculated with 4 windows each of 5 second duration.

values of η indicates comparatively higher average distance between the nodes. Thus at LBO, the average distance between the nodes become lowest.

For the highly premixed cases (F1 and F2), as equivalence ratio is reduced average degree centrality (k) initially remains constant, but starts increasing gradually as it enters the transition regime (Fig. 3.4b). The average phase space density may be linked with k as discussed in chapter 2. So, the average phase space density increases during the transition to LBO.

Figure 3.4(c) shows the variations of global clustering coefficient (C_G) for the highly premixed cases (F1 and F2). In the stable combustion regime, C_G remains moderately high. With reduction in equivalence ratio, C_G increases initially at a small rate at the start of the transition regime but increases at a high rate in the latter part of the transition regime. In other words, propensity of the network forming closed triangles among neighborhood nodes increases as lean blowout is approached.

Significant differences of the three RN metrics η, k and C_G between the stable combustion regime and the latter part of the transition regime indicate that an early warning can be obtained during the transition regime itself by monitoring these RN metrics. So, we infer that the RN metrics η, k and C_G are good candidates as early LBO prediction metrics for highly premixed configurations. Next, we turn to study the efficacy of the RN metrics, as early LBO prediction tools for partially premixed configurations.

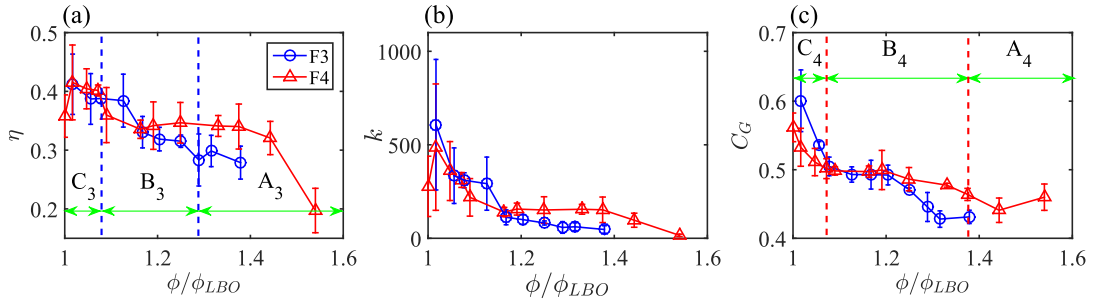

Figure 3.5: Variations of (a) global efficiency (η), (b) average degree centrality (k) and (c) global clustering coefficient (C_G) for F3 and F4 cases, as LBO is approached. A_3, B_3 and C_3 zones indicate the stable combustion regime, the transition regime and the near-LBO regime respectively, for F3 case. A_4, B_4 and C_4 zones indicate the stable combustion regime, the transition regime and the near-LBO regime respectively, for F4 case. The regimes A_3, B_3 and C_3 are demarcated by the blue dashed lines as shown in (a). The regimes A_4, B_4 and C_4 are demarcated by the red dashed lines as shown in (c). The error bars indicate the standard deviations calculated with 4 windows each of 5 second duration.

3.4.3 Variation of RN metrics for partially premixed flames

In Fig. 3.5(a), the variations of η are shown for the partially premixed cases (F3 and F4). For the F3 case, η initially increases at a slow rate after entering the transition regime but increases rapidly in the latter part of the transition regime. For the F4 case, as equivalence ratio is reduced, η significantly increases during the stable combustion regime and then remains approximately constant during the transition regime. However, η increases abruptly as the near-LBO regime is entered.

Figure 3.5(b) shows the changes in k as equivalence ratio is reduced, for F3 and F4 cases. For the F3 case, k is low during the stable combustion regime and increases at a slow rate during the first part of the transition regime. k increases with a much higher gradient in the latter part of the transition regime. For the F4 case, k increases at a rapid rate during the stable combustion regime itself. During the first part of the transition regime, k remains approximately constant and again starts to increase at a rapid rate as the system moves in the near.

Figure 3.5(c) shows the changes in C_G as equivalence ratio is reduced for F3 and F4 case. We see that for F3 case, C_G do not change significantly during the stable combustion regime. During the first part of the transition regime, C_G increases at a high rate. However, in the later stage of the transition regime, C_G becomes almost constant and starts to increase again only after entering the near-LBO regime. In the F4 case, C_G does not change significantly in the stable combustion regime and increases with a small gradient during the first part of transition regime. For the

rest of the transition regime, C_G remains almost constant and starts to increase again only after entering the near-LBO regime.

Thus, for the F3 case, the metrics η and k increases significantly during the latter part of the transition regime. So, an early LBO warning can be obtained during the latter part of the transition regime by monitoring the metrics η and k and setting suitable thresholds. However, significant variations in the metric C_G occur during the initial part of the transition regime. Hence, if C_G is used as early LBO prediction metric, the warning would be issued much earlier as compared to the LBO limit. For the F4 case, if C_G is used as early LBO prediction metric, a warning much earlier to LBO limit would be issued. On the other hand, if the metrics η and k are monitored, the LBO warning would be issued during the latter part of the transition regime.

Next, the relative sensitivity of the RN metrics for varying degrees of premixedness is discussed. For the premixed cases (F1 and F2), due to increasing trend of the RN metrics throughout the transition regime, each of η, k and C_G can be monitored as early prediction metrics. Further, the safety margin with respect to LBO may be fine-tuned depending on hardware or operational constraints. Similarly, for the F3 case, such fine tuning of the safety margin can be done when monitoring the LBO limit with the metrics η and k. However, the metric C_G for the F3 case and the metrics η and C_G for the F4 case can only provide a conservative early warning for LBO; in such cases, fine tuning of the safety margin based on operational constraints cannot be done. On the other hand, fine-tuning of the safety margin can be achieved by monitoring the metric k for partially premixed cases also.

We note that the increasing trend of RN metrics η, k and C_G during transition to LBO indicate a shift towards higher periodicity (or, higher determinism) as discussed in chapter 2. The above discussions clearly show that the dynamical transition to LBO at different degrees of premixedness is qualitatively similar. This is in spite of the fact that the flame characteristics at different degrees of premixing have significant differences, as reported in our previous studies [42], [128], [129] and as seen from time series also. However, in absolute terms, the network parameters show slightly different sensitivities and trends for highly premixed and partially premixed configurations. This shows that accurate information about the degree of premixedness in the combustor may be needed to (i) decide which RN metrics would be best suited for early prediction purpose, (ii) correctly access the proximity to LBO and (iii) decide the safety margin with which the combustor can be operated depending upon the operational constraints.

In practical situation, the early detection of LBO has to be done based on the RN metrics without any other external information. We note that the absolute

values of the different RN metrics may vary for different degrees of premixedness. For the highly premixed configuration (F1 case, Fig. 3.4), the following range of parameters may be indicative of stable combustion regime (A): $\eta \leq 0.2, k \leq 14$ and $C_G \leq 0.47$. For the transition regime (B), RN metrics attain the following ranges: $0.2 < \eta \leq 0.40, 14 < k \leq 500$ and $0.47 < C_G \leq 0.57$. For the near-LBO regime (C), RN metrics attain the following ranges: $\eta > 0.4, k > 500$ and $C_G > 0.57$. If the early warning is issued when the RN metrics attain values corresponding to near-LBO regime, early prediction of LBO can be achieved 5% - 10% ahead of LBO (between $\phi/\phi_{LBO} = 1.05 - 1.1$). For the least premixed configuration (F4 case, Fig. 3.5), the following range of parameters may be indicative of stable combustion regime (A_4): $\eta \leq 0.32, k \leq 150$ and $C_G \leq 0.46$. For the transition regime (B_4), RN metrics attain the following ranges: $0.32 < \eta \leq 0.36, 150 < k \leq 220$ and $0.46 < C_G \leq 0.50$. In the near-LBO regime (C_4), the ranges of RN metrics may be: $\eta > 0.36, k > 220$ and $C_G > 0.5$. If the early warning is issued when the RN metrics attain values corresponding to near-LBO regime, early prediction of LBO can be achieved 7% ahead of LBO if η or k is monitored. On the other hand, C_G is not a suitable early LBO metric for F4 case.

We note that the average path length L is inversely related to η as discussed above. So, the metric L would follow a decreasing trend for the present route to LBO. Godavarthi *et al.* [57] explored a different route to lean blowout with preceding thermoacoustic instability (thermoacoustic instability $\rightarrow$ intermittency $\rightarrow$ lean blowout). They found the average path length (L) to increase as the combustor moves from thermoacoustic instability to lean blowout. Thus the present finding indicates that the dynamical transition to lean blowout, with and without preceding thermoacoustic instability, are significantly different.

We recall that the intermittent high amplitude bursts in the CH* time series become gradually more prominent and of longer durations as lean blowout is approached, for the more premixed cases (F1-F3). In our previous study we have observed structures in the recurrence plots corresponding to type-II intermittency during the near-LBO regime for the F1-F3 cases[42]. In the F4 case, the intermittent structures typical to intermittency were not found in our previous study [42]. Still, for each of the F1-F4 cases, the recurrence quantification analysis (RQA) carried out in our previous study indicated a shift towards higher determinism as lean blowout is approached, as quantified by the RQ metric *determinism* (DET). Moreover, another parameter *laminarity* (LAM) also increased as lean blowout is approached, indicating a shift of dynamics towards a laminar or intermittent regime [42], [44]. So, the dynamics in the near-LBO regime for each of the F1-F4 cases is likely to be intermittent in nature.

In chapter 2, we report that the recurrence network measures η, k and C_G in-

creases as the combustor dynamics shifts from combustion noise to an intermittent state. Further, the increase of RN metrics can be easily linked with the shift of combustor dynamics towards higher determinism as shown in chapter 2. So, the trends observed for the RN measures in the present study corroborate with the finding of the previous study with RQ measures [42], that the dynamical transition from stable combustion to lean blowout without preceding thermoacoustic instability entails a shift of dynamics towards higher determinism.

3.4.4 Comparison of recurrence network metrics and recurrence quantification metrics, as early lean blowout prediction tools

Next, we discuss the relative merits of the recurrence quantification (RQ) and RN metrics as early lean blowout prediction tools. For brevity, we consider only two RQ metrics: determinism (DET) and laminarity (LAM), which were found to be robust early lean blowout predictors for various degrees of premixing [42]. During the transition regime, DET shows a monotonic increase with equivalence ratio for F1 case (Fig. 3.6a). For F2 case however, DET increases rapidly initially after entering the transition regime but becomes constant thereafter and only changes after entering the near-LBO regime. So, for F2 case, DET will issue warning much prior to lean blowout and can provide a conservative estimate of LBO limit only. However, F1 and F2 cases have very similar degree of premixing ($\kappa = 0.073$ and 0.075 for F1 and F2 respectively).

For the F1 case, LAM initially increases rapidly at the start but continue to increase at a much less rate during the latter part of the transition regime (Fig. 3.6b). On the other hand, for the F2 case LAM initially increases rapidly after entering the transition regime but then becomes almost constant. So, for the F2 case, LAM can only be used to get a conservative estimate of lean blowout limit. Thus the trends of DET and LAM varies significantly with slightest changes in degree of premixing. Even with significant calibration efforts, DET and LAM may only provide conservative estimates of LBO limit and thus may not be appropriate metrics when fine-tuning of safety margin is needed. On the other hand, the RN metrics η, k and C_G have very similar monotonic trends for F1 and F2; thus they are more suitable for fine tuning of safety margin at higher degrees of premixing, as discussed above. We infer that the RN metrics have an advantage over the RQ metrics, although both RN and RQ metrics are robust early LBO prediction tools.

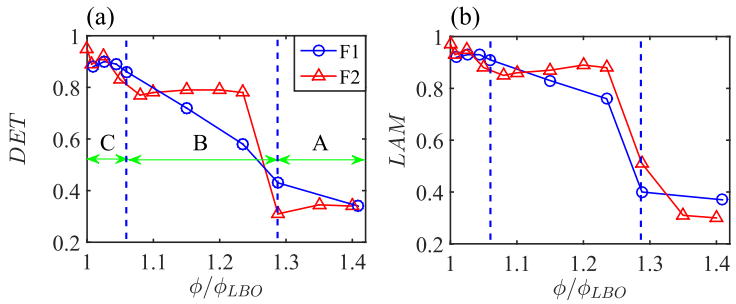

Figure 3.6: Variations of (a) determinism (DET) and (b) laminarity (LAM) for F1 and F2 cases, as LBO is approached. A, B and C zones indicate the stable combustion regime, the transition regime and the near-LBO regime respectively for both F1 and F2 cases. Reproduced from Chaos 30, 043115 (2020), with the permission of AIP Publishing.

3.4.5 Topology of the constructed recurrence networks

The structural changes in RN during the dynamic transition to LBO can be explored using visual representations of the network topologies. We attempt to link the topological changes in the recurrence network with changes in the RN metrics k and C_G during dynamic transition to LBO. Such an approach may be useful to better understand the changes observed in RN metrics as LBO is approached.

The network topologies are constructed with force atlas 2 algorithm. This algorithm has been used in many previous studies [97] under the Gephi framework [98] to generate complex network topologies. It is a iterative algorithm which brings together directly connected nodes and pushes away nodes which are not directly connected [97]. The network nodes are color coded according to the degree of the nodes. Also, the size of the nodes are linearly scaled from 1 to 100 unit with the lowest degree node having size 1 and highest degree node having size 100. Each link connects two nodes and the link color is same as the lower degree node connected to the link.

In order to explore the dynamics with network topologies, the highly premixed F1 case is considered (Fig. 3.7). At the stable combustion regime ($\phi/\phi_{LBO} = 1.41$), the network mostly consists of small greenish nodes indicating the prevalence of low degree nodes (Fig. 3.7a). This is reflected in average degree centrality (k) being small (Fig. 3.4b). Network corresponding to near-LBO regime ($\phi/\phi_{LBO} = 1.01$) shows the prevalence of comparatively higher degree nodes (Fig. 3.7b) which results in higher k in the near-LBO regime (Fig. 3.4b). Next we explore the link between the global clustering coefficient C_G (Fig. 3.4c) and RN topology. Several excursions from the core of the network towards the periphery of the network can be seen from the RN topologies (Fig. 3.7). These excursions

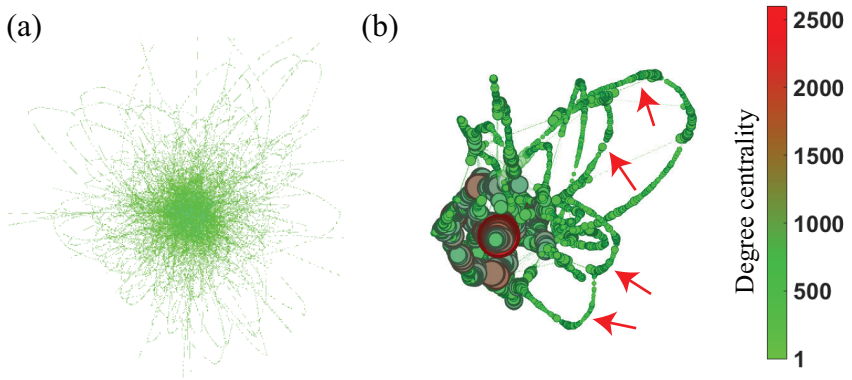

Figure 3.7: Recurrence network topology constructed with Gephi for F1 case at (a) stable combustion regime ($\phi/\phi_{LBO} = 1.41$) and (b) near-LBO regime ($\phi/\phi_{LBO} = 1.01$) respectively. The networks are constructed with 10000 data points corresponding to 5 second duration.

are indicated by a number of nodes arranged in arcs of various radii in the RN topology. Such structures are particularly prominent for near-LBO regime (indicated by red arrows in Fig. 3.7b). At the stable combustion regime, most of the nodes in such arcs have a degree of two as seen from Fig. 3.7(a). Thus it may be said that the system state visits the corresponding phase space regions only once. On the other hand, the nodes in such arcs are considerably larger in size for the RN corresponding to near-LBO regime (Fig. 3.7b). This indicates frequent visitations from the network core to the network periphery. The frequent excursions of the system state to the corresponding phase space regions lead to increased clustering in the RN. In light of previous literature [78], the increased clustering of the RN is consistent with the presence of intermittent dynamics near LBO. We note that in previous literature [57], the network topology in the stable combustion regime and near-LBO regime were found to be qualitatively similar. In the present study, however, the stable combustion regime and near-LBO regime have significant differences in network topology as discussed above. This fact again highlights the differing dynamical transition to LBO in absence of thermoacoustic instability preceding lean blowout.

3.4.6 Degree distribution of recurrence network

To further characterize the recurrence networks at stable combustion and near-LBO regime, we study the degree distribution of the nodes. Presence of power law degree distribution in various types of complex networks has been reported in literature [57], [109]. A complex network is said to follow a power law degree distribution when, it follows the law $P(X) \sim X^{-\gamma}$. Here, $P(X)$ is the probability

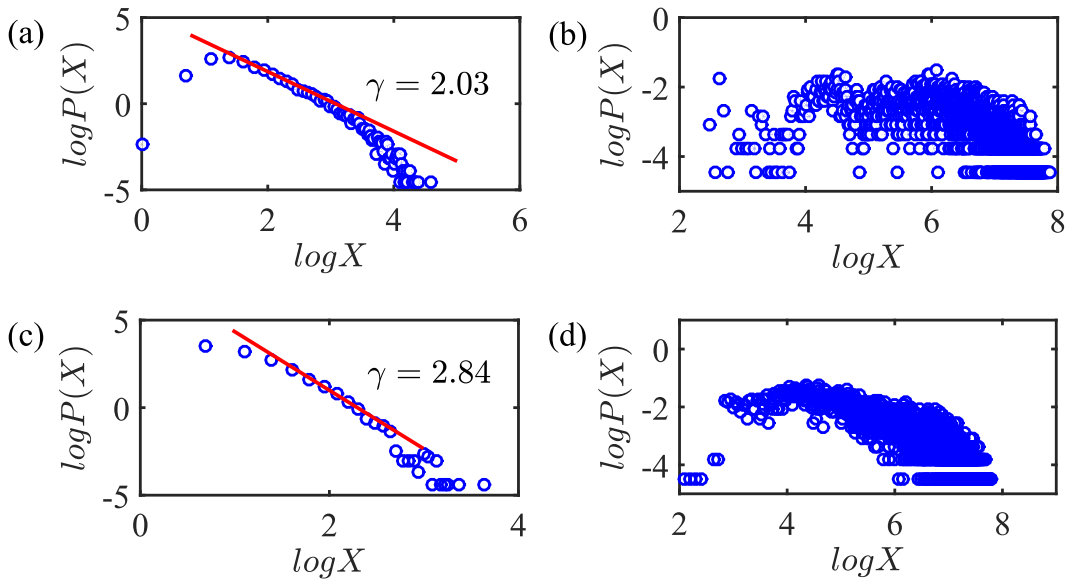

Figure 3.8: Breakdown of the power law degree distribution as lean blowout is approached. (a) and (b) show the degree distribution at stable combustion regime ($\phi/\phi_{LBO} = 1.41$) and near-LBO regime ($\phi/\phi_{LBO} = 1.01$) respectively, for F1 case. (c) and (d) show the degree distributions at stable combustion regime ($\phi/\phi_{LBO} = 1.54$) and near-LBO regime ($\phi/\phi_{LBO} = 1.0$) respectively, for F4 case. The recurrence networks are constructed with 10000 data points corresponding to 5 second duration.

of finding a node with degree X in the network. If the power law coefficient (γ) is such that $2 < \gamma < 3$, the network is said to have a scale-free nature [138] as such networks do not have a particular characteristic scale [57], [109]. Both stable combustion regime and near-LBO regime are known to have power law degree distributions for turbulent premixed configurations [39], [57], [87].

Figure 3.8 shows the degree distributions during the stable combustion and near-LBO regimes for F1 and F4 cases. In both the F1 and F4 cases, most nodes of the RN corresponding to the stable combustion regime follow a single power law degree distribution with $2 < \gamma < 3$ (Fig. 3.8a,c). So, the RNs at stable combustion regimes follows a scale-free degree distribution for highly premixed as well as partially premixed configurations. In the near-LBO regime of the highest premixedness case (F1), the power law nature is absent (Fig. 3.8b). For the near-LBO regime of the partially premixed configuration (F4), the scatters are very large so that the presence of power law is arguable (Fig. 3.8d).

This apparently contradictory finding, concerning the degree distribution in the near-LBO regime, with the literature [39], [57] is likely due to the presence of intermittent events at the near-LBO regime (extinction-reignition bursts for the more premixed cases and flame pulsations in the less premixed cases). We note that Godavarthi *et al.* [57] observed the power law structure to get destroyed

ϕ/ϕ_{LBO}	1.41	1.288	1.235	1.15	1.06	1.044	1.026	1.01
η	5255.1	1233.2	564.6	346.6	325.2	316.9	339.0	316.6
k	1597.5	326.9	124.0	71.0	66.9	61.9	70.4	63.3
C_G	159.4	161.5	173.0	131.9	119.2	128.1	120.8	124.0

Table 3.2: Computational time (in seconds) of the global RN metrics for the F1 case, corresponding to optimally embedded RN with a window size of 5 seconds (10000 data points).

during intermittency. However, the intermittent behavior reported in their paper was obtained close to thermoacoustic instability and away from LBO.

3.4.7 Practical implementation strategies for early LBO prediction with recurrence network approach

The results presented above provide a proof of concept that the recurrence network tool can early detect LBO. Table 3.2 shows the time requirement for calculating the three RN metrics for the F1 case, with a window size of 5 seconds (corresponding to 10000 data points) and optimal embedding. We note that the computational time for the RN metrics are found out by running the in-house recurrence network code on an i5 4^{th} generation computer with 16 GB RAM. The computational times shown here include the time for adjacency matrix construction and creation of shortest path matrix (if required). Thus, the computational time for C_G includes the time required for creation of adjacency matrix. Similarly, computational time for η includes the time required to create adjacency matrix and shortest path matrix. We observe the recurrence networks are computationally expensive which makes the online implementation of RN difficult. Next, we suggest a couple of approaches based on recurrence network that can significantly reduce the computational time without compromising the efficacy of the recurrence network tool: (i) short time series based RN with embedding dimension of one ($D = 1$) and (ii) short time series based optimally embedded RN.

First, a 1-D RN is constructed with 1 second time window (corresponding to 2000 data points) to explore the dynamical transition. Mean values of the global RN metrics over 5 such consecutive windows (corresponding to first 5 seconds data) are shown in Figs. 3.9 and 3.10. We note that 1-D RN results should not be compared with the optimally embedded RN. Thus we have normalized the values of the RN metrics between 0 to 1 to avoid confusion about the dynamical state in question. To construct the 1-D RN, a arbitrarily chosen fixed recurrence threshold $\epsilon = 0.034$ is used similar to a previous study [57]. However, we have checked that the trends of the 1-D RN metrics remain similar for any fixed recurrence threshold.

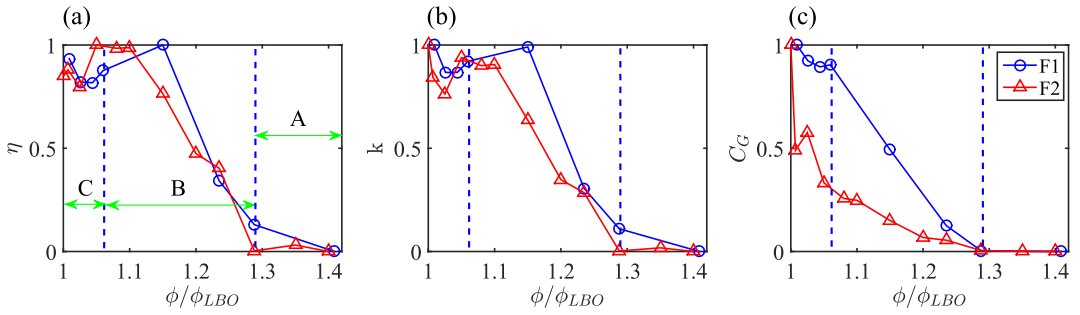

Figure 3.9: (a), (b) and (c) show the different global RN metrics for the F1 and F2 cases, found with an embedding dimension $D = 1$ and time window of 1 second (2000 data points). The plots (a-c) are the mean values of the global RN metrics calculated from 5 such consecutive windows. A, B and C respectively indicate the stable combustion regime, transition regime and near-LBO regime.

ϕ/ϕ_{LBO}	1.41	1.288	1.235	1.15	1.06	1.044	1.026	1.01
η	18.9	17.5	21.9	21.9	20.4	20.7	19.6	18.8
k	0.2	0.2	0.2	0.2	0.2	0.2	0.2	0.2
C_G	0.2	0.2	0.2	0.2	0.2	0.2	0.2	0.2

Table 3.3: Computational time (in seconds) of the global RN metrics for the F1 case, corresponding to 1-D RN, with a window size of 1 second (2000 data points).

Because in this case the phase space of the combustor is not optimally unfolded, the sensitivity of the RN method reduces to some extent. For the highly premixed cases (F1, F2), the 1-D RN metrics η, k and C_G show increasing trends as LBO is approached (Fig. 3.9). However, η and k saturate at 10% to 15% ahead of the LBO limit. So, for the highly premixed configurations, η and k may act as conservative early LBO prediction tools which would issue early LBO warning at a safety margin of 10% - 15%. The metric C_G however, follows a monotonically increasing trend up to the LBO limit. So, the combustor may be run reliably with a thin safety margin (4% -6% of the LBO limit) if C_G is used as a early LBO metric. On the other hand, for the partially premixed configurations, each of the metrics η,k and C_G exhibit almost monotonically increasingly trends (Fig. 3.10). Thus in these cases, fine-tuning of safety margin is possible by judicious selection of RN thresholds. The time requirement for 1-D RN metrics k and C_G are very less throughout the operating range, having a computational time around 0.2 seconds (Table 3.3). In short, the results indicate that 1-D RN is a robust tool for early LBO detection, but the absolute trends and sensitivities of the RN metrics vary with degree of premixedness of the combustor.

In some cases it may be important to operate the combustor with a thin safety margin. In such cases, short time series (window size of 1 second, corresponding to

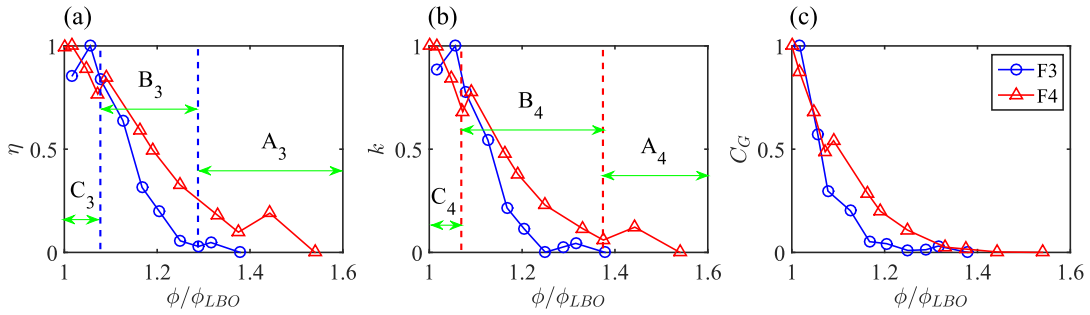

Figure 3.10: (a), (b) and (c) show the different global RN metrics for the F3 and F4 cases, found with an embedding dimension $D = 1$ and time window of 1 second (2000 data points). The plots (a-c) are the mean values of the global RN metrics calculated from 5 such consecutive windows. A_3, B_3 and C_3 zones indicate the stable combustion regime, the transition regime and the near-LBO regime respectively, for F3 case. A_4, B_4 and C_4 zones indicate the stable combustion regime, the transition regime and the near-LBO regime respectively, for F4 case.

2000 data points) based optimally embedded RN may be more useful. The mean global RN metrics, calculated from 5 successive windows (corresponding to first 5 seconds data), are shown in Fig. 3.11. Here we see that the metrics η, k and C_G follow qualitatively similar trends as those corresponding to 5 second windows. So with this approach, each of the three metrics can detect LBO with a small safety margin (4%-6% prior to LBO limit for the F1 case). On the other hand, η and k are also able to provide conservative estimates of LBO limit as they follow approximately monotonic trends during approach of LBO. Because the network is constructed with a small time window, the absolute values of the global RN metrics differs to some extent from those calculated with 5 second windows (Fig. 3.4. With the short duration optimally embedded RN, the computational time for the metrics k and C_G becomes less than 1 second as the combustor deviates from stable combustion state (Table 3.4). In this regard, it may be noted that use of open source parallelized codes may reduce the computational time for global RN metrics in order of magnitudes [139]–[141]. In short, the recurrence network with a long time window would be computationally costly but most accurate from dynamical exploration point of view. On the other hand, an optimally embedded short time duration RN is more suitable if the combustor is to be run with relatively thin margin whereas 1-D RN may be suitable if the combustor is to be operated away from LBO limit and a relatively high safety margin is acceptable.

As the different degrees of premixedness are surrogate for different combustor configurations, the implication of the results presented in the manuscript is that RN is likely to be an effective early LBO prediction tool for various combustor geometries. In this sense, RN is likely to be more general and require less data for calibration purpose as compared to purely data driven approaches.

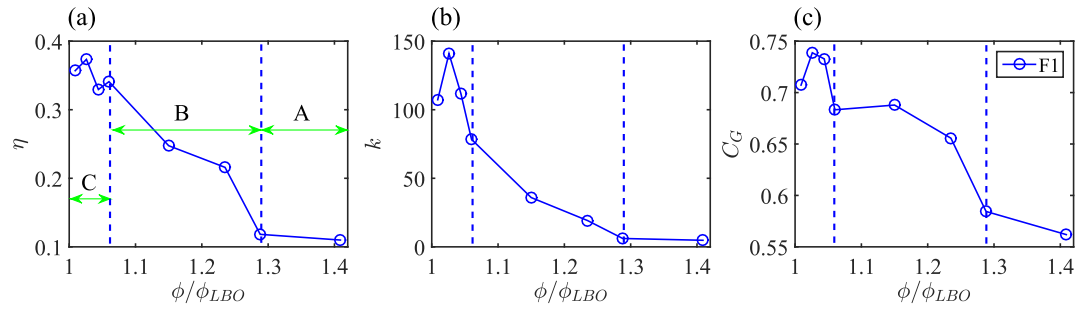

Figure 3.11: (a), (b) and (c) show the different global RN metrics for the F1 case, obtained from optimally embedded RN with a window size of 1 second (corresponding to 2000 data points). The plots (a-c) are the mean values of the global RN metrics calculated from 5 such consecutive windows. A, B and C respectively are the stable combustion, transition and near-LBO regimes.

ϕ/ϕ_{LBO}	1.41	1.288	1.235	1.15	1.06	1.044	1.026	1.01
η	135.1	40.1	7.05	2.25	2.64	2.64	1.58	1.87
k	3.30	3.49	1.95	0.834	0.88	0.76	0.62	0.78
C_G	3.30	3.49	1.96	0.83	0.88	0.76	0.62	0.79

Table 3.4: Computational time (in seconds) of the global RN metrics for the F1 case, corresponding to optimally embedded RN constructed with a window size of 1 second (2000 data points).

However, because the absolute trends may vary significantly depending on degree of premixedness, minimum amount of calibration for particular combustor configurations are likely to be necessary.

3.5 Summary

Lean premixed combustors are highly susceptible to lean blowout flame instability, which can cause fatal accident in aircrafts or expensive shutdown in stationary combustors. However, the lean blowout limit of a combustor may vary significantly depending on a number of variables that cannot be controlled in practical situations. Although a large literature exists on the lean blowout phenomena, a robust strategy for early lean blowout detection is still not available. To address this gap, we study lean blowout without preceding thermoacoustic instability, using a nonlinear dynamical tool, recurrence network. Lean blowout via this route is relatively unexplored, especially from the perspective of dynamical science. As lean blowout is approached, the time series signal transforms from low amplitude aperiodic oscillations (in the stable combustion regime) to ensemble of low amplitude and high amplitude aperiodic oscillations (in the near-LBO regime). For

highly premixed flames, extinction-reignition events near lean blowout are seen. These events are absent for partially premixed flames. This shows that the flame behavior in the near lean blowout regime, for varying degrees of premixedness, are significantly different. Three recurrence network parameters: global efficiency, average degree centrality and global clustering coefficient, are chosen as metrics for early prediction of lean blowout. We observe that the characteristics of the time series near lean blowout limit is highly dependent on the degree of premixedness in the combustor. Still, for different degrees of premixedness, each of the three recurrence network metrics increases during transition to lean blowout, indicating a shift towards periodicity. Thus qualitatively the recurrence network metrics show similar trends for different degrees of premixing, which show their robustness. However, the sensitivities and absolute trends of the recurrence network metrics are found to be significantly different for highly premixed and partially premixed configurations. By exploring the dynamical transition with RN metrics, we find that the dynamic transition to LBO with and without preceding thermoacoustic instability are significantly different (the dynamic transition to LBO with preceding thermoacoustic instability has been reported in previous literature and the latter has been studied in this chapter). Thus the results obtained in this study indicate that prior knowledge about (i) the degree of premixedness and (ii) the route to lean blowout, may be required for accurate early prediction of lean blowout. We observe the power law degree distribution of recurrence network to break down close to lean blowout limit, due to the intermittent dynamics in the near-LBO regime. Finally, we show that the visible structural changes in the recurrence network topology can be linked to the changes in the recurrence network metrics, helping to better understand the dynamical transition to lean blowout.

Citation acknowledgment

Some parts of this chapter are reproduced with permission from the publication(s) listed below.

1. “Early detection of lean blowout using recurrence network for varying degrees of premixedness", Chaos: An Interdisciplinary Journal of Nonlinear Science, 32, 063105, 2022 (DOI: 10.1063/5.0077436).

2. “Application of recurrence quantification analysis for early detection of lean blowout in a swirl-stabilized dump combustor", Chaos: An Interdisciplinary Journal of Nonlinear Science, 30(4), 043115, 2020 (DOI: 10.1063/1.5131231).

CHAPTER 4

Synchronization characteristics of two candle flame oscillators with comparable and different oscillation amplitudes

4.1 Introduction

Recent research have proven the necessity of examining the interplay of oscillatory processes, including flame-flame interaction, to comprehend the thermoacoustic instability phenomena in turbulent combustors [142]–[150]. Candle flame oscillators (CFO), i.e. oscillating candle flames, are among the most basic forms of oscillators for studying flame-flame interplay.

Kitahata *et al.* [48] investigated the unsteady behavior of candles both experimentally and numerically. Candle flame is a type of nonpremixed flame that remains steady in absence of external disturbances. The supply rate of fuel (gaseous paraffin) to a single candle stick is limited. For such instance, the air supply from the surrounding air is adequate to maintain a constant rate of burning [48]. On the other hand, when a number of candles are set in close proximity, the flames of the separate candles combine to form a single flame when the candle sticks are lighted. In such a scenario, all the constituent candle sticks provide gaseous paraffin to the combined flame. In this situation, the oxygen supply from the surrounding air is insufficient to support a steady flame [48]. The candle flame

thus experiences self-sustaining periodic fluctuations with a frequency of roughly 10–11 Hz [48], [50], [52], [151].

The effects of flame-flame interplay on the the combustors' dynamical features are frequently investigated with the synchronization framework. Such studies are helpful in understanding the occurrence of thermoacoustic instability in modern gas turbine combustors and in suggesting measures to prevent it [150]. Synchronization of coupled self-excited oscillating processes is a common occurrence in both natural and physical settings [152]. It is formally defined as, "*adjustments of rhythms due to weak coupling between oscillators*" [153]. Synchronization has a significant impact on the working of the system in question, and depending on the circumstances, it may be beneficial or undesired [152].

The synchrony of two oscillating processes may result in a variety of dynamical states. Of these, amplitude death (AD) is the desired dynamical state from the perspective of thermoacoustic instability research. It is the dynamical state in which the interplay between the coupled oscillating systems produces almost complete suppression of pulsations in each of them [150], [154]–[156].

Interplay of CFOs has been the subject of a few recent studies. Different dynamical states have been documented as the distance between a pair of CFOs is changed. Using a scale analysis, Kitahata *et al.* [48] demonstrated that thermal radiation is a crucial coupling mechanism for CFO synchronization. Gergely *et al.* [157] improved Kitahata *et al.*'s numerical model of CFOs and verified the new model with experimental findings. Because thermal radiation is inversely proportional to the distance squared (l^2), Chen *et al.* [53] hypothesized that increasing l would result in a decrease in radiation coupling. Okamoto *et al.* [151] investigated the flame-flame interplay with three coupled CFOs. The CFOs were placed at the corners of an equilateral triangle. They discovered that the coupling strength between the CFOs is not a simple function of distance between them (l). Dange *et al.* [52] observed presence of vortices in the surrounding air of the CFOs. They inferred that these vortices are caused by unsteady combustion of the CFOs. They suggested that the interplay of these vortices may have a role in the synchronization phenomena. Forrester [47] observed presence of master-slave coupling between a ring of candles and a candle placed at the center of the ring.

The interplay between a set of CFOs results in various dynamical states, including: (i) in-phase (IP) synchrony [50], [53], [151], (ii) anti-phase (AP) synchronization [48], [50], (iii) amplitude death (AD) [50], [52], [151], (iv) 'rotation' mode [151] and (v) desynchronization (DS) [48], [50], [53]. In-phase (IP) synchronization is a situation in which the paired oscillators oscillate approximately together, i.e. the phase lag between the two oscillators is close to zero. Anti-phase (AP) synchronization, on the other hand, is a situation in which the paired oscillators

oscillate in an alternate manner. In other words, the phase lag between the two oscillators is close to 180° at AP state. Desynchronization occurs when there is no consistent phase correlation between the paired oscillators. Thus the phase difference between the two oscillators often is seen to increase or decrease in a monotonic manner. The different dynamical states will be discussed in a greater detail later in this chapter. The dynamical transitions caused by interplay of a couple of CFOs, as reported in previous literature, are summarized in Table 4.1.

Literature	D (mm)	N_1, N_2	l (mm)	Dynamics
Kitahata *et al.* [48]	6	3,3	$l < 30$	IP
			$l \sim 30$	IP, or AP, or alternating between IP and AP
			$30 \leq l \leq 46$	AP
			$l \sim 47$	AP, or DS, or alternating between AP and DS
			$l > 47$	DS
Manoj *et al.* [50]	8	4,4	$0 \leq l \leq 8$	IP
			$l \sim 10$	alternating between IP and AP
			$10 < l < 20$	AD
			$l \sim 20$	alternating between IP and AP
			$20 < l < 52$	AP
			$l > 52$	DS
Chen *et al.* [53]	6	3,6	$15 < l < 35$	near-IP
			$35 < l < 55$	near-AP
			$l > 55$	DS

Table 4.1: The different dynamical states caused by the interplay of a pair of CFOs as reported in previous research. The diameter of a candle is D. The number of candles in the two coupled CFOs are N_1 and N_2 respectively. The distance between the two CFOs is denoted by l.

The interplay of two identical CFOs has been the subject of a number of experimental investigation [50], [52]. In practice, however, completely identical

oscillators are extremely rare, and minor differences always exist [153]. The implications of minute differences in the coupled flame oscillators, on synchronization behavior, have received less attention, particularly from an experimental perspective. Thomas *et al.* [156] investigated two coupled Rijke tubes having different oscillation amplitudes. Manoj *et al.* [50] showed that oscillators with a varying number of candles have differing amplitudes of pulsations. Chen *et al.* [53] observed the synchronization phenomena between a pair of CFOs having considerable flame intensity disparities. In their study, one CFO had a flame intensity 60% greater than the other CFO. They found a 'near-IP' and a 'near-AP' state as a result of the interplay of the two CFOs. Still, to acquire a better understanding of synchronization behavior owing to CFO interplay, the properties of 'near-IP' and 'near-AP' states need to be investigated further. For example: (i) what are the differences between the IP and AP states and the 'near-IP' and 'near-AP' states? (ii) Will varying the extent of disparity between the CFOs induce major changes in the dynamical properties of the 'near-IP' and 'near-AP' states? We attempt to address these points in this chapter using quantitative indicators such as phase relationship of the two CFOs and amplitude correlation (calculated with Pearson correlation coefficient). Furthermore, the synchrony of CFOs is a dynamically rich phenomenon. Thus, it would be worthwhile to systemically investigate how the disparity of the coupled CFOs affects the flame synchrony, by parametrically increasing the distance between the CFOs.

To fill this research gap, we conduct a comprehensive assessment of the synchronization behavior caused by the interaction of CFOs with similar and differing amplitude of pulsations. In the remainder of this study, we refer to sets of CFOs with similar and differing amplitudes of pulsations as simply similar and differing sets of CFOs, respectively, for conciseness. Thus, by a 'similar set of CFO' we indicate that each CFO consists of three candle sticks. By a 'dissimilar set of CFO', we indicate a set of coupled CFOs that consist of either (i) 3 and 4 candles or (ii) 3 and 5 candles. The Experimental design is covered in further depth later in this chapter.

We observe a variety of dynamical states by adjusting the distance between the CFOs over a reasonable range. We find that the synchronization behavior is markedly different when caused by the interplay of a similar set of CFOs and by differing sets of CFOs. For example, the CFOs are more prone to amplitude death for a similar set of interacting CFOs than for a differing set of interacting CFOs. This research might help to better understand synchronization in real-world scenarios, where minor burner-to-burner differences are prevalent [150]. It can also help to advance modeling of interacting diffusion flames.

4.2 Experimental test rig and data collection

4.2.1 Experimental test rig

Figure 4.1 shows the experimental setup, which comprises of 2 CFOs, both having 3 or a higher number of candles. Each candle is 10 cm tall and 0.7 cm in diameter. We note that the rate of fuel (vaporized paraffin) supply to the candle flame and the amplitude of pulsations can both be affected by the geometry of individual candle sticks [48]. CFO dynamics are heavily influenced by the rate of fuel supply [48]. Furthermore, the amplitude of pulsations and coupling strength are known to be interrelated [50].

The schematic of the interacting candle flame setup is shown in Fig. 4.2(a). The top views of the several arrangements of similar and differing sets of CFOs are shown in Figs. 4.2(b-d). These are (i) 3 candles in both CFOs (Fig. 4.2b), (ii) 3 candles in a CFO and 4 candles in the remaining CFO (Fig. 4.2c), and (iii) 3 candles in a CFO and 5 candles in the remaining CFO (Fig. 4.2d). For the rest of this study, we will refer to these arrangements as 3/3, 3/4, and 3/5 configurations, respectively. The CFOs are made by bundling the desired number of candles and binding the bundle with tape around the center of the candle sticks. The CFOs are then firmly set on wood boards, ensuring that they are vertically aligned. The candle wicks are sufficiently near in this arrangement so that when ignited, the flames of the separate candles combine. Next, this combined flame starts to oscillate in a self-sustaining manner.

The edge-to-edge distance between the wood boards (l) is used as a proxy for the distance between the CFOs. As the CFOs are situated at the edges of the wood boards, l is almost equal to the distance between the coupled CFOs (Fig. 4.2a). The wood boards are slid along a straight path (guiding line) to adjust the distance between the CFOs, maintaining the edges of the wood boards on the guiding line. At the start, the distance between the CFOs is 5 mm, and it is increased by 5 mm at a time up to 80 mm.

The oscillators are positioned at the borders of the wood boards. Thus the connecting line between the geometric centers of the CFOs remains parallel to the guiding line. A standard scale is placed along the guiding line to determine the distance between the CFOs. The entire arrangement is set up on a wood table. To make sure that the oscillators stay free of external disturbances, the investigation is carried out in a closed chamber with a quiescent setting. In comparison to the distance between the CFOs and the height of the candle, the dimensions of the chamber are substantially larger. Therefore, wall effects are considered to be insignificant in this study.

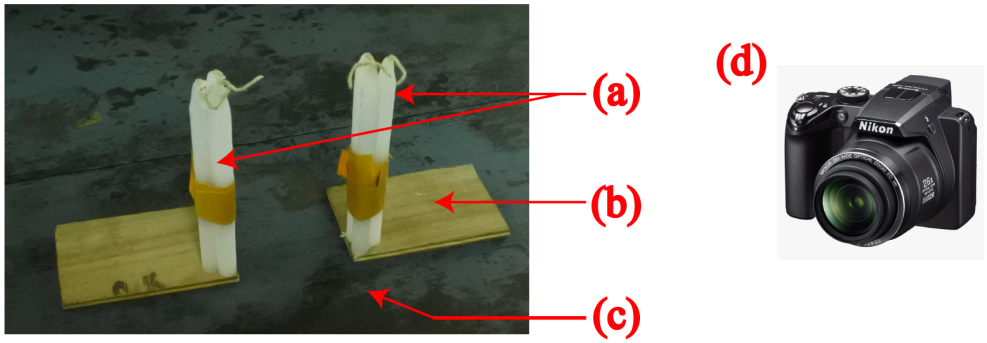

Figure 4.1: Experimental Setup for studying the interplay between two candle flame oscillators (CFO). (a) shows two candle stick assemblies that exhibit self-sustaining pulsations when ignited. (b) shows the Wooden holding plates. (c) is the wooden table and (d) is the camera.

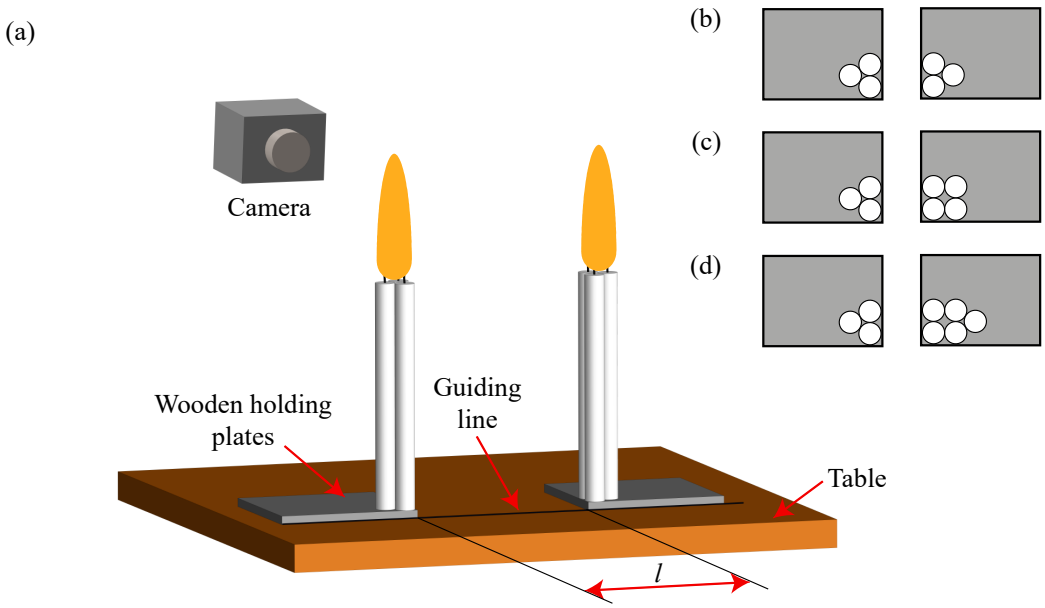

Figure 4.2: Setup for studying the interplay between two candle flame oscillators (CFO). The distance between the CFOs is l.

4.2.2 Data collection and creation of intensity time series

We wait 2 minutes after igniting the oscillators so that the transient part of the dynamics dies down. The movies of flame pulsations are then taken using a Nikon Coolpix P100 camera at 240 frames per second for 10 seconds. 10 such movies are taken in sequence for each operating point. To evaluate the relative phase dynamics of the coupled oscillators, flame intensity information is first retrieved from the flame movies. Each video frame is divided into two frames, each containing a flame corresponding to a CFO. The cropped frames are chosen in such a way that at all times, the whole flame of a CFO is caught in the relevant frame and no portion of the flame from the other CFO is visible in it. Next, the RGB frames are transformed to gray-scale frames with help of a Matlab command: *rgb2gray*. The average intensity of the gray-scale frame is an estimate of the flame intensity of the corresponding CFO at that instant. In this way, we get time histories of intensity pulsations ($y(t)$) for both the CFOs. We also test the flame dynamics with several physical sets of CFOs having the same composition and dimensions to confirm that the synchronization phenomena are unaffected by the specific sets of candle sticks.

4.3 Short description of time series analysis adopted in this chapter

This section discusses the various tools that are used to analyze the intensity pulsations ($y(t)$ of the CFOs. We observe that when the two CFOs consist of a differing number of candles, their amplitude of pulsations is also different. Furthermore, even CFOs with an equal number of candles might have substantially different pulsation amplitudes during various dynamical states. However, we limit our attention to the phase correlation between the CFOs rather than the variation in pulsation amplitude. To do so, we mean-subtract the intensity time-series data ($y(t)$) as follows: $I(t) = y(t) - \overline{y}$, and normalize $I(t)$ as discussed next.

We generate the analytical time series $\xi(t) = I(t) + iI_H(t) = A(t)e^{i\Psi(t)}$ using the mean-subtracted signal $I(t)$. $A(t)$ is the amplitude of the time series at time t while $\Psi(t)$ is the instantaneous relative phase (or, instantaneous phase difference of the two CFOs) at t. The Hilbert transform of $I(t)$ is denoted by $I_H(t)$, which is computed as:

$$I_H(t) = H[I(t)] = PV\frac{1}{\pi}\int_{-\infty}^{\infty}\frac{I(\tau)}{t-\tau}d\tau \tag{4.1}$$

PV indicates the Cauchy principal value [158]. The intensity signal $I(t)$ is

normalized by dividing it by instantaneous amplitude $A(t)$, as described below.

$$X(t) = I(t)/A(t) \tag{4.2}$$

To explore the various dynamical states, we use the normalized intensity signal ($X(t)$), along with power spectrum (obtained with fast Fourier transform), instantaneous relative phase ($\phi(t)$) and average relative phase ($\langle\phi(t)\rangle$) of the two CFOs. The instantaneous relative phase between the two CFOs ($\phi(t)$) is calculated as, $\phi(t) = \Psi_1(t) - \Psi_2(t)$. Here, the phases of the two CFOs at time t are $\Psi_1(t)$ and $\Psi_2(t)$.

With 5-seconds duration windows, $X(t)$ and $\phi(t)$ are computed. We observe that a 5 seconds time window translates to 47-57 pulsation cycles, depending on the CFO pulsation period of the two oscillators. During the various synchronization states, the frequency of the coupled oscillators is found to be between 9.5 and 11.5 Hz. We verify that no phase slip happens during the 5-second window that is used to explore the synchronization state. We also ensure that both the CFOs exhibit a dynamically stable behavior. This is done by visually observing the relative phase behavior. A sharp change in the relative phase between the two CFOs indicates a phase slip event. Similarly, an unsteady trend in the relative phase during the 5-second window indicates that the dynamical state is not stable for that window.

It is worth noting that the paired oscillators often demonstrate multi-stability characteristics. In other words, the coupled CFOs exhibit different synchronization states at different realizations. Therefore, we derive the statistically prevalent synchronization state from the 100 seconds of captured data. The multi-stability results are described in detail in the appendix of this chapter. It is important to note that the paired CFOs often experience phase slips, making the precise calculation of relative phases over an extended period a challenging task. However, the greater the number of pulsations in the given time window, the more precisely the synchronization state can be assessed. As a compromise between these two criteria, we use a 5-seconds long time window for the current investigation. Therefore, for further investigation of the dynamical properties of the interacting CFOs, a representative window of 5 seconds, corresponding to the prevalent synchronization state, is used.

The average relative phase ($\langle\phi(t)\rangle$) is determined as follows. We consider the CFOs to be phase-locked if the instantaneous relative phase of the two CFOs remains confined during the 5 seconds period. In such circumstances, $\langle\phi(t)\rangle$ may be computed for the 5 seconds window as $\langle\phi(t)\rangle = \frac{1}{\Delta t}\sum_{t=0}^{\Delta t}\phi(t)$. Here, Δt equals 5 seconds. To make the average phase correlation of the two CFOs easy to comprehend, the values of $\langle\phi(t)\rangle$ are wrapped from -180° to 180°. Next, the modulus

of the average relative phase ($|\langle\phi(t)\rangle|$) is shown in this study. This is because the absolute value of the average relative phase is the main criteria to assess the synchronization state. If the instantaneous relative phase between the two CFOs does not remain bounded within a reasonable limit during the 5 seconds period, then the CFOs are not phase-locked. As a result, the average relative phase would have no meaning. In this study, if the criterion, $\max\phi(t) - \min\phi(t) \leq 180^\circ$ is satisfied for the 5 second time series analyzed, we consider $\phi(t)$ to be bounded.

The Pearson correlation coefficient (ρ), which estimates the linear relationship between the amplitudes of two time series, is another effective metric for studying amplitude relationships between the interacting CFOs [50]. It has been observed that $\rho \approx 1$ during IP synchronization and $\rho \approx -1$ during AP synchronization [50]. It is calculated as,

$$\rho = \frac{N(\sum y_1 y_2) - (\sum y_1 \sum y_2)}{\sqrt{(N\sum y_1^2 - (\sum y_1)^2)(N\sum y_2^2 - (\sum y_2)^2)}} \tag{4.3}$$

In Eq. 4.3, the length of the time series ($N = 1200$ in our example) is denoted by N. Thus, the calculations corresponding to in Eq. 4.3 are performed across time instants 1 to N.

4.3.1 Synchronization theory principles pertinent to this study

Synchronization is a nonlinear event in which the pulsations in the interacting oscillators are modified due to weak interplay between the oscillators. Depending on the nature and intensity of the interaction, various types of synchrony can occur. For ease of comprehension, the various synchronization states relevant to the current investigation are described next. The synchronization state is considered as in-phase (IP) synchronization when the instantaneous relative phase of the pair of oscillators is bound within a reasonable limit during the 5 seconds period and the average relative phase $|\langle\phi(t)\rangle| \approx 0^\circ$. The dynamical state is called an anti-phase (AP) synchronization if the relative phase between the two CFOs is bounded and $|\langle\phi(t)\rangle| \approx 180^\circ$ [159]. We define the dynamical state as lag synchronization (LS) if $|\langle\phi(t)\rangle|$ is between IP and AP but is not near any of them. Amplitude death (AD) is a synchronization state in which the interaction between the CFOs produces almost complete suppression of pulsations in both the CFOs [150], [154]–[156]. Partial amplitude death (PAD) is a synchronization state in which the pulsations of one CFO become almost completely suppressed whereas the pulsations in the other CFO persist. Desynchronization (DS) occurs when there is no clear phase correlation between the paired oscillators, allowing the

relative phase of the coupled CFOs to increase or decrease monotonically.

4.4 Results

4.4.1 Visual observation of flame dynamics corresponding to isolated and coupled candle flame oscillators

The changes in flame dynamics, that occurs when the distance between the paired CFOs is altered, may be observed from flame snapshots corresponding to the two CFOs at various time instants. First, we study the flame dynamics corresponding to the solitary CFOs and then compare them with that of the interacting CFOs. Figures 4.3 and 4.4 show images of isolated CFOs containing three and five candles respectively, at various time instants. In each of these situations, two phenomena may be observed. First, a periodic lengthening and shortening of the flame. Second, a portion of the flame occasionally splits from the main flame to produce a puff. For brevity, we refer to the candle flame oscillators with 3, 4, and 5 candles as oscillator-3, oscillator-4, and oscillator-5 respectively. We see that the puff dimension corresponding to oscillator-5 is substantially greater than that of oscillator-3.

The behaviors of the two oscillators are markedly different when they are in close proximity so that interplay between the CFOs become possible. Here, the flame behaviors of the coupled oscillators are discussed for a few example scenarios. In Fig. 4.5, the two CFOs are shown to lengthen and shorten at the same moment at $l = 5$ mm for the 3/3 configuration. Later, with time series analysis, we demonstrate that this scenario corresponds to in-phase (IP) synchrony. Now, we investigate the CFO dynamics at $l = 10$ mm for the 3/3 configuration (Fig. 4.6). For this scenario, the flames of both CFOs are seen to occupy the same positions at various time instants. Therefore, the dynamic state here is amplitude death (AD). Figure 4.7 depicts the CFO dynamics attained at $l = 40$ mm for the 3/4 configuration. However, determining the synchronization state using merely flame snapshots in this scenario would be a challenging task. This synchronization state will be discussed in detail later in this chapter.

Figure 4.8 depicts the CFO behavior attained at $l = 80$ mm for the 3/5 configuration. We conclude that the oscillator-3 remains in the same position at different time instants from the flame images taken. On the other hand, the snapshots corresponding to oscillator-5 indicate a presence of distinct periodic pulsations in it. We demonstrate later in this chapter that this synchronization scenario is the partial amplitude death (PAD) state. A thorough assessment of the dynamical characteristics of the CFOs cannot be obtained only from visual observation of

Figure 4.3: Flame images of a solitary candle flame oscillator (CFO) comprising three candles. The snapshots are captured at an interval of 0.0375 seconds.

Figure 4.4: Flame images of a solitary candle flame oscillator (CFO) comprising five candles. The snapshots are captured at an interval of 0.0375 seconds.

the flame. To that purpose, we now investigate the time-series features of solitary and coupled candle flame oscillators.

4.4.2 Dynamical properties of the solitary candle flame oscillators

We investigate the dynamical characteristics of the solitary oscillators to compare and contrast them with the dynamical characteristics of the coupled CFOs. Figure 4.9 depicts the intensity time series ($y(t)$) for the solitary CFOs consisting of 3, 4, and 5 candles. For ease of visual inspection, the time series pertaining to the first 2 seconds only are presented in Fig. 4.9, which indicates the presence of periodic pulsations in all 3 configurations. The RMS of the flame intensity and the predominant frequencies of the CFOs, determined from time series of 5 seconds duration, are displayed in Table 4.2.

As the number of candles in a CFO increases, the frequency of the CFO decreases. To quantify the dissimilarity of the different CFOs, we compare the RMS value of the intensity of the solitary CFOs. We observe that the oscillator-4 has

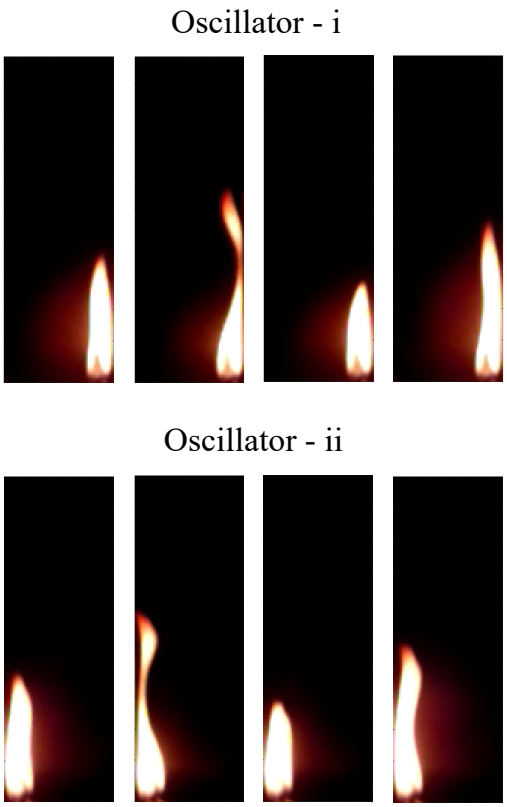

Figure 4.5: Flame pictures of the two coupled CFOs at $l = 5$ mm for the 3/3 configuration. Both the CFOs, namely the oscillator-i and oscillator-ii, contain 3 candles. The snapshots are captured at an interval of 0.0375 seconds.

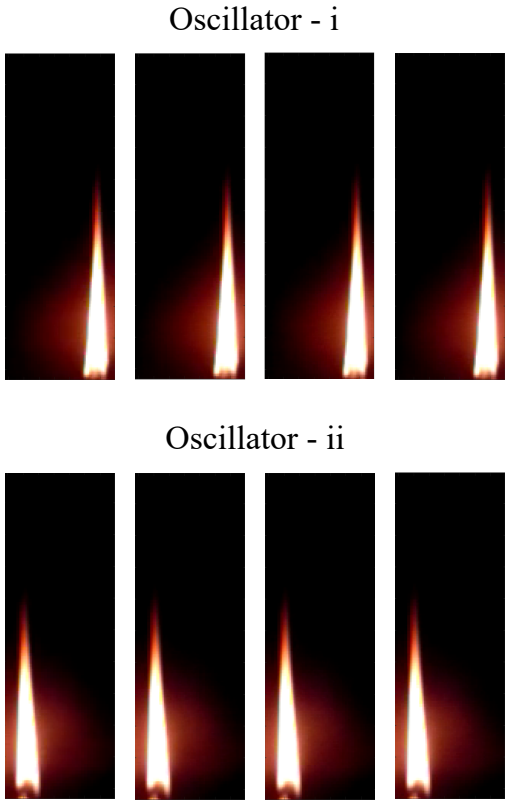

Figure 4.6: Flame pictures of the two coupled CFOs at $l = 10$ mm for the 3/3 configuration. Both the CFOs, namely the oscillator-i and oscillator-ii, contain 3 candles. The snapshots are captured at an interval of 0.0375 seconds.

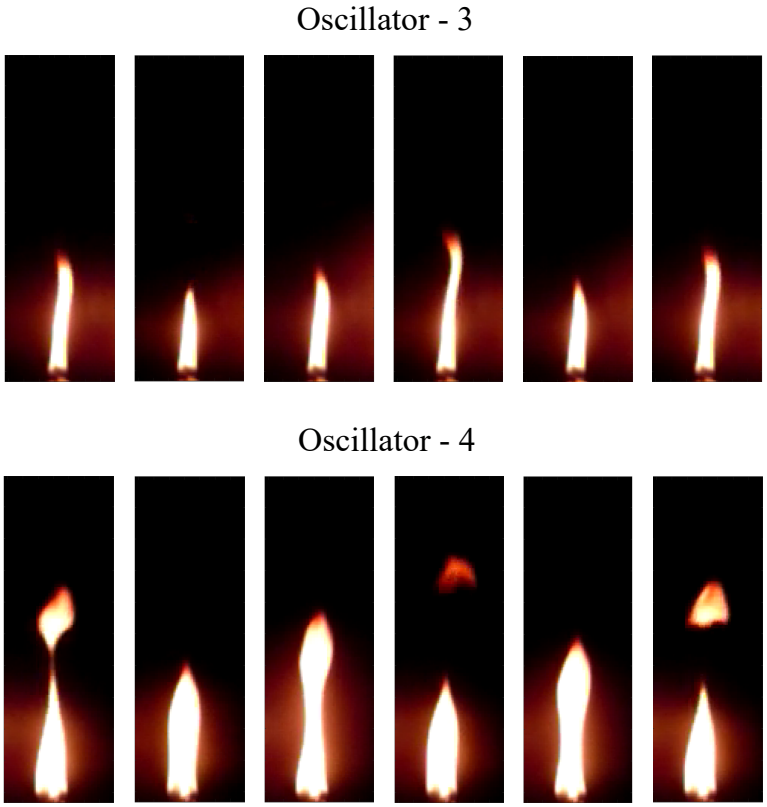

Figure 4.7: Flame pictures of the two coupled CFOs at $l = 40$ mm for the 3/4 configuration. The CFO with 3 candlesticks and 4 candlesticks, is denoted as oscillator-3 and oscillator-4 respectively. The snapshots are captured at an interval of 0.0375 seconds.

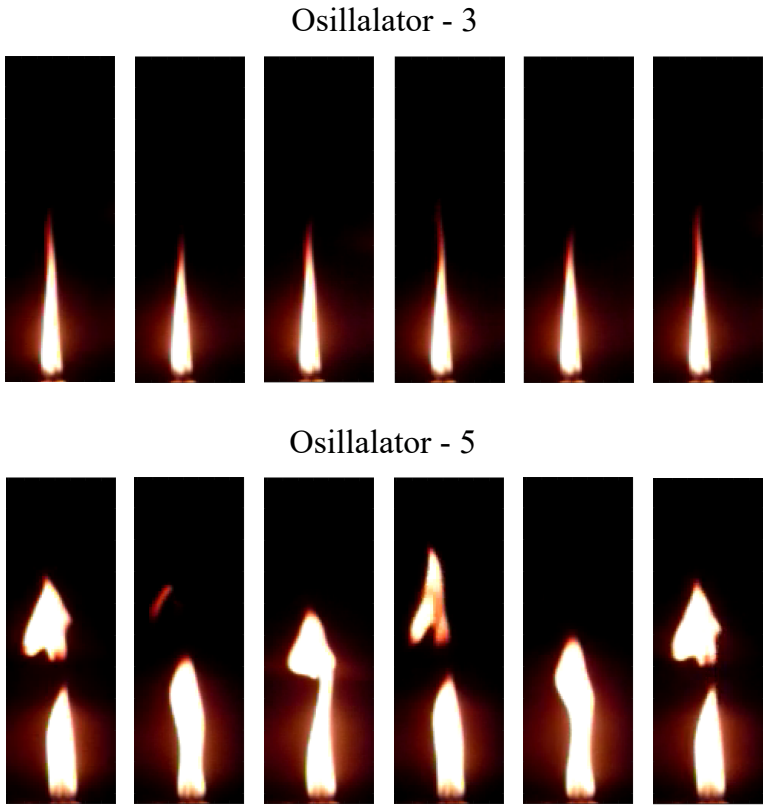

Figure 4.8: Flame pictures of the two coupled CFOs at $l = 80$ mm for the 3/5 configuration. The CFO with 3 candlesticks and 5 candlesticks, is denoted as oscillator-3 and oscillator-5 respectively. The snapshots are captured at an interval of 0.0375 seconds.

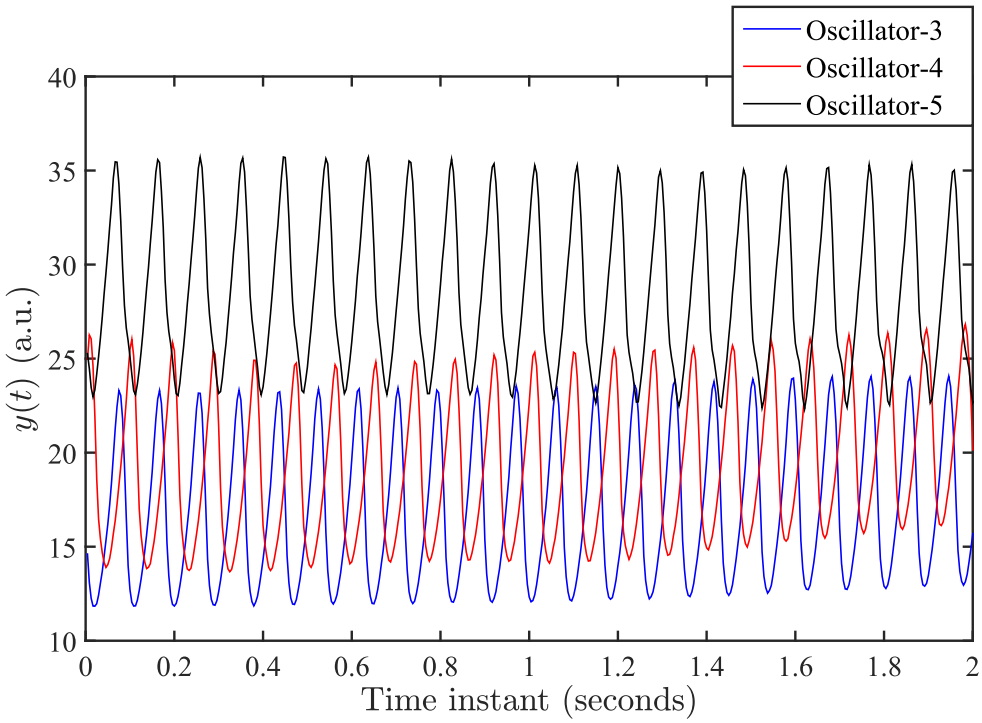

Figure 4.9: The intensity time series $y(t)$ for the different solitary candle flame oscillators (CFO). The terms Oscillator-3, Oscillator-4, and Oscillator-5 denote CFOs having 3, 4, and 5 candle sticks, respectively.

10.5% higher RMS intensity as compared to the oscillator-3. Similarly, oscillator-5 has 59.4% higher RMS intensity as compared to the oscillator-3. Therefore, the 3/4 and 3/5 configurations can be regarded as the slightly differing and considerably differing sets of candle flame oscillators, respectively. The two oscillators in the 3/3 configuration may be assumed to be almost identical as both are built of three candle sticks with same nominal shape and composition. As discussed before, the dynamical characteristics of coupled oscillators differ significantly from those of solitary oscillators. Next, we describe how the interplay between the oscillators affects their amplitude of pulsations.

4.4.3 Effect of interplay of the CFOs on their amplitude of pulsations

Figures 4.10(a-b) depict the intensity time series for the 3/3 configuration at various CFO distances (l). The peaks and valleys of the time series of the two CFOs are seen to be roughly coincident at $l = 5$ mm (Fig. 4.10a). In-phase (IP) synchronization is therefore likely to be the dynamical state here. At this point, the oscillators' pulse amplitudes are comparable. This can be anticipated as both the oscillators comprise 3 candle sticks. Amplitude death (AD) occurs at $l = 10$ mm, when the pulsations in both oscillators cease as the distance l between them

Number of candle sticks in the oscillator	Dominant frequency (Hz)	RMS value of Intensity (a.u.)
3	11.4 (± 0.2)	18.0
4	11.1 (± 0.2)	19.9
5	10.7 (± 0.2)	28.7

Table 4.2: RMS intensities and prevalent frequencies for the CFOs with varying numbers of candle sticks. The standard deviations of the CFO frequency, determined using 15 sets of 5-seconds movies captured in succession, are shown in brackets.

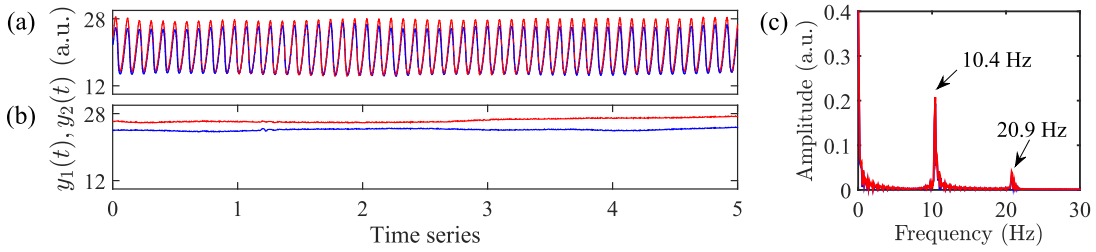

Figure 4.10: Time series of intensity $(y_1(t), y_2(t))$ for a pair of CFOs (3/3 configuration) as the distance between them changes. In-phase (IP) synchrony is obtained at (a) $l = 5$ mm and amplitude death (AD) is obtained at (b) $l = 10$ mm, respectively. (c) Shows the strongest peak in the amplitude spectrum (10.4 Hz), for the IP state at $l = 5$ mm.

increases (Fig. 4.10b). Up to $l = 80$ mm, this dynamical behavior persists. A close examination of Fig. 4.10(b) reveals that the CFOs are not entirely stable during amplitude death. Instead, the intensity values show minute drifts over time. We observe that at this dynamical state, removing or putting out one of the CFOs causes the other CFO to quickly recover its self-sustaining pulsations. This suggests that the observed suppression of pulsations is not a transient feature but rather the result of interplay of the two CFOs.

As the distance between the oscillators is changed, the 3/4 and 3/5 configurations exhibit similar dynamical transitions in intensity time series. Therefore, for conciseness, we describe the time series at different l for the 3/5 configuration only. The time series for the 3/5 configuration at $l = 10$ mm is shown in Fig. 4.11(a). In this scenario, the peak-to-peak amplitude of pulsations in oscillator-5 is significantly higher than that of oscillator-3. This is due to the greater supply of molten paraffin wax in the oscillator-5 [48]. The AD state continues to occur at $l = 15 - 35$ mm (Fig. 4.11b). The pulsations in both CFOs re-establishes at $l = 40$ mm and continues for up to $l = 45$ mm (Fig. 4.11c). Another AD regime is observed at $l = 50 - 65$ mm. During $l = 65 - 80$ mm, the pulsations in CFO-3

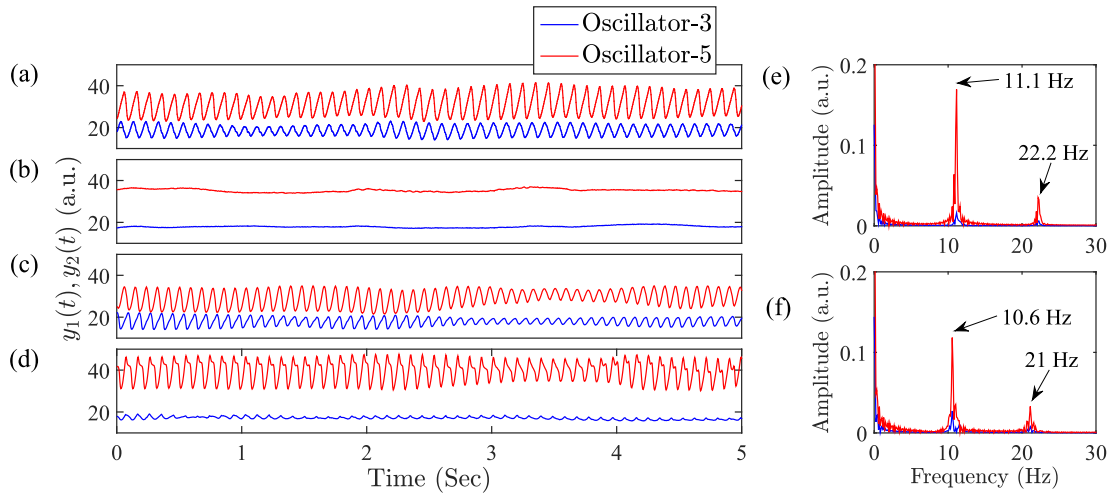

Figure 4.11: Intensity time series $(y_1(t), y_2(t))$ for the significantly differing set of CFOs (3/5 configuration) as the distance between them changes. (a) Both CFOs exhibit pulsations at $l = 10$ mm. (b) Amplitude death happens at $l = 15$ mm. The time series pertaining to $l = 45$ mm, at which both CFOs resume oscillations, is shown in (c). The partial amplitude death (PAD) pertaining to $l = 80$ mm is shown in (d). The power spectrum for the PAD states, at $l = 70mm$ and $l = 80m$, for the 3/5 configuration, is shown respectively in (e) and (f).

(shown in Fig. 4.11d in blue) are absent while the CFO-5 (shown in Fig. 4.11d in red) again starts to exhibit pulsations. Therefore, this dynamical state corresponds to partial amplitude death (PAD). Again, a careful look at the time series reveals that, at this point, weak pulsations are present in the CFO-3 also. This may be seen from the amplitude spectrum at $l = 70$ mm and $l = 80$ mm, where no significant peak can be observed (Fig. 4.11e and Fig. 4.11f respectively.) As will be demonstrated later in this chapter, minor amplitude pulsations continue to occur at PAD states for the seemingly dead CFO for the 3/4 configuration as well. Next, we describe various synchronization states primarily by exploring the relative phase data of the CFOs.

4.4.4 Exploration of the various types of synchrony observed in this study

To assess the dynamical states of the CFOs, we examine the normalized time series $(X_1(t), X_2(t))$, as well as the instantaneous phase difference $\phi(t)$ (Fig. 4.12) in tandem. The time series pertaining to the two CFOs (3/3 configuration) at $l = 5$ mm (Figs. 4.12a-b) is seen to have coincident peaks and valleys. At this moment, $|\langle\phi(t)\rangle| \approx 0°$, which confirms that IP synchronization is the dynamical state here.

The 3/5 configuration does not encounter the IP synchrony. Instead, it is

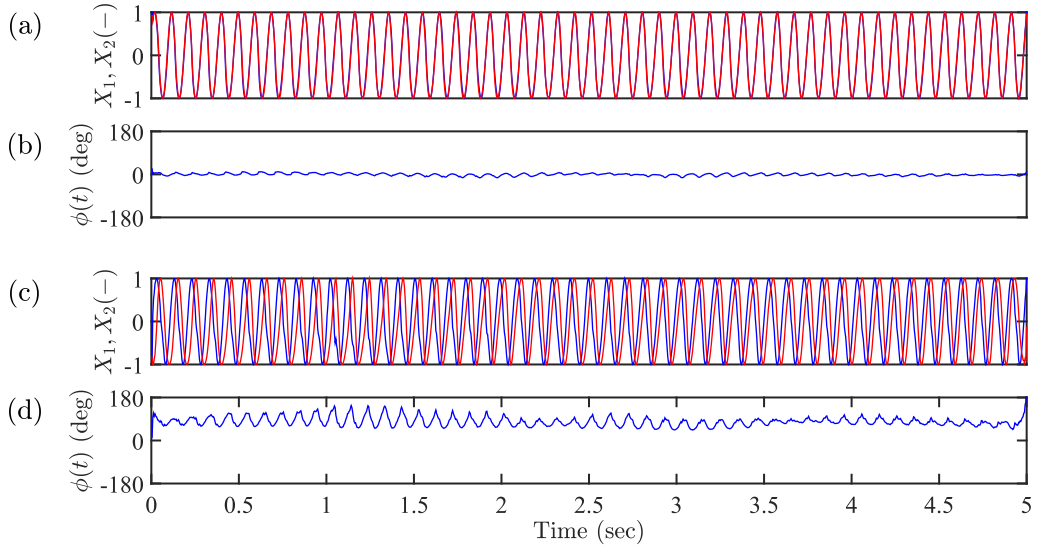

Figure 4.12: In-phase (IP) synchrony is achieved at $l = 5$ mm for the 3/3 configuration, as can be observed from (a) normalized time series and (b) instantaneous relative phase $\phi(t)$ (presented in degrees). The normalized time series and instantaneous relative phase $\phi(t)$ (given in degrees) for the lag synchrony obtained at $l = 10$ mm for the 3/5 configuration, are presented in (c) and (d), respectively.

discovered that the lag synchronization takes place when the two CFOs are closest to one another ($l = 5-10$ mm). A phase lag, for instance, may be seen between the time series pertaining to the two CFOs at $l = 10$ mm (Fig. 4.12c). Here, $|\langle\phi(t)\rangle|$ is 79° (Fig. 4.12d) and the dynamical state corresponds to lag synchronization. The instantaneous relative phase of the two CFOs $\phi(t)$ displays much greater pulsations for the various LS states seen in this study than they do during IP states (for example, see Fig. 4.12b).

Since the Hilbert transform is invalid for such synchronization states, the amplitude death (AD) and partial amplitude death (PAD) are not described here using $X(t)$ and $\phi(t)$. In these scenarios, the variation of the mean position of the time series becomes of the same order as the pulsation amplitude of the seemingly dead CFOs. Due to this, the analytic plane lacks a singular center of rotation [153]. Such drift in these scenarios is a sign of the flame's intrinsic transitory dynamics. After going through various types of synchronization states encountered in this study in detail, we will now concentrate on the dynamical transitions for the 3/3, 3/4, and 3/5 configurations, as the distance between the CFOs is changed.

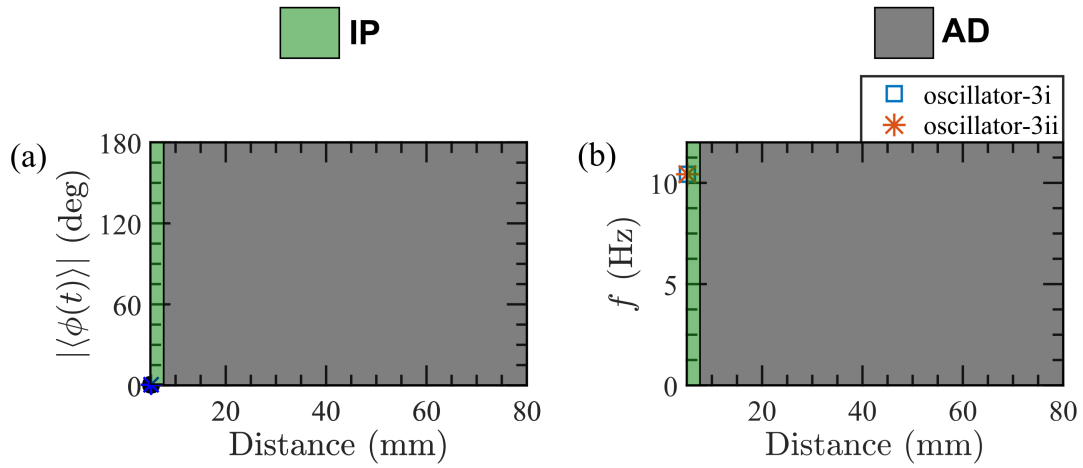

Figure 4.13: Average relative phase or average phase difference of the two CFOs ($|\langle\phi(t)\rangle|$) at various synchronization states, for the 3/3 configuration, are presented in (a). The dominant frequency (f) of the CFOs, at various synchronization states, for the 3/3 configuration, are shown in (b). For ease of understanding the phase relationship of the two CFOs, $\langle\Phi(t)\rangle$ is wrapped from -180° to 180°.

4.4.5 Transitions in synchronous behavior for various configurations

The phase and frequency correlation of the coupled CFOs is used to study the dynamical transitions in the similar (3/3 configuration) as well as differing sets of CFOs (3/4 and 3/5 configurations). Fig. 4.13 demonstrates the changes in the dominant frequency (f) and the $|\langle\phi(t)\rangle|$ for the 3/3 configuration as the distance between the coupled CFOs is changed. The interplay of the CFOs leads them to oscillate in an in-phase (IP) state at $l = 5$ mm. Here, the CFO's prevalent frequency is 10.4 Hz (Fig. 4.13b). As seen from table 4.2, this frequency is lower than the solitary CFO's prevalent frequency (11.4 Hz). The two CFOs display amplitude death states at all other distance between them ($l = 10 - 80$ mm) for the 3/3 configuration (Figs. 4.13a-b).

The transitions in synchronous behavior for the 3/4 configuration are now described. When the CFOs are most proximate ($l = 5$ mm), IP synchronization is seen for the 3/4 configuration, akin to the 3/3 configuration, as shown in Figs. 4.14(a-b). Further increment in l, however, result in the emergence of an AD regime ($l = 0 - 20$ mm), an LS regime ($l = 25 - 45$ mm), and then another AD regime ($l = 50 - 60$ mm) respectively. Finally, one of the CFOs stops pulsating during the PAD regime ($l = 65 - 80$ mm).

When the CFOs are closest to each other ($l = 5 - 10$ mm) for the 3/5 configuration (Figs. 4.14c-d), an LS regime is encountered. We examine the sensitivity of the synchronization state on the initial situation (initial phase difference) with

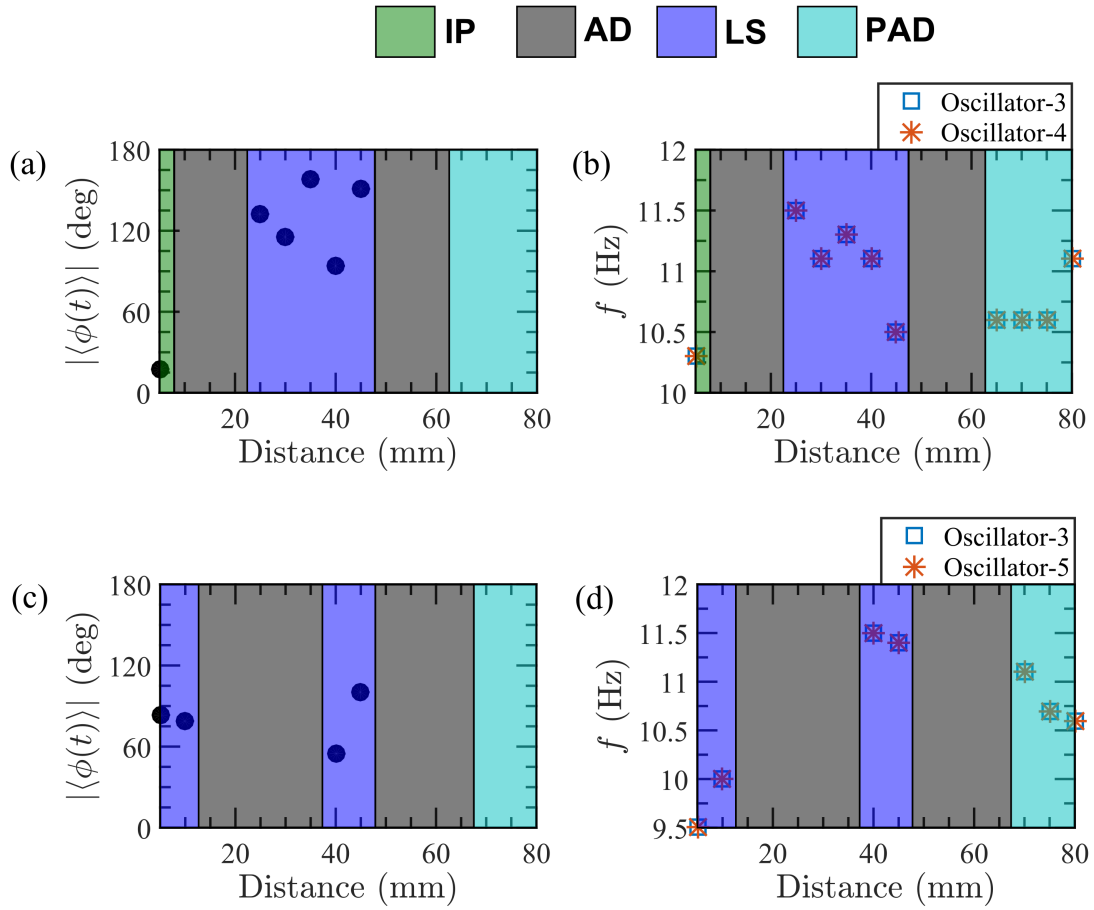

Figure 4.14: Average relative phase or average phase difference of the two CFOs ($|\langle\phi(t)\rangle|$) for the 3/4 configuration, at various synchronization states, is presented in (a). We note that $|\langle\phi(t)\rangle|$ is the absolute value of the average relative phase and it is represented in degrees. The dominant frequency (f) of the CFOs for the 3/3 configuration, at various synchronization states, is depicted in (b). The average relative phase and dominant frequency for the 3/5 configuration are presented in (c) and (d) respectively. For ease of understanding the phase relationship of the two CFOs, $\langle\Phi(t)\rangle$ is wrapped from -180° to 180°.

many realizations. However, we do not observe any instances of IP synchronization for the 3/5 configuration. However, akin to the 3/4 configuration, AD begins to manifest when l is incremented ($l = 15 - 35$ mm). An LS regime ($l = 40 - 45$ mm) is produced, akin to the 3/4 configuration, as l is incremented further. But the LS regimes are significantly narrower in width for the 3/5 configuration as compared to the 3/4 configuration. Another AD regime ($l = 50 - 65$ mm) starts as l is further incremented.

During $l = 65 - 80$ mm, one of the oscillators experiences an almost total suppression of pulsations resulting in the onset of the PAD regime. It is important to note that the dynamical transition in 3/4 and 3/5 configurations have significant similarities between them, except when the two coupled CFOs are closest to one another (i.e. when $l = 5$ mm). For example, there is a LS regime with AD regimes on its two flanks for both 3/4 and 3/5 configurations. For both these configurations, a PAD state is encountered when the distance between the CFOs is significantly high. Moreover, a variety of dynamical states is observed for both the 3/4 and 3/5 configurations as l is varied. In contrast, an AD regime is seen to exist throughout the range of l ($l = 10 - 80$ mm) for the 3/3 configuration apart from an IP state when the two CFOs are most proximate ($l = 5$ mm). We observe that the frequency (f) and the average relative phase ($|\langle\phi(t)\rangle|$) of the two CFOs vary substantially with l in no particular sequence (Fig. 4.14) for the 3/4 and 3/5 configurations. This is true even if these LS states are part of the same LS regime. To put it another way, no definite correlation exists between $|\langle\phi(t)\rangle|$ and f with l.

The Pearson correlation coefficient ρ provides additional information on the amplitude relationship between the coupled CFOs at different dynamical states. The changes in ρ, with different distances between the coupled CFOs, are depicted in Fig. 4.15 for the 3/3, 3/4, and 3/5 configurations. We observe that the value of ρ in the IP regime is approximately 1. This is anticipated given that at the IP state, the amplitude crests of the two CFOs almost coincide (Fig. 4.15a). In contrast, the ρ values in the lag synchronization regimes range from -0.74 to 0.43.

Next, we investigate the synchronization state at $l = 35$ mm for the 3/4 configuration. We find that at this point,$|\langle\phi(t)\rangle| = 158^\circ$ (Fig. 4.14a) and $\rho = -0.74$ (Fig. 4.15b). Therefore, here $|\langle\phi(t)\rangle|$ is near to but lower than 180° and ρ is higher than but near to -1. Based on these facts, we infer that the synchronization state at this point is an LS synchrony that is close to the AP synchrony. These facts also indicate that the findings of the two metrics $|\langle\phi(t)\rangle|$ and ρ, regarding the nature of synchrony at a particular point, in general support each other.

As seen in Fig. 4.15, there are multiple LS states where the value of ρ approaches zero. Normally, when desynchrony between the two CFOs is established, ρ approaches zero as there would be no definite amplitude correlation in such a

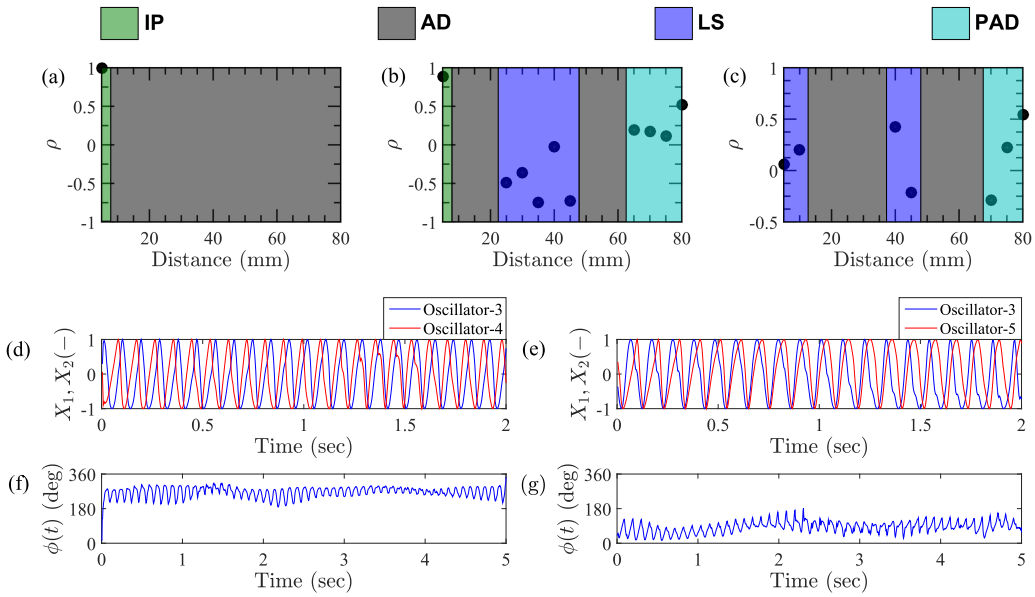

Figure 4.15: (a), (b), and (c) show the Pearson correlation coefficients for the 3/3, 3/4, and 3/5 configurations respectively, as the distance between the CFOs is changed. The normalized time series of an LS state, obtained at $l = 40$ mm of 3/4 configuration, is shown in (d) and the corresponding instantaneous relative phase plot is shown in (f). The normalized time series of another LS state, obtained at $l = 5$ mm for the 3/5 configuration, is shown in (e) and the corresponding instantaneous relative phase plot is shown in (g). The CFO with 3, 4, and 5 candles is indicated by Oscillator-3, Oscillator-4, and Oscillator-5, respectively.

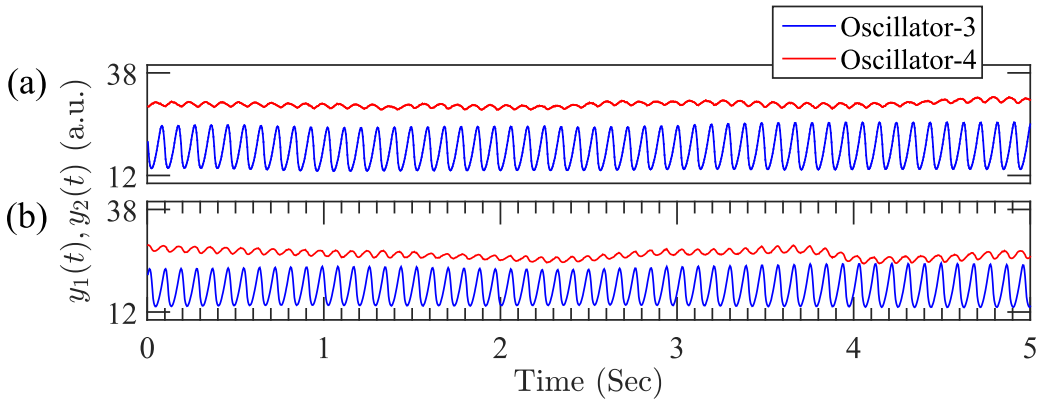

Figure 4.16: The intensity time series $(y_1(t), y_2(t))$ at $l = 70$ mm and $l = 80$ mm, respectively, for the 3/4 configuration, where PAD states are obtained.

case [50]. We look at two examples: the 3/4 configuration at $l = 40$ mm and the 3/5 configuration at $l = 5$ mm. In each of these two cases, $\rho \approx 0$. According to Fig. 4.14, the dynamics in these scenarios corresponds to LS states.

We use the normalized time series $(X_1(t), X_2(t))$ and instantaneous relative phase $(\phi(t))$ graphs to explain this anomalous behavior. We consider two example cases: (i) at $l = 40$ mm corresponding to the 3/4 configuration (Figs. 4.15(d,f) respectively) and (ii) at $l = 5$ mm corresponding to the 3/5 configuration (Figs. 4.15(e,g) respectively). Here we highlight that magnified views of the normalized time series, corresponding to two seconds duration, are displayed in Fig. 4.15 for better visualization only; the critical key parameters ($|\langle\phi(t)\rangle|$, f, ρ etc.) are computed using five seconds data. The $\phi(t)$ of the two oscillators are observed to be restricted within a certain range in Figs. 4.15(f,g), showing the presence of phase-locked conditions in these two examples. We discover that the synchronization state at $l = 40$ mm of the 3/4 configuration corresponds to the average relative phase of $|\langle\phi(t)\rangle| = 94°$. Further, $|\langle\phi(t)\rangle| = 83°$ at $l = 5$ mm for the 3/5 configuration. Since $|\langle\phi(t)\rangle| \approx 90°$ for these situations, these dynamical states are LS states. We further note that these dynamical states are at almost equal distance between the IP and AP states. This is why ρ is approximately zero in these situations, which is the average ρ of IP and AP synchrony.

We now examine a few typical PAD instances that occurred in our study. Figure 4.16 depicts two representative time series during PAD states for the 3/4 configuration. In these two scenarios, oscillator-4 experiences an apparent amplitude death, whereas oscillator-3 continues to oscillate. The pulsation amplitude of oscillator-4 does not, however, become zero. Close examination of the normalized time series at $l = 70$ mm, for the 3/4 configuration, reveals a phase lag between the amplitude crests corresponding to the two CFOs (Fig. 4.16a). Consequently,

here $\rho = 0.17$ (Fig. 4.15b). The phase lag between the amplitude crests of the two time series, however, is significantly decreased at a higher distance ($l = 80$ mm) between the CFOs (Fig. 4.16b). The strong correlation of the two time series amplitude at $l = 80$ mm ($\rho = 0.52$) supports this conclusion. We then investigate the PAD states for the 3/5 configuration, where the two CFOs have significantly differing characteristics. Visual examination of the time series at $l = 80$ mm (Fig. 4.11d), where the dynamic state corresponds to PAD, shows that oscillator-3's pulsation amplitude is significantly reduced here while the pulsation amplitude of oscillator-5 is the same as in the prior instance. The amplitude crests of the two CFOs roughly coincide in time at this distance ($l = 80$ mm), leading to an enhanced correlation value ($\rho = 0.55$).

4.5 Discussions

The interplay of two CFOs, for both similar and differing sets of oscillators, is discussed in previous section along with several novel findings. The insights gained from these observations are described below.

When CFOs are closest to one another during the interplay of a similar set of CFOs, IP synchronization is achieved. At all other distances between the similar set of CFOs, the amplitude death continues to occur. In contrast, during the interplay of differing sets of CFOs (i.e. 3/4 and 3/5 configurations), the amplitude of pulsations as well as the synchronization states change in a significant way as the distance between the CFO is varied. In particular, for the differing sets of CFOs, as the dynamical state shifts from IP/LS to PAD (Figs. 4.11a,c-d) with an increase in distance between the CFOs, the amplitude of pulsations in one of the CFOs is seen to reduce gradually (if we ignore the interim AD regimes in which neither CFO exhibits pulsations). A possible evidence that the two CFOs are strongly coupled is the considerable changes in amplitude of pulsations evinced by the CFOs, as the dynamical state changes. This is because weak coupling may only affect the CFOs' phase, but a strong coupling can affect the coupled CFOs' amplitude as well [153]. Liu *et al.* [160], [161] experimentally and numerically examined the interplay of two Lorenz oscillators, created with electrical circuits. They found that the pulsation amplitudes in two identical oscillators become increasingly different as the coupling strength between them is varied. Finally, they saw that one oscillator experiences amplitude death while the other keep oscillating. In the current investigation, a similar path to PAD is seen.

For all phase-locked situations, we see significant fluctuations in the instantaneous relative phase $\phi(t)$ (see, for example, Figs. 4.12(b,d) and Figs. 4.15(f,g)).

Numerous experimental systems, including coupled CFO systems, have been shown to experience these variations. This might be a consequence of the intrinsic fluctuations in candles [53]. It may also be due to the intrinsic noisiness of the interacting CFOs [153]. Typically, an oscillating relative phase is obtained when two periodic oscillators, having the same frequency but differing waveforms, interact with each other.

For both 3/4 and 3/5 configurations, we see the emergence of two AD regimes separated by an LS regime. We designate these areas as multiple regimes of amplitude death in accordance with the literature [162]. In contrast, we detect a single AD regime for the 3/3 configuration. Several analytical and numerical investigations have reported multiple regimes of amplitude death [156], [160]–[170].

The existence of multiple regimes of AD is not trivial. Such occurrences illustrate the complicated link between the observed dynamical states and the system's τ_c (the time delay of coupling). This phenomenon has been found in a wide number of literature where it is typically represented in a $K - \tau_c$ parameter space. Here, K is the coupling strength of the two oscillators. As an illustrative example, the reader may refer to Fig. 4 of the study by Reddy *et al.* [162].

Furthermore, we detect LS regimes in the 3/4 and 3/5 configurations (i.e. for the differing sets of interacting CFOs) but not in the 3/3 configurations (i.e. in the similar set of interacting CFOs). This is anticipated since it is known that LS only happens when the coupled oscillators are different from one another [171], [172]. We note that multiple LS regimes are present in the significantly differing set of CFOs (i.e. the 3/5 configuration), separated by an AD regime (Fig. 4.14c-d). Previous studies have reported the presence of an amplitude death regime, which separates two LS regimes located at both flanks of it. Biwa *et al.* [173], for instance, investigated the interplay between two thermoacoustic oscillators and discovered the existence of LS-like states on each side of an AD regime. To the best of the author's knowledge, multiple LS regimes brought about by the interaction of two CFOs have not been reported to date.

Additionally, we report that partial amplitude death can occur due to the interplay of the differing sets of oscillators but not due to the interplay of the similar set of CFOs. Numerous studies, from a theoretical perspective, have discussed the partial amplitude death (PAD) state [168], [174], [175]. Recently, Dange *et al.* [51] observed that the interaction of two Rijke tube oscillators, having a substantial difference in frequency, may cause the onset of PAD. As far as we know, the onset of PAD due to the interplay of two CFOs has not been reported in the literature to date.

The average relative phase $\langle\phi(t)\rangle$ and frequencies of the two oscillators (f), as previously indicated, do not exhibit any specific trends with a variation in

l. Additionally, we observe that parametric variation of a single variable l (the distance between the CFOs) can cause the occurrences of multiple AD regimes and multiple LS regimes, for the differing sets of CFOs (i.e. for the 3/4 and 3/5 configurations), as seen in Fig. 4.14. These results reveal the intricate relationship between the synchronization states and the distance (l) between the CFOs. It is understood that as l varies, the time delay of interaction (τ_c) is also likely to change [51]. However, it is probable that when changing l, the coupling strength (K) between the CFOs also changes. The complicated nature of CFO interactions has been documented previously. According to Manoj *et al.* [50], the CFO interactions may be the result of indirect coupling through an intermediary medium as well as time delay coupling. Previous literature has reported the existence of a fluid-dynamical connection between the CFOs [52]. The interplay of vortices, produced by buoyancy-induced instability surrounding the flames, is what causes this fluid dynamical connection [52]. Keeping these evidences of complex nature of coupling between the CFOS, we contend that it might not always be possible to change τ_c by changing l without a corresponding change in K. If this is the case, parametric change of l may lead to complex dynamical transitions in the $K - \tau_c$ parameter space. Additional insights into such complicated dynamical transitions may be provided by a numerical model of interacting CFOs. In a future study, this facet of the problem will be addressed.

4.6 Summary

This chapter contrasts the synchronization behavior brought on by the interplay of candle flame oscillators (CFO) that have similar and differing amplitudes of pulsations. We discover significant differences between the dynamical transitions obtained due to the interplay of similar and differing sets of CFOs. It is seen that in close vicinity, the interplay of the similar set of CFOs establishes in-phase synchronization. However, when the interacting CFOs are significantly different, a lag synchronization state is encountered in close vicinity. Further, interplay of CFOs is seen to result in amplitude death (AD) across the operational range, except in close vicinity, if the interacting CFOs have similar amplitude of pulsations. In contrast, the interplay of CFOs is seen to result in dynamically rich transitions if the interacting CFOs have differing amplitude of pulsations. Such dynamical transitions are seen to consist of multiple amplitude death (AD) regimes, multiple lag synchronization (LS) regimes, and a partial amplitude death (PAD) regime. Overall, a simple dynamical transition is seen due to the interplay of a similar set of CFOs while a significantly complicated dynamical transition is seen due to the interplay of a differing set of CFOs.

In this study, we systemically explore the dynamically rich transitions in simple diffusion flame oscillators. This work may help to better understand the synchronization phenomena encountered in real-world scenarios, caused by flame-flame interaction.

Citation acknowledgment

Some parts of this chapter are reproduced with permission from the publication(s) listed below.

1. **Arijit Bhattacharya**, Sirshendu Mondal, Somnath De, Achintya Mukhopadhyay and Swarnendu Sen, "Synchronization behavior between two candle flame oscillators with similar and dissimilar amplitudes of oscillations",Combustion Theory and Modelling (DOI: 10.1080/13647830.2023.2165966).

Appendix

The results of the multi-stability analysis are shown in Tables 4.3 - 4.5. We see that the amplitude death state is dominant throughout the operating range for the 3/3 case, except in close proximity to the CFOs where IP synchronization is the dominant dynamic state. On the other hand, for 3/4 and 3/5 cases, the dynamical transitions encountered, as the distance between the two CFOs is varied, are more complex.

Useful insights about the synchronization state may be obtained by close visual inspection of the time series corresponding to the CFOs, as discussed in the main text of this chapter. Here we briefly discuss how the visual inspection of time series is carried out in this study. As an example, we consider the partial amplitude death (PAD) states encountered at $l = 70-80$ mm for the 3/4 case (Fig. 4.16 in the main manuscript). At PAD, the intensity time series $(y_1(t), y_2(t))$ corresponding to the two CFOs have significant differences in amplitude of oscillations, with one of the oscillators having a very small amplitude of oscillations. Thus we normalize the intensity time series with the Matlab function 'normalize' for ease of visualization. Figure Fig. 4.17 shows the normalized time series $(x_1(t), x_2(t))$ corresponding to the two CFOs during a PAD state for the 3/4 case. At $l = 70$ mm, we observe that the peaks of the oscillator-3 and oscillator-5 have a substantial time lag between them (Fig. 4.17a). On the other hand, at $l = 80$ mm, the time lag between the CFOs is much less (Fig. 4.17b). To quantify the difference in the time lag between the CFOs, we randomly chose two adjacent peaks corresponding to the two CFOs (indicated by the red and blue dots in the normalized time series in Fig. 4.17 and

Distance between the oscillators (mm)	Synchronization state
5	IP-80 sec, AD - 20 sec
10	AD- 100 sec
15	AD- 100 sec
20	AD- 100 sec
25	AD- 100 sec
30	AD- 100 sec
35	AD-74 sec, LS - 26 sec
40	AD- 100 sec
45	AD- 95 sec, LS -5 sec
50	AD- 100 sec
55	AD- 100 sec
60	AD- 100 sec
65	AD- 90 sec, PAD - 10 sec
70	AD- 90 sec, PAD - 10 sec
75	AD- 66 sec, PAD - 34 sec
80	AD- 65 sec, PAD - 35 sec

Table 4.3: Synchronization states when both the candle flame oscillators consist of 3 candles (3/3 case). The total experimental duration is 100 seconds, consisting of 10 experiments each of 10 seconds duration.

determine the time lag between them. Let t_1 and t_2 indicate the time lag between the CFOs at $l = 70$ mm and $l = 80$ mm respectively. We find that $t_1 = 0.032$ seconds while $t_2 = 0.004$ seconds. As $t_1/t_2 \approx 8$, the change in the time lag between these two cases is significant. We infer that at $l = 70$ mm, the synchronization state is lag synchronization whereas at $l = 80$ mm the CFOs may be considered approximately in-phase (IP).

Distance between the oscillators (mm)	Synchronization state
5	IP-84 sec, AD - 16 sec
10	IP-10 sec, AD - 90 sec
15	LS - 9 sec, AD - 91 sec
20	AD- 100 sec
25	LS - 70 sec, AD - 30 sec
30	LS - 88 sec, AD - 12 sec
35	LS - 95 sec, AD - 5 sec
40	LS - 95 sec, AD - 5 sec
45	LS - 62 sec, AD - 20 sec, PAD - 18 sec
50	AD - 52 sec, PAD - 25 sec, LS - 23 sec
55	AD - 81 sec, PAD - 14 sec, LS - 5 sec
60	AD - 75 sec, PAD - 23 sec, LS - 2 sec
65	AD - 75 sec, LS - 15 sec, AD - 10 sec
70	PAD - 90 sec, AD - 10 sec
75	PAD - 97 sec, AD - 3 sec
80	PAD - 79 sec, LS - 21 sec

Table 4.4: Synchronization states when the two candle flame oscillators consist of 3 candles and 4 candles (3/4 case). The total experimental duration is 100 seconds, consisting of 10 experiments each of 10 seconds duration.

Distance between the oscillators (mm)	Synchronization state
5	LS - 87 sec, AD - 13 sec
10	LS - 80 sec, AD - 20 sec
15	AD- 100 sec
20	AD- 100 sec
25	AD- 58 sec, LS - 37 sec, PAD - 5 sec
30	AD- 100 sec
35	AD - 80 sec, LS - 16 sec, PAD - 4 sec
40	AD - 52 sec, LS - 45 sec, PAD - 3 sec
45	LS - 85 sec, AD - 9 sec, PAD - 6 sec
50	AD - 97 sec, PAD - 3 sec
55	AD - 97 sec, PAD - 3 sec
60	AD - 74 sec, PAD - 23 sec, LS - 3 sec
65	AD - 92 sec, PAD - 5 sec, LS - 3 sec
70	PAD - 61 sec, LS - 22 sec, AD - 17 sec
75	PAD - 58 sec, LS - 24 sec, AD - 18 sec
80	PAD - 84 sec, LS - 16 sec

Table 4.5: Synchronization states when the two candle flame oscillators consist of 3 candles and 5 candles (3/5 case). The total experimental duration is 100 seconds, consisting of 10 experiments each of 10 seconds duration.

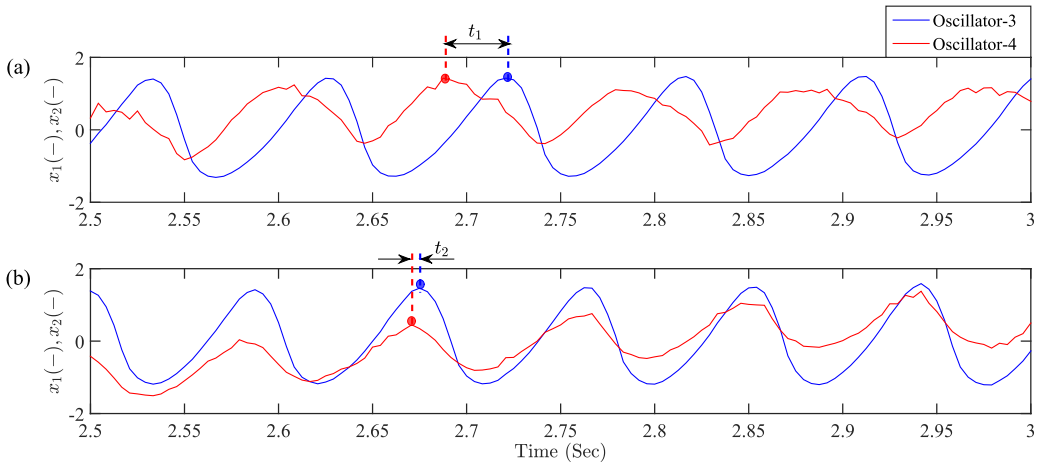

Figure 4.17: (a) and (b) show the zoomed-in and normalized time series $(x_1(t), x_2(t))$ corresponding to PAD states for 3/4 case at $l = 70$ mm and $l = 80$ mm respectively.

CHAPTER 5

Flame dynamics visualization near lean blowout in multi-burner combustors

5.1 Introduction

Most of the previous flame visualization studies on LBO phenomena have been done with single-burner combustors. However, most of the combustors in the industry today have annular or can configuration [176]. Adjacent burners in multi-burner combustors are likely to have an impact on one another's flame dynamics, especially close to the LBO/TAI instabilities [150]. Recent research has demonstrated significant differences between multi-burner and single-burner combustors concerning the near-LBO flame dynamics [177]. Physical phenomena like standing, spinning, slanting mode, etc. have been discovered for annular combustors which cannot be captured in a single-burner combustor [17], [22], [178]. Moreover, significant differences between the flow fields of an annular combustor and a single-burner combustor, having identical burners, have been found [46]. In recent literature, it has been reported that the interaction of flames in the multi-burner combustor produces significantly new physical phenomena like flame merging, interaction of adjacent flame roots and partial lift-off [56], [179], [180]. Ciardiello *et al.* [55] found that correlations based on single-burner combustors do not predict flame extinction limits correctly. Finally, flame visualization is important to understand LBO combustion physics, which is often highly complex in turbulent combustors. However, prior studies with multi-burner combustors have not

adequately and systematically explored the visual flame dynamics.

To bridge this gap in literature, in this chapter we visually examine the multi-burner combustors' flame dynamics during the transition to LBO and investigate how flame interactions impact the combustor's overall flame dynamics. The experimental rigs used in this study are an annular combustor (AC) and a linear array combustor (LAC). Both combustors have lean premixed swirl-dump stabilized configurations; such a configuration is frequently used as a simple model of lean premixed pre-vaporized gas turbine combustors used in stationary power plants and aircraft [29], [131]. We systematically study the changes in flame dynamics, during the approach to LBO in AC and LAC, by gradually reducing fuel flow rate while keeping air flow rate constant.

Another objective of this chapter is to identify whether there exists any significant difference between the AC and LAC. Therefore, in the first part of this chapter, we describe the flame dynamics of an annular combustor with 4 number of burners, and in the second part of this chapter, the flame dynamics of a linear array combustor with 3 burners are discussed. Next, we discuss the similarities and dissimilarities observed in the flame dynamics corresponding to the linear array combustor and annular combustors. Moreover, in practical modern combustors, the air-fuel mixture often does not have sufficient time or space for complete premixing. As a result, they are often partially premixed. Thus we also explore the differences in near-LBO flame dynamics of AC and LAC, at varying degrees of premixedness.

The remainder of this chapter is organized as follows. In section 5.2, the experimental test rigs and instruments used for this study are described in detail. In section 5.3, the changes in flame characteristics during the transition to lean blowout (LBO) are explored with the AC for various degrees of premixedness. Next, the visual changes in flame dynamics during the transition to LBO are explored for the LAC configuration with various burner-to-burner distances and degrees of premixedness. Moreover, the near-LBO dynamics observed for analogous AC and LAC configurations are compared. In section 5.4, we compare our results with those of previous studies. Finally, in section 5.5, the findings of this study are summarized.

5.2 Experimental test rigs and instruments used in this study

The experimental rigs used to study the LBO phenomena are an annular combustor with 4 identical burners and a linear array combustor with 3 identical

burners (Fig. 5.1). The schematic of the annular and linear array combustors is shown in Fig. 5.2. The annular combustor used in this study is a simple stepped-down model of industrial annular combustors. However, due to its small size, the annular test rig has a small radius and hence a high curvature in comparison to the industrial annular combustors. The effect of high curvature on near-LBO flame dynamics may be identified by studying the analogous linear array combustor, where the radius is infinite i.e. the curvature is zero. The combustion chamber of the annular combustor consists of an annular section between an outer quartz tube with an inner diameter of 140 mm and an inner quartz tube with an outer diameter of 30 mm. Thus the radial gap in the annular chamber is $(140 - 30)/2 = 55$ mm. The combustion chamber corresponding to the linear array combustor has an inner cross-section of 200 mm $\times$ 55 mm and consists of 4 flat quartz plates. The mean center-to-center spacing between the burners along the circumferential direction in the annular combustor is 55 mm. The center-to-center spacing between the burners in the linear array combustor can be fixed at 45, 55, and 65 mm, with a spacer arrangement. Also, the height of the combustion chamber (250 mm) in these two cases is equal. Moreover, identical burners are used in both combustors. Therefore, the annular combustor and linear array combustor (with a burner-to-burner spacing of 55 mm) may be considered to be analogous configurations.

The swirlers used in the burners have 6 number of vanes with a vane angle $\theta = 60^\circ$ with the axial direction. The swirlers have a height of 15 mm and a blade thickness of 1 mm. The swirlers are placed snugly inside the premixing tube (Fig. 5.1a3) such that their top end remains 15 mm below the dump plane. A solid cylindrical bluff body is attached at the center of each swirler. The bluff bodies have a diameter $d_h = 8$ mm and a length of 30 mm. These bluff bodies act as the center-body of swirlers. The bluff bodies are positioned such that their tips are at the dump plane level. Thus the swirl number for the burners of the multi-burner combustors can be calculated as,

$$S_W = \frac{2}{3}\left[\frac{1 - (\mathrm{d_h/d})^3}{1 - (\mathrm{d_h/d})^2}\right] \tag{5.1}$$

Here, the outer diameter of the swirler $d = 29$ mm. So, the swirler number is $S_W = 1.02$.

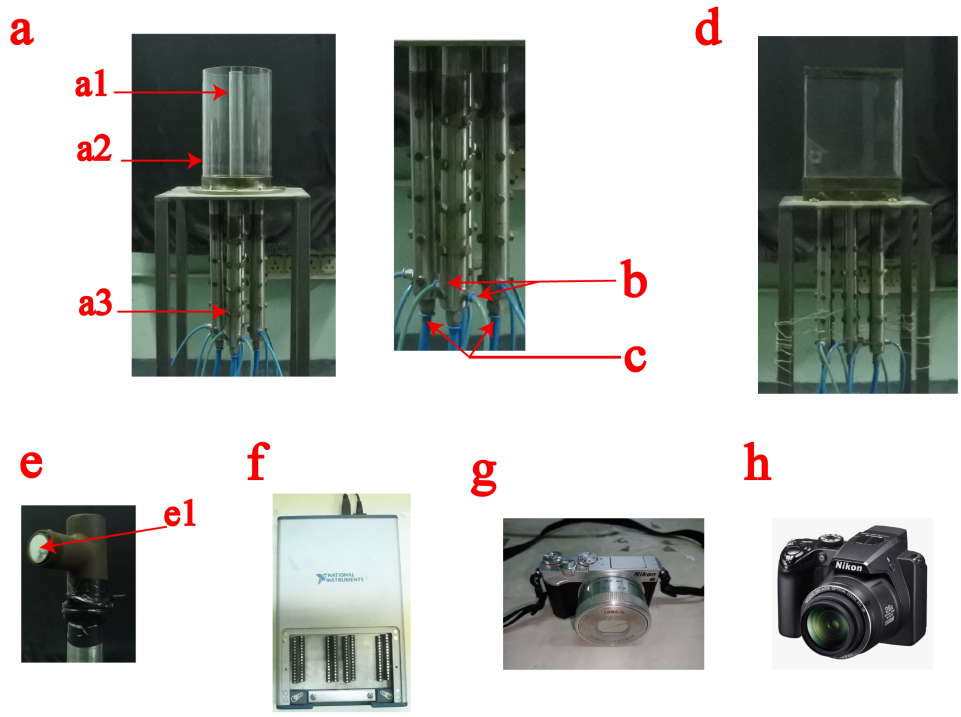

Figure 5.1: The experimental test rigs and instruments used for data acquisition. (a) annular combustor (AC), (a1) inner quartz tube of AC, (a2) outer quartz tube of AC, (a3) Premixing tubes, (b) fuel input ports, (c) air input ports, (d) linear array combustor (LAC). (e) photo-multiplier tube (PMT), (e1) CH* filter, (f) USB-DAQ, (g) camera I (Nikon J5), and (h) camera II (Nikon Coolpix P100).

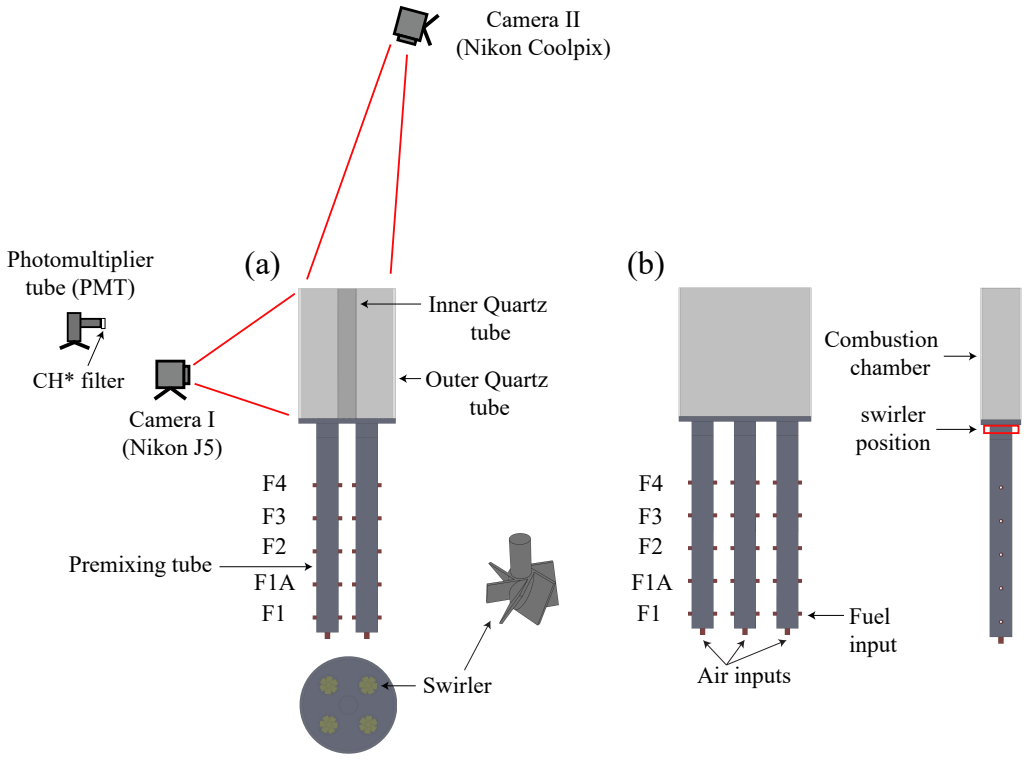

Figure 5.2: Schematic of the experimental test rig. (a) and (b) show the annular combustor (AC) and the linear array combustor (LAC) respectively. The camera II (Nikon Coolpix P100) is placed at an angle of 10° with the vertical.

5.2.1 Experimental procedure

The fuel used in this study is liquefied petroleum gas (LPG) consisting of 40% propane and 60% butane by volume [1]. LPG exhibits similar extinction-reignition events in the near-LBO state as compared to complex hydrocarbons normally used in practical gas turbines [2]. Moreover, LPG is cheap and has high availability. LPG flow rate is measured with 4 rotameters (CVG instruments, LPG, 0 - 7 liter per minute (lpm), accuracy: ±2% of full scale reading). LPG is input into the premixing tubes through 2 ports, spaced 180° apart for symmetric dispersal along the cross-section of the premixing tube. The air enters through the bottom of the premixing tube along the axial direction at atmospheric pressure and temperature. Air is supplied through 4 rotameters (CVG instruments, air, 0 - 100 lpm, accuracy: ±2% of full scale reading). The flow rate of air per burner is kept fixed at 80 lpm whereas the LPG flow rate is reduced to approach LBO, starting from a stable combustion state that is far away from LBO.

Because LPG flow rate is very less as compared to air flow rate, the total flow rate remains almost constant during the experiments. Thus, the Reynolds number, evaluated just prior to the dump plane, can be calculated as, $Re = \frac{4\dot{m}_{air}}{\pi d_e \mu_{air}} = 5390$. Here, $\dot{m}_{air}$ is the air mass flow rate, d_e is the effective diameter of the annular space between the solid bluff body ($d_h = 8$ mm) and inner diameter of premixing tube ($d_{premix} = 29$ mm). Thus, $d_e = d_{premix} - d_h = 21$ mm. μ_{air} indicates the dynamic viscosity of air. We note that the combustors always remain in the turbulent regime ($Re > 4000$) during the experiments.

The degree of premixedness is varied by varying the air-fuel mixing length. For this purpose, a number of fuel injection ports are positioned along the axial direction. The fuel injection ports used in this thesis are denoted as F1, F2, F3, and F4 respectively henceforth (Fig. 5.2). The air-fuel mixing lengths (l) for the F1, F2, F3, and F4 cases are 330 mm, 230 mm, 180 mm, and 130 mm respectively. We note that there is another port F1A (with $l = 280$ mm) in the annular and linear array test rigs (Fig. 5.2) at which the flame dynamics is found to be highly similar to the flame dynamics corresponding to F1 port. Therefore, the F1A case is not explored in this study.

5.2.2 Data acquisition equipment

For flame visualization, we use simple RGB images obtained with two CMOS cameras, Nikon J5 (camera I) and Nikon Coolpix P100 (camera II). The current chapter focuses on burner-to-burner interactions and flame-to-flame interactions.

[1] Data corresponding to the chemical composition of LPG is taken from the website of Indian Oil Corporation, https://www.iocl.com.

A relatively low frame rate (60 fps) is found to be sufficient for this purpose. During this study shutter speed, ISO sensitivity, and F-stop for the Nikon J5 camera are kept fixed at 1/400 second, 12800, and 3.5 respectively. Shutter speed, ISO sensitivity, and F-stop for the Nikon Coolpix P100 camera are kept fixed at 1/120, ISO 3200, and 2.8. We find that these settings are optimal for the two cameras. It may be noted that the F-stop is indicative of the aperture of the lens. We keep the F-stop value at the minimum possible for the cameras as we find that a higher F-stop reduces the brightness of the flame significantly. This approach is important to capture the flame near the LBO limit, where the flame is seen to have very low intensity. Similarly, the ISO value is taken as the maximum possible value to increase the flame brightness as much as possible. Having a high shutter speed captures the instantaneous flame image while reducing flame brightness. Therefore, a compromise between these two aspects has to be made. Flame videos are captured for a duration of 20 seconds for each operating condition. After capturing the flame videos, instantaneous flame images are extracted from them using Matlab software.

CH* chemiluminescence signal, characteristic of heat release rate in the combustor [130], [134] is captured during the experiment, for in-depth exploration of the dynamical transition to LBO. That study will be discussed in a later chapter of this thesis. A photo-multiplier tube (PMT) (Hamamatsu, model 931A), fitted with a CH* bandpass filter, is used to obtain the CH* signal. The PMT is positioned in a way that the entire flame is visible to it. The CH* filter centers at 430 nm with 10 nm full width half maximum. The PMT output then passes through the built-in amplifier, powered with a 15 V DC supply, to produce voltage output. The voltage signal is input into the data acquisition (DAQ) hardware at a sampling rate of 2 kHz for a duration of 20 seconds for each operating condition. The DAQ used in this study is a USB-DAQ (National Instruments, USB-6343, 16-Bit, maximum sampling rate - 500 kHz).

5.3 Results

In this study, by varying the mixing length of the combustor we vary the degree of premixedness. We note that premixedness can be linked to the homogeneity of the air-fuel mixture. The relation of homogeneity of the air-fuel mixture with the air-fuel mixing lengths is explored in this study using numerical simulations. We can quantify the homogeneity of the air-fuel mixture with a simple point summary metric based on the mixture fraction (ψ) of the air-fuel mixture. We note that mixture fraction is defined as the mass flow rate of fuel divided by the total mass flow rate of oxidizer and fuel. Mathematically,

$$\psi = \frac{\dot{m}_f}{\dot{m}_f + \dot{m}_{ox}}. \tag{5.2}$$

Here, $\dot{m}_f$ and $\dot{m}_{ox}$ indicates the mass flow rate of fuel (LPG) and mass flow rate of oxidizer (air) respectively. A parameter κ is defined as the ratio of standard deviation in mixture fraction to mean value of mixture fraction i.e., $\kappa = \sigma_\psi/\overline{\psi}$. κ may be taken as a very simple metric to indicate the heterogeneity in the air-fuel mixedness [128].

For brevity, we denote the annular combustor (AC) configuration corresponding to fuel injection through F1, F2, F3, and F4 ports as AC-F1, AC-F2, AC-F3, and AC-F4 cases respectively. On the other hand, the degree of premixedness is also varied in the linear array combustor while keeping the burner-to-burner distance fixed at 55 mm. Accordingly, we denote these cases as LAC-F1-55, LAC-F2-55, LAC-F3-55, and LAC-F4-55 when the fuel is injected through F1, F2, F3, and F4 ports respectively. Next, the burner-to-burner distance of the linear array combustor (LAC) is also varied. The linear array configurations having the highly premixedness (F1 case) and burner-to-burner distances of 65, 55, and 45 mm are referred to as LAC-F1-65, LAC-F1-55, and LAC-F1-45 cases respectively, for the remainder of this thesis.

In Fig. 5.3, a simplified 3D model of the annular combustor, used for the numerical simulation of the cold flow, is shown. An unstructured mesh is used to calculate the degree of homogeneity of the air-fuel mixture, for the AC-F1 case. The mesh size is taken as 5 mm. The meshing is carried out in Ansys Workbench. A realizable $k - \epsilon$ model is used as the turbulence model. We assume the flow to remain incompressible. The species transport model is used to simulate the mixing of air and fuel. A cold flow, steady state, RANS simulation is carried out to calculate κ at a plane positioned 15 mm upstream of the dump plane (i.e. just downstream of the swirlers), similar to an earlier literature [128]. The numerical simulation is carried out in Ansys Fluent 14.5. Looking at table 5.1, we infer that AC-F1 has the highest degree of premixedness among the cases considered. We further observe that the κ increases with a decrease in air-fuel mixing length (l), similar to as reported in an analogous single-burner combustor [128]. We note that for ease of numerical simulation, propane is considered as the fuel. However, the trend of κ should be similar if LPG is used as fuel. κ exhibit similar variations with change in the degree of premixedness for the LAC configuration and therefore is not shown here for brevity.

We observe that the variation in the degree of premixedness and burner-to-burner spacing changes the LBO limit slightly. The air and LPG flow rates for the highly premixed configurations (i.e. the F1 case), in the annular and linear

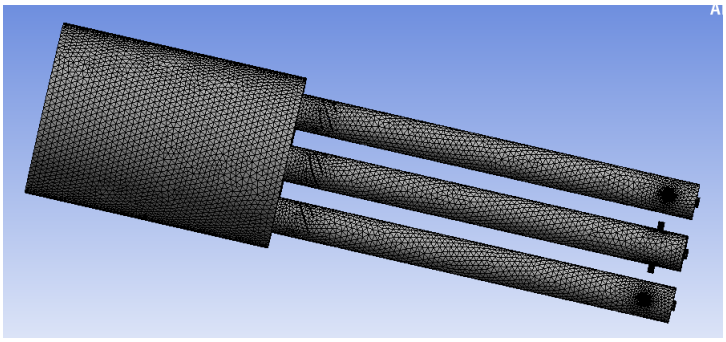

Figure 5.3: The simplified 3D model of the annular combustor used for calculating the degree of homogeneity of the air-fuel mixture, for the AC-F1 case.

	κ at $\phi = 0.95$	κ at $\phi = 0.6$
F1	0.056	0.058
F2	0.22	0.28
F3	0.44	0.49
F4	0.68	0.78

Table 5.1: Degree of premixedness (κ) for the annular combustor (AC) at the stable combustion state ($\phi = 0.95$) and the near-LBO state ($\phi = 0.6$). The air-fuel mixing lengths (l) for the F1, F2, F3, and F4 cases are 330 mm, 230 mm, 180 mm, and 130 mm respectively. For the numerical simulation, the fuel used is propane.

array combustors, are shown in table 5.2. For both the annular and linear array combustors, with the different configurations described above, the starting point of the experiments is kept fixed at $\phi = 0.95$ i.e. close to the stoichiometric condition. The LBO limits for different degrees of premixing, corresponding to the annular combustor, are found to remain the same ($\phi = 0.56$). For the linear array combustor, the starting point of the experiments is close to the stoichiometric condition ($\phi = 0.95$) while the LBO limits vary to some extent depending on the burner-to-burner distance or degree of premixing. For the linear array combustor, the LBO limits are $\phi = 0.63$, $\phi = 0.63$, and $\phi = 0.56$ for the LAC-F2-55, LAC-F3-55, and LAC-F4-55 cases respectively. Similarly, when we study the LBO phenomena with different burner-to-burner spacing, the starting points of the experiments are the same ($\phi = 0.95$). The LBO limits for the linear array combustor are $\phi = 0.60$, $\phi = 0.63$, and $\phi = 0.60$ with 45, 55, and 65 mm spacing between the burners respectively. We note that the fuel injection port is kept fixed at F1 when the effects of varying burner-to-burner spacing on the near-LBO dynamics are explored.

The measurement uncertainty corresponding to the flow rates can be calculated from the accuracy ratings of the rotameters. The uncertainty for air is ± 1.6 lpm for a flow rate of 80 lpm, and that for LPG is ± 0.1 lpm for a flow range of 2.7 – 1.6 lpm (table 5.2).

	AC-F1 case	LAC-F1-55 case
Flow rate of air (in lpm)	320	240
Flow rate of air per burner (in lpm)	80	80
Global equivalence ratio (ϕ)	0.95 - 0.56	0.95 – 0.63

Table 5.2: Operating range for the AC-F1 case (4 burners, 55 mm burner-to-burner distance) and LAC-F1-55 case (3 burners, 55 mm burner-to-burner distance). The air flow rate shown here are equally distributed to the burners of the combustors.

5.3.1 Flame visualization with annular combustor

5.3.1.1 Flame visualization in annular combustor with highly premixed configurations

We normalize the equivalence ratios (ϕ) of different operating points by dividing them by the equivalence ratio at LBO (ϕ_{LBO}). We note that the Nikon J5 camera (camera I) is positioned in a way to capture the frontal view, line of sight flame image. The following discussion is based on the flame images taken with camera I.

First, we focus on the flame behavior corresponding to the AC-F1 case i.e. where the mixing length is highest (l = 330 mm). For the AC-F1 case, at the stable combustion state ($\phi/\phi_{LBO} = 1.69$), flame oscillations exhibit significant high frequency pulsations but do not undergo any significant changes in flame intensity (Fig. 5.4a). At this point ($\phi/\phi_{LBO} = 1.69$), the flame remains attached to the dump plane at all instants during the experiment. With reduction in equivalence ratio ($\phi/\phi_{LBO} = 1.43$), flame intensity reduces markedly (Fig. 5.4b). However, flame elongation does not occur (or at least not visibly distinguishable). Close to the LBO limit, ($\phi/\phi_{LBO} = 1.062$), the individual flames from the four burners become elongated and lift off leading to a significant weakening of the flames (Fig. 5.4c). At this point, these individual flames exhibit significant oscillations. During such oscillations, the overall volume of the combustor occupied by the flame varies in a significant way. Next, we explore this phenomenon in detail.

Figures 5.5 - 5.6 show the oscillatory behavior of flame at the near-LBO state ($\phi/\phi_{LBO} = 1.062$) for the AC-F1 case. At time $t = 0$ sec, the flame occupies a small volume in the combustor and is very weak (as apparent from flame intensity). The situation at $t = 0$ sec may be considered a 'partial' extinction event in analogy to the extinction event in the single-burner combustor. We name this event as 'partial' extinction because, in this situation, flames corresponding to a few burners are in extinguished condition but the other burners are lighted. Therefore, even during the extinction event, the flame occupies a significant part of the combustor.

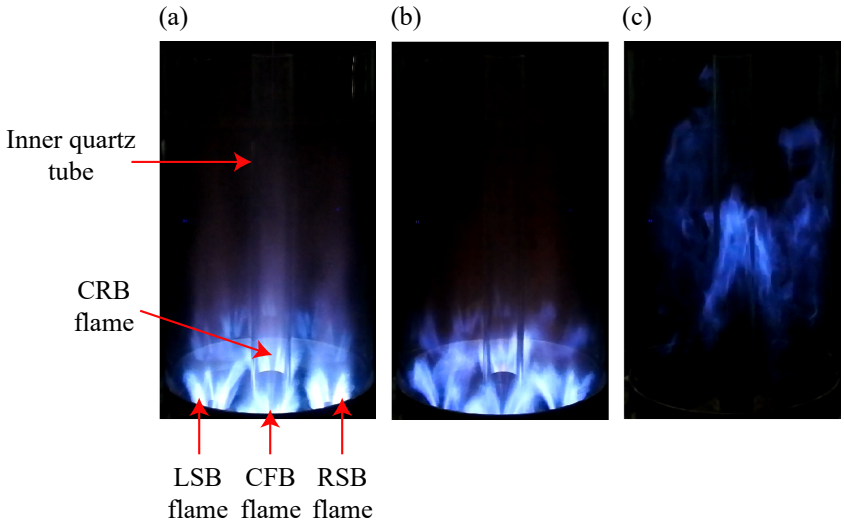

Figure 5.4: (a), (b) and (c) show the flame characteristics corresponding to the stable combustion state ($\phi/\phi_{LBO} = 1.69$), a intermediate state ($\phi/\phi_{LBO} = 1.43$) and the near-LBO state ($\phi/\phi_{LBO} = 1.062$) respectively for the AC-F1 case. LSB, RSB, CFB, and CRB are the left-hand side burner (as viewed on page), right-hand side burner, center-front burner, and center- rear burner, respectively.

This is in contrast to the extinction-reignition event that has been reported for an analogous single-burner combustor, where during the extinction event, the flame occupies negligible volume in the combustor [128].

This partial extinction event is followed by a significant expansion of the flame between $t = 0.144 - 1.392$ sec during which time the visible flame intensity also increases significantly (Figs. 5.5 - 5.6). Therefore, this event may be considered a 'partial' reignition event as the reignition occurs only in the extinguished burner(s). Here, we note that in the annular combustor configurations, it is difficult to understand the mechanism of reignition due to the overlapping of flames in different planes. Later in this chapter, the mechanism of reignition will be discussed with the LAC. After the reignition event, the flame again becomes weakened and progressively occupies a lesser volume. At $t = 2$ sec (Fig. 5.6), the flame again becomes partially extinguished. At this point, some part of the flame exists only as a weakened flame kernel (marked by a red circle in the image corresponding to $t = 2$ sec).

In contrast to the partial extinction-reignition events seen in this study, previous study with an analogous single-burner combustor has reported significantly prominent extinction-reignition events. In that case, only flame kernels occupying insignificant volume of the combustor, were seen to be present during the extinction events [128]. These flame kernels were seen to cause the subsequent reignition events in the single-burner combustor [128].

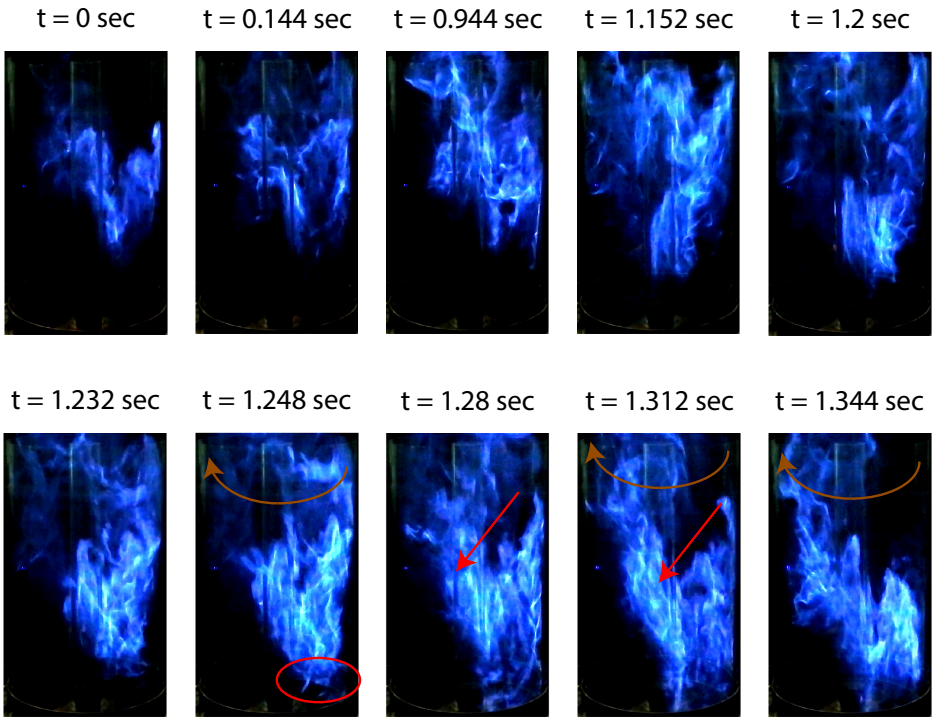

Figure 5.5: The extinction-reignition event and a flame rotation event, at the near-LBO state ($\phi/\phi_{LBO} = 1.062$), observed in the AC-F1 case.

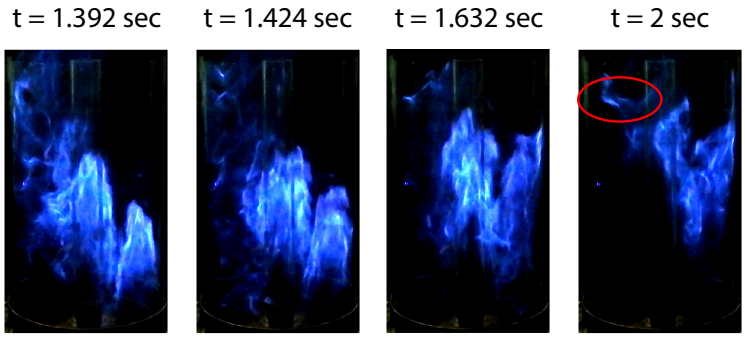

Figure 5.6: The extinction-reignition event and a flame rotation event, at the near-LBO state ($\phi/\phi_{LBO} = 1.062$), observed in the AC-F1 case (continued from above).

Apart from the extinction-reignition events, several other interesting flame dynamics are observed in the near-LBO state corresponding to the AC-F1 case. For example, the individual flames, that are in lifted and elongated condition at the near-LBO state, often merge (i.e individual flame fronts cannot be easily distinguished) and then split again. For example, at $t = 1.392$ sec (Fig. 5.6), flame fronts of the individual flames, corresponding to the different burners, can be separately identified. However, at the near-LBO state for the AC-F1 case, the

flames remain in merged condition for most of the experimental duration.

In the near-LBO regime, often the merged flame randomly reattaches to one of the burner tips. The reattachment lasts only for a fraction of a second. For example, in Fig. 5.5, the merged flame attaches to a burner at $t = 1.248$ sec (marked by a red circle). Subsequently, the flame detaches from the burner at $t = 1.632$ sec (Fig. 5.6). However, due to the overlapping of flames situated at different planes, the flame merging-unmerging behavior, the flame attachment-detachment phenomena etc. are difficult to visualize with the annular combustor. Therefore, these phenomena will be discussed in detail later in this chapter for the linear array configurations where they can be easily visualized.

During the partial-reignition events, distinct rotational movement of flames is observed which is described next. We note that the in frontal line-of-sight flame images corresponding to the annular combustor, two burners are positioned on the two side of the flame image (the right-hand side burner RSB and the left-hand side burner LSB). On the other hand, the center of the flame images corresponds to (often overlapped) flames corresponding to center-front burner (CFB) and center-rear burner (CRB). The behavior of the LSB and RSB flames are mostly focused in the following discussions as they are easy to study. In some cases, the behavior of the CFB and CRB flames are also described.

Between $t = 1.2 - 1.248$ sec (Fig. 5.5), an flame attachment event (marked by a red circle) occurs on the right-hand side burner (RSB, as viewed on page) of the combustor. During the same period, the flame corresponding to the left-hand side burner (LSB, as viewed on page) of the combustor exists only as a weakened kernel (marked by a red arrow). Next, between $t = 1.232 - 1.344$ sec, we observe a distinct rotational motion of the flame (direction of the rotation is shown by a brown arrow) from the RSB to LSB which reignites the accumulated unburnt mixture in the combustor space corresponding to LSB. During this rotational motion, the transfer of flame packets to the LSB, where a weak flame is present, is shown by red arrows. As the accumulated unburnt air-fuel mixture gets consumed, the LSB flame again gradually weakens (Fig. 5.6) and exists as a severely weakened flame kernel at $t = 2$ sec. In other words, another partial extinction event occurs in the combustor at $t = 2$ sec.

The flame rotation event and extinction-reignition events are difficult to visualize from the frontal view of the annular combustor. Further, the top view of the combustor is difficult to obtain as in that case the camera lens becomes exposed to high-temperature exhaust gas emanating from the combustor. Therefore, flame videos are captured using an additional camera (Nikon Coolpix P100, camera II), placed at an angle of 10° with the vertical. This viewing angle is chosen as it is convenient to explore the extinction-reignition events and flame rotation events

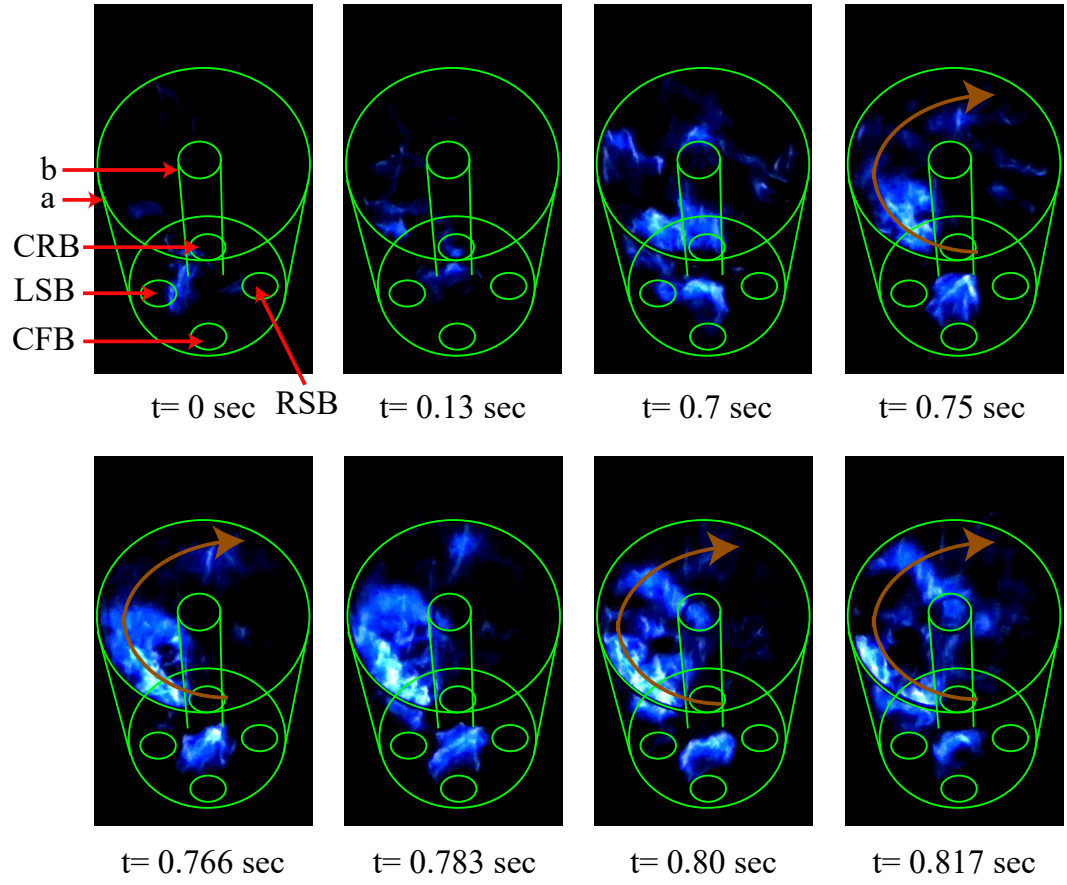

Figure 5.7: Extinction-reignition event at the near-LBO state ($\phi/\phi_{LBO} = 1.062$), as viewed at an angle of 10° with the vertical for the AC-F1 case. Here the reignition event ($t = 0.70 - 0.90$ sec) occurs as the surviving flame propagates in the combustor along the circumferential direction. The green outlines indicate (i) the outer quartz tube (a), (ii) the inner quartz tube (b), and (iii) the positions of the four burners (LSB, CFB, RSB, and CRB) in the dump plane, as viewed with the camera II.

while not exposing the camera lens to high-temperature exhaust gas. The snapshots with this view at the near-LBO state ($\phi/\phi_{LBO} = 1.062$) are shown in Figs. 5.7 - 5.8. Here, the green outlines indicate (i) the inner and outer quartz tubes which makes up the annular combustion chamber, and (ii) the position of the four burners in the dump plane, as viewed with the camera II. At this point, we note that the flame images with camera I and camera II are not synchronized i.e. the time stamps corresponding to the Figs. 5.5, 5.6, 5.7 and 5.8 are arbitrary. Further, the two cameras capture the flame images from opposite direction so that the LSB of the camera I (i.e. the camera capturing the frontal view of flames) is the RSB of the (camera II).

In Fig. 5.7, at $t = 0$ sec, we observe that the flame in the right-hand side burner

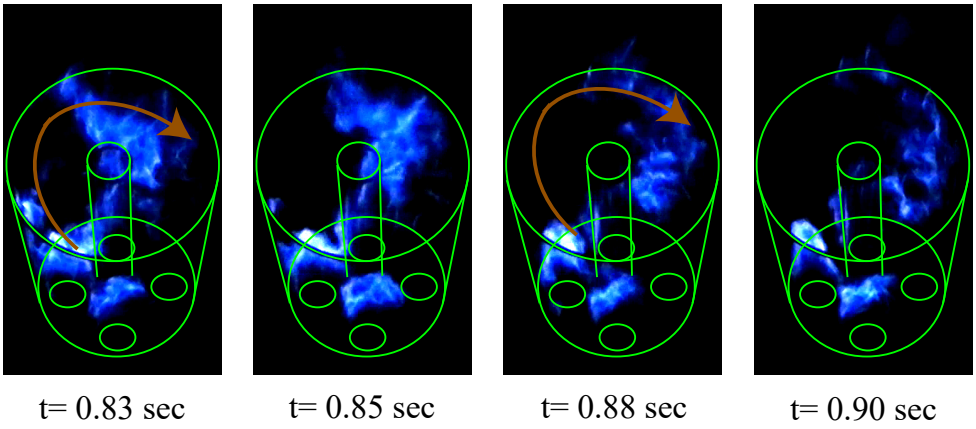

Figure 5.8: Extinction-reignition event at the near-LBO state ($\phi/\phi_{LBO} = 1.062$), as viewed at an angle of 10° with the vertical for the AC-F1 case. Here the reignition event ($t = 0.70 - 0.90$ sec) occurs as the surviving flame propagates in the combustor along the circumferential direction. The green outlines indicate (i) the outer quartz tube (a), (ii) the inner quartz tube (b), and (iii) the positions of the four burners (LSB, CFB, RSB, and CRB) in the dump plane, as viewed with the camera II (continued from above).

(RSB) of the combustor is severely weakened and exists as a small flame kernel. Further, the flame corresponding to the center-front burner is in extinguished condition. On the other hand, the flame in the left-hand side burner (LSB) of the combustor has a comparatively higher flame intensity. Overall, at this instant ($t = 0$ sec), the flames corresponding to the different burners occupy a small part of the combustor volume. Such a situation may be considered a 'partial' extinction event as discussed above.

Between, $t = 0.13-0.7$ sec, a reignition event occurs. Due to this, at $t = 0.7$ sec, the flame occupies a significantly larger volume and the flame intensity increases considerably. However, at this instant, the RSB flame (i.e. flame corresponding to the right-hand side burner of the combustor) has a very low intensity indicating a partial extinction event. It is likely that due to the severely weakened flame kernel at the right-hand side of the combustion chamber, unburnt air-fuel mixture is accumulated in that region. During $t = 0.75-0.90$ sec (Figs. 5.7 - 5.8), the flame front corresponding to the left-hand side burner is seen to traverse the combustor along the circumferential direction to reignite the accumulated unburnt air-fuel mixture in the right-hand side of the combustion chamber. In short, the extinction-reignition event occurs along with a rotational movement of the flame along the circumferential direction. A brighter flame is observed during the reignition event, as it consumes the unburned air-fuel mixture that is accumulated as a result of local flame extinction.

We note that even though camera I and camera II are not synchronized, the above discussed flame images, obtained with camera I and camera II, corresponds approximately to the same time instants. For example, the extinction-reignition events shown in the frontal view images (Figs. 5.5 - 5.6) show partial extinction in the combustor region corresponding to LSB. With the camera II view (Figs. 5.7 - 5.8), the RSB flame is seen to suffer partial extinction. We recall that LSB of frontal view image is RSB of the flame image obtained with camera II.

Next, we focus on the flame dynamics in the AC-F2 case (Fig. 5.9), corresponding to $l = 230$ mm. For the AC-F2 case also, high-frequency pulsations are seen in the flames at the stable combustion regime ($\phi/\phi_{LBO} = 1.69$, Fig. 5.9a). However, the intensity of the individual flames, corresponding to the different burners does not show any significant variation with time. The individual flames also remain steadily attached to their respective burners. As the equivalence ratio is reduced to approach LBO, a gradual weakening of the flame (as apparent from visible flame intensity) can be seen. At $\phi/\phi_{LBO} = 1.19$, the flames corresponding to two burners get elongated (Fig. 5.9b). On the other hand, the flames from the other two burners remain attached to their respective burners. This indicates the presence of some dissimilarity between the burners which are introduced despite our best efforts to evenly distribute the air and fuel flows to the different burners. The dissimilarity of the burners may be due to the minute differences in the manufactured burners, even though the burner design is the same. We note that such minute differences in the manufactured burners are quite likely in practical multi-burner combustors also. At the near-LBO state ($\phi/\phi_{LBO} = 1.0625$), all four individual flames elongate and lift up (Fig. 5.9c). At this state, the extinction-reignition phenomena similar to the AC-F1 case are seen which is omitted for brevity.

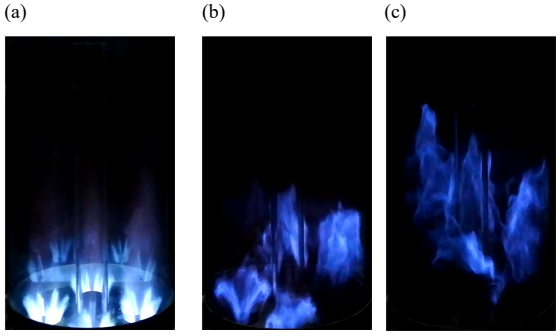

Figure 5.9: (a), (b) and (c) show the flame characteristics corresponding to the stable combustion state ($\phi/\phi_{LBO} = 1.69$), a intermediate state ($\phi/\phi_{LBO} = 1.19$) and the near-LBO state ($\phi/\phi_{LBO} = 1.0625$) respectively for the AC-F2 case.

5.3.1.2 Flame visualization in annular combustor with partially premixed configurations

Next, we describe the near-LBO flame behavior of the partially premixed annular configurations. For the AC-F3 case (l = 180 mm), at the stable combustion regime ($\phi/\phi_{LBO} = 1.69$), the individual flames (corresponding to the various burners) remain on the burner tip even though the flames exhibit high frequency fluctuations, similar to AC-F1 and AC-F2 cases (Fig. 5.10a). However, the flame intensity of the flames remains approximately constant at this state. As LBO is approached, the flames gradually weaken. At $\phi/\phi_{LBO} = 1.31$, the flame intensity and flame structure start to exhibit significant fluctuations (Fig. 5.10b). As equivalence ratio is reduced slightly ($\phi/\phi_{LBO} = 1.25$), the LSB flame (flame corresponding to left-hand side burner) elongates and lifts up (Fig. 5.10c). At $\phi/\phi_{LBO} = 1.19$, the flames corresponding to center-front burner (CFB) and LSB are in lifted condition (Fig. 5.10d). With further reduction of equivalence ratio ($\phi/\phi_{LBO} = 1.0625$), all four individual flames get elongated and lifts up (Fig. 5.10e). At this point, the flame intensity weakens considerably.

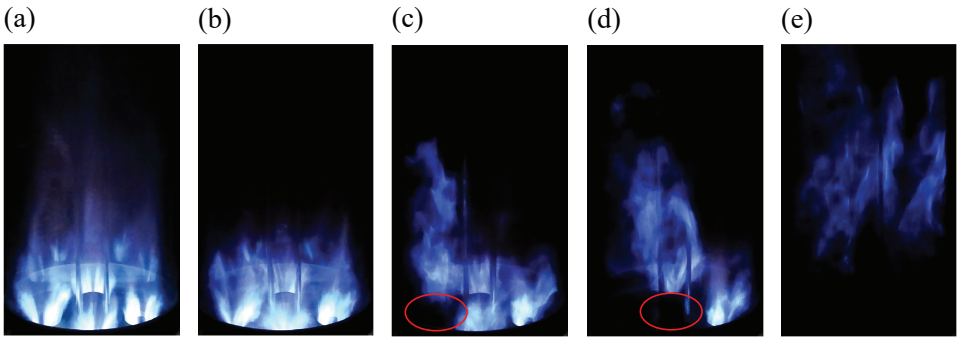

Figure 5.10: The flame characteristics at various equivalence ratios as LBO is approached for the AC-F3 case: (a) $\phi/\phi_{LBO} = 1.69$, (b) $\phi/\phi_{LBO} = 1.31$, (c)$\phi/\phi_{LBO} = 1.25$, (d) $\phi/\phi_{LBO} = 1.19$, and (e) $\phi/\phi_{LBO} = 1.0625$.

For the AC-F3 case, significant qualitative changes in the flame structure and flame intensity in the different flames are seen, even far away from LBO. These changes are described next in detail (Figs. 5.11 - 5.12). At $\phi/\phi_{LBO} = 1.31$, at $t = 0$ sec (Fig. 5.11a), the flame corresponding to the left-hand side burner (LSB) of the annular combustor is in lifted condition. At $t = 0.13$ sec, the visible flame intensity in the LSB flame reduces significantly (marked by a red circle). At $t = 0.18$ sec, the LSB flame intensity increases significantly as the flame reattaches to the LSB. At $t = 1.08$ sec, the LSB flame again lifts off and weakens. Further, at $t = 1.13$ sec, the LSB flame reattaches to the left-hand side burner and consequently, the visual flame intensity increases significantly. The lift-off (with a consequent reduction in

flame intensity) and reattachment (with a consequent increase in flame intensity) of the LSB flame repeat in cycles. During such attachment-detachment events in the LSB flame, the flames corresponding to the other burners remain attached to their corresponding burners. However, as equivalence is further reduced, the CFB flame (flame corresponding to the center-front burner) also starts to exhibit such detachment-reattachment behavior (not shown).

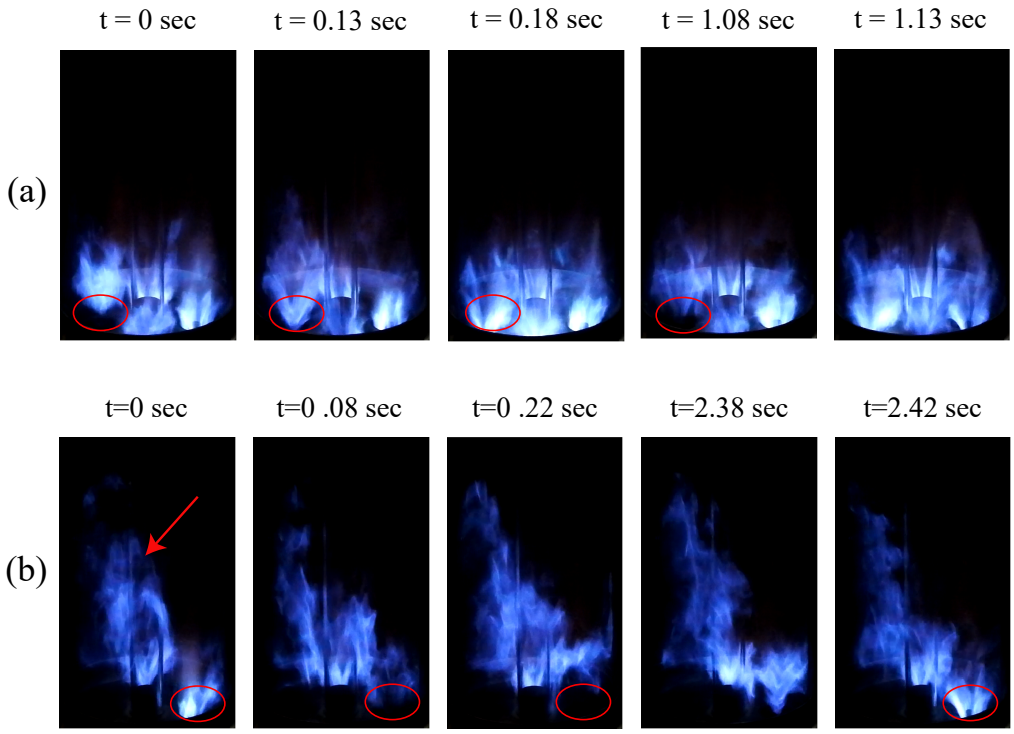

Figure 5.11: The flame dynamics at various equivalence ratios for the AC-F3 case at select ϕ/ϕ_{LBO}, at which significant qualitative changes in the flame dynamics occurs. (a) $\phi/\phi_{LBO} = 1.31$ and (b) $\phi/\phi_{LBO} = 1.19$.

At $\phi/\phi_{LBO} = 1.19$ (Fig. 5.11b), the RSB flame (flame corresponding to right-hand side burner) start to show recurrent detachment-reattachment behavior. During detachment, the RSB flame intensity reduces (for example, at $t = 0.08$ sec) while at reattachment, the RSB flame intensity increases (for example, at $t = 2.42$ sec) We note that at this point, both the LSB and CFB flames remain in lifted-off condition (marked by a red arrow in the image corresponding to $t = 0$ sec in Fig. 5.11b) and are anchored by the CRB flame (flame corresponding to the center- rear burner). On the other hand, the CRB flame is seen to be attached to the corresponding burner throughout the experimental duration.

At the near-LBO state ($\phi/\phi_{LBO} = 1.06$), all 4 flames in the annular combustor lifts up (Fig. 5.12). At this point, the individual flame contours become difficult to discern i.e. the individual flames remain merged throughout the experimental condition. The merged flame is seen to exhibit random attachment -detachment on various burners. For example, at $t = 0.12$ sec, the merged flame is in lifted condition while at $t = 0.136$ sec, it attaches to LSB burner and lifts off again at $t = 0.168$ sec.

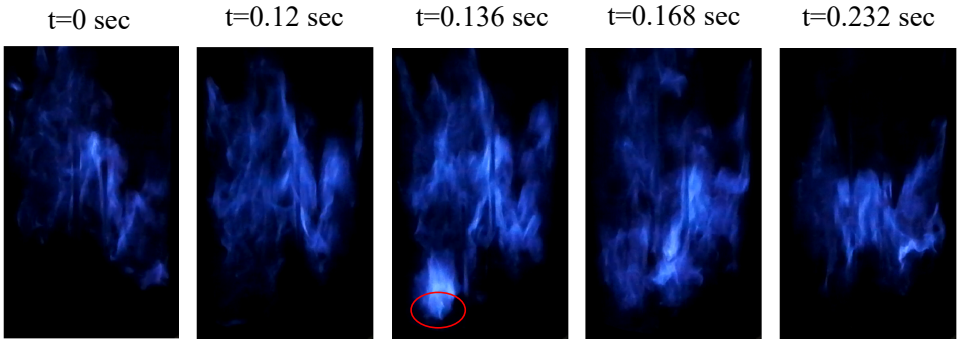

Figure 5.12: The flame dynamics at $\phi/\phi_{LBO} = 1.06$ for the AC-F3 case.

Next, we explore the flame characteristics during the transition to LBO for the AC-F4 case ($l = 130$ mm, Fig. 5.13) which is the least-premixed configuration studied in this chapter. In this case, at the stable combustion regime, the individual flames (corresponding to the different burners) exhibit high-frequency pulsations similar to F1 - F3 cases. At this point, the flames have high soot content as apparent from the yellowish color of the flames (Fig. 5.13a). Similar to AC-F1 - AC-F3 cases, the visual flame intensity of the flames reduces significantly with a reduction in equivalence ratio (Fig. 5.13b-d). With a reduction in ϕ, the sooty nature of the flames also disappears.

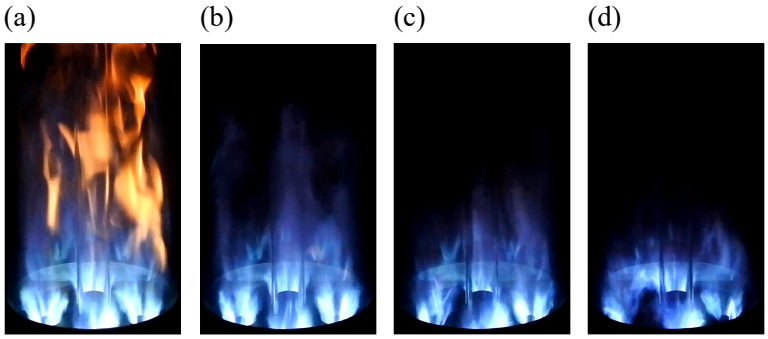

Figure 5.13: The flame characteristics at various equivalence ratios as LBO is approached for the AC-F4 case: (a) $\phi/\phi_{LBO} = 1.69$, (b) $\phi/\phi_{LBO} = 1.31$, (c) $\phi/\phi_{LBO} = 1.19$ and (d) $\phi/\phi_{LBO} = 1.06$.

The oscillating flame behavior at the near-LBO state ($\phi/\phi_{LBO} = 1.06$) is seen for the AC-F4 case also, which is discussed next (Fig. 5.14). Between $t = 0 - 0.16$ sec, we see a reduction in flame intensity in the LSB flame. At $t = 0.16$ sec, the LSB flame lifts off but still retains its compact nature. Next, at $t = 2.96$ sec, the lifted LSB flame is seen to have significantly elongated. Next, at $t = 3.2$ sec, the lifted LSB flame is seen to reattach to the corresponding burner. Just after this event, at $t = 3.44 - 4.48$ sec, we observe the flame intensity corresponding to the center-front burner (CFB) start to reduce. At $t = 4.48$ sec, the CFB flame lifts off and consequently undergoes a significant elongation. However, at $t = 5.36$ sec, the CFB flame (marked by a red arrow) is anchored by the RSB flame. At $t = 5.44$ sec, the CFB flame reattaches to the center-front burner. In short, for the AC-F4 case, one or more flames undergo(es) significant reduction and consequent increase in flame intensity. Such events may be considered partial extinction-reignition events, as the severely weakened flames cannot consume any significant amount of air-fuel mixture.

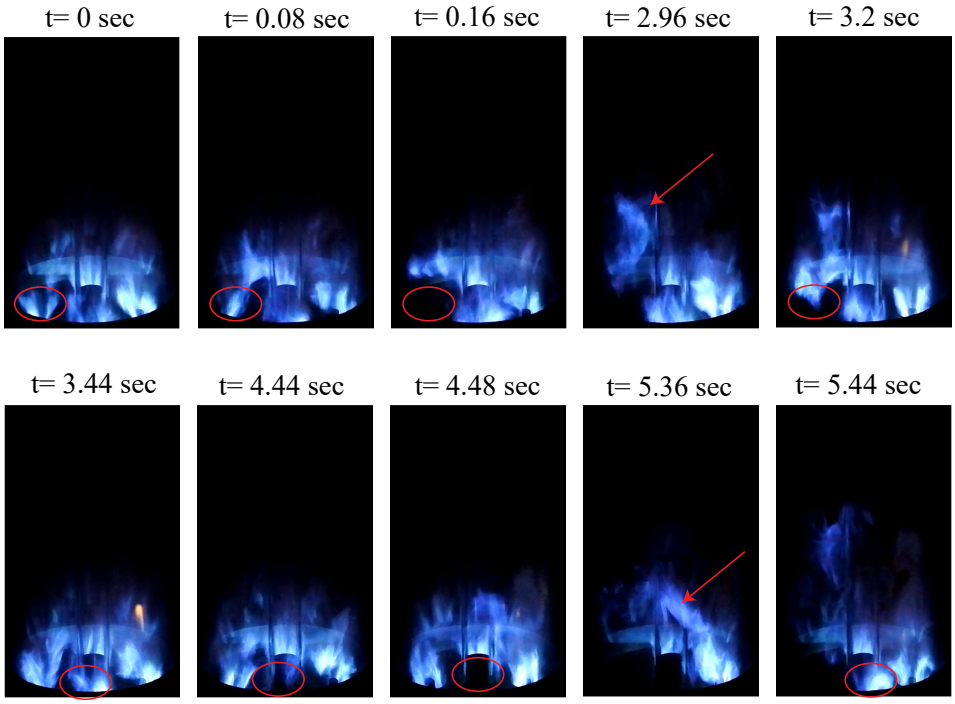

Figure 5.14: The extinction-reignition event observed in the AC-F4 configuration at the near-LBO state ($\phi/\phi_{LBO} = 1.06$).

From the above discussions, it is seen that the lift-off and reattachment events start to occur only just before the LBO limit, irrespective of the degree of premixing in the annular combustor. Moreover, the partial extinction-reignition events in which the flame corresponding to one or more burners gets extinguished occur close to the LBO limit for all degrees of premixing. The extinguished burners are

reignited by the flames from adjacent burners. Therefore, we infer that the flame dynamics at various degrees of premixing have significant similarities.

A significant difference in flame dynamics between highly premixed configurations (AC-F1, AC-F2) and partially premixed configurations (AC-F3, AC-F4) lies in the time scales corresponding to the lift-off and reattachment phenomena. For the AC-F1 - AC-F2 cases, at the near-LBO state, the flames remain in lifted-off condition for a major part of the experimental duration. In contrast, the reattachment events at the near-LBO state persist only for a fraction of a second. For the AC-F3 - AC-F4 cases, we observe that after a reattachment event, the flame remains attached to the burner for a significantly long time, often for $\sim 1-4$ seconds, before getting lifted off again. On the other hand, for the AC-F3 - AC-F4 cases, the lift-off condition of the flame also persists for a longer time (as compared to the AC-F1 - AC-F2 cases), often for $\sim 2-3$ seconds before reattaching to the corresponding burner. For the AC-F1 - AC-F3 cases, individual lifted and elongated flames often merge close to the LBO limit. However, this phenomenon is not seen in the AC-F4 case. Instead, for the AC-F4 case, the lifted flame gets anchored to one of the adjacent burners before getting reattached to the corresponding burner. In summary, there are some differences as well as similarities between how LBO occurs in the annular combustor for different degrees of premixing.

We observe that due to the presence of multiple flames, the extinction-reignition events are much less prominent for the annular configurations. This is because full extinction-reignition is prevented by burner-to-burner interaction occurring after partial extinction event. During the burner-to-burner interaction, often one of the adjacent flame reignites the extinguished burner. An example of such interaction is the flame propagation along the circumferential direction in Figs. 5.5 and 5.6. Further, flame-flame interaction, *e.g.*, anchoring of a lifted flame by an adjacent flame, prevents blow-out of the lifted flame (Fig. 5.14). We note that it is difficult to explore the near-LBO flame dynamics in more detail for the annular combustor. This is because, for the annular combustor, at least two burners at different planes get superimposed on one another in flame images. In the next section, the flame-flame interaction and burner-to-burner interaction are explored in more detail with the linear array combustor having the same burner-to-burner distance (55 mm) as the annular combustor.

5.3.2 Flame visualization with linear array combustor

A few recent studies have used linear array combustors (LAC) as a surrogate for annular combustors (AC) to investigate the LBO phenomenon. The LAC configuration is more amenable to flame characterization and data collection [177]

as the burners in the LAC configuration lie in the same plane. Furthermore, the lab-scale model gas turbine combustors are often fitted with quartz glasses as combustor chamber walls to facilitate optical diagnostics. The high curvature of the quartz glasses for the AC configurations creates significant reflection and refraction due to which optical diagnostics are difficult to implement. Moreover, the distance between the burners may be easily varied using a spacer arrangement in a LAC configuration. On the other hand, varying the distance between the burners in an AC configuration is only possible by turning on and off several burners in a symmetric manner [177]. However, this approach is only viable if the AC consists of a large number of burners. A large number of burners, however, would lead to a significantly complex and expensive test rig. Given these difficulties in optical diagnostics of the AC configurations, it is worthwhile to explore the flame characteristics of LAC, during the transition to LBO, at various degrees of premixing. This would help to understand whether the LBO phenomenon in AC and LAC configurations are similar i.e. whether LAC can be utilized as a proxy for the AC configuration for exploring the near-LBO flame dynamics. Towards this goal, next, we discuss the flame dynamics for the LAC with the same center-to-center distance (55 mm) between the burners as that of the AC.

5.3.2.1 Flame visualization in linear array configuration for different degrees of premixedness

Next, we discuss the flame characteristics at the stable, intermediate, and near-LBO states for the highly premixed linear array combustor (LAC-F1-55 case). At the stable combustion state ($\phi/\phi_{LBO} = 1.5$), the flame is seen to be highly compact with a low flame height and high flame intensity (Fig. 5.15a), similar to the AC-F1 case. At this point, the flames corresponding to the different burners also show high-frequency pulsations. With a reduction in equivalence ratio ($\phi/\phi_{LBO} = 1.28$), the flame intensity reduces and height increases i.e. the flame loses its compact nature (Fig. 5.15b). However, the flames are still attached to respective burners at this state. At the near-LBO state ($\phi/\phi_{LBO} = 1.05$), all three flames detach from respective burners and lift off (Fig. 5.15c). At this point, the flame exhibit various interesting dynamical features which are discussed in the following paragraphs. At this point, it is important to note that in the following discussions on the different LAC configurations, we denote the three flames corresponding to the different burners as the left-hand side burner flame (LSB flame), central burner flame (CB flame), and right-hand side burner flame (RSB flame), similar to the AC cases discussed above.

For linear array combustor with 55 mm burner-to-burner distance and a high

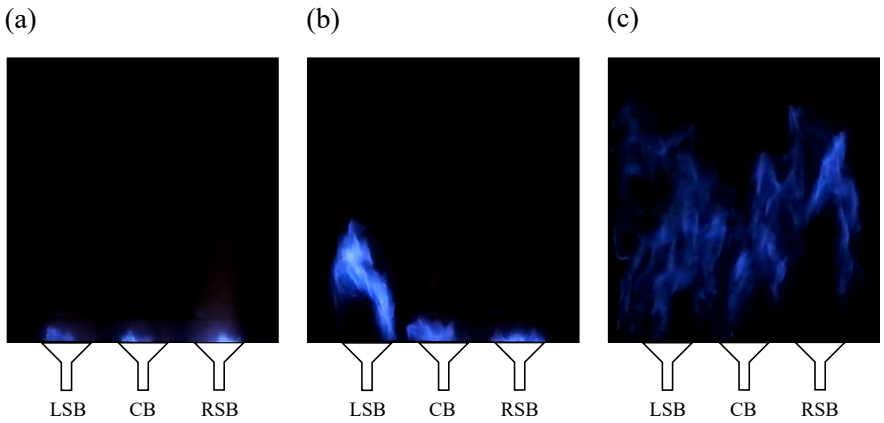

Figure 5.15: (a), (b), and (c) respectively show the stable combustion state, a intermediate state and the near-LBO state, for the LAC-F1-55 case.

premixedness (LAC-F1-55 case), partial extinction-reignition events in the near-LBO state ($\phi/\phi_{LBO} = 1.05$) are seen similar to the AC configurations (Figs. 5.16 - 5.19). For the LAC-F1-55 case, the attachment - detachment of flames (to and from their respective burners) occur simultaneously with the extinction-reignition events, similar to the AC-F1 case, as described next. At $t = 0$ sec (Fig. 5.16), the right-hand side flame (RSB flame) is lifted while the center burner flame (CB flame) and left-hand side burner flame (LSB flame) are attached to the respective burners (shown by red circles at the image corresponding to $t = 0$ sec). However, at $t = 0.512$ sec, the LSB flame detaches from the dump plane, weakens significantly, and is blown off at $t = 0.656$ sec. At $t = 0.656 - 0.688$ sec, we observe a transfer of flame packets from the CB flame to the LSB flame (indicated by a red circle).

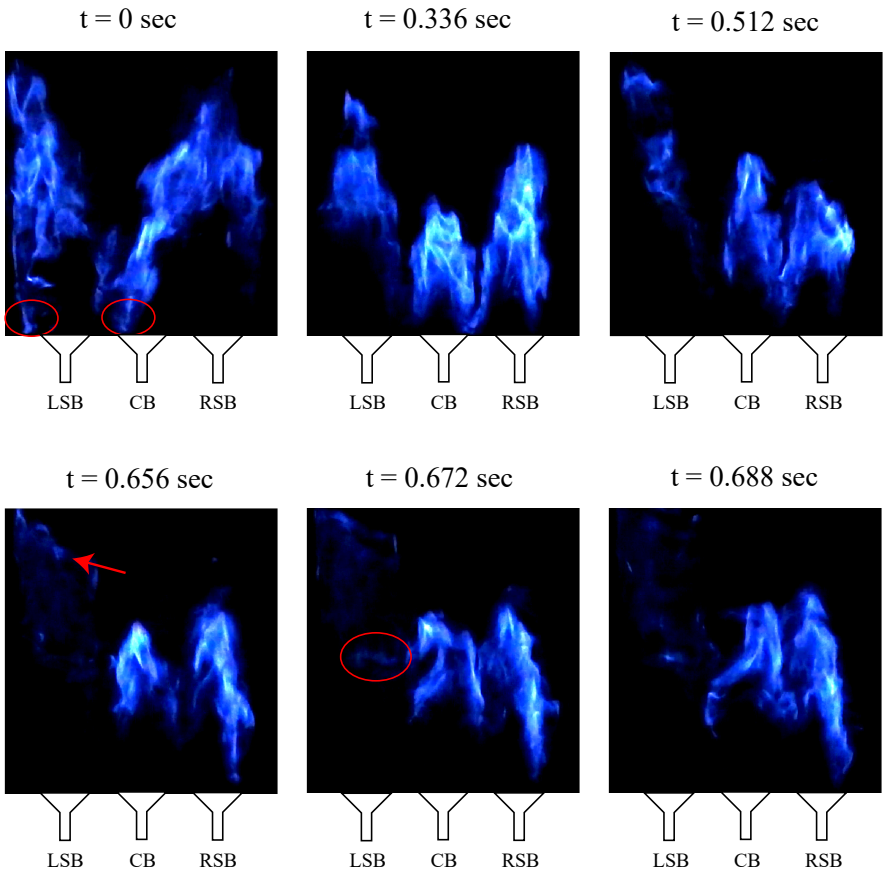

Figure 5.16: The extinction-reignition events and attachment-detachment events at the near-LBO state ($\phi/\phi_{LBO} = 1.05$) for the LAC-F1-55 case.

As a result, during $t = 0.704 - 0.912$ sec, the transferred flame packets (marked by a red arrow at $t = 0.912$ sec) causes a reignition in the left-hand side burner (LSB) (Figs. 5.17 and 5.18). Next, the LSB flame attaches to the central burner (CB) at $t = 1.04$ sec. At this point, the CB flame is also attached to the CB while the RSB flame is in a lifted-off state.

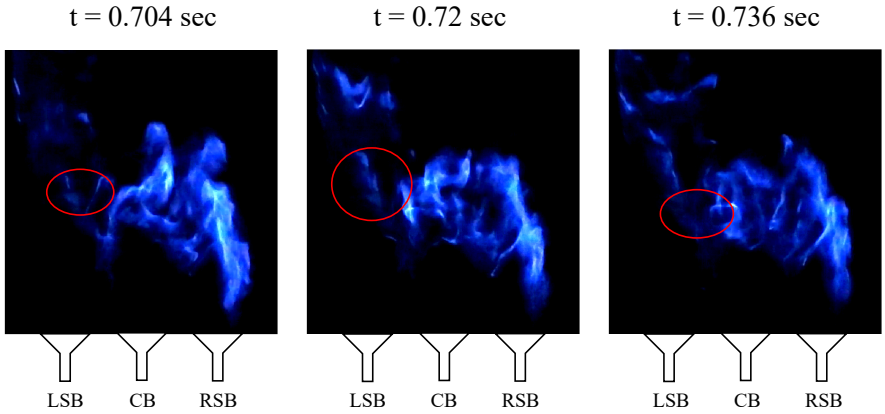

Figure 5.17: The extinction-reignition events and attachment-detachment events at the near-LBO state ($\phi/\phi_{LBO} = 1.05$) for the LAC-F1-55 case (continued from above).

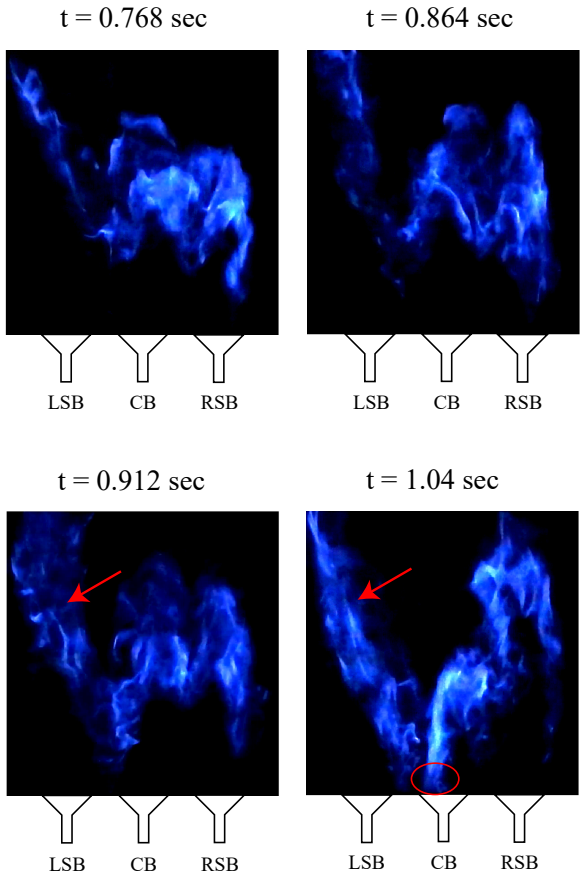

Figure 5.18: The extinction-reignition events and attachment-detachment events at the near-LBO state ($\phi/\phi_{LBO} = 1.05$) for the LAC-F1-55 case (continued from above).

The LSB flame attaches to LSB at $t = 1.376$ sec but detaches again at $t = 1.44$ sec (Fig. 5.19. At the near-LBO state, the flame merging (for example, at $t = 0.768$ sec) and flame unmerging (splitting) events also are seen. For example, at $t = 1.216$ sec, separate flame fronts of the three flames are visible indicating that a flame unmerging event has occurred. In short, the above results show that flame-to-flame and burner-to-burner interactions occur at the near-LBO state.

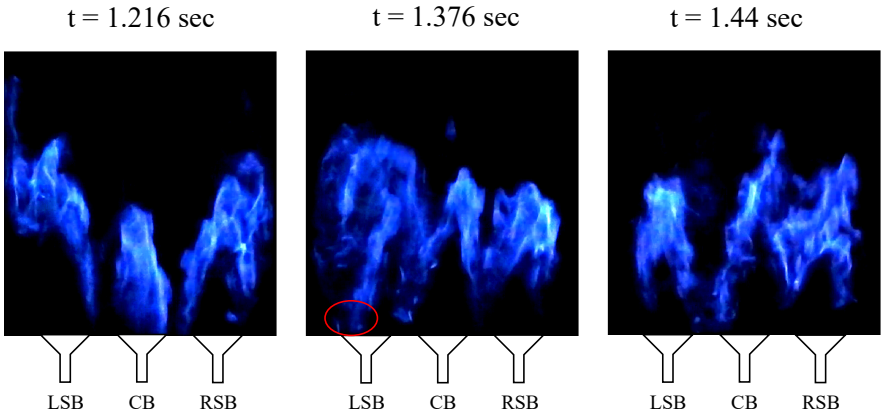

Figure 5.19: The extinction-reignition events and attachment-detachment events at the near-LBO state ($\phi/\phi_{LBO} = 1.05$) for the LAC-F1-55 case (continued from above).

As the side burners of the linear array combustor are confined on one side, the rotational motion of the flame during the reignition event, seen for the annular combustor, cannot be captured. However, the reignition events in the LAC configuration consist of a transfer of flame packets from adjacent burners to reignite the extinguished burner, similar to the AC configurations. Such a movement of flame during reignition is analogous to the rotational movement of flame seen during extinction-reignition in the AC configurations.

The stable flame characteristics for the LAC-F2-55 to LAC-F4-55 cases are very similar to AC-F2 to AC-F4 cases, respectively, and hence are omitted for brevity. Further, the LAC-F1-55 case and LAC-F2-55 case have very similar extinction-reignition behavior. Therefore next, we describe the flame behavior at the near-LBO state for the LAC-F3-55 case (Figs. 5.20 - 5.24). At the near-LBO state ($\phi/\phi_{LBO} = 1.055$), it is often seen that flames from the different burners often suffer a gradual reduction in flame intensity and consequently either extinguish or, become significantly weakened. For example, during $t = 0.08 - 0.144$ sec, the flame corresponding to the central burner gradually weaken and then is extinguished at $t = 0.144$ sec (Fig. 5.20). This partial extinction event causes the unburnt air-fuel mixture to accumulate around the central region of the combustion chamber.

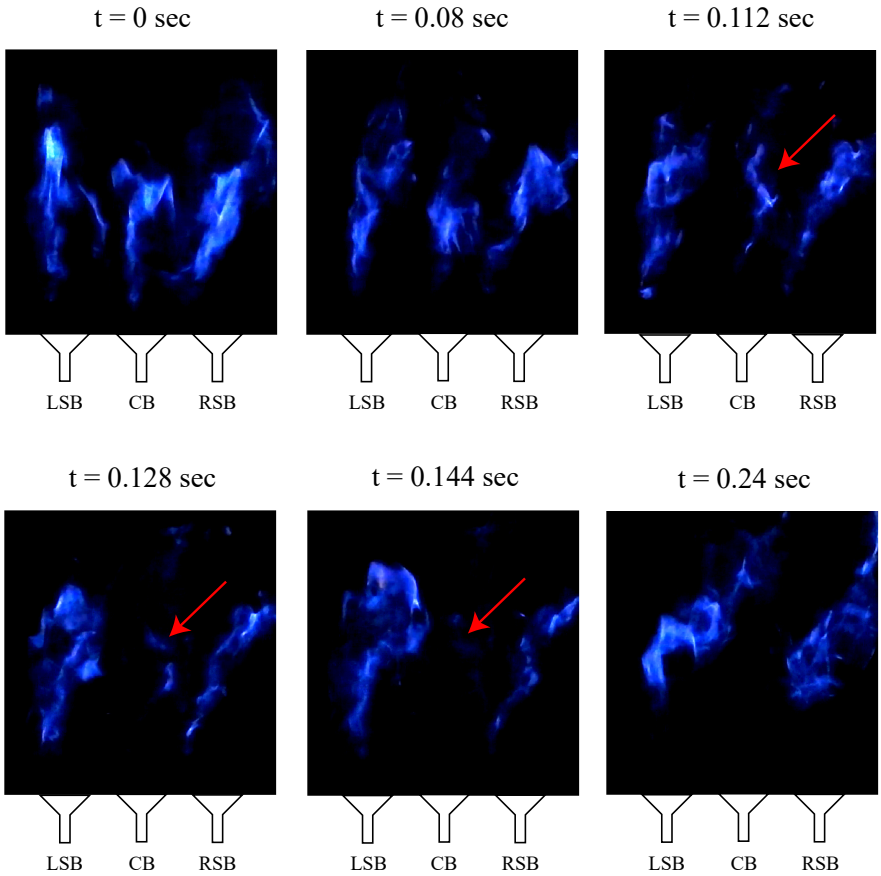

Figure 5.20: The extinction-reignition events and attachment-detachment events exhibited by the flame near the LBO limit ($\phi/\phi_{LBO} = 1.05$) for the LAC-F3-55 case.

Between $t = 0.4 - 0.656$ sec, the LSB and RSB flames expand significantly towards the center of the combustor and finally merge at $t = 0.656$ sec (Fig. 5.21).

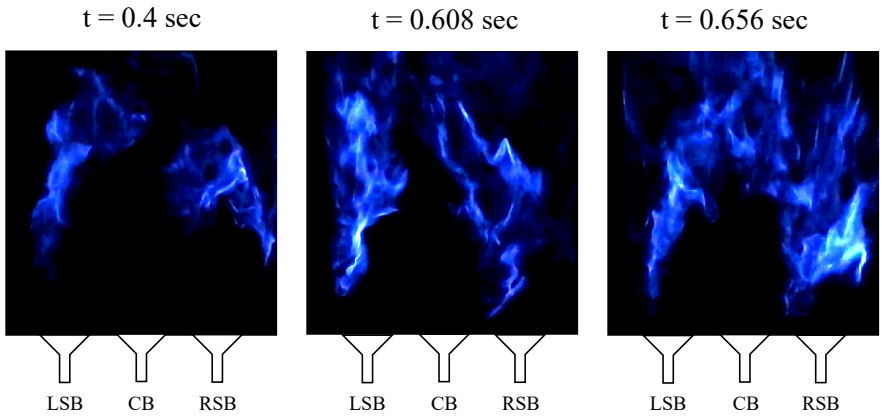

Figure 5.21: The extinction-reignition events and attachment-detachment events exhibited by the flame near the LBO limit ($\phi/\phi_{LBO} = 1.05$) for the LAC-F3-55 case (continued from above).

At $t = 0.752$ sec, the merged flame starts to again separate into three flames (Fig. 5.22). The middle part of the merged flame at $t = 0.752$ sec (marked by a red arrow) becomes the central flame after the flame splitting. At $t = 0.784$ sec, the flame contours of the three flames, corresponding to the three burners, can be identified separately i.e. the flame has split. At $t = 0.832$ sec, the central flame (marked by a red arrow) attaches to the central burner. At $t = 0.88$ sec, due to the attachment event the CB flame gains considerable strength (marked by a red arrow in image corresponding to $t = 0.88$ sec), as seen from visible flame intensity. This attachment in turn leads to attachment of the LSB flame to its corresponding burner at $t = 0.912$ sec. Further, the attachment of the CB flame at $t = 0.88$ sec leads to attachment of the RSB flame at $t = 0.928$ sec. Therefore, at $t = 0.928$ sec, all three flames are attached to their corresponding burners.

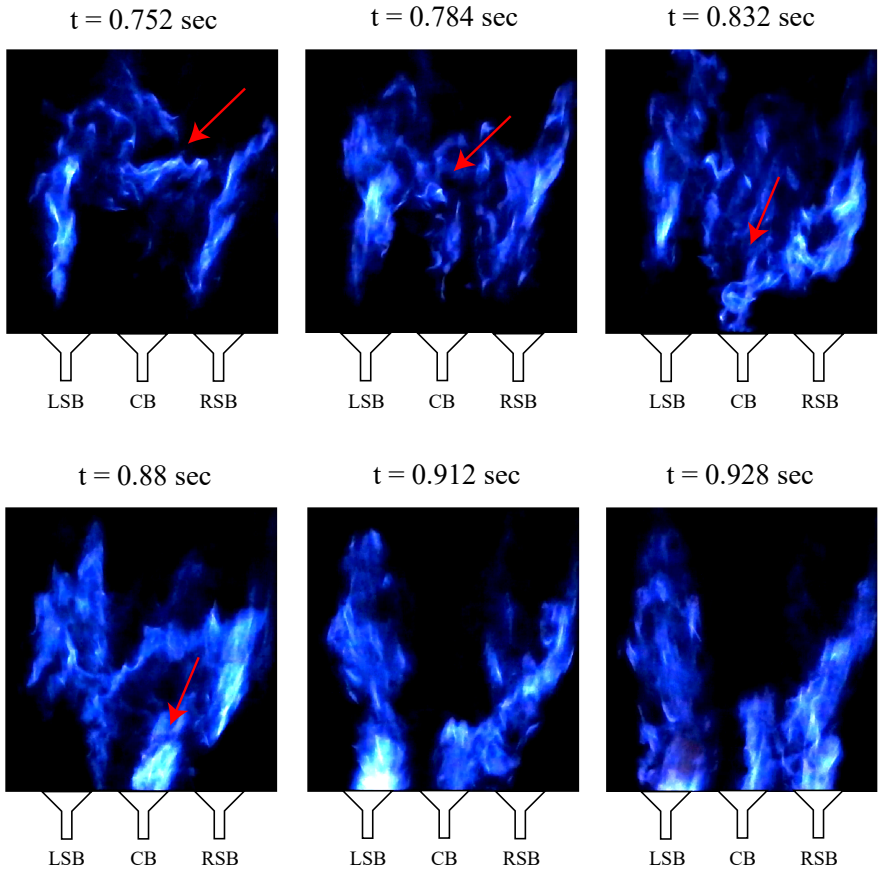

Figure 5.22: The extinction-reignition events and attachment-detachment events exhibited by the flame near the LBO limit ($\phi/\phi_{LBO} = 1.05$) for the LAC-F3-55 case (continued from above).

Similar to the central burner flame, the side burners often suffer partial extinction. We discuss one such situation below. At $t = 3.168$ sec, all three flames are in lifted situation (Fig. 5.23). However, at $t = 3.216$ sec, the flame corresponding to the central burner is extinguished. Between $t = 3.216 - 3.456$ sec, the flame corresponding to the right-hand side burner weakens considerably and is about to blow out at $t = 3.456$ sec (shown by a red arrow in the image corresponding to $t = 3.456$ sec). We observe that at the near-LBO state, if one flame gets extinguished, often the flame corresponding to the adjacent burner suffers extinction or, becomes significantly weakened. Next, at $t = 3.456$ sec, flame packets are transferred from the LSB flame to the central region of the combustion chamber (marked by a red circle in the image corresponding to $t = 3.456$). At $t = 3.472$ sec, these flame kernels expand significantly and at $t = 3.488$ sec, this expanded flame attaches to the central burner. At this instant, the RSB flame is in lifted condition (marked by a red arrow in the image corresponding to $t = 3.488$ sec).

However, at $t = 3.584$ sec, the RSB flame is anchored by the (newly formed) CB flame and is prevented from blowing out.

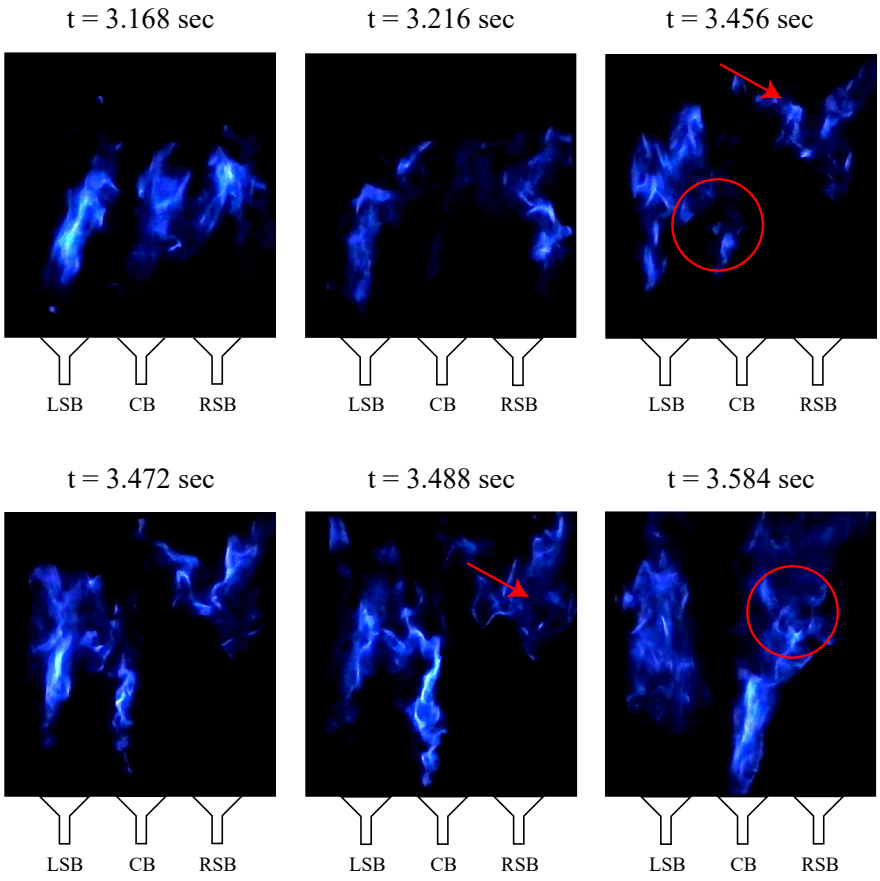

Figure 5.23: The extinction-reignition events and attachment-detachment events exhibited by the flame near the LBO limit ($\phi/\phi_{LBO} = 1.05$) for the LAC-F3-55 case (continued from above).

This situation persists till $t = 4.08$ sec (Fig. 5.24). At $t = 4.112$ sec, the CB flame is seen to expand significantly to cover the right-hand side region of the combustion chamber (the direction of flame expansion is shown by the brown arrows in images corresponding to $t = 4.112 - 4.144$ sec). At $t = 4.176$ sec, part of this expanded flame starts to move down and attaches to the RSB burner at $t = 4.368$ sec (marked by a red circle in the image corresponding to $t = 4.368$ sec). In short, for the F3 case, (i) extinction of a burner is often prevented by interaction of the adjacent burners (by anchoring the flame about to blowout), (ii) the reignition of the extinguished burner is often assisted by the flame corresponding to the adjacent burner, (iii) the extinction of a burner may trigger extinction/weakening of the adjacent flame and (iv) reignition of an extinguished burner may trigger reignition of the adjacent burner.

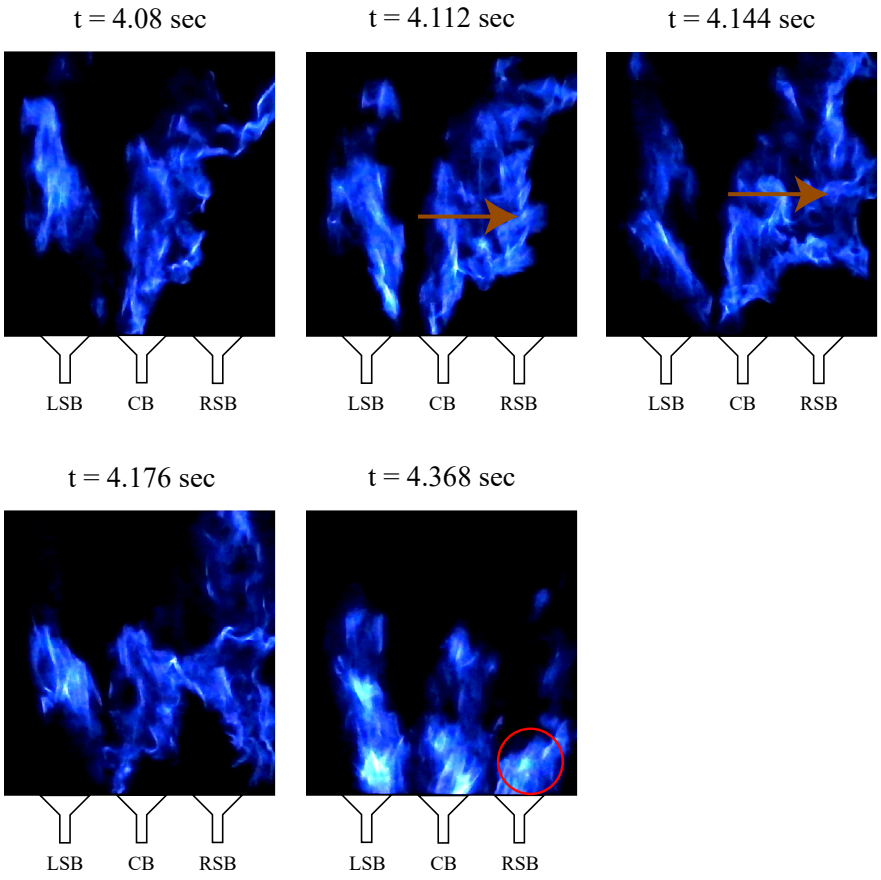

Figure 5.24: The extinction-reignition events and attachment-detachment events exhibited by the flame near the LBO limit ($\phi/\phi_{LBO} = 1.05$) for the LAC-F3-55 case (continued from above).

Next, we discuss the flame characteristics at the near-LBO state ($\phi/\phi_{LBO} = 1.06$) for the LAC-F4-55 case (Figs. 5.25 - 5.29). At $t = 0$ sec, the RSB flame is in extinguished condition (Fig. 5.25). At $t = 0.16 - 0.208$ sec, the CB flame gets elongated and transfers flame packets (indicated by a red arrow in the image corresponding to $t = 0.208$ sec) to the right-hand side of the combustion chamber. As a result, at $t = 0.224$ sec, a flame appears in the right-hand side zone of the combustion chamber. It attaches to the RSB burner at $t = 0.24$ sec. At $t = 0.288$ sec, this flame is fully attached to the RSB burner and has a significantly high flame intensity.

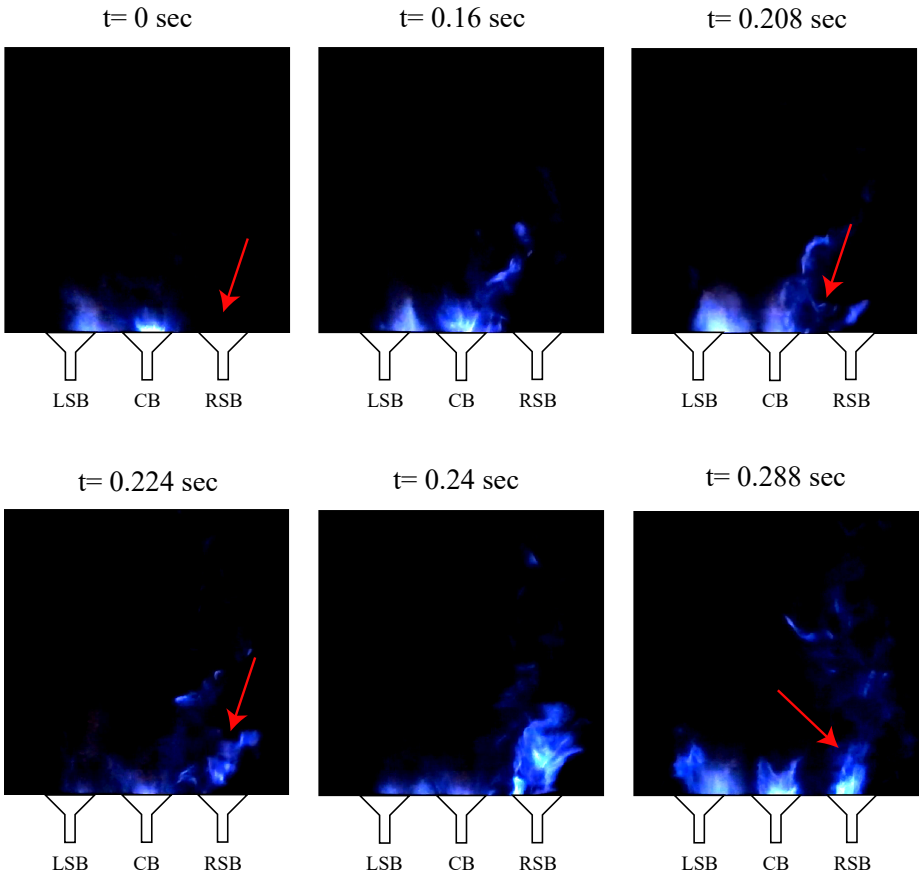

Figure 5.25: The extinction-reignition events and attachment-detachment events exhibited by the flame near the LBO limit ($\phi/\phi_{LBO} = 1.06$) for the LAC for the F4 case. The distance between the burners is equal to 55 mm (LAC-F4-55 case).

However, at $t = 0.88 - 0.928$ sec, the RSB flame again starts to weaken gradually (Fig. 5.26). At $t = 0.944$ sec, the RSB flame is seen to lift up. The RSB flame remains in lifted condition during $t = 0.944 - 1.072$ sec and continues to weaken gradually (Figs. 5.26 - 5.27). At $t = 1.232$ sec, RSB flame exists as a severely weakened flame kernel that is difficult to visually distinguish (marked by a red circle). This scenario may be considered a partial extinction as this severely

weakened flame kernel cannot consume any significant amount of air-fuel mixture.

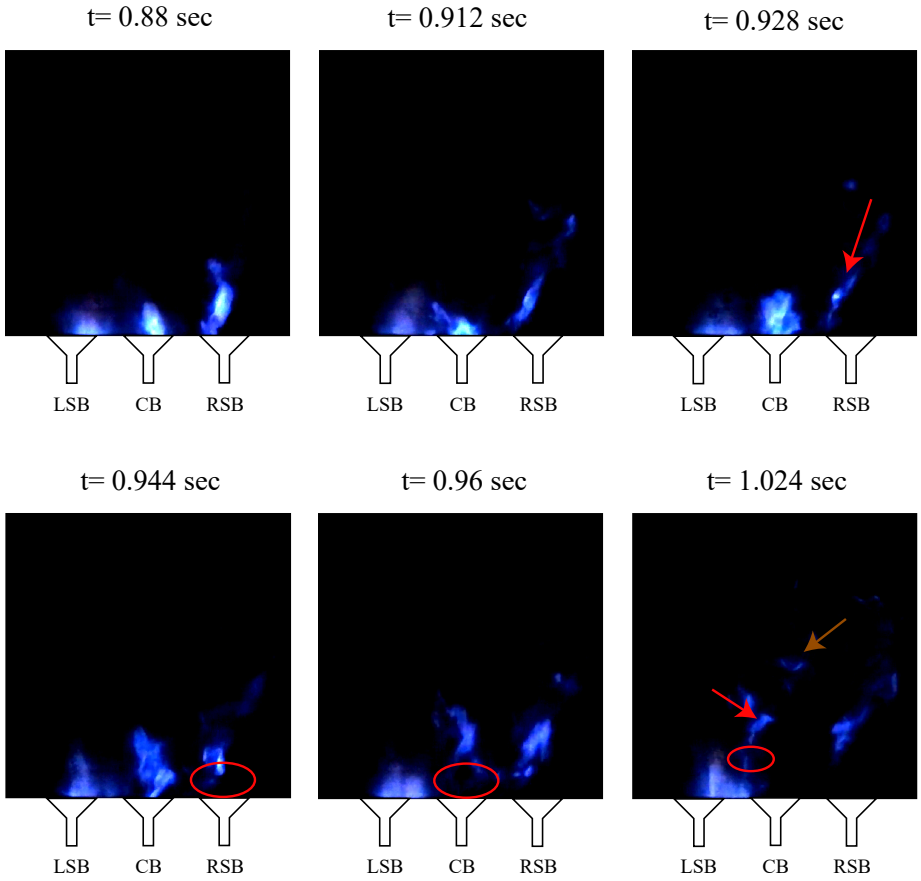

Figure 5.26: The extinction-reignition events and attachment-detachment events exhibited by the flame near the LBO limit ($\phi/\phi_{LBO} = 1.06$) for the LAC for the F4 case. The distance between the burners is equal to 55 mm (LAC-F4-55 case, continued from above).

Next, we describe the behavior of the CB flame during this time. As the RSB flame lifts up at $t = 0.944$ sec (Fig. 5.26), the adjacent CB flame also weakens significantly and lifts up at $t = 0.96$ sec. However, at $t = 1.024$ sec, the LSB flame is seen to anchor a part of the CB flame (the anchoring is marked by a red circle while the anchored CB flame is marked by a red arrow at the image corresponding to $t = 1.024$ sec) due to which the CB flame does not get extinguished. Another part of the CB flame, that is not anchored by the LSB flame, blows out (marked by a brown arrow at the image corresponding to $t = 1.024$ sec). Next, at $t = 1.056$ sec (Fig. 5.27), the CB flame is seen to expand significantly while remaining anchored by the LSB flame. Therefore, it is likely that during $t = 1.024 - 1.056$ sec, burnt high-temperature particles and radicals are supplied from the LSB flame to the CB flame which help to reignite and sustain the CB flame. At $t = 1.344$ sec, the CB flame is seen to reattach to its corresponding burner (marked by a red arrow

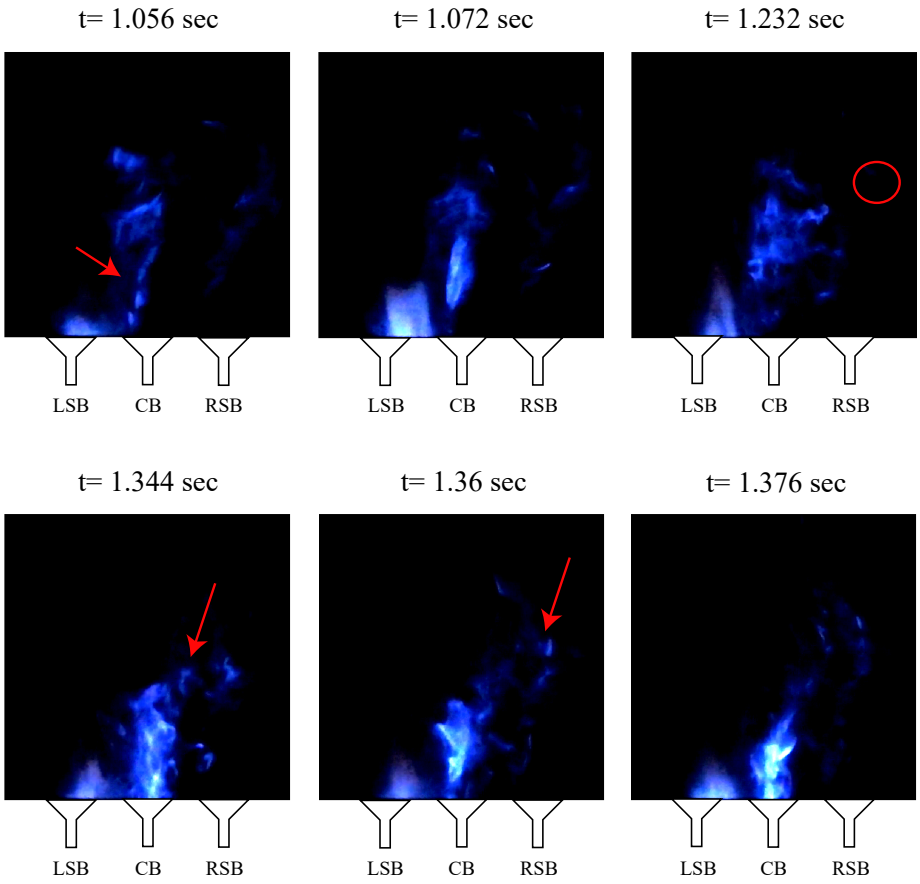

Figure 5.27: The extinction-reignition events and attachment-detachment events exhibited by the flame near the LBO limit ($\phi/\phi_{LBO} = 1.06$) for the LAC for the F4 case. The distance between the burners is equal to 55 mm (LAC-F4-55 case, continued from above).

in the image corresponding to $t = 1.344$ sec). Further, at this instant careful investigation reveals that the CB flame starts to transfer flame packets to the right-hand side region of the combustion chamber at a significant rate (marked by a red arrow in image corresponding to $t = 1.344$ sec). These flame packets can be seen to gradually expand during $t = 1.36 - 1.376$ sec (indicated by a red arrow in the image corresponding to $t = 1.36$ sec) although their visible intensity remains very low (as compared to a typical flame attached to a burner).

At $t = 1.616$ sec, a significant part of the low-intensity flame, located previously in the right-hand side region of the combustion chamber, gets extinguished (Fig. 5.28). However, during $t = 1.616 - 1.632$ sec, few flame kernels are seen to persist in the right-hand side part of the combustion chamber (marked by a red circle in the image corresponding to $t = 1.632$ sec). At $t = 1.648$ sec, these flame kernels reestablish the RSB flame which is seen in lifted condition at this instant. While the RSB flame exists as a severely weakened kernel during $t = 1.616 - 1.632$ sec,

the CB flame from the adjacent burner also starts to weaken gradually during $t = 1.632 - 1.648$ sec and its visible flame intensity reduces significantly.

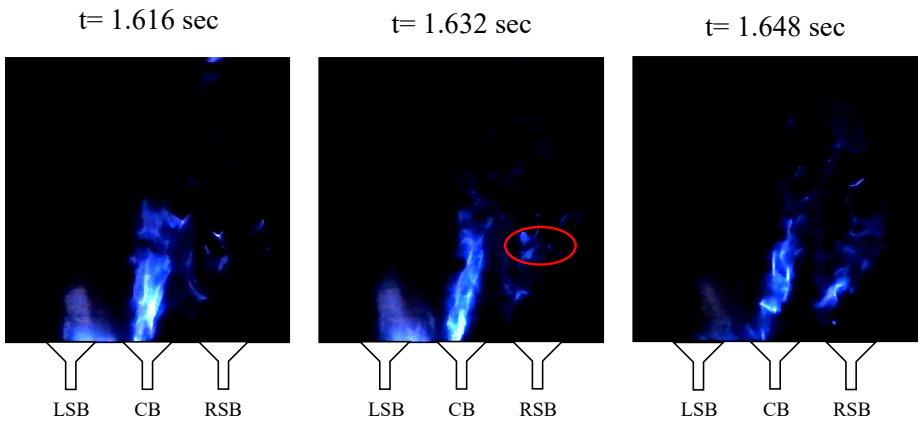

Figure 5.28: The extinction-reignition events and attachment-detachment events exhibited by the flame near the LBO limit ($\phi/\phi_{LBO} = 1.06$) for the LAC for the F4 case. The distance between the burners is equal to 55 mm (LAC-F4-55 case, continued from above).

At $t = 1.68$ sec, the CB flame lifts off from the corresponding burner (Fig. 5.29). At this same instant ($t = 1.68$ sec), however, the RSB flame reattaches to its corresponding burner (marked by a red arrow in the image corresponding to $t = 1.68$ sec). Due to this, the heat loss from the RSB flame reduces, resulting in a significant strengthening of the RSB flame at $t = 1.68$ sec. Moreover, the CB flame and RSB flame is seen to interact with each other at this instant through the transfer of flame packets (marked by a red circle in the image corresponding to $t = 1.68$ sec). Due to this interaction, the strength of the CB flame, as indicated by visual flame intensity, increases significantly at $t = 1.728$ sec. Further, the CB flame reattaches to its corresponding burner (marked by a red circle in the image corresponding to $t = 1.728$ sec). On the other hand, due to the adverse situation in the combustor, the RSB flame again weakens significantly at this instant ($t = 1.728$ sec). At $t = 1.744 - 1.76$ sec, the CB and RSB flames visibly interact with each other. As a result of this interaction, the weakened RSB flame regains its strength during $t = 1.76 - 1.904$ sec and reattaches to the corresponding burner at $t = 1.904$ sec.

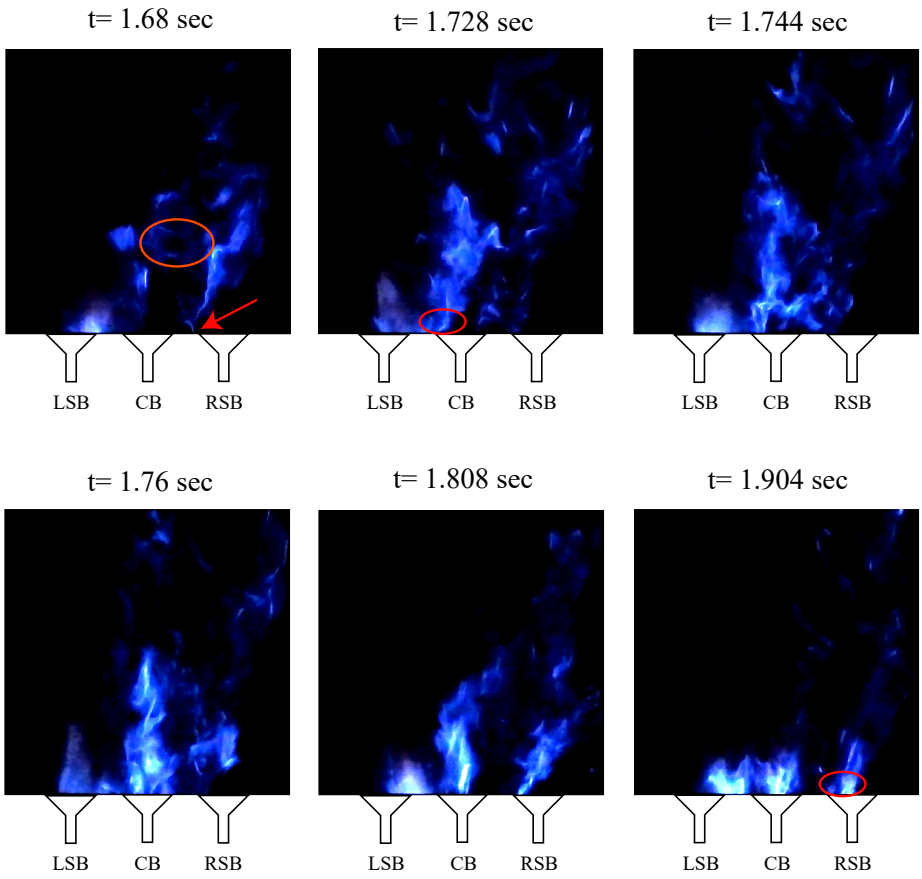

Figure 5.29: The extinction-reignition events and attachment-detachment events exhibited by the flame near the LBO limit ($\phi/\phi_{LBO} = 1.06$) for the LAC for the F4 case. The distance between the burners is equal to 55 mm (LAC-F4-55 case, continued from above).

Based on the above discussions, we infer that for various degrees of premixing the near-LBO flame dynamics corresponding to the annular combustor (AC) and linear array combustor (LAC) have significant similarities when the spacing between the burners in the AC and LAC are kept same (i.e. 55 mm). Random attachment-detachment of individual flames to corresponding burners, flame merging-unmerging, and partial extinction-reignition events (confined to one or more burners but not all) are seen for both AC and LAC configurations. From the flame videos of both AC and LAC, it is seen that the adjacent burners ignite the accumulated unburnt air-fuel mixture to reestablish the flame in the extinguished burner. In short, the flame-to-flame interactions and burner-to-burner interactions in both AC and LAC configurations significantly affect the flame dynamics at the near-LBO state and reduce the severity of the extinction-reignition events, as compared to an analogous single-burner combustor, reported in a previous study [128].

5.3.2.2 Effect of variation of burner-to-burner spacing on near-LBO flame dynamics in the linear array combustor

The flame behavior at the stable combustion state for the LAC-F1-65 case is closely similar to LAC-F1-55 case and therefore, is not repeated here. Next, we explore the near-LBO flame characteristics at various distances between the burners of the LAC. For the LAC-F1-65 case, (i) attachment-detachment phenomena and (ii) extinction-reignition phenomena in the individual flames, corresponding to the three burners, at the near-LBO state ($\phi/\phi_{LBO} = 1.06$), are prominent flame characteristics. Attachment-detachment phenomena are discussed next (Figs. 5.30 - 5.32). At $t = 0$ sec, the three flames, corresponding to the three burners, are in lifted condition (Fig. 5.30). We note that for the LAC-F1-65 case, the individual flames do not merge i.e. the flame contours of the three flames can be clearly distinguished throughout the experimental duration. This is in contrast to the near-LBO flame characteristics for the LAC-F1-55 case where flame merging and unmerging of the three flame fronts are often seen, possibly due to the lower distance between the burners.

Between $t = 0.064-0.096$ sec, the RSB flame expands significantly and attaches to its corresponding burner. At $t = 0.144$ sec, the strength of the RSB flame increases significantly, as indicated by visual flame intensity. Again considering, $t = 0.096 - 0.176$ sec, we see the CB flame is anchored by the RSB flame. After the RSB flame attaches to its corresponding burner, the CB flame also attaches to the central burner (CB) at $t = 0.176$ sec (the attachment event is shown by a red circle in the image corresponding to $t = 0.176$ sec).

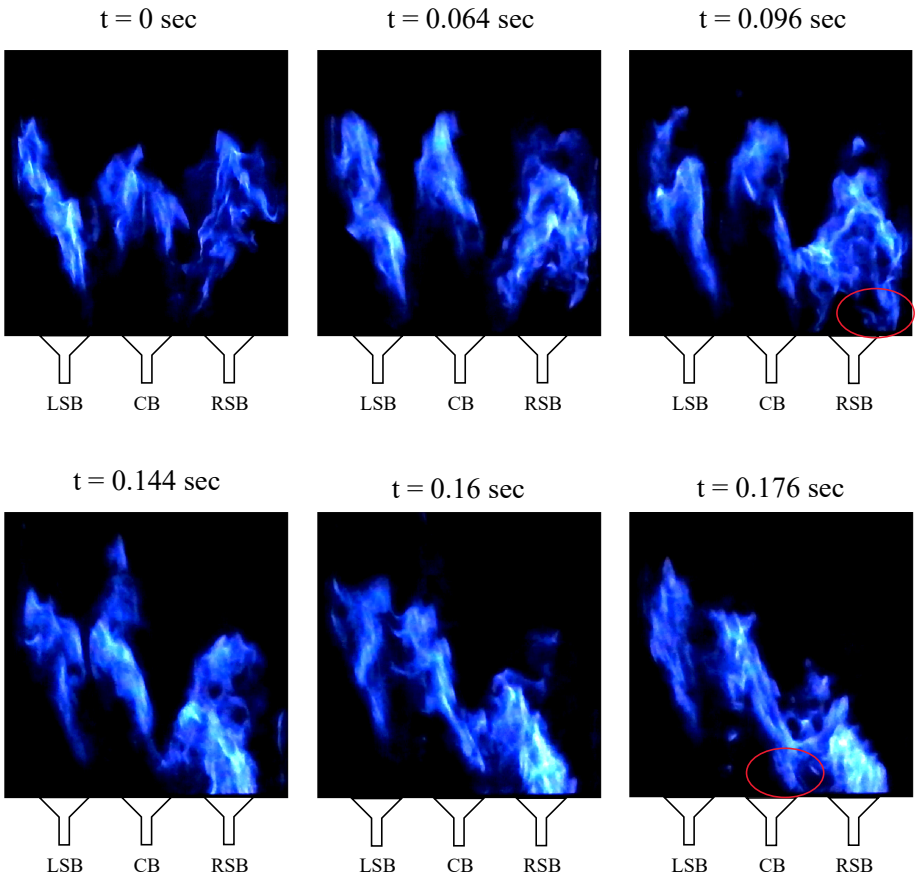

Figure 5.30: The attachment-detachment events close to the LBO limit ($\phi/\phi_{LBO} = 1.06$), as exhibited by individual flames corresponding the different burners in the LAC. The distance between the burners is equal to 65 mm. Fuel injection is done through port 1 (LAC-F1-65 case).

However, between $t = 0.208 - 0.288$ sec, both the CB and RSB flames are seen to lift-off so that at $t = 0.288$ sec, these two flames are barely attached to the dump plane (Fig. 5.31). After a fraction of second ($t = 0.352 - 0.464$ sec), all three flames are seen to be in lifted condition (Fig. 5.32). At $t = 0.496$ sec, the LSB flame is seen to attach to its corresponding burner due to which the flame intensity of the LSB flame increases significantly at subsequent instants ($t = 0.528$ sec). At this instant ($t = 0.528$ sec), the LSB flame, having gained significant strength, also interacts visibly with the CB flame. As a result of this interaction, the CB flame reattaches to the CB burner (not shown), and the attachment-detachment cycle repeats. In short, the flame attachment in the side burners often causes reattachment of the CB flame via flame-flame interactions.

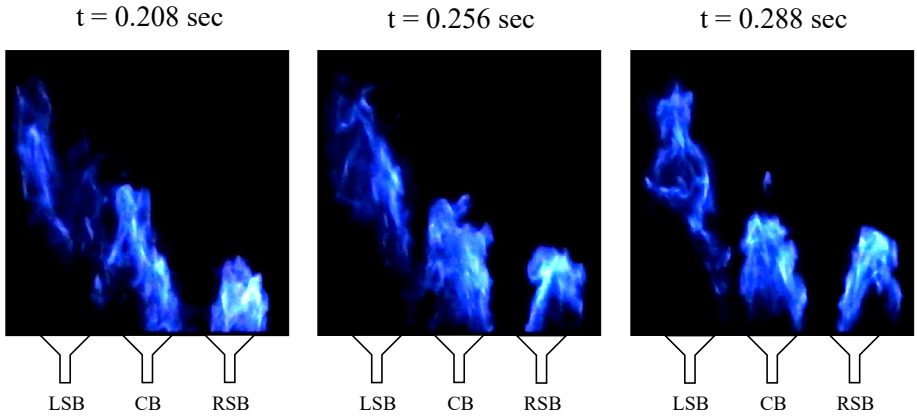

Figure 5.31: The attachment-detachment events close to the LBO limit (ϕ/ϕ_{LBO} = 1.06), as exhibited by individual flames corresponding the different burners in the LAC. The distance between the burners is equal to 65 mm. Fuel injection is done through port 1 (LAC-F1-65 case) (continued from above).

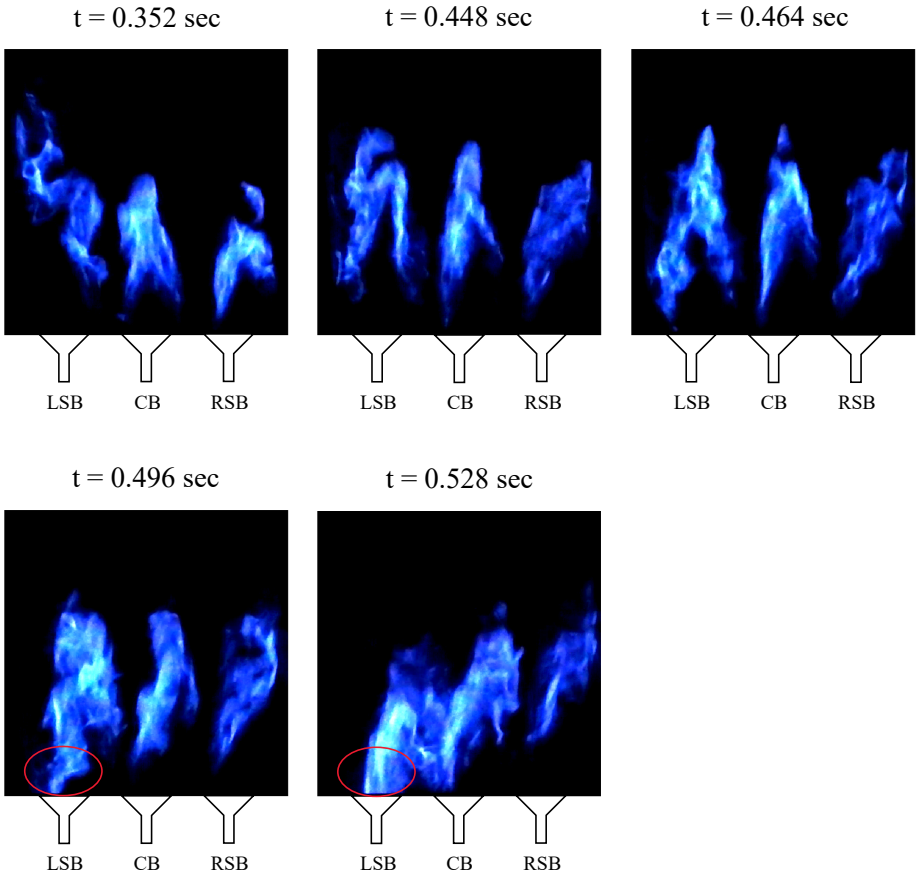

Figure 5.32: The attachment-detachment events close to the LBO limit (ϕ/ϕ_{LBO} = 1.06), as exhibited by individual flames corresponding the different burners in the LAC. The distance between the burners is equal to 65 mm. Fuel injection is done through port 1 (LAC-F1-65 case) (continued from above).

Next, we discuss the extinction-reignition behavior of the flame for the LAC-F1-65 case (Figs. 5.33 and 5.34). At $t = 0$ sec, we observe the LSB flame has significantly high strength (as indicated by visual flame intensity) and is attached to its corresponding burner. During $t = 0 - 0.16$ sec, the CB flame remains in lifted condition whereas the RSB flame gradually weakens. At $t = 0.176$ sec, the RSB flame becomes very low so it is difficult to visualize (the weakened flame is marked by a red circle in the image corresponding to $t = 0.176$ sec).

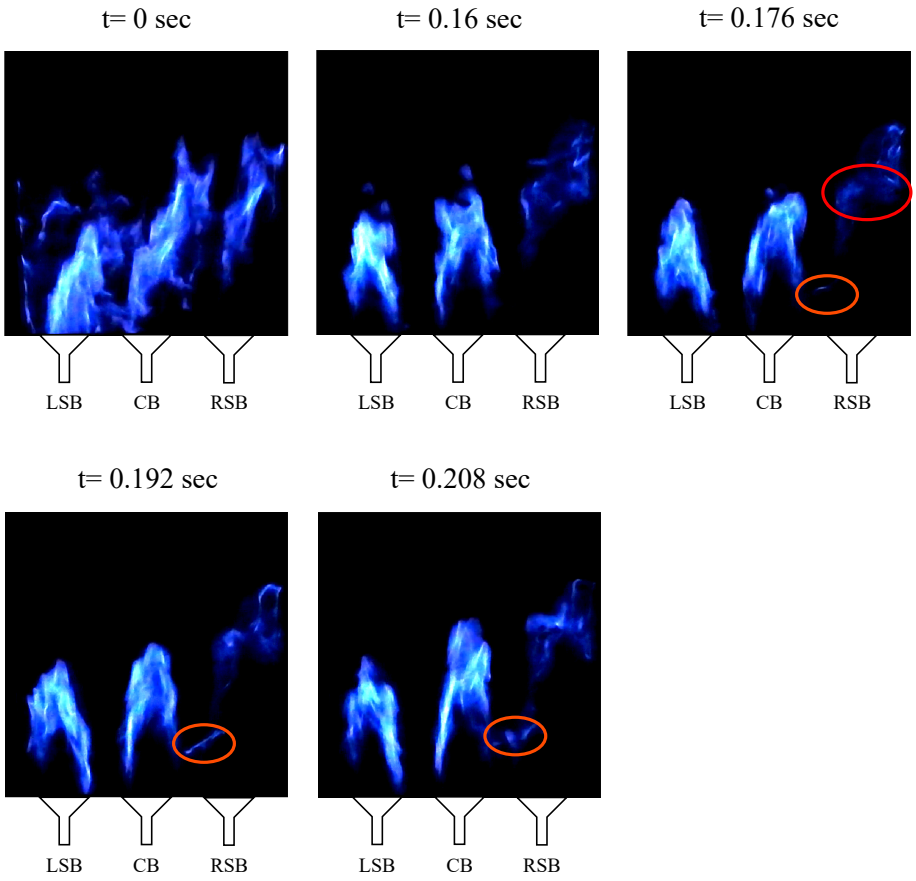

Figure 5.33: The extinction-reignition events close to the LBO limit for the LAC. The distance between the burners is equal to 65 mm (LAC-F1-65 case).

At this instant, we may consider the flame to have effectively blown out as the RSB flame is situated at a significant height over the dump plane. This weakened RSB flame is unlikely to be able to consume any significant fraction of the incoming air-fuel mixture. Thus this situation is practically equivalent to a partial extinction event. In this scenario, the unburnt air-fuel mixture is likely to accumulate in the right-hand side region of the combustion chamber. On the other hand, at the same instant ($t = 0.176$ sec), a flame kernel appears near the root of the CB flame which then moves towards the RSB flame, as seen from the flame image corresponding to $t = 0.192$ sec (the flame kernel is marked by a brown

circle on the images corresponding to $t = 0.176 - 0.24$ sec).

This flame kernel then expands during $t = 0.208 - 0.24$ sec in the right-hand side region of the combustion chamber, where accumulated unburnt air-fuel mixture is present (Figs. 5.33, 5.34). The flame kernel positioned thus is likely to supply a significant part of the burnt particles and radicals to the blown-off RSB flame. This helps the RSB flame to significantly regain its strength during $t = 0.272 - 0.304$ sec. In general, we observe that often the RSB and LSB flames become significantly weak for the LAC-F1-65 case. These situations may be considered analogous to the extinction-reignition events in a single-burner combustor. In short, severe extinction-reignition events, as seen in the analogous single combustor [128], are not observed in the LAC-F1-65 case.

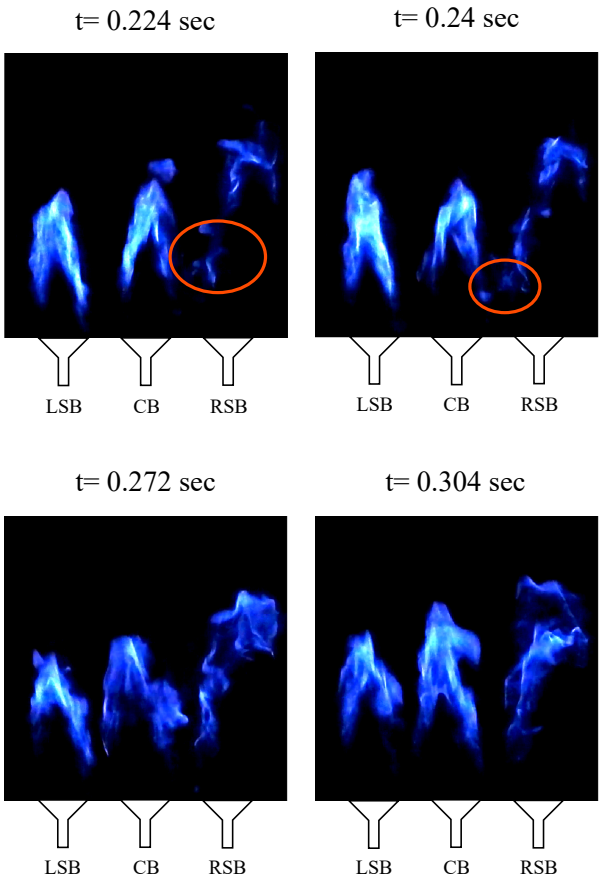

Figure 5.34: The extinction-reignition events close to the LBO limit for the LAC. The distance between the burners is equal to 65 mm (LAC-F1-65 case, continued from above).

Similar to the different AC and LAC configurations, the flames remain steady on the dump plane at the stable combustion state for the LAC-F1-45 case ($\phi/\phi_{LBO} = 1.06$,Fig. 5.35a). As equivalence ratio is reduced ($\phi/\phi_{LBO} = 1.18$), the flames corresponding to the three burners lift off (Fig. 5.35b). At the near-LBO state ($\phi/\phi_{LBO} = 1.06$), the three flames merge so that individual flame fronts cannot be discerned. For the LAC-F1-45 case, partial extinction-reignition events are absent at the near-LBO regime (Fig. 5.35c), unlike the LAC-F1-55 case or, LAC-F1-65 cases. This might be due to the significantly increased flame-flame interaction (in the form of merged flame at the near-LBO state) caused by a low burner-to-burner distance. However, the merged and lifted flame is seen to attach and detach randomly on individual burners (not shown), similar to previous configurations explored above.

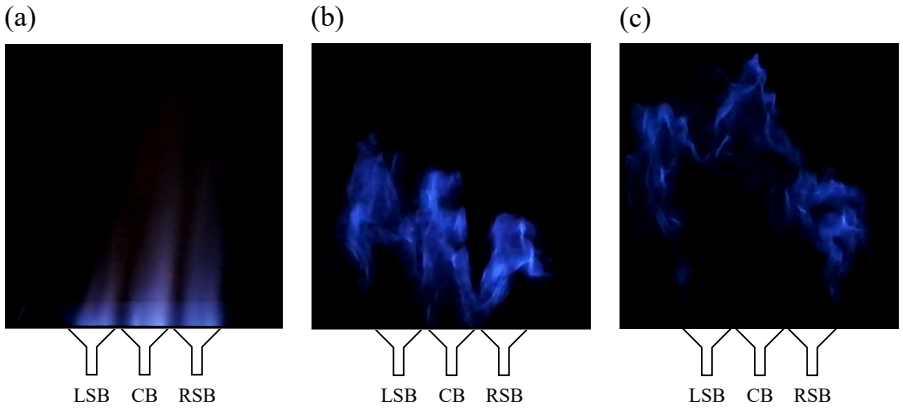

Figure 5.35: (a), (b) and (c) respectively show representative images corresponding to stable combustion, intermediate and near-LBO regime respectively. The distance between the burners is equal to 45 mm (LAC-F1-45 case).

The results obtained with LAC-F1-65, LAC-F1-55, and LAC-F1-55 cases indicate that the flame behavior at the near-LBO state is highly dependent upon burner spacing. However, as the experimentation facility has provision to vary the distance between burners only at selective distances ($d = 45, 55, and 65$ mm), a more detailed exploration of the dependence of burner spacing and near-LBO phenomena could not be done in the present study. Finally, during this study, we observe partial attachment-detachment of flame from burner tip, flame merging-unmerging, partial extinction-reignition, flame-to-flame interaction and burner-to-burner interaction, etc. events in the AC and LAC configurations at the near-LBO states. These events cannot be captured in single-burner combustors as only one flame is present in such systems.

5.4 Discussions

A few previous studies have discussed the flame-flame and burner-to-burner interactions in the multi-burner combustors at the near-LBO state [55], [56], [181]–[183]. In order to better understand the results obtained in this study, we next compare our results with those of previous studies.

In the present study, we observe that the LBO limit in the linear array combustor is slightly lower as compared to the annular combustor (section 5.3. Such a finding is also reported by Ciardiello *et al.* [56]. They infer that such a reduction in the LBO stability in the linear array combustor is due to increased heat loss in the linear array combustor, as the side walls are positioned close to the side walls.

One important question is the presence or absence of flame-flame and/or burner-to-burner interactions at the near-LBO state. Ciardiello *et al.* [55] reported that flame-flame interactions are more frequent at the stable combustion state than at the near-LBO state. Kwong *et al.* [182] did not find evidence of burner-to-burner interactions during the blow-off events. However, they observed burner-to-burner interactions during the reattachment of lifted flames to burners. In contrast, in the present work, flame-flame and burner-to-burner interactions are seen to increase with the approach of LBO. Moreover, we observe the flame-flame and burner-to-burner interactions to occur during the lift-off/blow-off and reignition/reattachment events.

Previous studies have explored the effects of flame-flame and burner-to-burner interactions on the LBO limit. Dolan *et al.* [181] reported that a combustor becomes more prone to LBO with an increase in burner-to-burner distance. In contrast, Ciardiello *et al.* [55] found that a greater distance between the burners results in comparatively higher stability of the combustor. In other words, the global flame extinction in the combustor occurs at a lower equivalence ratio when the distance between the burners is higher. Kwong *et al.* [183] reported that the burner-to-burner interactions do not necessarily lead to a reduction or increase in the LBO limit. They found that a two-burner configuration had greater stability against LBO than a one-burner configuration. However, the one-burner configuration was found to be more stable than a five-burner configuration. Based on their results, they infer that the relationship between the stability characteristics of a combustor and burner-to-burner interactions is significantly complex. The present study corroborates this finding, as discussed above.

Another important question is how the stability of a flame is affected when an adjacent flame lifts off (or, blows off). Kwong *et al.* [182], did not find any correlation between the location of the first burner that blows off and the order of subsequent blow-offs. Based on this fact, they concluded that the blow-off in one

burner does not influence the LBO in the adjacent burners. In contrast, Ciardiello *et al.* [55] observed that the lift-off of a flame often destabilizes the adjacent flame. We discover that blow-off in one burner frequently causes blow-off in the adjacent burner(s). Thus, our finding agrees with that of Ciardiello *et al.* [55].

The causes of destabilization of a flame due to adjacent flame blow-off (or, lift-off) have been discussed in previous studies. Ciardiello *et al.* [55] infer that the local fluid density changes when a flame lifts off or is extinguished. This results in flow redistribution which reduces the local equivalence ratios in the other burners. This causes the flames from the other burners to weaken and become prone to extinction. This explanation, however, cannot completely explain the results found in the present study, as discussed next. During the extinction/lift-off of a flame, the adjacent flame often exhibits significantly high intensity (for example, (i) at $t = 0.16$ sec in Fig. 5.25, (ii) at $t = 0.928$ sec in Fig. 5.26 and (iii) at $t = 1.376$ sec in Fig.5.27). The high intensity flame is indicative of a relatively high local equivalence ratio at the corresponding burner. Thus, the mixture flow redistribution may not be the only mechanism that destabilizes the adjacent flame. Further studies with advanced optical diagnostics are therefore needed to explain this phenomenon.

Kwong *et al.* [183] showed that the burner-to-burner interactions lead to reignition in the extinguished burners. Using OH* chemiluminescence imaging, Ciardiello *et al.* [56] identified the transfer of flame packets from an adjacent flame to the extinguished burner as the reignition mechanism. The present study finds quite a similar reignition mechanism at various degrees of premixedness and for various distances between the burners.

Kwong *et al.* [182] saw flame anchoring of the blown-off flame by one of the adjacent flames. They report that the flame anchored in such a way often reattaches to its corresponding burner at a later time, similar to that found in the present study. Further, Kwong *et al.* [183] report that the adjacent flame can act as a pilot to stabilize the flame. In the present study also, often one of the adjacent flames is seen to transfer flame packets to the combustor region corresponding to the extinguished burner, which eventually re-establishes the flame. In such cases, the adjacent flame can be considered as a pilot flame that stabilizes the blown-off flame. In short, the present study is in agreement with the recent studies that explored the near-LBO flame dynamics.

5.5 Summary

Flame visualization is important to understand LBO combustion physics, which is often highly complex in turbulent combustors. Most of the previous studies on

flame visualization in the near-LBO regime are based on single-burner combustors, even though most modern industrial combustors have multiple burners. In multi-burner combustors, the interaction of adjacent burners may influence the near-LBO flame behavior in a significant way. Further, slight dissimilarities in the interacting burners may profoundly influence the resulting flame dynamics. Therefore, in this chapter, we visually examine the multi-burner combustors' flame dynamics during the transition to LBO. We observe significant changes in the flame structure as LBO is approached. It is seen that the flame-to-flame interactions and burner-to-burner interactions (for example, the reignition of an extinguished burner by the flame corresponding to an adjacent burner) start to occur only close to the LBO limit. It is seen that the flame-to-flame and burner-to-burner interactions reduce the severity of the extinction events in the combustor at the near-LBO state. Often a lifted flame is seen to be anchored (and thus prevented from blowing out) by the flame from an adjacent burner. Further, an extinguished burner is often reignited by the flame from an adjacent burner. The lift-off and subsequent weakening of a flame are often accompanied by the lift-off and weakening of the adjacent flame. Partial attachment-detachment of flame from burner tip, flame merging-unmerging, partial extinction-reignition, flame-to-flame interaction (for example, anchoring of the lifted flame by the adjacent flame), and burner-to-burner interactions (for example, reignition of extinguished burner by the adjacent flame), etc. phenomena are seen at the near-LBO state for the annular and linear array combustors, which cannot be captured in single-burner combustors. These facts highlight the importance of further study on the lean blowout phenomenon in multi-burner combustors. On the other hand, we find closely similar flame dynamics, in the annular and linear array combustors, at the near-LBO state. This indicates that the linear array configuration may be used as a proxy for studying the transition to LBO in annular combustors. The insights obtained from the flame visualization study may be useful for further exploration of the near-LBO dynamics in multi-burner combustors, with sophisticated time series and/or image analysis tools.

CHAPTER 6

Lean blowout detection using topological data analysis

6.1 Introduction

The dependability and safety of the aircraft may be considerably increased with an online LBO monitoring system. Moreover, it would ensure efficient combustion [30] and a low NO_X emission. Moreover, a lower safety margin results in lower operating temperatures in the combustor, thereby reducing wear and tear on the combustor's mechanical parts, especially the turbine blades [184].

Most nonlinear techniques for early LBO detection have been developed based on experimental results with single-burner combustors. However, as discussed in chapter 5, the near-LBO characteristics of the single-burner combustor and multi-burner combustor have significant differences. Flame-to-flame interaction produces partial extinction-reignition, partial lift-off, and partial attachment-detachment of flames in the multi-burner combustors, as discussed in chapter 5. Further, flame interaction in gas turbine combustors is often known to cause mutual synchronization, significantly affecting the combustion stability and dynamics [142], [150]. Flame interaction can even trigger combustion instabilities or lean blowout [10], [185]. Moreover, significant changes in nonlinear flame responses due to interaction of neighboring flames have been noted in literature [54]. It is known that LBO is a significantly nonlinear phenomenon [40]–[42]. Thus it is likely that the dynamical transition to LBO may be significantly different in multi-burner combustors as compared to single-burner combustors, due to the interaction of adjacent flames. In such a case, some of the well-known early LBO detection tools

may not be that effective for early LBO prediction in multi-burner combustors. Thus it is imperative to study the efficacy of the different nonlinear techniques as early LBO prediction tools in multi-burner combustors.

To fill this gap in the literature, we examine the dynamical transition to LBO in the present study using topological data analysis (TDA), a novel method. Both a linear array combustor and an annular combustor are employed as the experimental rigs in this investigation. The experimental test rigs, instrumentation, and data acquisition procedures are described in detail in chapter 5 and hence not repeated here.

Time series analysis using topological data analysis (TDA) has become popular in recent times as a powerful tool of nonlinear science. Perea and Harer [186] have used persistent diagram analysis with a sliding window approach to quantify the periodicity in the time series. Gidea *et al.* [187], [188] have applied TDA to find early signs of critical transitions in financial markets. Myers *et al.* [189] have analyzed various well-known dynamical systems using TDA, including Lorenz, Rössler, logistic map, and Hénon map. Topological data analysis (TDA) has been used in biological sciences [190], in signal processing [191], image and texture reorganization [192], engineering [193], [194], financial analysis [195], video analysis [196], various applications in health monitoring [197]–[200] and neuroscience [201]. The above papers have shown that TDA can capture the dynamical transitions in different systems using the persistent topological features obtained from point cloud data (i.e. phase space representation of time series). TDA extracts information from a point cloud for a plethora of scales through a process called 'filtration' [189], [202]. Thus TDA does not require any threshold selection to find patterns in the point cloud data. In contrast, complex network and recurrence-based tools require careful selection of thresholds to extract useful information from point clouds [95]. Another advantage of TDA is its robustness against noise [193]. Simple TDA metrics, which summarize the structures inherent in the data, have been successfully used previously to explore dynamical transitions [189].

In the present study, we find the LBO to occur without preceding thermoacoustic instability. In such cases, the flame pulsations and intermittent extinction-reignition events in the near-LBO regime are seen to be the most important dynamical phenomena [42]. We found that the path to LBO, as encountered in this chapter, is from stable combustion $\rightarrow$ intermittent extinction-reignition phenomena $\rightarrow$ lean blowout. We find that a well-established nonlinear dynamical tool for early LBO detection, namely the recurrence network analysis (RNA) (chapter 3), is not sensitive to the approach of LBO for multi-burner configurations. This is because the RN metrics do not follow any significant trends during the transition to LBO, as will be shown later in this paper. Therefore, we explore the

dynamical shift towards LBO using a novel dynamical science-based tool, namely the topological data analysis. We find that simple TDA-based metrics are highly sensitive to the approach of LBO in the single-burner as well as the multi-burner combustors. Additionally, we propose a computationally inexpensive strategy for implementing TDA as a real-time early LBO detection tool.

The remainder of this chapter is structured as follows. A brief theoretical background of topological data analysis is provided in section 6.2. In section 6.3, the chemiluminescence time series characteristics are discussed. Further, the results obtained with topological data analysis and recurrence network analysis are presented. Moreover, a practical strategy for implementation of TDA in real-time scenarios is devised. Section 6.4 comprises a brief summary of the findings of this study.

6.2 Brief discussion on topological data analysis (TDA)

6.2.1 Theoretical background

Topological data analysis (TDA) combines concepts from mathematical topology with that of computer science. TDA provides quantifiable and robust metrics that can provide insights about the shape of the data analyzed. It is often used to explore the dynamical transitions in various physical phenomena. TDA counts the number of structures in given simplicial complex. Such structures (homologies) may be a connected chain which is a structure of zero dimension. Another type of structure is a void (sometimes called a loop) which is a structure of one dimension. Higher dimensional structures are also possible. However, in the present study, we focus on the 1-D homology groups (loops).

First, we must introduce the concept of a simplicial complex in order to understand the process by which TDA assesses the topological features of phase space embedded time series. Simplicial complexes have a lot of similarities with graphs (i.e. networks). During the construction of graphs, only binary information can be extracted from the point cloud (i.e. phase-space embedded time series), which corresponds to the presence or absence of edges between nodes [202]. Further, often graphs are generated from time series by searching for patterns in the data at a previously set scale. For example, in the case of a recurrence network, the recurrences of the underlying system are explored with a fixed recurrence threshold. Therefore, graphs may suffer from significant loss of information [189]. Moreover, during the construction of graphs, careful selection of thresholds must be done

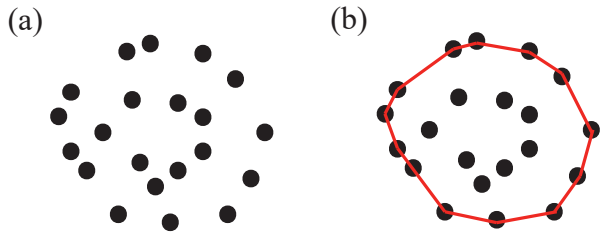

Figure 6.1: (a) shows a point cloud ψ. In (b), the convex hull (i.e. simplex) made up of all the points in ψ is shown. The boundary of the simplex is shown by a red line.

for proper uncovering of the underlying dynamics of the system [81], [94], [95]. In contrast, Simplicial complexes may contain higher dimensional information in terms of connected components (typically denoted as H_0 homology), loops or holes (denoted as H_1 homology) and other higher dimensional simplices like triangles and tetrahedrons [189], [202], [203]. Moreover, simplicial complexes contain information at all possible scales. Thus the Simplicial complexes can be considered as a generalized version of the graphs.

A simplex is the building block of a simplicial complex. Let a point cloud be ψ. Then, the convex hull in phase space, constituted by the set of points ψ is called a simplex $S(\psi)$ [204]. In that case, the points ψ are called the vertices of the simplex $S(\psi)$. For example, in Fig. 6.1(a) a point cloud is shown. The convex hull or simplex (indicated by a red line) formed using this set of points is shown in Fig. 6.1(b). Mathematically, a simplex $S(\psi)$ is defined as [195],

$$S(\psi) = \left\{ \psi : \psi = \sum_{p=0}^{n_v} a_p v_p, a_p \geq 0, \forall p \in \{0, \ldots, n_v\} \text{ and } \sum_{p=0}^{n_v} a_p = 1 \right\} \tag{6.1}$$

Here, n_v is the number of vertices in the simplex $S(\psi)$. If ω is a subset of ψ ($\omega \subseteq \psi$), then $S(\omega)$ is called a subset or face of the simplex $S(\psi)$ and is denoted by, $S(\omega) \preceq S(\psi)$ [189]. If a simplex is S, then its dimension is defined as, $dim(S) = |S| - 1$ where $|S|$ indicates the number of vertices in the simplex [189].

After discussing the concept of a simplex and a few of its important properties, we discuss the concept of a simplicial complex. A simplicial complex K_s is a set of different types of simplices satisfying two criteria: (1) that each subset of K_s is also in K_s and (2) the intersection of any two simplices in K_s is a subset of both the simplices [195], [205]. In other words, a simplicial complex K_s is simply a collection of a number of simplices $S(\psi)$ so that if $S(\psi) \in K_s$, and $S(\omega) \preceq S(\psi)$, then $S(\omega) \in K_s$ [189]. The dimension of the simplicial complex K_s is defined as the largest dimension of the simplices contained in it, $dim(K_s) = max_{S \in K_s} dim(S)$

[189].

Next, we describe how a simplicial complex can be extracted from the CH* chemiluminescence time series. First, we embed the CH* time series obtained from PMT into phase space using the delay-embedding technique [92]. Let the phase-space embedded time series (otherwise called a point cloud) be X. From X, a Rips complex, a type of simplicial complex, is generated as follows. Hyperspheres of radius ϵ (in short called the ϵ-balls) are drawn around the point cloud vertices $x, y \in X$. Overlapping of two ϵ-balls indicates an edge between the two vertices x and y. Thus if $d(x, y) \leq \epsilon$, then x, y is part of a simplex created with threshold ϵ. In other words, if U points (U being a subset of X i.e. $U \subset X$) forms a simplex between themselves for threshold ϵ, each pair of points in U ($x, y \in U$) will be at most ϵ distance apart [198]. The collection of all simplices thus obtained at threshold ϵ is referred to as a Rips complex, $Rips(X, \epsilon)$. ϵ can be considered as a resolution to search for patterns in the embedded time series X. Next, by varying the ϵ, a series of Rips complexes are generated. This process is called Vietoris-Rips filtration [206]. A filtration of simplicial complex K can be defined as an increasing series as follows,

$$K_1 \subset K_2 \subset K_3..... \subset K_n = K \tag{6.2}$$

The filtration process of K may also be defined by a monotonic function $f : K \to \mathbb{R}$, $\mathbb{R}$ being the set of real numbers. Consequently, if $\gamma, \delta \in K$ and $\gamma \subset \delta$, then $f(\gamma) \leq f(\delta)$. Thus, if the monotonic function values in the filtration process takes the values as $g_1, g_2, \ldots, g_n$, the resulting simplicial complexes, resulting during the filtration, can be expressed in the form $K_i = f^{-1}(-\infty, g_i]$.

Let us again focus back to our example of creating a filtration of simplicial complex from the phase-space embedded time series X. In this case, if $\epsilon = 0$, the Rips complex would consist of only disjoint points, with no connections among them whatsoever. As the threshold ϵ is varied, the ϵ-balls around the point cloud vertices increase in size, resulting in increasing overlap of the adjacent ϵ-balls. Thus, as the threshold ϵ is varied, several homology classes may be born which were not present before. For example, a connected chain (i.e. H_0 homology classes), which links several vertices, may be born which were not present in the preceding Rips complex. Similarly, new loops (i.e. H_1 homology classes) may form that were not present in the preceding Rips complexes. On the other hand, with an increase in ϵ, several homology classes may cease to exist i.e. die; for example, a few loops may get filled up. Thus the ϵ at which interesting persistent homologies are born and die can be found by gradually increasing the threshold ϵ [202]. Finally, at a particular ϵ, all the homology classes get filled up i.e. die

and the topology gets transformed into a single fully connected structure. At this point, no further information can be extracted from the point cloud.

Let a filtration of complexes $(K_i)_{i\in I}$ satisfy the rule: if $i \leq j$, then $K_i \subseteq K_j$. This relation translates to a linear map between the corresponding homologies: $H_n(K_i) \rightarrow H_n(K_j)$ where H_n indicates the n-dimensional homologies. A class $\alpha \in H_n(K_i)$ is said to born be born at i if it did not exist at just prior homology $H_n(K_{i-1})$. The class α is said to die at j if α is non-zero for $H_n(K_{j-1})$ but $\alpha = 0$ for $H_n(K_j)$. Then, i and j are referred to as the birth time and the death time of the class α. Let there be k number of classes in the n-dimensional homology group. Then, the corresponding persistent diagram which represents the life time of the different classes during the Rips filtration is represented in short as,

$$D = \{(b_1, d_1), (b_2, d_2), \ldots\ldots (b_k, d_k)\} \tag{6.3}$$

Here, D is the persistent diagram corresponding to the n-dimensional homology group. More elaborate mathematical details and computational algorithms on TDA may be found in previous literature [207]–[209]. We calculate the persistent diagram using the ripser function of the Python package Scikit-TDA [210]. We measure the distance between the point cloud vertices as per the Euclidean norm.

The persistent diagram is the basis for calculating the various TDA metrics. Thus, it is described in detail next. The persistence diagram is often represented by a 2-D plot where the x and y axes correspond to birth and death 'instants' (i.e. the ϵ corresponding to the birth and death of a homology class) respectively. Apart from pairs of birth and death instants, the persistent diagram is also thought to consist of an infinite number of fictitious classes that have simultaneous birth and death, i.e. have zero persistence [211]. As the birth and death times in such cases are equal, the persistence diagram plot always contains a diagonal line along the $x = y$ line.

Persistence or lifetime of the class α is defined as $pers(\alpha) = d_\alpha - b_\alpha$. Now the class α is represented by a dot having coordinate (b_α, d_α) in the persistent diagram plot. Therefore, the higher the persistence of a class α, the higher will be the distance of the dot corresponding to α from the $x = y$ diagonal of the persistent diagram plot.

In topological data analysis, the features of simplicial complexes that sustain for a wide range of ϵ (i.e. have a high lifetime) are called the persistent features. Often there is a relation between the scale of the feature under consideration and its persistence or lifetime. This is because the larger loops get filled up (i.e. die) at a significantly higher ϵ as compared to smaller loops. The highly persistent features represent true characteristics of the underlying dynamical system [203]. On the

other hand, the features having low persistence are typically due to noise. Thus the homology classes (represented by dots in the persistent diagrams) positioned at higher distances from the diagonal are more indicative of the underlying dynamics rather than the homology classes positioned closer to the diagonal.

If the maximum threshold of Rips filtration is low, then birth and death of features at larger scales may not be counted. For example, a higher threshold is often necessary to register the fill-up (i.e. death) of the large-scale loops in the topological space. On the other hand, the large-scale features are highly persistent and represent the true dynamical properties of the system under consideration, as discussed above. Thus, significant information about the underlying dynamical system will be lost if a low value of the maximum threshold of Rips filtration (ϵ_{max}) is chosen. Therefore, in the current study, the threshold for the Rips complex is taken as $\epsilon_{max} = +\infty$ so that the entire filtration can be obtained. In other words, all loops or holes that may appear at various possible ϵ in the topological space will be considered, regardless of their scale and persistence. However, this approach incurs the highest computational cost as it considers all possible feature scales.

Several studies on TDA have tracked the persistence of loop structures or holes (having homology dimension 1 and denoted as H_1 homology), during the Rips filtration process, to estimate the periodicity of the data [186], [189], [191], [212]. Sophisticated metrics of TDA, for example, bottleneck distance and p-Wasserstein distance exist but are difficult to implement [189]. On the other hand, point summary metrics of TDA, based on H_1 homology features, are lossy summaries but are easier to implement [189]. Consequently, they have been used by several studies for exploring dynamical transition in a various systems [189], [197]. Thus in this paper, we study if the point summary metrics, based on features of the H_1 homology classes, can correctly capture the dynamical transition to LBO.

Next, we discuss the definition of the different point summary metrics. The persistence of a class α in H_1 homology can be calculated as,

$$pers(\alpha) = d_\alpha - b_\alpha \tag{6.4}$$

If there are C number of classes, the maximum persistence among all the classes can be calculated as,

$$maxpers(D) = \max.\{pers(\alpha_1),\ pers(\alpha_2), \ldots\ldots,\ pers(\alpha_C)\} \tag{6.5}$$

Because large-scale loops take a longer time to get filled up, their persistence is higher [202]. Thus, a higher $maxpers(D)$ indicates the presence of a large-scale loop in the topological structure. A second metric used in the present study is $M(D)$. It is the ratio of the number of H_1 homology classes (denoted by $|D|$) in

the persistent diagram to the number of vertices (denoted by $|V|$) in the point cloud,

$$M(D) = \frac{|D|}{|V|} \tag{6.6}$$

$|V|$ is alternatively called the graph order. $|V|$ can be calculated as, $|V| = N - \tau_d(D-1)$ where, N is the number of points in the time series, τ_d is the optimal time delay and D is the optimal embedding dimension. If a system is periodic (i.e. deterministic), the number of H_1 homologies i.e. 1-D loops will be lower in comparison to if the system is chaotic (i.e. comparatively less deterministic) [189]. Thus, $M(D)$ is likely to be low for a periodic signal and comparatively high for a chaotic/stochastic signal [189].

Another useful parameter is the persistent entropy $E(D)$, which is analogous to the information-theoretic metric Shannon entropy [189]. Persistent entropy has been widely used to uncover hidden patterns in the data [205]. It can also be thought of as the complexity of the system topology [205]. Persistent entropy is scale-invariant and robust against noise in the input data [206], [211] and is defined as,

$$E(D) = -\sum_{\alpha \in D} \frac{Pers(\alpha)}{L(D)} \log_2\left(\frac{Pers(\alpha)}{L(D)}\right) \tag{6.7}$$

Here, $L(D)$ is the sum of persistences (i.e. lifetimes) of different classes in the persistent diagram, i.e. $L(D) = \sum_{\alpha \in D} pers(\alpha)$. However, $E(D)$ cannot be compared between different operating conditions as in that case the number of vertices in the point cloud also varies. Normalized entropy $E'(D)$ is a more useful metric that can be used for comparison of dynamic states [189]. It is given as,

$$E'(D) = \frac{E(D)}{\log_2 L(D)} \tag{6.8}$$

As persistent entropy (Eq. 6.7) is analogous to the Shannon entropy, the maximum entropy will be obtained when the lifetimes of the different H_1 homology classes become equal [213]. As the lifetime of the different H_1 homology classes become dissimilar from each other, the persistent entropy reduces. More elaborate discussions on the persistent entropy can be found in Rucco *et al.* [213]. Next, we provide a simple example explaining the calculation of the persistent diagram and related point summary metrics.

Figure 6.2 show a simple example of Rips filtration process. The point cloud X (Fig. 6.2a) have 22 vertices. When $\epsilon < 5$, the Rips complex consists only of the disconnected vertices. Thus the number of components in the resulting simplicial complex would be equal to 22. At $\epsilon = 5$ (Fig. 6.2b), ϵ-balls intersect with the

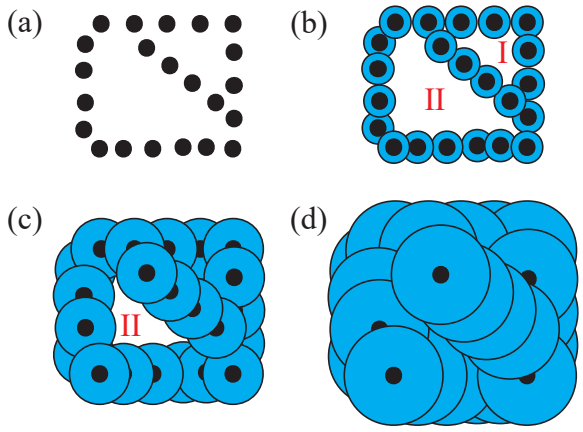

Figure 6.2: Example of filtration creating a sequence of Rips complexes $Rips(X, \epsilon)$ is described with a point cloud X. (a) shows the point cloud X. (b), (c) and (d) respectively indicate the resulting complexes for $\epsilon = 5, 14, 26$ respectively. We note that unit of ϵ is arbitrary.

neighboring ϵ-balls, and the simplicial complex thus comprises a connected chain (i.e. a H_0 homology group). Moreover, two holes I and II, corresponding to H_1 homology, come into existence. At $\epsilon = 14$ unit (Fig. 6.2c), loop I gets filled up (i.e. dies) so only loop II remains in the simplicial complex. At still higher threshold ($\epsilon = 26$), loop II also dies (Fig. 6.2d). Thus, the persistence of loop I and II are given as $pers(I) = 14 - 5 = 9$ and $pers(II) = 26 - 5 = 21$. So, $maxpers(D) = 21$ for the example in Fig. 6.2. Further, $M(D) = |D|/|V| = 2/22 = 0.091$ and $E(D) = -0.88$ so that $E'(D) = -0.1796$. We note that the persistence or lifetime of loop II is higher as compared to loop I. This is expected as loop II is larger compared to loop I. A more detailed discussion on the calculation and significance of persistence diagram metrics can be found in literature [189].

6.2.2 Using topological data analysis to investigate well-known dynamical systems

Previous literature has shown that the TDA can distinguish between the periodic and chaotic signals from one another [189]. Still, for completeness of this chapter, we discuss the behavior of the TDA metrics $maxpers(D)$, $M(D)$ and $E'(D)$, for periodic and chaotic dynamics, with several well-known dynamical systems. The periodic and Chaotic signals used in the present study are obtained with (i) a Rössler system, (ii) a Chua circuit, and (iii) a Lorenz system, in the way described below.

Rössler system: The equations corresponding to the Rossler system are as follows,

$$\frac{dx}{dt} = -y - x, \frac{dy}{dt} = x + ay, \frac{dz}{dt} = b + z(x - c) \tag{6.9}$$

The equation 6.9 is solved with the parameters $a = 0.2, b = 2.0, c = 4.0$ which produces a periodic signal. Solving the equation 6.9 with the parameters, $a = 0.43, b = 2.0, c = 4.0$ results in a chaotic signal.

Chua circuit: The equations corresponding to the Chua circuit are as follows,

$$\begin{aligned} \frac{dx}{dt} &= \alpha(y - x - f(x)) \\ \frac{dy}{dt} &= \gamma(x - y + z) \\ \frac{dz}{dt} &= -\beta y \end{aligned} \tag{6.10}$$

Here, $f(x) = m_1 x + \frac{1}{2}(m_0 + m_1)|(|x + 1| - |(|x - 1|)$. A periodic signal is obtained when the equation 6.10 is solved with the parameters: $\alpha = 15.6, \gamma = 1.0, \beta = 50, m_0 = -1.1429, m_1 = -0.714$. A chaotic signal is obtained when the equation 6.10 is solved with the parameters: $\alpha = 15.6, \gamma = 1.0, \beta = 25, m_0 = -1.1429, m_1 = -0.714$.

Lorenz system: The equations corresponding to the Lorenz system are as follows,

$$\frac{dx}{dt} = \sigma(y - x), \quad \frac{dy}{dt} = x(\rho - z) - y, \quad \frac{dz}{dt} = xy - \beta z \tag{6.11}$$

Solving the equation 6.11 with the parameters $\sigma = 10.0, \beta = 8.0/3.0$ and $\rho = 180$ produces a periodic signal. On the other hand, solving this equation with parameters $\sigma = 10.0, \beta = 8.0/3.0$ and $\rho = 50$ produces a chaotic signal.

In each of the above three systems, the time series is sampled at 20 Hz and a 1000 sec signal is obtained. We analyze only the last 8000 data points, corresponding to the last 400 seconds, to avoid transient dynamics in the system we are examining [189]. Table 6.1 shows the values of the TDA metrics for the three dynamical systems described above, during periodic and chaotic regimes. We observe that the largest Liapunov coefficient (Λ) is approximately zero when the signal is periodic while for a chaotic signal, $\Lambda > 0$, as expected. We observe that the TDA metrics differ significantly between periodic and chaotic regimes. This indicates that the TDA metrics can distinguish different dynamical states in a system under investigation.

Next, we explore the phase plots of the chaotic and periodic states of the Lorenz system which will help to better understand the underlying dynamics. At the chaotic state (Fig. 6.3a), the phase plot seems to be of a highly complex shape consisting of a large number of loops. On the other hand, at the periodic state

	Rossler system		Chua circuit system		Lorenz system	
	Periodic	Chaotic	Periodic	Chaotic	Periodic	Chaotic
Λ	0.0011	0.09644	0	0.394	0	0.147
$maxpers(D)$	2.895	0.605	1.07	0.492	1.806	0.56
$M(D)$	0.00125	0.501	0.00125	0.78	0.00125	0.80
$E'(D)$	-1	0.824	-1	0.40	-1	0.392

Table 6.1: Values of the largest Liapunov exponent (Λ) and the TDA metrics $maxpers(D)$, $M(D)$ and $E'(D)$ for different well-known dynamical systems, at periodic and chaotic states.

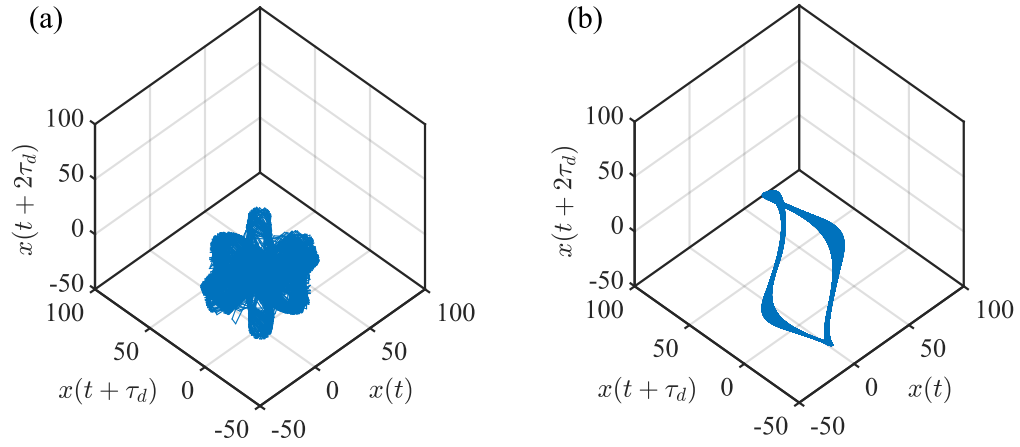

Figure 6.3: Phase plots of the Lorenz system (Eq. 6.11), (a) at chaotic state and (b) at periodic state.

(Fig. 6.3b), a single loop is present.

Next, we describe the features of the persistent diagrams for the chaotic and periodic states of the Lorenz system described above (Fig. 6.4). Here, the persistent diagram visually represents the birth and death information of only the loop structures (i.e. 1-D holes), as obtained from the Rips filtration process, as only the H_1 homology classes are considered in this study. The blue dots indicate the various H_1 homology classes. We note that each dot in the persistent diagram may represent a finite number of classes that have the same birth and death instants due to the multiplicity property of the persistent diagram [187]. The red diagonal line is indicative of the $x = y$ line. The diagonal represents the infinite number of fictitious points which have zero persistence i.e. their birth and death instants are the same.

From Fig. 6.4(a), we observe that at the chaotic state, a significant number of blue dots, representative of various H_1 homology classes, are positioned quite close to the diagonal line. In contrast, the persistent diagram corresponding to the periodic state (Fig. 6.4b) has a single blue dot (indicated by an arrow) located at a significantly high distance from the diagonal line. Therefore, the results indicate

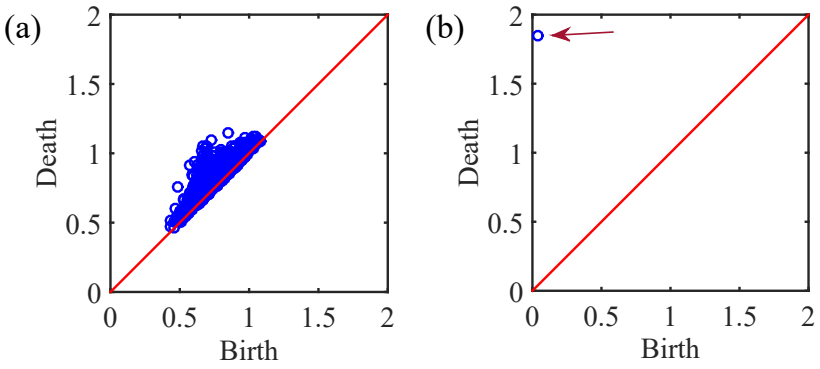

Figure 6.4: Persistent diagram of the Lorenz system (Eq. 6.10). (a) at chaotic state and (b) at periodic state.

the presence of a single, highly persistent loop in the topological space at the periodic state. We note that this is indeed the case (Fig. 6.3b).

6.2.3 Sub-level set filtration approach to topological data analysis

The TDA tool with suitable under-sampling is computationally cheap. However, properly embedding a time series extracted from experimental systems may sometimes require careful selection of embedding dimension and optimal time delay. Thus it is important to check whether the TDA without phase-space embedding has a reasonable efficacy as an early LBO prediction tool. One such technique to implement TDA is the sub-level set filtration technique, with which the series of simplicial complexes (i.e. the filtration) can be generated from the original time series itself. Therefore, phase embedding is not required. Next, we discuss the sub-level set filtration technique. Let a time series be denoted as $f(t)$ where t is time. Therefore the function, $f : t \to \mathbb{R}$ may be considered as the height coordinate [194]. f may have local maxima and minima. Then, the λ sub-level set for function f is given as,

$$L_\lambda = \{t : f(t) \leq \lambda\} = f^{-1}([-\infty, \lambda]) \tag{6.12}$$

Let, λ_1 and λ_2 be two levels with which two sub-level sets are found which are L_{λ_1} and L_{λ_2} respectively. Let, $\lambda_1 > \lambda_2$. Then, the criterion that $L_{\lambda_1} \supseteq L_{\lambda_2}$ must be met. By varying the level λ, a series of sub-level sets are formed which are represented in short as, $\{L_\lambda\}_{\lambda \in \mathbb{R}}$.

The sub-level set filtration process may be easilly understood by imagining a (fictitious) rising water level [194]. In this filtration, at first the 'water level' is considered to be at the minimum value of $f(t)$. As the water level starts to

increase gradually, it encounters the local minima and maxima of the time series. Each time a local minima of the $f(t)$ is reached, as the water level increases, a feature is born. Each feature encountered may be thought to be a water 'pool' [194]. As water level rises, these 'pools' gradually starts to fill up. As the water level increases further, some of the 'pools' merge together. For example, let us consider the merging of two loops, which were born at different times. In that case, by Elder rule convention, it is said that the newer 'pool' (i.e. the 'pool' born later) die while the older loop (i.e. the 'pool' born earlier) remains [194], [214]. Each water 'pool' i.e. feature can be considered as a connected chain and hence corresponds to the H_0 homology classes. Next, we present a simple illustrative example of sub-level set filtration.

In Fig. 6.5(a), a time series, corresponing to the chaotic state of the Lorenz system discussed above, is shown. At the lowest minima in this time series ($\lambda = -0.83$), the 'pool' I (i.e. feature I) is encountered. The λ at this point is the birth instant of 'pool' I ($b_I = -0.83$). As the 'water level' λ is slightly increased ($\lambda = -0.79$), the 'pool' II is encountered (i.e. ($b_{II} = -0.79$). With further increase of λ, 'pool' III ($\lambda = -0.72$) and 'pool' IV ($\lambda = -0.7$) are encountered. In other words, $b_{III} = -0.72$ and $b_{IV} = -0.7$. At $\lambda = -0.25$, the 'pools' III and IV merge together. Therefore, by following the Elder rule, it is considered that the pool IV dies at this point (i.e. the death instant of IV, $d_{IV} = -0.25$). At $\lambda = -0.13$, the 'pools' I and II merge together so that it is said that loop II dies at this point (i.e. $d_{II} = -0.13$). At $\lambda = 0.045$, the 'pool' V is encountered (i.e. $b_V = 0.045$). With further increase of the 'water level' ($\lambda = 0.87$), 'pools' I and V merge together so that at this point 'pool' V dies ($d_V = 0.87$). Finally, at $\lambda = 1$, the 'pools' I and III merge together so that feature III dies at this point. We note that the 'pool' I do not die during the time window chosen. Therefore, the death instant of 'pool' I is considered to be infinity ($d_I = \infty$). In the persistent diagram corresponding to this time series (Fig. 6.5b), we note that the red horizontal line corresponds to the $\lambda = \infty$ line. The red diagonal line is the $x = y$ line.

6.3 Results and discussions

6.3.1 Time series characteristics

In this study, we focus on the highly premixed annular and linear array configurations which have a burner-to-burner spacing of 55 mm (in other words, the AC-F1 and LAC-F1-55 configurations). We find that as the equivalence ratio (ϕ) is reduced, LBO occurs in the annular and linear array combustors without the occurrence of preceding thermoacoustic instability. We observe that LBO occurs

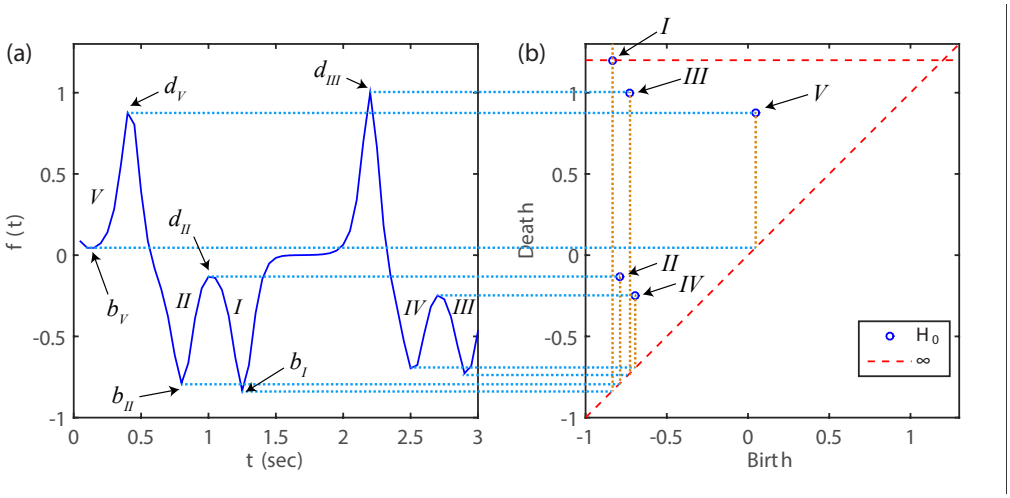

Figure 6.5: (a) shows the time series corresponding to the chaotic state of the Lorenz system described above. (b) shows the corresponding persistent diagram that is calculated with the sub-level set approach. The various H_0 homology classes are indicated by blue dots. b_I - b_V and d_I - d_V respectively indicate the birth and death instants of the $I - V$ 'pools' or features (H_0 homology classes). The time series shown in (a) is normalized by dividing it by the maximum amplitude of the time series.

at a slightly different equivalence ratio for the annular and linear array combustors as discussed in chapter 5 (table 5.2). Therefore, to compare the transition to LBO in the annular and linear combustors, we normalize the equivalence ratio (ϕ) by dividing it by the equivalence ratio at LBO (ϕ_{LBO}).

Figures 6.6(a-c) show the CH* time series for the AC-F1 case. We note that the stable combustion state ($\phi/\phi_{LBO} = 1.69$) corresponds to an aperiodic time series with a high mean CH* chemiluminescence value (Fig. 6.6a). In comparison, the oscillations around the mean are very less, indicating that the heat release rate fluctuations in the combustor at this point are much less. As we lower the fuel (liquid petrolium gas (LPG)) flow rate ($\phi/\phi_{LBO} = 1.44$), the mean of the time series reduces, signifying the reduction of heat release rate in the combustor (Fig. 6.6b). At this state also, the CH* time series consists of low amplitude aperiodic oscillations (in comparison to the mean CH* signal). Just prior to LBO ($\phi/\phi_{LBO} = 1.06$), the CH* time series has a still lower mean (Fig. 6.6c). However, along with the low amplitude aperiodic oscillations, high amplitude aperiodic oscillations are observed at this state. At this point, the CH* amplitude often approaches zero, indicating a significantly low heat release rate. Such a situation corresponds to an extinction event in the combustor [128]. During the extinction event, fresh air-fuel mixture builds up due to the absence of a widespread flame in the combustor (chapter 5). This situation is followed by a reignition event where the accumulated unburnt air-fuel mixture gets consumed. During this reignition

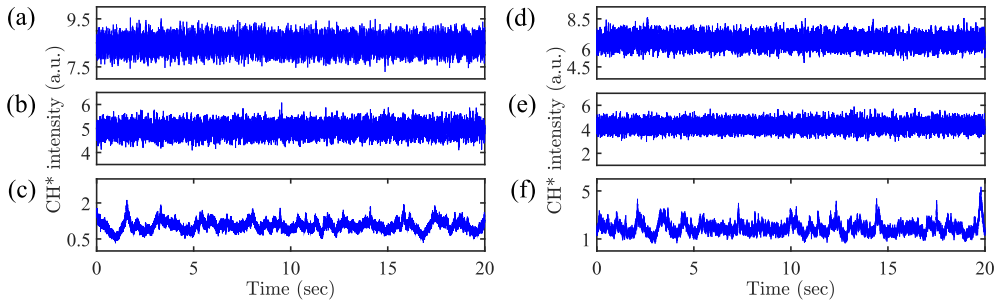

Figure 6.6: CH* chemiluminescence time series for the AC-F1 case are shown at (a) $\phi/\phi_{LBO} = 1.69$, (b) $\phi/\phi_{LBO} = 1.44$, (c) $\phi/\phi_{LBO} = 1.06$. CH* chemiluminescence time series for the LAC-F1-55 case are shown at (d) $\phi/\phi_{LBO} = 1.5$, (e) $\phi/\phi_{LBO} = 1.28$, (f) $\phi/\phi_{LBO} = 1.05$.

event, the heat release rate increases sharply, resulting in high amplitude peaks in CH* time series (in comparison to the mean CH* signal) as seen in Fig. 6.6(c).

Next, we describe the changes observed in time series characteristics of the LAC-F1-55 mm case as LBO is approached (Figs. 6.6d-f). We find that the time series of stable combustion state (Fig. 6.6d) and near-LBO state (Fig. 6.6f) for the LAC-F1-55 case corresponds closely with those of the AC-F1 case (Fig. 6.6(a) and Fig. 6.6(c) respectively). In both cases, the high amplitude pulses in the time series start to occur close to the LBO limit (Figs. 6.6c,f). The intermediate states between the stable combustion and near-LBO regimes exhibit a gradual reduction in the mean of the CH* signal, as the equivalence ratio is reduced, while exhibiting low amplitude oscillations around the mean (Figs. 6.6b,e).

As discussed above, the near-LBO CH* time series observed in the present study consists of low amplitude and high amplitude aperiodic oscillations. In contrast, conventional intermittency manifests as an ensemble of low amplitude aperiodic oscillations and high amplitude periodic oscillations [40]. Thus the dynamical state of the AC-F1 and LAC-F1-55 combustors, at the near-LBO regime is a relatively less explored type of intermittency. Visual inspection of the time series alone cannot provide further insight into the dynamical transition to LBO.

Next, we explore the frequency characteristics corresponding to the stable combustion state and near-LBO state for the highly premixed annular combustor (AC-F1 case) and linear array combustors (LAC-F1-55 case). The power spectrums, corresponding to the stable combustion states for the AC-F1 and LAC-F1-55 cases, are shown in Fig. 6.7(a) and Fig. 6.7(c) respectively. The power spectrums corresponding to near-LBO states for the AC-F1 and LAC-F1-55 cases are shown in Fig. 6.7(b) and Fig. 6.7(d) respectively. The results show that in the stable combustion states, no prominent frequency peak is present whereas, in the near-LBO states, the low-frequency component of the power spectrum increases significantly.

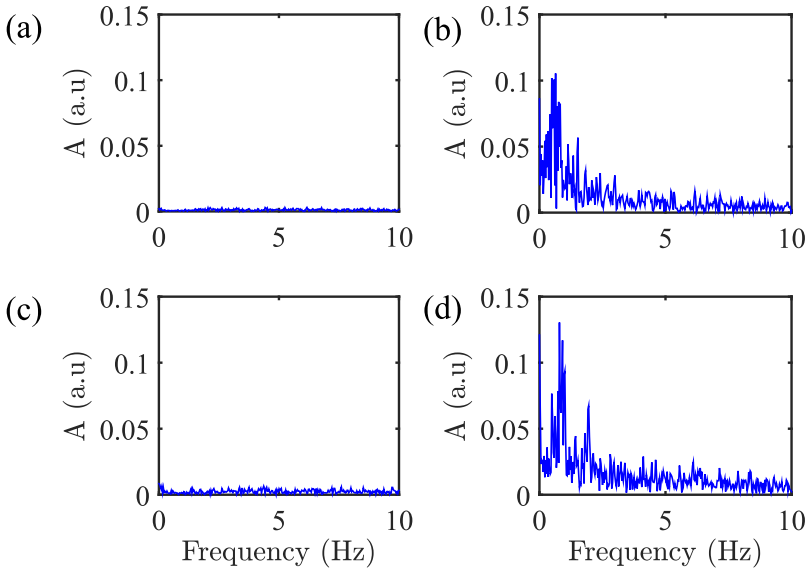

Figure 6.7: Power spectrum (a) at stable combustion state ($\phi/\phi_{LBO} = 1.69$) and (b) a near-LBO state ($\phi/\phi_{LBO} = 1.06$), for AC-F1 case. (c) and (d) respectively show the Power spectrum at stable combustion state ($\phi/\phi_{LBO} = 1.5$) and a near-LBO state ($\phi/\phi_{LBO} = 1.05$), for the LAC-F1-55 case, with B2B distance = 55 mm.

This fact is quite in line with the previous literature. However, we note that high-amplitude pulses in the CH* time series, which causes the qualitative changes in the power spectrum mentioned above, start appearing just before LBO. Therefore, the frequency-based tools may not be suitable for real-time early LBO prediction. For the same reason, the amplitude thresholding techniques are also unlikely to be suitable for early LBO detection in the AC-F1 or LAC-F1-55 cases. Thus next we explore the transition to lean blowout with well-known dynamical science-based tools: recurrence network 3 and topological data analysis.

6.3.2 Exploration of the dynamical transition to lean blowout in multi-burner combustors with recurrence network analysis

To explore the dynamical transition to LBO using recurrence network, we under-sample (with various under-sampling factors: 10, 20, and 40) the time series in order to reduce the computational cost. Next, the time series is delay-embedded into phase space [91]. Embedding dimension is calculated with the false neighbor method (FNN) [92]. Optimal time delay is calculated as the time delay corresponding to the first zero of the autocorrelation function [215]. The optimal recurrence threshold (ϵ_r) is found to be 7.7% of the maximum phase space

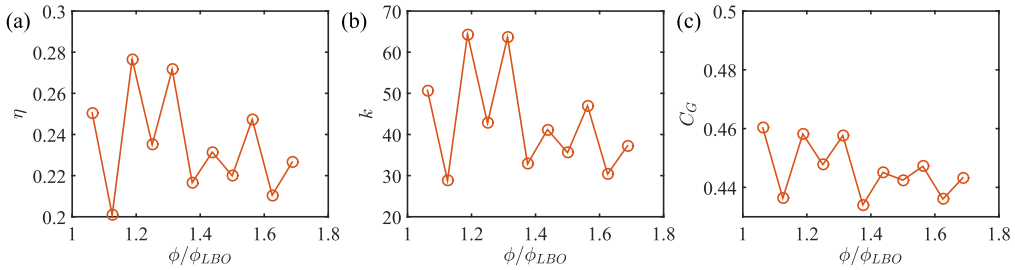

Figure 6.8: Variation in the RN metrics as LBO is approached by reducing equivalence ratio for the AC-F1 case. (a) global efficiency (η), (b) average degree centrality (k), (c) global clustering coefficient (C_G).

distance as discussed in the appendix of this chapter. From the point cloud (in other words, the phase-embedded time series), the RN metrics global efficiency (η), average degree centrality (k), and global clustering coefficient (C_G) are calculated.

The variations in the RN metrics η, k, and C_G, for the AC-F1 case, are shown in Figs. 6.8(a-c). Similar results are obtained for the LAC-F1-55 case also which is not shown here to avoid repetition. We observe that the RN metrics do not exhibit any significant trends during the approach of LBO. Therefore, we infer that the RN is not a suitable tool for exploring the dynamical transition to LBO in multi-burner combustors. This failure of the RN technique to detect impending LBO might be due to the additional complexity introduced in the flame dynamics by the presence of several oscillating flames, instead of a single oscillating flame. It may also be due to the lossy nature of the recurrence network algorithm, which searches for patterns in the data at a specific scale (i.e. the recurrence threshold ϵ_r). Next, we explore the dynamical transition with the topological data analysis (TDA) tool. TDA is more general as compared to RNA and does not suffer from the loss of information when searching for patterns in the data, as discussed in section 6.2 in this chapter.

6.3.3 Exploration of the dynamical transition to lean blowout in single-burner and multi-burner combustors with topological data analysis

For the TDA analysis, the CH* time series is under-sampled (with various under-sampling factors: 10, 20, and 40) to reduce the computational cost. Next, the CH* time series are normalized before generating the point cloud so that the change in amplitude of the CH* signal, as LBO is approached, does not affect the different TDA metrics. This normalization of time series is automatically taken care of for the recurrence network analysis, as in that case the recurrence threshold

is chosen as a percentage of the maximum diameter of phase space. First, we explore the dynamical transition to LBO in the single-burner combustor for the highest degree of premixing (i.e. F1 case) with the TDA metrics as this transition is already known (chapter 3). Next, the insights obtained from this exercise can be used to compare the dynamical transition to LBO in the multi-burner combustors.

At the stable combustion state ($\phi/\phi_{LBO} = 1.41$), we see that the various H_1 homology classes (indicated by blue dots) are concentrated into a small region close to the diagonal (Fig. 6.9a). In contrast, at the near-LBO state ($\phi/\phi_{LBO} = 1.01$), the H_1 homology classes are positioned over a significantly larger region on the persistent diagram (Fig. 6.9b). Further, a much higher number of blue dots are positioned at significant distances from the $x = y$ diagonal at the near-LBO state as compared to that at the stable combustion state ($\phi/\phi_{LBO} = 1.41$). Nevertheless, most of the blue dots are located close to the diagonal at either state. We infer that most of the loops in the point cloud at both the stable combustion state and near-LBO state are small due to which they get filled up (i.e. die) quickly. This qualitative similarity in the persistent diagrams, corresponding to two distinctly different dynamical states, can be easily explained, as described below.

We note that distinct 1-D loop structures are found in phase space plots and network topologies corresponding to strongly periodic systems [37], [57]. For a predominantly periodic system, the loop corresponding to the periodic component is of the largest scale in the point cloud as compared to the other components (if any). Due to this, the loop corresponding to the periodic component requires the highest time to get filled during the Rips filtration process and consequently has the highest persistence (i.e. lifetime). Therefore, often the persistent diagram corresponding to a periodic system consists of a single dot (representing the single, highly persistent H_1 homology class) positioned at a significant distance from the diagonal. As an example, we recall the persistent diagram corresponding to the periodic state of the Lorenz system (Fig. 6.4b).

In contrast, in the present study, we find that the time series corresponding to the single-burner combustor consists of aperiodic oscillations at both the stable combustion state and the near-LBO state, as discussed previously in chapter 3. The absence of a strongly periodic component in the time series leads to the absence of a distinct large scale loop structure in the point cloud (i.e. phase space embedded time series). This results in absence of highly persistent H_1 homology classes in topological space. From the above discussions, the slightly increased tendency of the blue dots to be positioned away from the $x = y$ diagonal, at the near-LBO state as compared to the stable combustion state, may be indicative of the comparatively larger scale loops at the near-LBO state. Indeed, the comparatively larger scale loop-like structures are found in the recurrence network

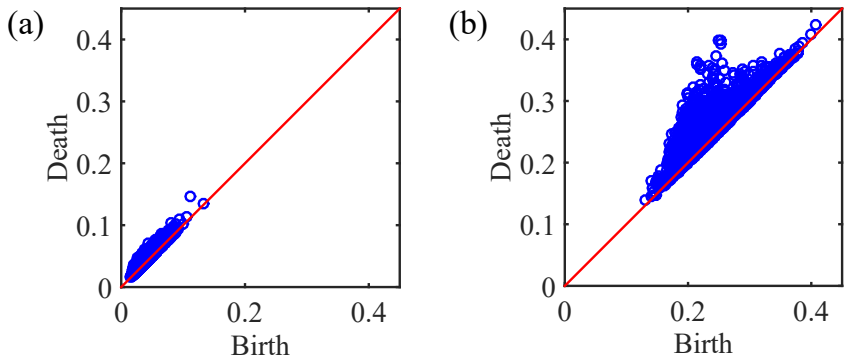

Figure 6.9: Persistent diagram (a) at stable combustion state ($\phi/\phi_{LBO} = 1.41$) and (b) at near-LBO state ($\phi/\phi_{LBO} = 1.01$), for the single-burner combustor (F1 case). Blue dots indicate H_1 homology classes.

topologies, at the near-LBO state for the single-burner combustor, as discussed in chapter 3 (Fig. 3.7b). Next, we discuss the persistent diagrams at the stable combustion and near-LBO states for the multi-burner combustors.

The persistent diagrams at the stable combustion state ($\phi/\phi_{LBO} = 1.69$) and the near-LBO state ($\phi/\phi_{LBO} = 1.06$) for the annular combustor (AC-F1 case) are shown in Figs. 6.10(a) and 6.10(b) respectively. Here also, we observe that the blue dots (indicating the various H_1 homology classes) are concentrated on a relatively small region near the diagonal in the persistent diagram corresponding to the stable combustion state. On the other hand, the blue dots are positioned across a significantly larger region on the persistent diagram corresponding to the near-LBO state. Still, most classes have very small persistence both at stable combustion state and near-LBO state (as most blue dots are placed close to the diagonal). Again this qualitative similarity in the persistence diagrams is expected, as the time series corresponding to both the stable combustion state and the near-LBO state for the annular combustor consist of aperiodic oscillations as discussed above (Fig. 6.6). Therefore, large-scale loops are absent which in turn leads to the absence of highly persistent H_1 homology classes. The persistent diagrams for the LAC-F1-55 case are similar to the single-burner and AC-F1 configurations, so they are not repeated here.

After discussing the changes in the persistent diagrams during the dynamical transition to LBO, we next focus on the efficacy of the TDA metrics as early LBO prediction tools. The changes in the persistent diagrams are quantified using the TDA metrics $maxpers(D)$, $M(D)$, and $E'(D)$. For effective early detection of LBO, the warning of impending LBO has to be issued with enough time allowance so that control actions can be actuated before LBO occurs [42]. Keeping in mind this criterion, first, we examine the variations in the TDA metrics during the

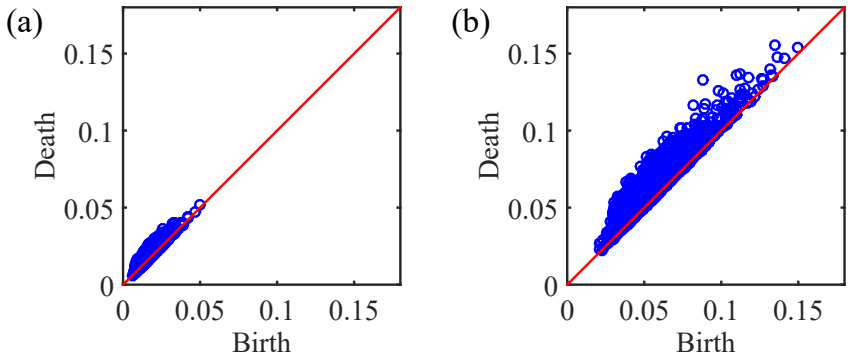

Figure 6.10: Persistent diagram (a) at stable combustion state ($\phi/\phi_{LBO} = 1.69$) and (b) at near-LBO state ($\phi/\phi_{LBO} = 1.06$), for AC-F1 case. Blue dots indicate H_1 homology classes.

transition to LBO for the single-burner combustor (Fig. 6.11). We observe that $maxpers(D)$ show a monotonically increasing trends as LBO is approached (Fig. 6.11a). $maxpers(D)$ indicates the lifetime of the most persistent loop in the topological space. Lifetime i.e. persistent of a loop, in turn, is dependent upon the scale of the loop as the larger a loop the more time it requires to get filled up (i.e. die) during the Rips filtration process. Therefore, an increase in $maxpers(D)$ may be linked with the presence of a loop having a significantly higher scale (as compared to the scale of the loops corresponding to the stable combustion state). Therefore, we infer that the approach of LBO is likely to entail a shift towards increased periodicity (i.e. determinism).

In contrast with the behavior of metric $maxpers(D)$, $M(D)$ does not show any significant trend during approach of LBO (Fig. 6.11b). Previous studies report that $M(D)$ can capture the periodicity - chaos transition accurately [189]. However, the path to LBO explored in this study does not encounter a preceding thermoacoustic instability (i.e. strongly periodic dynamics). Therefore, we infer that $M(D)$ cannot capture the chaos-chaos transition during the approach of LBO when LBO occurs without preceding thermoacoustic instability.

We note that the metric $E'(D)$ may be interpreted as the Shannon entropy of the persistence of loops contained in the persistence diagram. Therefore increased dissimilarity of the persistence time of the different H_1 homology classes would lead to a reduction in $E'(D)$ and increased similarity of the persistence time would increase $E'(D)$. In the present study, we observe the $E'(D)$ to reduce with an almost monotonic trend as LBO is approached (Fig. 6.11c). This simply indicates that the persistence of the different loops contained in the persistent diagram gradually becomes dissimilar as LBO is approached. This fact is easily explained. At the stable combustion state ($\phi/\phi_{LBO} = 1.41$), the different loops contained in

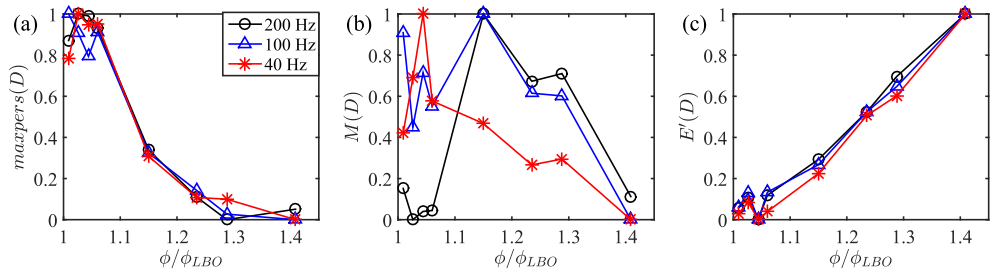

Figure 6.11: (a), (b) and (c) indicate the persistent metrics: $maxpers(D)$, $M(D)$, and $E'(D)$ respectively, for the single-burner combustor (F1 case) at various equivalence ratios.

the persistent diagram are likely to have similar persistences, a fact that can be seen from the relatively small region that the blue dots occupy on the persistent diagram (Fig. 6.9a). Therefore, the high value of $E'(D)$ in the stable combustion state is expected. In the near-LBO regime, (i) the blue dots occupy a larger region in the persistent diagram (Fig. 6.9b) and (ii) several points are at relatively higher distances from the diagonal line (as compared to the stable combustion state). Therefore, in the near-LBO regime, $E'(D)$ reduces as few of the loops (i.e. few of the H_1 homology classes) become significantly more persistent as compared to the other H_1 homology classes. Finally, from an information science perspective, because Shannon entropy is linked to the complexity of the underlying system, we can also say that the complexity of the underlying dynamics reduces as the combustor approaches LBO.

Due to the almost monotonic nature of the trends of the TDA metrics $maxpers(D)$ and $E'(D)$ during the approach to LBO, we infer that they can be used to early predict LBO. In a practical situation, the warning of impending LBO would be issued when an early prediction metric crosses the previously chosen threshold. The monotonic trends of the TDA metrics enable fine-tuning of the TDA metric thresholds so that the early LBO warning can be issued at an optimal safety margin. In practical combustors, optimal LBO safety margin may depend on various operational constraints including hardware limitations and the timescale of the phenomena. Therefore, the ability to fine-tune the LBO safety margin is a highly desirable property in an early LBO prediction tool, from the practical implementation point of view. Next, we explore the dynamical transition in multi-burner combustors with TDA, to check whether the TDA metrics are effective in early detecting LBO in multi-burner combustors.

Figure 6.12 shows the variation in the three TDA metrics, $maxpers(D)$, $M(D)$, and $E'(D)$, during the transition to LBO for the AC-F1 case. On the other hand, the Fig. 6.13 shows the variation of the $maxpers(D)$, $M(D)$, and $E'(D)$ for

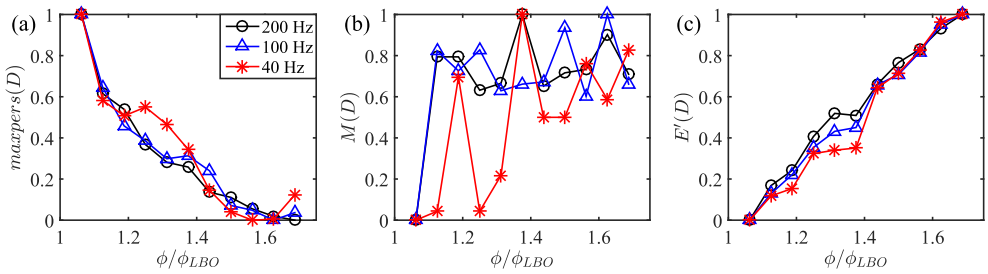

Figure 6.12: (a), (b) and (c) indicate the persistent metrics: $maxpers(D)$, $M(D)$, and $E'(D)$ respectively, for the AC-F1 case.

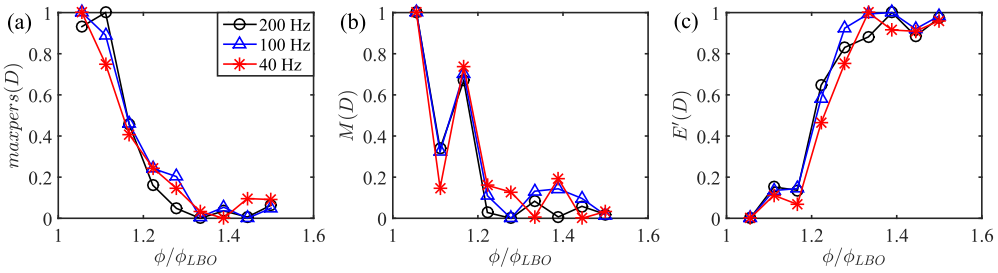

Figure 6.13: (a), (b) and (c) indicate the persistent metrics: $maxpers(D)$, $M(D)$, and $E'(D)$ respectively, for the LAC-F1-55 case.

the LAC-F1-55 case. In both cases, the TDA metrics $maxpers(D)$ and $E'(D)$ show almost monotonic trends as LBO is approached. The trends of the metrics $maxpers(D)$ and $E'(D)$ are qualitatively similar to those observed for the single-burner combustor. These results indicate a qualitatively similar dynamical transition to LBO in the AC-F1, LAC-F1-55, and the single-burner cases. In contrast, in all three cases, $M(D)$ exhibits poor sensitivity to the approach of LBO, corroborating our inference that $M(D)$ is not a suitable metric for early LBO detection when LBO occurs without preceding thermoacoustic instability. In short, TDA metrics $maxpers(D)$ and $E'(D)$ are likely to be effective as early LBO prediction tools in single cup as well as multi-burner combustors. Further, the monotonic trends of the TDA metrics enable fine-tuning of the LBO safety margin for the multi-burner combustors also.

Next, we check the trends of the TDA metrics $maxpers(D)$ and $E'(D)$ for various under-sampling factors (Figs. 6.11, 6.12, and 6.13). The results reveal that $maxpers(D)$ and $E'(D)$ exhibit quite similar trends with approach of LBO, even for a significantly low sampling rate (50 Hz). This fact indicates that low-sampling rate sensors can be used to acquire the combustor signal without affecting the TDA's effectiveness as an early LBO detection tool. A lower sampling rate sensor is likely to be less sophisticated and therefore a low cost and rugged instrument. A low cost and rugged sensor is highly desirable for practical implementation

ϕ/ϕ_{LBO}	1.6875	1.625	1.5625	1.5	1.4375	1.375	1.3125	1.25	1.1875	1.125	1.0625
t for 200 Hz signal	26.5	26.9	27	26.5	26.3	25.8	27.4	27.3	27.3	26.4	24.8
t for 100 Hz signal	9.1	6.5	6.4	6.2	6	6.3	6	6.3	6.2	6	5.3
t for 50 Hz signal	1.4	1.3	1.3	1.3	1.4	1.3	1.3	1.3	1.4	1.4	1.2

Table 6.2: Computational time t (in seconds) of the three TDA metrics, for the AC-F1 case. The time window considered for calculation is 20 seconds. The computational time shown here is the cumulative time for calculation of the three TDA metrics and includes the computational time for phase space embedding.

as the sensors installed on gas turbine combustors are likely to be exposed to highly corrosive environment along with high temperature and pressure. A lower sampling rate also reduces the computational time for calculating the various TDA metrics in a significant way (table 6.2). This is highly advantageous from practical point of view. For example, if the time series of 20 seconds duration is under-sampled by a factor of 10 (i.e. the sampling rate of the CH* time series is reduced to 200 Hz), calculation of TDA metrics requires 25-27 seconds (table 6.2). On the other hand, under-sampling by a factor of 20 (i.e. the sampling rate of the CH* time series is reduced to 100 Hz) requires 5-9 seconds of computational time and under-sampling by a factor of 40 (i.e. the sampling rate of the CH* time series is reduced to 50 Hz) requires 1.2-1.4 seconds. Therefore, the TDA metrics may be applicable as real time early LBO prediction tools with a reduced sampling rate.

6.3.4 Practical strategy for early detection of LBO using TDA

As discussed above, the TDA tool is computationally inexpensive. However, a disadvantage of such a tool is the need for properly embedding the time series in phase space. Therefore, it is worthwhile to check the efficacy of the TDA tool without optimally embedding the time series in phase space. One technique to implement TDA without phase-space embedding is the sub-level set TDA approach, where TDA is applied to the original time series itself.

Figure 6.14 shows that the TDA metrics calculated with sub-level set approach follow quite similar trends as compared with TDA metrics calculated with proper embedding (Fig. 6.12). In this scenario also, $maxpers(D_S)$ and $E'(D_S)$ show a monotonic trend during transition to LBO. Here, we note that D_S indicates the persistence diagram obtained with sub-level set approach. Therefore, the sub-level set TDA metrics $maxpers(D_S)$ and $E'(D_S)$ can be used to monitor the LBO limit. Further, a fine-tuning of safety margin can be done with careful threshold selection of the TDA metrics $maxpers(D_S)$ and $E'(D_S)$. As seen from table 6.3, the computational time for the TDA metrics, when calculated with this technique,

ϕ/ϕ_{LBO}	1.6875	1.625	1.5625	1.5	1.4375	1.375	1.3125	1.25	1.1875	1.125	1.0625
t for 200 Hz signal	1.9	2	2.1	2.1	2.1	2	2.1	2.1	2.1	2	2.1
t for 50 Hz signal	1.4	1.3	1.3	1.3	1.4	1.3	1.3	1.3	1.4	1.4	1.2

Table 6.3: Computational time t (in seconds) of the three TDA metrics, for the AC-F1 case, calculated with the sub-level set time series approach. The time window considered for calculation is 20 seconds. The computational time shown here is the cumulative time for calculation of the three TDA metrics $maxpers(D_S)$, $M(D_S)$, and $E'(D_S)$.

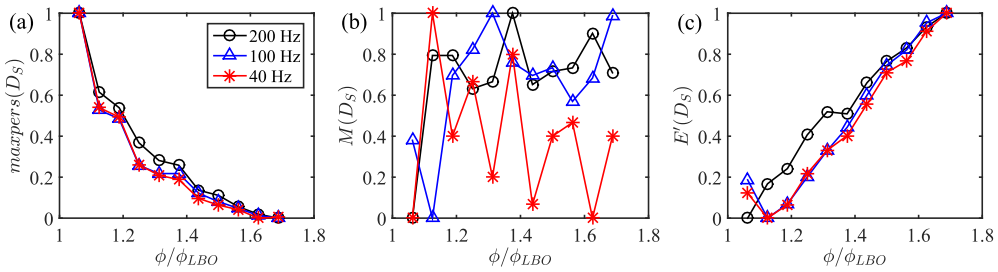

Figure 6.14: (a), (b) and (c) indicate the sub-level set TDA metrics $maxpers(D_S)$, $M(D_S)$, and $E'(D_S)$ respectively, for the AC-F1 case.

is significantly less. For example, the computational time is $\approx$ 2 seconds for the 200 Hz signal (i.e. when the CH* signal is under-sampled by a factor of 10) and $\approx$ 1.4 seconds for the 50 Hz signal (i.e. when the CH* signal is under-sampled by a factor of 40). These facts, along with the additional benefit that no embedding is required, indicate that the sub-level set approach to TDA might be more suitable as an online early LBO prediction tool in practical scenarios.

6.4 Chapter summary

Online monitoring of combustion dynamics may enable early prediction of lean blowout and help the combustor run more safely and reliably. Previously suggested early LBO detection tools have mostly been developed based on experimental data from single-burner combustors. However, recent literature has found significant differences in the dynamical behavior of multi-burner and single-burner combustors. In light of this, it is worthwhile to study the efficacies of the well-established early LBO prediction tools for multiple-burner combustors.

We find that some of the established tools may not be suitable for early detecting LBO in multi-burner combustors. Thus in this study, we propose a novel technique, topological data analysis (TDA), for early LBO prediction in multi-burner combustors. TDA studies the persistent topological features of phase-space embedded chemiluminescence time series. TDA searches for patterns in the data on all possible scales; consequently it does not require a previously set threshold

to search for patterns in the data. Therefore, TDA is a robust dynamical tool and is resistant to noise in the data. The results obtained in this chapter show TDA to be an effective early LBO predictor for single-burner and multi-burner combustors.

Moreover, we observe that TDA metrics $maxpers(D)$ and $E'(D)$ follow monotonic trends during the transition to LBO. Such monotonic trends would enable fine-tuning of the LBO safety margin (the safety margin at which early warning of impending LBO would be issued) which is a very useful feature in an early detection tool from practical implementation point of view. The LBO safety margin can be set by selecting suitable thresholds of TDA metrics so that crossing the thresholds will issue an early LBO warning. The ability to fine-tune the LBO safety margin, based on the time-scale of the LBO phenomena, operational constraints, and hardware limitations, is a highly desirable feature in a real-time early detection tool. Fine-tuning the safety margin will also enable optimal operation of the combustor, for example (i) minimizing the possibility of triggering thermoacoustic instability and/or LBO, (ii) maintaining fuel economy, (iii) minimizing incomplete combustion, while also (iv) conforming to strict NO_X emission norms.

The TDA metrics are computationally cheap which highlights their suitability for real-time LBO monitoring. The TDA metrics are also seen to have closely matching monotonic trends at various sampling rates. This fact indicates that TDA may be used on data taken with low sampling rate sensors. Therefore, a low-cost, simple and rugged sensor can be used for data acquisition. Such a sensor is highly desirable from a practical application point of view, as the sensor installed on a gas turbine combustor would be exposed to a highly corrosive environment, high temperature, and pressure. Finally, we observe that the sub-level set TDA technique is highly effective as an early LBO prediction tool. Further, the sub-level set TDA metrics show approximately monotonic changes during the transition to LBO. This fact indicates that the sub-level set TDA tool is suitable for fine-tuning the LBO safety margin which is a highly desirable feature from a practical implementation point of view. The sub-level set TDA tool does not require phase-space embedding, therefore enabling easier implementation in a practical scenario.

Appendix

To correctly capture the dynamical transition using recurrence network analysis (RNA), the recurrence threshold ϵ_r has to be selected on a rigorous basis. In the present study, the algorithm suggested by Eroglu *et al.* [94] is used to select the ϵ_r. We parametrically vary ϵ_r over a suitable range and calculate the adjacency matrix $\mathbf{a}$ for each ϵ_r as described in chapter 3. Next the Laplacian matrix $\mathbf{L}$ of

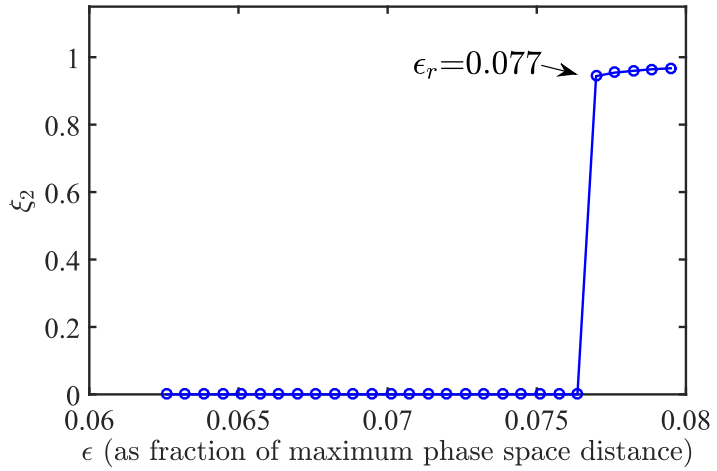

Figure 6.15: ξ_2 vs recurrence threshold (ϵ_r) at the near-LBO state ($\phi/\phi_{LBO} = 1.06$) for the AC-F1 case. ξ_2 is the second minimum Eigen value of the Laplacian matrix.

adjacency matrix **a** is calculated. The second minimum Eigen value (ξ_2) of the Laplacian matrix is calculated for each value of ϵ_r. ξ_2 is plotted against ϵ_r (Fig. 6.15) and the minimum ϵ_r at which $\xi_2 > 0$ is chosen as the optimal ϵ_r. The theoretical justification behind this algorithm is that when $\xi_2 > 0$, no disconnected nodes remain in the recurrence network. Based on Fig. 6.15, we set the optimal $\epsilon_r = 7.7\%$ of the maximum phase space distance.

CHAPTER 7

Conclusions and future work recommendations

7.1 Conclusions of the present work

A significant number of previous studies have focused on the thermoacoustic instability (TAI) and lean blowout (LBO) phenomena in single-burner premixed combustors. However, in practical combustors, multiple interacting flames are present. Such interactions are likely to affect the dynamical transitions to LBO/TAI in a significant manner. Further, often partially premixed flames are used in practical scenarios due to space constraints and less time available for air-fuel mixing. Therefore, in this thesis, we systemically study the dynamical behavior of various types of isolated and interacting flames (premixed, partially premixed, and diffusion flames), using flame visualization and various well-established tools of dynamical science.

An important part of exploring flame behavior is to study the underlying dynamical nature of the flame. As the first step to this goal, we explore the dynamical behavior of thermoacoustic instability (TAI), which is a simple and distinct dynamical phenomenon. For this study, we use a Rijke tube test rig with inverse diffusion flame, which is a reliable low NO_X technology suitable for gas turbine combustors. TAI is characterized by large amplitude pressure oscillations in the combustor, which often damage the mechanical components of the combustor. The transition from the stable combustion state to TAI is analyzed with the recurrence network, a dynamical science-based tool. From this study, we find that the recurrence network measures can accurately capture the dynamical transition from the stable combustion state to TAI. Various novel intermediate dynamical states are also found during the transition to TAI. Further, we link the recurrence network measures to the changes in recurrence network topologies, as LBO is ap-

proached, thereby improving our understanding of the different recurrence network measures. Next, we find a presence of multiple scales even during TAI. Previous literature reported the presence of a single characteristic scale at TAI corresponding to premixed flame. Further, it is seen that the network degree distribution, at the stable combustion state, does not adhere to a scale-free nature or even a single power law. Previous studies with premixed combustors, however, have observed the occurrence of scale-free and/or single power-law degree distribution at the stable combustion states. These differences in the dynamical properties, at different combustion states, may result from the inverse diffusion flame's differing mixing and scaling laws with those of premixed flames. Therefore, these results highlight the importance of studying the dynamical transition to TAI in other non-premixed and co-flow-type combustors.

Next, we study the lean blowout instability that occurs without a preceding thermoacoustic instability, using recurrence network analysis. Lean blowout (LBO) via this route is relatively unexplored, especially from the perspective of dynamical science. For this route to LBO, the dynamical change in the underlying system is subtle, as well-defined dynamical states *e.g.* periodicity, are not encountered during the approach to LBO. We aim to develop a robust early LBO detection tool that can be used on an online basis for a wide range of combustor configurations. Such a tool would enable the combustor to operate with optimal settings safely and reliably. For this study, we use a single-burner combustor as the test rig. We observe that as LBO is approached, the time series signal transforms from low amplitude aperiodic oscillations (at the stable combustion state) to an ensemble of low amplitude and high amplitude aperiodic oscillations (at the near-LBO state). We observe that the characteristics of the time series near the LBO limit are highly dependent on the degree of premixedness in the combustor. We find that the recurrence network (RN) metrics can detect the approach of LBO, irrespective of the degree of premixedness in the single-burner combustor. This fact shows that the RN is a robust and suitable early LBO detection tool for a wide range of combustor configurations. Further, the RN analysis revealed that the approach to LBO entails a shift toward periodicity. We find that the dynamic transitions to LBO with and without preceding thermoacoustic instability are significantly different. The results indicate that accurate early LBO prediction may require prior knowledge of (i) the degree of premixedness and (ii) the route to LBO. Further, we observe that the intermittent extinction-reignition events at the near-LBO state cause the power law degree distribution in the RN to break down. Finally, we show that the visible structural changes in the RN topology can be linked to the changes in the RN metrics as LBO is approached, helping to better understand the dynamical transition.

Recent studies have shown that flame-flame interplay can affect flame behavior in a significant way. Next, we study the synchronization behavior brought on by the interplay of candle flame oscillators (CFOs) that have a similar and differing amplitude of pulsations. We discover significant differences between the dynamical transitions obtained due to the interplay of similar (in terms of the amplitude of pulsations in the two interacting CFOs) and differing sets of CFOs. It is seen that in close vicinity, the interplay of a similar set of CFOs establishes in-phase synchronization (IP). However, the interplay of a differing set of CFOs produces a lag-synchronization (LS) state when the CFOs are in close vicinity. Further, the interplay of a similar set of CFOs results in amplitude death (AD) across the operational range, except in close vicinity. In contrast, the interplay of a differing set of CFOs is seen to result in dynamically rich transitions, consisting of multiple AD and LS regimes and a PAD regime. In short, the dynamical transition due to the interplay of a similar set of CFOs is simple whereas that for a differing set of CFOs is highly complex. This study might help to better understand the synchronization phenomena encountered in real-world scenarios, caused by flame-flame interplay.

Flame visualization is important to understand LBO combustion physics, which is often highly complex in turbulent combustors. Next, we visually examine the multi-burner combustors' flame dynamics during the transition to LBO. We observe significant changes in the flame structure as LBO is approached. It is seen that the flame-to-flame interactions and burner-to-burner interactions start to occur only close to the LBO limit. It is seen that the flame-to-flame and burner-to-burner interactions reduce the severity of the extinction events in the combustor at the near-LBO state. Often a lifted flame is seen to be anchored (and thus prevented from blowing out) by the flame from an adjacent burner. Further, an extinguished burner is often reignited by the flame from an adjacent burner. The lift-off and subsequent weakening of a flame are often accompanied by the lift-off and weakening of the adjacent flame. Partial attachment-detachment of flame from burner tip, flame merging-unmerging, partial extinction-reignition events, flame-to-flame interaction (for example, anchoring of the lifted flame by the adjacent flame), and burner-to-burner interactions (for example, reignition of extinguished burner by the adjacent flame), etc. phenomena are seen at the near-LBO state for the annular and linear array combustors, which cannot be captured in single-burner combustors. These facts highlight the importance of further study on the lean blowout phenomenon in multi-burner combustors. On the other hand, we find closely similar flame dynamics, in the annular and linear array combustors, at the near-LBO state. This indicates that the linear array configuration may be used as a proxy for studying the transition to LBO in the annular combustors.

The insights obtained from the flame visualization study may be useful for further exploration of the near-LBO dynamics in multi-burner combustors, for example, with sophisticated time series and/or image analysis tools.

Previously suggested early LBO detection tools have mostly been developed based on experimental data from single-burner combustors. However, recent literature has found significant differences in the flame dynamics of multi-burner and single-burner combustors at the near-LBO state. In light of this, it is worthwhile to study the efficacies of the well-established early LBO prediction tools for multiple-burner combustors. Indeed, we find that some of the established tools may not be suitable for early detecting LBO in multi-burner combustors. Thus, we propose a novel technique, topological data analysis (TDA), for early LBO prediction in multi-burner combustors. TDA is a robust dynamical tool and is resistant to noise in the data. The results obtained during this study show TDA to be an effective early LBO predictor for single-burner and multi-burner combustors. Further, the monotonic trends of the TDA metrics during the transition to LBO may enable fine-tuning of the LBO safety margin which is a useful feature in an early detection tool, from a practical implementation point of view. We find that the TDA metrics are computationally cheap which highlights their suitability for real-time LBO monitoring. Further, the results indicate that TDA may be used with data taken with low sampling rate sensors. Therefore, a low-cost, simple and rugged sensor can be used for data acquisition. Finally, we observe that a variation of the TDA technique: the sub-level set TDA tool is also effective as an early LBO prediction tool. This approach to TDA does not require phase-space embedding, is computationally very inexpensive, and therefore, is easy to implement in a practical scenario. Further, the monotonic trends of the sub-level set TDA metrics indicate that fine-tuning of the LBO safety margin can be achieved with this technique also.

This study explores the flame behavior in various configurations, in the presence and absence of flame-flame interactions, using flame visualization and well-established dynamical science-based tools. Several insights are obtained during this thesis work which may prove useful in understanding the TAI and LBO instabilities in practical gas turbine combustors.

7.2 Scope for future works

The study on the TAI phenomenon for a Rijke tube with inverse diffusion flame reveals significant differences in scaling laws at TAI between this configuration and those previously reported for premixed configurations. Further, few relatively novel intermediate states, between high dimensional chaos and periodicity (at

thermoacoustic instability), are found in this study. Therefore, future studies may focus on studying the scaling laws and the novel intermediate dynamical states (i) by parametrically varying the air and fuel flow, (ii) by introducing a swirler to alter the flow field inside the Rijke tube, and (iii) by prior mixing of a fraction of the LPG flow in the oxidizer stream to alter the degree of premixedness of the inverse diffusion flame. Further, a detailed numerical study may help to understand the presence of both the slow and fast timescales at the thermoacoustic instability.

Significant variations are seen in the candle flame dynamics due to the interplay of similar and differing sets of CFOs. For the interplay of a differing set of CFOs, a rich dynamical transition is seen as the distance between the CFOs is varied. Future work may focus on a detailed numerical study of interacting candle flames, which is likely to provide sound reasoning behind the dynamical transition obtained. Such a study may also lead to improved reduced-order modeling that can capture the complex dynamical transitions reported in this thesis.

In 2-D flame images of the annular combustor, flames positioned at different planes overlap with each other, creating difficulties in flame visualization. A more elaborate exploration of the flame interaction in the annular combustor can be done by incorporating slight changes in the experimental test rig. These include, (i) replacing the inner quartz tube with a solid metal body and (ii) increasing the diameter of the inner metal body. Further, (iii) it is worthwhile to see the effects of varying the swirl number of the burners on the interaction of flames. Next, (iv) the spacer arrangement in the linear array combustor may be modified to enable a more detailed study of the effect of distance between the burners on the flame behavior at various equivalence ratios.

In this thesis work, time series analysis based on data obtained from multi-burner combustors is carried out. These results reveal that the presence of multiple flames is likely to affect the efficacy of the various early LBO prediction tools. Therefore, the sensitivities and efficacies of the various well-established early LBO/TAI detection tools may be explored with these multi-burner combustors. Finally, future studies may modify and augment the various nonlinear dynamical science-based tools to detect LBO/TAI with non-stationary time series data, as opposed to quasi-steady data.

Bibliography

[1] A. H. Lefebvre, *Gas turbine combustion*. CRC press, 1998.

[2] A. Mukhopadhyay, R. R. Chaudhari, T. Paul, S. Sen, and A. Ray, "Lean blow-out prediction in gas turbine combustors using symbolic time series analysis," *Journal of Propulsion and Power*, vol. 29, no. 4, pp. 950–960, 2013.

[3] R. Sujith and V. R. Unni, "Complex system approach to investigate and mitigate thermoacoustic instability in turbulent combustors," *Physics of Fluids*, vol. 32, no. 6, p. 061 401, 2020.

[4] L. Vanquickenborne and A. Van Tiggelen, "The stabilization mechanism of lifted diffusion flames," *Combustion and Flame*, vol. 10, no. 1, pp. 59–69, 1966.

[5] J. W. S. B. Rayleigh, *The theory of sound*. Macmillan, 1896, vol. 2.

[6] Y. Huang and V. Yang, "Dynamics and stability of lean-premixed swirl-stabilized combustion," *Progress in energy and combustion science*, vol. 35, no. 4, pp. 293–364, 2009.

[7] G. A. Richards, J. D. Thornton, E. H. Robey, and L. Arellano, "Open-Loop Active Control of Combustion Dynamics on a Gas Turbine Engine," *Journal of Engineering for Gas Turbines and Power*, vol. 129, no. 1, pp. 38–48, Mar. 2006, ISSN: 0742-4795. DOI: 10.1115/1.2204978.

[8] H. Gotoda, M. Amano, T. Miyano, T. Ikawa, K. Maki, and S. Tachibana, "Characterization of complexities in combustion instability in a lean premixed gas-turbine model combustor," *Chaos: An Interdisciplinary Journal of Nonlinear Science*, vol. 22, no. 4, p. 043 128, 2012.

[9] G. Boudier, L. Gicquel, T. Poinsot, D. Bissieres, and C. Bérat, "Comparison of les, rans and experiments in an aeronautical gas turbine combustion chamber," *Proceedings of the Combustion Institute*, vol. 31, no. 2, pp. 3075–3082, 2007.

[10] G. Staffelbach, L. Gicquel, G. Boudier, and T. Poinsot, "Large eddy simulation of self excited azimuthal modes in annular combustors," *Proceedings of the Combustion Institute*, vol. 32, no. 2, pp. 2909–2916, 2009.

[11] P. Wolf, G. Staffelbach, L. Y. Gicquel, J.-D. Müller, and T. Poinsot, "Acoustic and large eddy simulation studies of azimuthal modes in annular combustion chambers," *Combustion and Flame*, vol. 159, no. 11, pp. 3398–3413, 2012.

[12] A. S. Morgans and S. R. Stow, "Model-based control of combustion instabilities in annular combustors," *Combustion and flame*, vol. 150, no. 4, pp. 380–399, 2007.

[13] N. Noiray, M. Bothien, and B. Schuermans, "Investigation of azimuthal staging concepts in annular gas turbines," *Combustion Theory and Modelling*, vol. 15, no. 5, pp. 585–606, 2011.

[14] S. J. Illingworth, A. S. Morgans, and C. W. Rowley, "Feedback control of cavity flow oscillations using simple linear models," *Journal of Fluid Mechanics*, vol. 709, pp. 223–248, 2012.

[15] M. Bauerheim, J.-F. Parmentier, P. Salas, F. Nicoud, and T. Poinsot, "An analytical model for azimuthal thermoacoustic modes in an annular chamber fed by an annular plenum," *Combustion and Flame*, vol. 161, no. 5, pp. 1374–1389, 2014.

[16] G. Campa and S. M. Camporeale, "Prediction of the thermoacoustic combustion instabilities in practical annular combustors," *Journal of Engineering for Gas Turbines and Power*, vol. 136, no. 9, 2014.

[17] J.-F. Bourgouin, D. Durox, J. P. Moeck, T. Schuller, and S. Candel, "Characterization and modeling of a spinning thermoacoustic instability in an annular combustor equipped with multiple matrix injectors," *Journal of Engineering for Gas Turbines and Power*, vol. 137, no. 2, 2015.

[18] S. Chaudhuri and B. M. Cetegen, "Blowoff characteristics of bluff-body stabilized conical premixed flames with upstream spatial mixture gradients and velocity oscillations," *Combustion and flame*, vol. 153, no. 4, pp. 616–633, 2008.

[19] M. Stöhr, I. Boxx, C. Carter, and W. Meier, "Dynamics of lean blowout of a swirl-stabilized flame in a gas turbine model combustor," *Proceedings of the Combustion Institute*, vol. 33, no. 2, pp. 2953–2960, 2011.

[20] J. Lepers, W. Krebs, B. Prade, P. Flohr, G. Pollarolo, and A. Ferrante, "Investigation of thermoacoustic stability limits of an annular gas turbine combustor test-rig with and without helmholtz-resonators," in *Turbo Expo: Power for Land, Sea, and Air*, vol. 4725, 2005, pp. 177–189.

[21] G. Gelbert, J. P. Moeck, C. O. Paschereit, and R. King, "Feedback control of unstable thermoacoustic modes in an annular rijke tube," *Control Engineering Practice*, vol. 20, no. 8, pp. 770–782, 2012.

[22] G. Ghirardo and M. P. Juniper, "Azimuthal instabilities in annular combustors: Standing and spinning modes," *Proceedings of the Royal Society A: Mathematical, Physical and Engineering Sciences*, vol. 469, no. 2157, p. 20 130 232, 2013.

[23] J. R. Dawson and N. A. Worth, "Flame dynamics and unsteady heat release rate of self-excited azimuthal modes in an annular combustor," *Combustion and Flame*, vol. 161, no. 10, pp. 2565–2578, 2014.

[24] N. A. Worth and J. R. Dawson, "Modal dynamics of self-excited azimuthal instabilities in an annular combustion chamber," *Combustion and Flame*, vol. 160, no. 11, pp. 2476–2489, 2013.

[25] J.-F. Bourgouin, D. Durox, T. Schuller, J. Beaunier, and S. Candel, "Ignition dynamics of an annular combustor equipped with multiple swirling injectors," *Combustion and Flame*, vol. 160, no. 8, pp. 1398–1413, 2013.

[26] E. Machover and E. Mastorakos, "Spark ignition of annular non-premixed combustors," *Experimental Thermal and Fluid Science*, vol. 73, pp. 64–70, 2016.

[27] E. Machover and E. Mastorakos, "Experimental investigation on spark ignition of annular premixed combustors," *Combustion and Flame*, vol. 178, pp. 148–157, 2017.

[28] S. Nair and T. Lieuwen, "Acoustic detection of blowout in premixed flames," *Journal of Propulsion and Power*, vol. 21, no. 1, pp. 32–39, 2005.

[29] T. Muruganandam, S. Nair, D. Scarborough, *et al.*, "Active control of lean blowout for turbine engine combustors," *Journal of Propulsion and Power*, vol. 21, no. 5, pp. 807–814, 2005.

[30] T. Yi and E. J. Gutmark, "Combustion instabilities and control of a multiswirl atmospheric combustor," *Journal of Engineering for Gas Turbines and Power*, vol. 129, pp. 31–37, 2007.

[31] R. K. Bompelly, "Lean blowout and its robust sensing in swirl combustors," Ph.D. dissertation, Georgia Institute of Technology, 2013.

[32] R. R. Chaudhari, R. P. Sahu, S. Ghosh, A. Mukhopadhyay, and S. Sen, "Flame color as a lean blowout predictor," *International Journal of Spray and Combustion Dynamics*, vol. 5, no. 1, pp. 49–65, 2013.

[33] S. Sarkar, A. Ray, A. Mukhopadhyay, and S. Sen, "Dynamic data-driven prediction of lean blowout in a swirl-stabilized combustor," *International Journal of Spray and Combustion Dynamics*, vol. 7, no. 3, pp. 209–241, 2015.

[34] S. Mondal, S. De, A. Mukhopadhyay, S. Sen, and A. Ray, "Early prediction of lean blowout from chemiluminescence time series data," *Combustion Science and Technology*, vol. 194, no. 6, pp. 1108–1135, 2022.

[35] C. Bhattacharya, J. O'Connor, and A. Ray, "Data-driven detection and early prediction of thermoacoustic instability in a multi-nozzle combustor," *Combustion Science and Technology*, vol. 194, no. 7, pp. 1481–1512, 2022.

[36] L. Kabiraj and R. Sujith, "Nonlinear self-excited thermoacoustic oscillations: Intermittency and flame blowout," *Journal of Fluid Mechanics*, vol. 713, no. 376-397, p. 13, 2012.

[37] H. Gotoda, H. Nikimoto, T. Miyano, and S. Tachibana, "Dynamic properties of combustion instability in a lean premixed gas-turbine combustor," *Chaos: An Interdisciplinary Journal of Nonlinear Science*, vol. 21, no. 1, p. 013 124, 2011.

[38] H. Gotoda, Y. Shinoda, M. Kobayashi, Y. Okuno, and S. Tachibana, "Detection and control of combustion instability based on the concept of dynamical system theory," *Physical Review E*, vol. 89, no. 2, p. 022 910, 2014.

[39] H. Gotoda, H. Kinugawa, R. Tsujimoto, S. Domen, and Y. Okuno, "Characterization of combustion dynamics, detection, and prevention of an unstable combustion state based on a complex-network theory," *Physical Review Applied*, vol. 7, no. 4, p. 044 027, 2017.

[40] V. Nair and R. Sujith, "Intermittency as a transition state in combustor dynamics: An explanation for flame dynamics near lean blowout," *Combustion Science and Technology*, vol. 187, no. 11, pp. 1821–1835, 2015.

[41] V. R. Unni and R. I. Sujith, "Precursors to blowout in a turbulent combustor based on recurrence quantification," in *52nd AIAA/SAE/ASEE Joint Propulsion Conference*, 2016, p. 4649.

[42] S. De, A. Bhattacharya, S. Mondal, A. Mukhopadhyay, and S. Sen, "Application of recurrence quantification analysis for early detection of lean blowout in a swirl-stabilized dump combustor," *Chaos: An Interdisciplinary Journal of Nonlinear Science*, vol. 30, no. 4, p. 043 115, 2020.

[43] V. R. Unni and R. Sujith, "Multifractal characteristics of combustor dynamics close to lean blowout," *Journal of Fluid Mechanics*, vol. 784, pp. 30–50, 2015.

[44] U. Sen, T. Gangopadhyay, C. Bhattacharya, A. Mukhopadhyay, and S. Sen, "Dynamic characterization of a ducted inverse diffusion flame using recurrence analysis," *Combustion Science and Technology*, vol. 190, no. 1, pp. 32–56, 2018.

[45] B.-J. LEE*, J.-S. Kim, and S. Lee, "Enhancement of blowout limit by the interaction of multiple nonpremixed jet flames," *Combustion science and technology*, vol. 176, no. 4, pp. 481–497, 2004.

[46] D. Fanaca, P. Alemela, C. Hirsch, and T. Sattelmayer, "Comparison of the flow field of a swirl stabilized premixed burner in an annular and a single burner combustion chamber," *Journal of Engineering for Gas Turbines and Power*, vol. 132, no. 7, 2010.

[47] D. M. Forrester, "Arrays of coupled chemical oscillators," *Scientific reports*, vol. 5, p. 16 994, 2015.

[48] H. Kitahata, J. Taguchi, M. Nagayama, *et al.*, "Oscillation and synchronization in the combustion of candles," *The Journal of Physical Chemistry A*, vol. 113, no. 29, pp. 8164–8168, 2009.

[49] Y. Nagamine, K. Otaka, H. Zuiki, H. Miike, and A. Osa, "Mechanism of candle flame oscillation: Detection of descending flow above the candle flame," *Journal of the Physical Society of Japan*, vol. 86, no. 7, p. 074 003, 2017.

[50] K. Manoj, S. A. Pawar, and R. Sujith, "Experimental evidence of amplitude death and phase-flip bifurcation between in-phase and anti-phase synchronization," *Scientific reports*, vol. 8, no. 1, pp. 1–7, 2018.

[51] S. Dange, K. Manoj, S. Banerjee, S. A. Pawar, S. Mondal, and R. Sujith, "Oscillation quenching and phase-flip bifurcation in coupled thermoacoustic systems," *Chaos: An Interdisciplinary Journal of Nonlinear Science*, vol. 29, no. 9, p. 093 135, 2019.

[52] S. Dange, S. A. Pawar, K. Manoj, and R. Sujith, "Role of buoyancy-driven vortices in inducing different modes of coupled behaviour in candle-flame oscillators," *AIP Advances*, vol. 9, no. 1, p. 015 119, 2019.

[53] T. Chen, X. Guo, J. Jia, and J. Xiao, "Frequency and phase characteristics of candle flame oscillation," *Scientific reports*, vol. 9, no. 1, pp. 1–13, 2019.

[54] N. A. Worth and J. R. Dawson, "Cinematographic oh-plif measurements of two interacting turbulent premixed flames with and without acoustic forcing," *Combustion and Flame*, vol. 159, no. 3, pp. 1109–1126, 2012.

[55] R. Ciardiello, A. W. Skiba, R. L. Gordon, and E. Mastorakos, "Experimental assessment of the lean blow-off in a fully premixed annular combustor," *Experimental Thermal and Fluid Science*, vol. 112, p. 109 994, 2020.

[56] R. Ciardiello, R. S. Pathania, I. El Helou, and E. Mastorakos, "Lean blow-off investigation in a linear multi-burner combustor operated in premixed and non-premixed modes," *Applications in Energy and Combustion Science*, vol. 9, p. 100 041, 2022.

[57] V. Godavarthi, V. Unni, E. Gopalakrishnan, and R. Sujith, "Recurrence networks to study dynamical transitions in a turbulent combustor," *Chaos: An Interdisciplinary Journal of Nonlinear Science*, vol. 27, no. 6, p. 063 113, 2017.

[58] P. Kasthuri, V. R. Unni, and R. Sujith, "Bursting and mixed mode oscillations during the transition to limit cycle oscillations in a matrix burner," *Chaos: An Interdisciplinary Journal of Nonlinear Science*, vol. 29, no. 4, p. 043 117, 2019.

[59] V. Nair, G. Thampi, and R. Sujith, "Intermittency route to thermoacoustic instability in turbulent combustors," *Journal of Fluid Mechanics*, vol. 756, p. 470, 2014.

[60] V. Godavarthi, S. A. Pawar, V. R. Unni, R. Sujith, N. Marwan, and J. Kurths, "Coupled interaction between unsteady flame dynamics and acoustic field in a turbulent combustor," *Chaos: An Interdisciplinary Journal of Nonlinear Science*, vol. 28, no. 11, p. 113 111, 2018.

[61] A. P. Dowling, "Nonlinear self-excited oscillations of a ducted flame," *Journal of fluid mechanics*, vol. 346, pp. 271–290, 1997.

[62] S. J. Illingworth, I. C. Waugh, and M. P. Juniper, "Finding thermoacoustic limit cycles for a ducted burke-schumann flame," *Proceedings of the Combustion Institute*, vol. 34, no. 1, pp. 911–920, 2013.

[63] M. Tyagi, S. Chakravarthy, and R. Sujith, "Unsteady combustion response of a ducted non-premixed flame and acoustic coupling," *Combustion Theory and Modelling*, vol. 11, no. 2, pp. 205–226, 2007.

[64] O. Schafer, R. Koch, and S. Wittig, "Flashback in lean prevaporized premixed combustion: Nonswirling turbulent pipe flow study," *J. Eng. Gas Turbines Power*, vol. 125, no. 3, pp. 670–676, 2003.

[65] B. A. Rabee, "The effect of inverse diffusion flame burner-diameter on flame characteristics and emissions," *Energy*, vol. 160, pp. 1201–1207, 2018.

[66] S. Mahesh and D. Mishra, "Flame stability and emission characteristics of turbulent lpg idf in a backstep burner," *Fuel*, vol. 87, no. 12, pp. 2614–2619, 2008.

[67] S. Choi, T. Y. Kim, H. K. Kim, J. Koo, J. S. Kim, and O. C. Kwon, "Properties of inverse nonpremixed pure o2/ch4 coflow flames in a model combustor," *Energy*, vol. 93, pp. 1105–1115, 2015.

[68] L. Sze, C. Cheung, and C. Leung, "Appearance, temperature, and nox emission of two inverse diffusion flames with different port design," *Combustion and flame*, vol. 144, no. 1-2, pp. 237–248, 2006.

[69] J. Miao, C. Leung, C. Cheung, Z. Huang, and W. Jin, "Effect of h2 addition on oh distribution of lpg/air circumferential inverse diffusion flame," *international journal of hydrogen energy*, vol. 41, no. 22, pp. 9653–9663, 2016.

[70] Y. Choy, H. Zhen, C. Leung, and H. Li, "Pollutant emission and noise radiation from open and impinging inverse diffusion flames," *Applied energy*, vol. 91, no. 1, pp. 82–89, 2012.

[71] C. Kaplan and K. Kailasanath, "Flow-field effects on soot formation in normal and inverse methane–air diffusion flames," *Combustion and Flame*, vol. 124, no. 1-2, pp. 275–294, 2001.

[72] D. M. STANSEL, N. M. LAURENDEAU, and D. W. SENSER, "Co and nox emissions from a controlled-air burner: Experimental measurements and exhaust correlations," *Combustion science and technology*, vol. 104, no. 4-6, pp. 207–234, 1995.

[73] G. W. Sidebotham and I. Glassman, "Flame temperature, fuel structure, and fuel concentration effects on soot formation in inverse diffusion flames," *Combustion and flame*, vol. 90, no. 3-4, pp. 269–283, 1992.

[74] A.-M. Kypraiou, N. Worth, and E. Mastorakos, "Experimental investigation of the response of premixed and non-premixed turbulent flames to acoustic forcing," in *54th AIAA aerospace sciences meeting*, 2016, p. 2156.

[75] K. T. Kim, J. G. Lee, B. D. Quay, and D. Santavicca, "Response of partially premixed flames to acoustic velocity and equivalence ratio perturbations," *Combustion and Flame*, vol. 157, no. 9, pp. 1731–1744, 2010.

[76] L. Dong, C. Cheung, and C. Leung, "Heat transfer characteristics of an impinging inverse diffusion flame jet–part i: Free flame structure," *International journal of heat and mass transfer*, vol. 50, no. 25-26, pp. 5108–5123, 2007.

[77] V. Hariharan and D. P. Mishra, "Experimental characterization of circumferentially arranged fuel port inverse jet diffusion flame burner," *Combustion Science and Technology*, pp. 1–20, 2019.

[78] R. V. Donner, Y. Zou, J. F. Donges, N. Marwan, and J. Kurths, "Recurrence networks—a novel paradigm for nonlinear time series analysis," *New Journal of Physics*, vol. 12, no. 3, p. 033 025, 2010.

[79] R. V. Donner, Y. Zou, J. F. Donges, N. Marwan, and J. Kurths, "Ambiguities in recurrence-based complex network representations of time series," *Physical Review E*, vol. 81, no. 1, p. 015 101, 2010.

[80] R. V. Donner, M. Small, J. F. Donges, *et al.*, "Recurrence-based time series analysis by means of complex network methods," *International Journal of Bifurcation and Chaos*, vol. 21, no. 04, pp. 1019–1046, 2011.

[81] N. Marwan, J. F. Donges, Y. Zou, R. V. Donner, and J. Kurths, "Complex network approach for recurrence analysis of time series," *Physics Letters A*, vol. 373, no. 46, pp. 4246–4254, 2009.

[82] P. Bergé, Y. Pomeau, C. Vidal, D. Ruelle, and L. S. Tuckerman, "Order within chaos : Towards a deterministic approach to turbulence," 1984.

[83] J. Argyris, G. Faust, and M. Haase, "Routes to chaos and turbulence. a computational introduction," *Philosophical Transactions of the Royal Society of London. Series A: Physical and Engineering Sciences*, vol. 344, no. 1671, pp. 207–234, 1993.

[84] R. Jacob, K. Harikrishnan, R. Misra, and G. Ambika, "Recurrence network measures for hypothesis testing using surrogate data: Application to black hole light curves," *Communications in Nonlinear Science and Numerical Simulation*, vol. 54, pp. 84–99, 2018.

[85] H. Lange and S. Boese, "Recurrence quantification and recurrence network analysis of global photosynthetic activity," in *Recurrence Quantification Analysis*, Springer, 2015, pp. 349–374.

[86] R. Jacob, K. Harikrishnan, R. Misra, and G. Ambika, "Characterization of chaotic attractors under noise: A recurrence network perspective," *Communications in Nonlinear Science and Numerical Simulation*, vol. 41, pp. 32–47, 2016.

[87] M. Murugesan and R. Sujith, "Combustion noise is scale-free: Transition from scale-free to order at the onset of thermoacoustic instability," *Journal of Fluid Mechanics*, vol. 772, pp. 225–245, 2015.

[88] S. Boccaletti, V. Latora, Y. Moreno, M. Chavez, and D. Hwang, *Complex networks: Structure and dynamics, physical reports 424 (4/5): 175–308*, 2006.

[89] M. Newman, *Networks*. Oxford university press, 2018.

[90] K. Matveev and F. Culick, "A study of the transition to instability in a rijke tube with axial temperature gradient," *Journal of Sound and Vibration*, vol. 264, no. 3, pp. 689–706, 2003.

[91] F. Takens, "Detecting strange attractors in turbulence," in *Dynamical systems and turbulence, Warwick 1980*, Springer, 1981, pp. 366–381.

[92] H. Kantz and T. Schreiber, *Nonlinear time series analysis*. Cambridge university press, 2004, vol. 7.

[93] L. Cao, "Practical method for determining the minimum embedding dimension of a scalar time series," *Physica D: Nonlinear Phenomena*, vol. 110, no. 1-2, pp. 43–50, 1997.

[94] D. Eroglu, N. Marwan, S. Prasad, and J. Kurths, "Finding recurrence networks' threshold adaptively for a specific time series," *Nonlinear Processes in Geophysics*, 2014.

[95] N. Marwan, M. C. Romano, M. Thiel, and J. Kurths, "Recurrence plots for the analysis of complex systems," *Physics reports*, vol. 438, no. 5-6, pp. 237–329, 2007.

[96] M. Jacomy, T. Venturini, S. Heymann, and M. Bastian, "Forceatlas2, a continuous graph layout algorithm for handy network visualization designed for the gephi software," *PloS one*, vol. 9, no. 6, e98679, 2014.

[97] A. M. Eren, H. G. Morrison, P. J. Lescault, J. Reveillaud, J. H. Vineis, and M. L. Sogin, "Minimum entropy decomposition: Unsupervised oligotyping for sensitive partitioning of high-throughput marker gene sequences," *The ISME journal*, vol. 9, no. 4, pp. 968–979, 2015.

[98] M. Bastian, S. Heymann, and M. Jacomy, "Gephi: An open source software for exploring and manipulating networks," in *Third international AAAI conference on weblogs and social media*, 2009.

[99] Y. Zou, R. V. Donner, M. Thiel, and J. Kurths, "Disentangling regular and chaotic motion in the standard map using complex network analysis of recurrences in phase space," *Chaos: An Interdisciplinary Journal of Nonlinear Science*, vol. 26, no. 2, p. 023 120, 2016.

[100] M. A. Harrison and Y.-C. Lai, "Route to high-dimensional chaos," *Physical Review E*, vol. 59, no. 4, R3799, 1999.

[101] M. A. Harrison and Y.-C. Lai, "Bifurcation to high-dimensional chaos," *International Journal of Bifurcation and Chaos*, vol. 10, no. 06, pp. 1471–1483, 2000.

[102] K. Stefański, "Modelling chaos and hyperchaos with 3-d maps," *Chaos, Solitons & Fractals*, vol. 9, no. 1-2, pp. 83–93, 1998.

[103] H. Gotoda, Y. Asano, K. H. Chuah, and G. Kushida, "Nonlinear analysis on dynamic behavior of buoyancy-induced flame oscillation under swirling flow," *International Journal of Heat and Mass Transfer*, vol. 52, no. 23-24, pp. 5423–5432, 2009.

[104] H. Gotoda, K. Michigami, K. Ikeda, and T. Miyano, "Chaotic oscillation in diffusion flame induced by radiative heat loss," *Combustion Theory and Modelling*, vol. 14, no. 4, pp. 479–493, 2010.

[105] L. Kabiraj, A. Saurabh, H. Nawroth, and C. O. Paschereit, "Recurrence analysis of combustion noise," *AIAA Journal*, vol. 53, no. 5, pp. 1199–1210, 2015.

[106] V. Nair and R. Sujith, "Multifractality in combustion noise: Predicting an impending combustion instability," *Journal of Fluid Mechanics*, vol. 747, pp. 635–655, 2014.

[107] K. Venkataraman, L. Preston, D. Simons, B. Lee, J. Lee, and D. Santavicca, "Mechanism of combustion instability in a lean premixed dump combustor," *Journal of Propulsion and Power*, vol. 15, no. 6, pp. 909–918, 1999.

[108] J. Tony, E. Gopalakrishnan, E. Sreelekha, and R. Sujith, "Detecting deterministic nature of pressure measurements from a turbulent combustor," *Physical Review E*, vol. 92, no. 6, p. 062 902, 2015.

[109] R. Albert and A.-L. Barabási, "Statistical mechanics of complex networks," *Reviews of modern physics*, vol. 74, no. 1, p. 47, 2002.

[110] P. Kasthuri, I. Pavithran, A. Krishnan, *et al.*, "Recurrence analysis of slow–fast systems," *Chaos: An Interdisciplinary Journal of Nonlinear Science*, vol. 30, no. 6, p. 063 152, 2020.

[111] Y. S. Choy, H. S. Zhen, C. W. Leung, C. S. Cheung, and R. C. K. Leung, "Noise generation by open inverse diffusion flames," *Journal of Vibration and Control*, vol. 20, no. 11, pp. 1671–1681, 2014.

[112] W. C. Strahle, "Refraction, convection, and diffusion flame effectsin combustion-generated noise," in *Symposium (International) on Combustion*, Elsevier, vol. 14, 1973, pp. 527–535.

[113] R. Wayland, D. Bromley, D. Pickett, and A. Passamante, "Recognizing determinism in a time series," *Physical review letters*, vol. 70, no. 5, p. 580, 1993.

[114] P. Subramanian, S. Mariappan, R. Sujith, and P. Wahi, "Bifurcation analysis of thermoacoustic instability in a horizontal rijke tube," *International journal of spray and combustion dynamics*, vol. 2, no. 4, pp. 325–355, 2010.

[115] E. Karlis, Y. Hardalupas, and A. Taylor, "Effects of inert fuel diluents on thermoacoustic instabilities in gas turbine combustion," *AIAA Journal*, vol. 58, no. 6, pp. 2643–2657, 2020.

[116] S. Taamallah, K. Vogiatzaki, F. M. Alzahrani, E. M. Mokheimer, M. Habib, and A. F. Ghoniem, "Fuel flexibility, stability and emissions in premixed hydrogen-rich gas turbine combustion: Technology, fundamentals, and numerical simulations," *Applied energy*, vol. 154, pp. 1020–1047, 2015.

[117] H. Nicholson and J. P. Field, "Some experimental techniques for the investigation of the mechanism of flame stabilization in the wakes of bluff bodies," in *Symposium on combustion and flame, and explosion phenomena*, Elsevier, vol. 3, 1948, pp. 44–68.

[118] Y.-C. Chao, Y.-L. Chang, C.-Y. Wu, and T.-S. Cheng, "An experimental investigation of the blowout process of a jet flame," *Proceedings of the Combustion Institute*, vol. 28, no. 1, pp. 335–342, 2000.

[119] Z. Yin, I. Boxx, and W. Meier, "Influence of self-sustained jet oscillation on a confined turbulent flame near lean blow-out," *Proceedings of the Combustion Institute*, vol. 36, no. 3, pp. 3773–3781, 2017.

[120] T. Pagliaroli and G. Troiani, "Wavelet and recurrence analysis for lean blowout detection: An application to a trapped vortex combustor in thermoacoustic instability," *Physical Review Fluids*, vol. 5, no. 7, p. 073 201, 2020.

[121] H. Li, X. Zhou, J. B. Jeffries, and R. K. Hanson, "Active control of lean blowout in a swirl-stabilized combustor using a tunable diode laser," *Proceedings of the Combustion Institute*, vol. 31, no. 2, pp. 3215–3223, 2007.

[122] F. Li, L. Xu, M. Du, L. Yang, and Z. Cao, "Ion current sensing-based lean blowout detection for a pulse combustor," *Combustion and Flame*, vol. 176, pp. 263–271, 2017.

[123] T. Muruganandam, S. Nair, Y. Neumeier, T. Lieuwen, and J. Seitzman, "Optical and acoustic sensing of lean blowout precursors," in *38th AIAA/ASME/SAE/ASEE Joint Propulsion Conference & Exhibit*, 2002, p. 3732.

[124] T. Muruganandam, B. Kim, R. Olsen, *et al.*, "Chemiluminescence based sensors for turbine engines," in *39th AIAA/ASME/SAE/ASEE joint propulsion conference and exhibit*, 2003, p. 4490.

[125] M. G. De Giorgi, A. Sciolti, S. Campilongo, and A. Ficarella, "Image processing for the characterization of flame stability in a non-premixed liquid fuel burner near lean blowout," *Aerospace Science and Technology*, vol. 49, pp. 41–51, 2016.

[126] L. Chang, Z. Cao, B. Fu, Y. Lin, and L. Xu, "Lean blowout detection for bluff-body stabilized flame," *Fuel*, vol. 266, p. 117 008, 2020.

[127] J. G. Hong, K. C. Oh, U. D. Lee, and H. D. Shin, "Effect of the unmixedness of unburned gases on the pressure fluctuations in a dump combustor," *Energy & fuels*, vol. 22, no. 4, pp. 2221–2228, 2008.

[128] S. De, A. Bhattacharya, S. Mondal, A. Mukhopadhyay, and S. Sen, "Investigation of flame behavior and dynamics prior to lean blowout in a combustor with varying mixedness of reactants for the early detection of lean blowout," *International Journal of Spray and Combustion Dynamics*, vol. 11, p. 1 756 827 718 812 519, 2019.

[129] S. De, A. Biswas, A. Bhattacharya, A. Mukhopadhyay, and S. Sen, "Use of flame color and chemiluminescence for early detection of lean blowout in gas turbine combustors at different levels of fuel–air premixing," *Combustion Science and Technology*, 2019.

[130] K. T. Kim, J. G. Lee, B. D. Quay, and D. A. Santavicca, "Reconstruction of heat release response of partially premixed flames," *Combustion science and technology*, vol. 183, no. 2, pp. 122–137, 2010.

[131] S. Terhaar, B. Ćosić, C. Paschereit, and K. Oberleithner, "Suppression and excitation of the precessing vortex core by acoustic velocity fluctuations: An experimental and analytical study," *Combustion and Flame*, vol. 172, pp. 234–251, 2016.

[132] A. K. Dutta, G. Ramachandran, and S. Chaudhuri, "Investigating thermoacoustic instability mitigation dynamics with a kuramoto model for flamelet oscillators," *Physical Review E*, vol. 99, no. 3, p. 032 215, 2019.

[133] R. Jacob, K. Harikrishnan, R. Misra, and G. Ambika, "Uniform framework for the recurrence-network analysis of chaotic time series," *Physical Review E*, vol. 93, no. 1, p. 012 202, 2016.

[134] A. G. Gaydon and H. G. Wolfhard, *Flames, their structure, radiation, and temperature*. Chapman & Hall, 1979.

[135] Y. Zou, R. V. Donner, N. Marwan, J. F. Donges, and J. Kurths, "Complex network approaches to nonlinear time series analysis," *Physics Reports*, vol. 787, pp. 1–97, 2019.

[136] R. C. Hilborn *et al.*, *Chaos and nonlinear dynamics: an introduction for scientists and engineers*. Oxford University Press on Demand, 2000.

[137] N. Marwan, N. Wessel, U. Meyerfeldt, A. Schirdewan, and J. Kurths, "Recurrence-plot-based measures of complexity and their application to heart-rate-variability data," *Physical review E*, vol. 66, no. 2, p. 026 702, 2002.

[138] A. Clauset, C. R. Shalizi, and M. E. Newman, "Power-law distributions in empirical data," *SIAM review*, vol. 51, no. 4, pp. 661–703, 2009.

[139] L. Djinevski, I. Mishkovski, and D. Trajanov, "Accelerating clustering coefficient calculations on a gpu using opencl," in *International Conference on ICT Innovations*, Springer, 2010, pp. 276–285.

[140] Z. Shi and B. Zhang, "Fast network centrality analysis using gpus," *BMC bioinformatics*, vol. 12, no. 1, pp. 1–7, 2011.

[141] C. L. Staudt, A. Sazonovs, and H. Meyerhenke, "Networkit: A tool suite for large-scale complex network analysis," *Network Science*, vol. 4, no. 4, pp. 508–530, 2016.

[142] H. Jegal, K. Moon, J. Gu, L. K. Li, and K. T. Kim, "Mutual synchronization of two lean-premixed gas turbine combustors: Phase locking and amplitude death," *Combustion and Flame*, vol. 206, pp. 424–437, 2019.

[143] S. A. Pawar, A. Seshadri, V. R. Unni, and R. Sujith, "Thermoacoustic instability as mutual synchronization between the acoustic field of the confinement and turbulent reactive flow," *Journal of Fluid Mechanics*, vol. 827, pp. 664–693, 2017.

[144] S. Mondal, V. R. Unni, and R. Sujith, "Onset of thermoacoustic instability in turbulent combustors: An emergence of synchronized periodicity through formation of chimera-like states," *Journal of Fluid Mechanics*, vol. 811, p. 659, 2017.

[145] S. Mondal, S. Pawar, and R. Sujith, "Synchronous behaviour of two interacting oscillatory systems undergoing quasiperiodic route to chaos," *Chaos: An Interdisciplinary Journal of Nonlinear Science*, vol. 27, no. 10, p. 103 119, 2017.

[146] S. Murayama and H. Gotoda, "Attenuation behavior of thermoacoustic combustion instability analyzed by a complex-network-and synchronization-based approach," *Physical Review E*, vol. 99, no. 5, p. 052 222, 2019.

[147] J. P. Moeck, D. Durox, T. Schuller, and S. Candel, "Nonlinear thermoacoustic mode synchronization in annular combustors," *Proceedings of the Combustion Institute*, vol. 37, no. 4, pp. 5343–5350, 2019.

[148] Y. Guan, V. Gupta, K. Kashinath, and L. K. Li, "Open-loop control of periodic thermoacoustic oscillations: Experiments and low-order modelling in a synchronization framework," *Proceedings of the Combustion Institute*, vol. 37, no. 4, pp. 5315–5323, 2019.

[149] K. Moon, H. Jegal, J. Gu, and K. T. Kim, "Combustion-acoustic interactions through cross-talk area between adjacent model gas turbine combustors," *Combustion and Flame*, vol. 202, pp. 405–416, 2019.

[150] K. Moon, Y. Guan, L. K. Li, and K. T. Kim, "Mutual synchronization of two flame-driven thermoacoustic oscillators: Dissipative and time-delayed coupling effects," *Chaos: An Interdisciplinary Journal of Nonlinear Science*, vol. 30, no. 2, p. 023 110, 2020.

[151] K. Okamoto, A. Kijima, Y. Umeno, and H. Shima, "Synchronization in flickering of three-coupled candle flames," *Scientific reports*, vol. 6, p. 36 145, 2016.

[152] A. Prasad, S. K. Dana, R. Karnatak, J. Kurths, B. Blasius, and R. Ramaswamy, "Universal occurrence of the phase-flip bifurcation in time-delay coupled systems," *Chaos: An Interdisciplinary Journal of Nonlinear Science*, vol. 18, no. 2, p. 023 111, 2008.

[153] A. Pikovsky, J. Kurths, M. Rosenblum, and J. Kurths, *Synchronization: a universal concept in nonlinear sciences*. Cambridge university press, 2003, vol. 12.

[154] G. Saxena, A. Prasad, and R. Ramaswamy, "Amplitude death: The emergence of stationarity in coupled nonlinear systems," *Physics Reports*, vol. 521, no. 5, pp. 205–228, 2012.

[155] A. Koseska, E. Volkov, and J. Kurths, "Oscillation quenching mechanisms: Amplitude vs. oscillation death," *Physics Reports*, vol. 531, no. 4, pp. 173–199, 2013.

[156] N. Thomas, S. Mondal, S. A. Pawar, and R. Sujith, "Effect of time-delay and dissipative coupling on amplitude death in coupled thermoacoustic oscillators," *Chaos: An Interdisciplinary Journal of Nonlinear Science*, vol. 28, no. 3, p. 033 119, 2018.

[157] A. Gergely, B. Sándor, C. Paizs, R. Tötös, and Z. Néda, "Flickering candle flames and their collective behavior," *Scientific reports*, vol. 10, no. 1, pp. 1–13, 2020.

[158] C. Fox, "A generalization of the cauchy principal value," *Canadian Journal of Mathematics*, vol. 9, pp. 110–117, 1957.

[159] I. I. Blekhman, *Synchronization in science and technology*. ASME press, 1988.

[160] L. Wei-Qing, Y. Jun-Zhong, and X. Jing-Hua, "Experimental observation of partial amplitude death in coupled chaotic oscillators," *Chinese Physics*, vol. 15, no. 10, p. 2260, 2006.

[161] W. Liu, J. Xiao, and J. Yang, "Partial amplitude death in coupled chaotic oscillators," *Physical Review E*, vol. 72, no. 5, p. 057 201, 2005.

[162] D. R. Reddy, A. Sen, and G. L. Johnston, "Time delay effects on coupled limit cycle oscillators at hopf bifurcation," *Physica D: Nonlinear Phenomena*, vol. 129, no. 1-2, pp. 15–34, 1999.

[163] R. N. Madan, *Chua's circuit: a paradigm for chaos*. World Scientific Publishing Co., 1993.

[164] D. Biswas, N. Hui, and T. Banerjee, "Amplitude death in intrinsic time-delayed chaotic oscillators with direct–indirect coupling: The existence of death islands," *Nonlinear Dynamics*, vol. 88, no. 4, pp. 2783–2795, 2017.

[165] R. Dodla, A. Sen, and G. L. Johnston, "Phase-locked patterns and amplitude death in a ring of delay-coupled limit cycle oscillators," *Physical Review E*, vol. 69, no. 5, p. 056 217, 2004.

[166] R. Xiao, Z. Sun, X. Yang, and W. Xu, "Emergence of death islands in fractional-order oscillators via delayed coupling," *Communications in Nonlinear Science and Numerical Simulation*, vol. 69, pp. 168–175, 2019.

[167] R. Xiao, Z. Sun, X. Yang, and W. Xu, "Amplitude death islands in globally delay-coupled fractional-order oscillators," *Nonlinear Dynamics*, vol. 95, no. 3, pp. 2093–2102, 2019.

[168] F. M. Atay, "Total and partial amplitude death in networks of diffusively coupled oscillators," *Physica D: Nonlinear Phenomena*, vol. 183, no. 1-2, pp. 1–18, 2003.

[169] W. Zou and M. Zhan, "Partial time-delay coupling enlarges death island of coupled oscillators," *Physical Review E*, vol. 80, no. 6, p. 065 204, 2009.

[170] D. R. Reddy, A. Sen, and G. L. Johnston, "Experimental evidence of time-delay-induced death in coupled limit-cycle oscillators," *Physical Review Letters*, vol. 85, no. 16, p. 3381, 2000.

[171] M. G. Rosenblum, A. S. Pikovsky, and J. Kurths, "From phase to lag synchronization in coupled chaotic oscillators," *Physical Review Letters*, vol. 78, no. 22, p. 4193, 1997.

[172] S. Taherion and Y.-C. Lai, "Observability of lag synchronization of coupled chaotic oscillators," *Physical Review E*, vol. 59, no. 6, R6247, 1999.

[173] T. Biwa, S. Tozuka, and T. Yazaki, "Amplitude death in coupled thermoacoustic oscillators," *Physical Review Applied*, vol. 3, no. 3, p. 034 006, 2015.

[174] L. Rubchinsky and M. Sushchik, "Disorder can eliminate oscillator death," *Physical Review E*, vol. 62, no. 5, p. 6440, 2000.

[175] J. Yang, "Transitions to amplitude death in a regular array of nonlinear oscillators," *Physical Review E*, vol. 76, no. 1, p. 016 204, 2007.

[176] H. C. Mongia, T. Held, G. Hsiao, and R. Pandalai, "Challenges and progress in controlling dynamics in gas turbine combustors," *Journal of Propulsion and Power*, vol. 19, no. 5, pp. 822–829, 2003.

[177] R. Ciardiello, "Transient phenomena in annular combustors," Ph.D. dissertation, University of Cambridge, 2021.

[178] J.-F. Bourgouin, D. Durox, J. Moeck, T. Schuller, and S. Candel, "A new pattern of instability observed in an annular combustor: The slanted mode," *Proceedings of the Combustion Institute*, vol. 35, no. 3, pp. 3237–3244, 2015.

[179] G. Ramachandran, A. K. Dutta, H. Durairaj, and S. Chaudhuri, "On the interaction of swirling flames in a lean premixed combustor," *Journal of Engineering for Gas Turbines and Power*, vol. 142, no. 3, 2020.

[180] C. Ruan, L. Zhang, F. Chen, *et al.*, "Thermoacoustic instability characteristics and flame/flow dynamics in a multinozzle lean premixed gas turbine model combustor operated with high carbon number hydrocarbon fuels," *Energy & Fuels*, vol. 35, no. 2, pp. 1701–1714, 2021.

[181] B. J. Dolan, R. Villalva Gomez, S. Pack, and E. J. Gutmark, "Effect of nozzle spacing on nox emissions and lean operability," in *54th AIAA Aerospace Sciences Meeting*, 2016, p. 2150.

[182] W. Y. Kwong and A. M. Steinberg, "Blowoff and reattachment dynamics of a linear multinozzle combustor," *Journal of Engineering for Gas Turbines and Power*, vol. 141, no. 1, p. 011 015, 2019.

[183] W. Y. Kwong and A. M. Steinberg, "Effect of internozzle spacing on lean blow-off of a linear multinozzle combustor," *Journal of Propulsion and Power*, vol. 36, no. 4, pp. 540–550, 2020.

[184] S. Nair and T. Lieuwen, "Near-blowoff dynamics of a bluff-body stabilized flame," *Journal of Propulsion and power*, vol. 23, no. 2, pp. 421–427, 2007.

[185] D. Kim, J. Park, D. Han, and K. T. Kim, "Symmetry-breaking for the control of combustion instabilities of two interacting swirl-stabilized flames," *Combustion and Flame*, vol. 194, pp. 180–194, 2018.

[186] J. A. Perea and J. Harer, "Sliding windows and persistence: An application of topological methods to signal analysis," *Foundations of Computational Mathematics*, vol. 15, no. 3, pp. 799–838, 2015.

[187] M. Gidea and Y. Katz, "Topological data analysis of financial time series: Landscapes of crashes," *Physica A: Statistical Mechanics and its Applications*, vol. 491, pp. 820–834, 2018.

[188] M. Gidea, D. Goldsmith, Y. Katz, P. Roldan, and Y. Shmalo, "Topological recognition of critical transitions in time series of cryptocurrencies," *Physica A: Statistical mechanics and its applications*, vol. 548, p. 123 843, 2020.

[189] A. Myers, E. Munch, and F. A. Khasawneh, "Persistent homology of complex networks for dynamic state detection," *Physical Review E*, vol. 100, no. 2, p. 022 314, 2019.

[190] P. Bendich, J. S. Marron, E. Miller, A. Pieloch, and S. Skwerer, "Persistent homology analysis of brain artery trees," *The annals of applied statistics*, vol. 10, no. 1, p. 198, 2016.

[191] M. Robinson, *Topological signal processing*. Springer, 2014, vol. 81.

[192] C. Li, M. Ovsjanikov, and F. Chazal, "Persistence-based structural recognition," in *Proceedings of the IEEE Conference on Computer Vision and Pattern Recognition*, 2014, pp. 1995–2002.

[193] F. A. Khasawneh and E. Munch, "Chatter detection in turning using persistent homology," *Mechanical Systems and Signal Processing*, vol. 70, pp. 527–541, 2016.

[194] J. R. Tempelman and F. A. Khasawneh, "A look into chaos detection through topological data analysis," *Physica D: Nonlinear Phenomena*, vol. 406, p. 132 446, 2020.

[195] S. Majumdar and A. K. Laha, "Clustering and classification of time series using topological data analysis with applications to finance," *Expert Systems with Applications*, vol. 162, p. 113 868, 2020.

[196] C. J. Tralie and J. A. Perea, "(quasi) periodicity quantification in video data, using topology," *SIAM Journal on Imaging Sciences*, vol. 11, no. 2, pp. 1049–1077, 2018.

[197] S. Emrani, T. Gentimis, and H. Krim, "Persistent homology of delay embeddings and its application to wheeze detection," *IEEE Signal Processing Letters*, vol. 21, no. 4, pp. 459–463, 2014.

[198] A. Dirafzoon, N. Lokare, and E. Lobaton, "Action classification from motion capture data using topological data analysis," in *2016 IEEE global conference on signal and information processing (globalSIP)*, IEEE, 2016, pp. 1260–1264.

[199] F. Erden and A. E. Cetin, "Period estimation of an almost periodic signal using persistent homology with application to respiratory rate measurement," *IEEE Signal Processing Letters*, vol. 24, no. 7, pp. 958–962, 2017.

[200] S. Majumder, F. Apicella, F. Muratori, and K. Das, "Detecting autism spectrum disorder using topological data analysis," in *ICASSP 2020-2020 IEEE International Conference on Acoustics, Speech and Signal Processing (ICASSP)*, IEEE, 2020, pp. 1210–1214.

[201] J. Brown and T. Gedeon, "Structure of the afferent terminals in terminal ganglion of a cricket and persistent homology," *PloS one*, vol. 7, no. 5, e37278, 2012.

[202] X. Xu, N. Drougard, and R. N. Roy, "Topological data analysis as a new tool for eeg processing," *Frontiers in Neuroscience*, vol. 15, 2021.

[203] N. Ravishanker and R. Chen, "An introduction to persistent homology for time series," *Wiley Interdisciplinary Reviews: Computational Statistics*, vol. 13, no. 3, e1548, 2021.

[204] F. Chazal and B. Michel, "An introduction to topological data analysis: Fundamental and practical aspects for data scientists," *Frontiers in artificial intelligence*, vol. 4, 2021.

[205] M. Rucco, F. Castiglione, E. Merelli, and M. Pettini, "Characterisation of the idiotypic immune network through persistent entropy," in *Proceedings of ECCS 2014*, Springer, 2016, pp. 117–128.

[206] N. Atienza, L. M. Escudero, M. J. Jimenez, and M. Soriano-Trigueros, "Characterising epithelial tissues using persistent entropy," in *International Workshop on Computational Topology in Image Context*, Springer, 2019, pp. 179–190.

[207] A. Zomorodian and G. Carlsson, "Computing persistent homology," *Discrete & Computational Geometry*, vol. 33, no. 2, pp. 249–274, 2005.

[208] H. Edelsbrunner, D. Letscher, and A. Zomorodian, "Topological persistence and simplification," in *Proceedings 41st annual symposium on foundations of computer science*, IEEE, 2000, pp. 454–463.

[209] H. Edelsbrunner and J. L. Harer, *Computational topology: an introduction*. American Mathematical Society, 2022.

[210] N. Saul and C. Tralie, "Scikit-tda: Topological data analysis for python," *URL https://doi. org/10.5281/zenodo*, vol. 2533369, 2019.

[211] A. Karan and A. Kaygun, "Time series classification via topological data analysis," *Expert Systems with Applications*, vol. 183, p. 115 326, 2021.

[212] J. Berwald, M. Gidea, and M. Vejdemo-Johansson, "Automatic recognition and tagging of topologically different regimes in dynamical systems," *arXiv preprint arXiv:1312.2482*, 2013.

[213] M. Rucco, R. Gonzalez-Diaz, M.-J. Jimenez, *et al.*, "A new topological entropy-based approach for measuring similarities among piecewise linear functions," *Signal Processing*, vol. 134, pp. 130–138, 2017.

[214] A. D. Myers, F. A. Khasawneh, and B. T. Fasy, "Anapt: Additive noise analysis for persistence thresholding," *Foundations of Data Science*, vol. 4, no. 2, p. 243, 2022.

[215] A. M. Fraser and H. L. Swinney, "Independent coordinates for strange attractors from mutual information," *Physical review A*, vol. 33, no. 2, p. 1134, 1986.

Signature of the Candidate : Arijit Bhattacharya

(Arijit Bhattacharya)

Date : 2.11.2022